NORTHWESTERN UNIVERSITY

# Graphene-Mediated Cathode Interfaces for Lithium-Ion Batteries

A DISSERTATION

SUBMITTED TO THE GRADUATE SCHOOL

IN PARTIAL FULFILLMENT OF THE REQUIREMENTS

for the degree

DOCTOR OF PHILOSOPHY

Field of Materials Science and Engineering

By

Norman Luu

EVANSTON, ILLINOIS

June 2023

## ABSTRACT

Graphene-Mediated Cathode Interfaces for Lithium-Ion Batteries

Norman Luu

Lithium-ion battery technology is a critically important component of the emerging renewable energy infrastructure. Since battery technology was first commercialized in the 1990s, significant progress has been made in materials development, motivated by the prospect of higher energy and power densities, increased cycling longevity, and faster charging and discharging rates. However, new strategies to enhance the performance of battery materials can be realized by drawing inspiration from other scientific fields that have simultaneously experienced exponential growth. Nanomaterials present exciting value propositions for energy storage technologies due to the ability to control and engineer unique optoelectronic properties that emerge at the atomically thin limit. Therefore, integrating materials and knowledge from both fields provides a unique opportunity to significantly improve lithium-ion battery technology.

This thesis centers around the combination of graphene and lithium-ion battery cathode materials. Through microstructural control of battery electrodes, material and cell testing, and extensive materials characterization, this thesis explores the impact of graphene coatings on the performance of Ni-rich layered oxides across wide operational conditions. Controlling the sensitive surface chemistry of $LiNi_{0.8}Al_{0.15}Co_{0.05}O_2$ (NCA) nanoparticles enables subsequent graphene coating procedures, which improve cycle life and rate capability performance at low temperatures. Similarly, graphene coatings are found to mitigate the high-voltage chemomechanical degradation of $LiNi_{0.5}Mn_{0.3}Co_{0.2}O_2$ (NMC532), suggesting a relationship

between particle surface conductivity and the severity of such degradation. Finally, the extreme ambient sensitivity of $LiNiO_2$ (LNO) can be easily addressed by a hydrophobic surface coating composed of graphene and ethyl cellulose, which itself is conducive to excellent electrochemical behavior.

Together, these results demonstrate that graphene coatings are a facile and effective method to enhance the electrochemical performance of Ni-rich layered oxide cathodes for lithium-ion batteries. This work has an immediate impact for improving the library of commercially relevant cathode materials used for consumer electronics and electric vehicles. Although demonstrated here for Ni-rich layered oxides, this thesis establishes the prospect of utilizing graphene to control degradation and enhance reaction kinetics in other emerging energy storage systems. Overall, this work highlights the importance of understanding and controlling degradation for next-generation electrochemical energy storage technologies.

## ACKNOWLEDGMENTS

As I look back on my PhD, I find myself reflecting on the many twists and turns that this journey has taken me through. It has been challenging and exciting, confusing and humbling, and filled with many more questions than I can count. Fortunately, I was surrounded by an incredible group of people who encouraged me to become a more well-rounded scientist, a deeper critical thinker, and a better individual. I believe that we are reflections of those closest to us, and I am grateful for having interacted with so many people who have been a source of inspiration, friendship, and support. There are far too many people for me to thank, including those who are not explicitly mentioned here – so if we have crossed paths, thank you for helping me along my journey.

First, I would like to thank Professor Mark Hersam for his mentorship, advice, and guidance over the last 8 years. He took me into his research group as an undergraduate student and has seen me grow into the researcher and critical thinker that I am today. During my PhD, Mark never hesitated to ask difficult questions that ultimately pushed my research to new directions and greater heights. I have drawn and continue to draw inspiration from his approach to science, advocacy, leadership, persistence, intellectual curiosity, and unparalleled rebounding ability on the basketball court.

Thank you to my thesis committee members: Professor Michael Bedzyk, Professor Vinayak Dravid, and Dr. Eungje Lee. They provided vital feedback and were eager to join scientific collaborations, which helped me significantly on numerous projects during my PhD. Special thanks to Professor Bedzyk, who worked closely with me when we revamped the laboratory sessions for MSE 361: Crystallography and Diffraction.

The many projects that I worked on during my PhD would not have been possible without the expertise and guidance of my collaborators. Thank you to Dr. Elahe Moazzen, Dr. Ozge Kahvecioglu, Dr. Kun He, Dr. Wenyun Li, Professor Xiaobing Hu, and Professor Scott Barnett. They provided me with the materials and tools to tackle my investigations and steered me in the right direction when I drifted off-course. I also relied on Dr. Carla Shute and the MatCI facility, Dr. Xinqi Chen and the Keck-II facility, Dr. Bruce Buchholz and the PLD Core, Rebecca Sponenburg and the Quantiative Bio-element Imaging Center, Jerry Carsello and the Jerome B. Cohen X-Ray Diffraction Facility, Tirzah Abbott and the NUANCE Center, and Dr. Mike Guise and Dr. Denis Keane at the Advanced Photon Source.

I also would like to acknowledge the funding sources that were vital to this research – the CEES EFRC at Argonne National Laboratory, the Exelon Corporation, The Graduate School, and the NSF. Damien Despinoy and Volexion generously provided nickel-rich and lithium-rich cathode materials that were vital to the research conducted in the latter half of my PhD. In addition, my research would not have been possible without the support of the Office of Research Safety, the Fisher Stockroom staff, and the Materials Science and Engineering office staff. I would also like to individually thank Michele McManmon, who has been a vital part of nearly every purchase order I can remember making in graduate school.

I would not be writing my thesis without my mentors. Stretching back to my undergraduate days, Professor Kathleen Stair has been an incredible source of technical knowledge and advice, an unflinching advocate for the materials science department, and a large reason why I decided to pursue a PhD at all. Dr. Kan-Sheng Chen, my first research mentor in undergrad, channeled my

overzealousness into scientific curiosity and sparked my excitement for energy storage. I jumped headfirst into battery science with Dr. Jin-Myoung Lim during my first year in graduate school. I gained a huge appreciation for his approach to cell testing, his unfailing ability to generate new ideas, and his skill for roasting coffee beans to make the best cup of coffee that Cook Hall has ever seen. Finally, Dr. Kyu-Young Park taught me about poise, scientific expertise, and professionalism in a way that I continue to draw inspiration from. I would not be here if not for him.

I would also like to thank the members of the Hersam Group, who have been excellent scientific collaborators and constant sources of joy and laughter. My time in Cook 1055 was incredibly memorable thanks to Julia Downing, Dr. Ana Moraes, Sonal Rangnekar, Dr. David Lam, Dr. Sam Amsterdam, Dr. Jin-Myoung Lim, Nathan Bradshaw, Janan Hui, Dr. Dominic Goronzy, Santiago Diaz-Arauzo, and the leftover snacks piled on the server computer desk after group meetings. I will cherish cursing at the heating pipes together every winter. Thank you to the members of the battery subgroup over the years, who I have learned so much from: Dr. Kyu-Young Park, Dr. Jin-Myoung Lim, Carlos Torres, Cory Thomas West, Dr. Woo Jin Hyun, Mark Tan, Frank Huang, Dr. Lei Li, Dr. Kan-Sheng Chen, and Dr. Jungwoo Ted Seo. Our conversations ranged from materials processing and electrochemistry fundamentals to the myriad of challenges surrounding lithium-ion battery commercialization. Through these talks, I gained a uniquely holistic view of battery development that would have otherwise been hard to find in graduate school. Furthermore, I interacted with many other Hersam Group colleagues over the last several years. Although I may not be a co-author on a publication with many of my colleagues, our day-to-day conversations were nonetheless critical to my success. I often relied on their expertise for materials characterization and processing, for everything from answering quick questions about vacuum

filtration to helping me fit spectroscopy data. In no particular order: Dr. Suyog Padgaonkar, Lindsay Chaney, Lidia Kuo, Dr. Shay Wallace, Tyler Gish, Dr. Dmitry Lebedev, Professor Vinod Sangwan, Thomas Song, Justin Qian, Eden Aklile, Hong Youl Mike Park, Dr. Qiucheng Li, Maryam Khalaj, Anushka Dasgupta, Riddhi Ananth, Stephanie Liu, Brendan Kerwin, Mitchell Walker, Dr. Beata Szydłowska, Dr. Shreyash Hadke, Dr. Iqbal Utama, Dr. Xiaodong Yan, Dr. Min-A Kang, Dr. Seung Won Lee, Dr. Xiaoyu Sui, Dr. Paul Das, Dr. Nicholas Williams, Dr. Linda Guiney, Dr. Hocheon Yoo, Dr. William A. Gaviria Rojas, Dr. Jiangtan Yuan, Dr. Megan Beck, Dr. Hadallia Bergeron, Professor Xiaolong Liu, Professor Ethan Secor, Professor Joohoon Kang, Dr. Itamar Balla, Dr. Spencer Wells, and Dr. Karl Putz.

To my mentees – Patricia Lohman Meza, Andre M. Tayamen, and Davy Zeng – thank you for taking a chance on me. I am truly grateful to have been a part of all of your journeys and I cannot wait to see what is in store for you. I apologize for all our meetings that could have been an email.

Beginning in the second year of my PhD, I held weekly meetings with researchers across the Materials Science and Engineering department who were also working on lithium-ion battery research. Isaac Dyer, Dr. Elahe Moazzen, Dr. Cesar Villa, Dr. Kent Griffith, Shane Patel, and Dr. Colin Campbell made the battery subgroup at Northwestern a true source of collaboration and discussion. I am glad that we were able to share resources and knowledge with each other and write a few interesting articles along the way.

Beyond research, I invested a significant part of my time at Northwestern on expanding education outreach with *Splash at Northwestern*. Having grown up in Chicago, I was enthusiastic about joining an organization aimed at giving back to local communities by providing educational

enrichment to Chicagoland high school students. I am extremely grateful for Dr. Shelby Hatch, Dr. David Lam, Dr. Stephanie Ger, Dr. Chris Mizzi, Dr. Michael Moody, Dr. Tiffany Ly, Dr. Lionel Fiske, and Dr. Petras Swissler, who brought me into *Splash* during my first year of graduate school. Over the next three years, I got the opportunity to work many like-minded people who shared my passion for education outreach: Shreya Chimpiri, Professor Leslie Hamachi, Zhiheng Sheng, Thomas Sheridan, Chloe Chow, Rohith Jayaraman, Ethan Lipka, Zach Ladwig, and the folks at Learning Unlimited across the country. Together, we grew the program– even holding a virtual Splash event in 2020 – and I am excited to see how *Splash* will evolve in years to come.

To my high school debate coaches Mr. Robb Berry and Aaron Davis – over 10 years ago, you helped me gain a work ethic and curiosity that has carried me through this journey. Thank you.

To my teammates and friends from Tesla – despite only working with you all for a few short months, I learned so much about failure analysis, metallurgy, and performing world-class engineering at scale. Thank you for answering my many questions, giving me the freedom to search for answers, and supporting my professional growth.

To Dr. Nick Geisendorfer, Dr. Liban Jibril, and Matthew Cheng: even though our schedules were hectic, I will always treasure how we never hesitated to grab a meal when one of us wanted to catch up and commiserate. To my IM basketball teammates: I am glad that you were able to see me at my athletic peak.

To Carlos – you were an excellent collaborator and a more than excellent friend. As your roommate, I learned so much about food, Real Madrid, and your diabolical Catan strategies. I am

extremely grateful that we both survived the pandemic together, and I will be rooting for you and the many successes in your future.

To my friends from high school, undergrad, and whom I have just recently met – thank you for always welcoming me with open arms and reaching out to catch up. Our board game nights, climbing sessions, Dungeons and Dragons afternoons, potlucks, road trips, and holiday celebrations helped keep me grounded and sane these last few years.

To Sarah, Terence, Helen, Steven, Jackson, and Nari – I would not have been able to make it through this journey without you, and I value your advice more than you know. Our Friday dinners are some of my most treasured memories – especially our cast-iron pizza nights. Let's say that I won all those Mario Kart races.

Most of all, I am eternally grateful to my family. Growing up in Chicago, I was incredibly fortunate to have my aunts, uncles, and cousins close by. I loved getting together to celebrate birthdays, weddings, and for no real reason at all. Their support has meant the world to me.

To my brothers – I have learned tremendously from the way you carry yourselves and the ways that you help others. Kyle – you continually show me how to take things less seriously and to make room to breathe. Eric – I am inspired by how your determination, passion, and sense of responsibility weave through everything you do.

To my parents – thank you for your unwavering support, love, and sacrifice. You were here when I started this journey, and I am so happy that you can see me at its conclusion. This is for you.

Finally, to my partner Annie – your patience, presence, and love have made tough times feel so much easier. You inspire me every day. Thank you for believing in me.

## LIST OF ABBREVIATIONS

| | |
|---|---|
| 1C | current required to charge or discharge in 1 hour |
| 2D | two-dimensional |
| 3D | three-dimensional |
| APS | Advanced Photon Source |
| CB | carbon black |
| CCCV | constant current-constant voltage cycling |
| CEI | cathode-electrolyte interphase |
| $cm^{-1}$ | wavenumber |
| $cm^2\ V^{-1}s^{-1}$ | carrier mobility |
| D50 | median particle size |
| DEMS | differential electrochemical mass spectrometry |
| DFT | density functional theory |
| DRIFTS | diffuse reflectance infrared Fourier transform spectroscopy |
| DRT | distribution function of relaxation times |
| DRX | disordered rocksalt |
| EC | ethyl cellulose |
| EC/EMC | ethylene carbonate/ethyl methyl carbonate |
| EELS | electron energy loss spectroscopy |
| EIS | electrochemical impedance spectroscopy |
| eV | electron volt |

| | |
|---|---|
| FCE | first cycle Coulombic efficiency |
| FFT | fast Fourier transform |
| FIB | focused ion beam |
| FTIR | Fourier transform infrared spectroscopy |
| g | gram |
| g $cc^{-1}$ | density |
| GrEC | graphene-ethyl cellulose |
| Gr-nNCA | graphene-coated NCA nanoparticles |
| Gr-R-nNCA | graphene-coated refined NCA nanoparticles |
| HAADF | high angle annular dark field |
| HF | hydrofluoric acid |
| HOMO | highest occupied molecular orbital |
| ICP-MS | inductively coupled plasma mass spectrometry |
| L | Layered |
| LCO | lithium cobalt oxide, $LiCoO_2$ |
| LFP | lithium iron phosphate, $LiFePO_4$ |
| LIB | lithium-ion battery |
| LMNA | lithium manganese nickel aluminum oxide |
| LMNO | lithium manganese nickel oxide |
| LMO | lithium manganese oxide, $LiMn_2O_4$ |
| LMR-NMC | lithium-and manganese-rich NMC |

| | |
|---|---|
| LNO | lithium nickel oxide, $LiNiO_2$ |
| LNO-Gr | LNO coated with graphene |
| LNO-Gr-EC | LNO coated with graphene and ethyl cellulose |
| LPE | liquid phase exfoliation |
| LUMO | lowest unoccupied molecular orbital |
| mAh | capacity |
| mAh $cm^{-3}$ | volumetric capacity |
| mAh $g^{-1}$ | gravimetric capacity |
| mg | milligram |
| mg $cm^{-2}$ | electrode loading |
| MPa | Megapascal |
| MS | mass spectrometry |
| MWCNT | multiwalled carbon nanotubes |
| N:P | negative to positive areal capacity ratio |
| NCA | lithium nickel cobalt aluminum oxide, $LiNi_{0.8}Co_{0.15}Al_{0.05}O_2$ |
| NCM | see NMC |
| NMC | lithium nickel manganese cobalt oxide |
| NMC111 | lithium nickel manganese cobalt oxide, $LiNi_{0.33}Mn_{0.33}Co_{0.33}O_2$ |
| NMC532 | lithium nickel manganese cobalt oxide, $LiNi_{0.5}Mn_{0.3}Co_{0.2}O_2$ |
| NMC622 | lithium nickel manganese cobalt oxide, $LiNi_{0.6}Mn_{0.2}Co_{0.2}O_2$ |
| NMC811 | lithium nickel manganese cobalt oxide, $LiNi_{0.8}Mn_{0.1}Co_{0.1}O_2$ |

| | |
|---|---|
| NMC-CBPVDF | NMC electrode with carbon black and polyvinylidene fluoride |
| NMC-GrEC | graphene-coated NMC electrode |
| NMP | N-Methyl-2-pyrrolidone |
| nNCA | NCA nanoparticles |
| PEDOT | poly(3,4-ethylenedioxythiophene) |
| PFTE | polyfluorotetraethylene |
| ppb | part per billion |
| ppm | part per million |
| PVDF | polyvinylidene fluoride |
| RF | R-factor |
| rGO | reduced graphene oxide |
| RH | relative humidity |
| R-nNCA | refined NCA nanoparticles |
| RPM | rotations per minute |
| RQ | Randles circuit |
| RS | Rocksalt |
| S | Spinel |
| SEI | solid-electrolyte interphase |
| SEM | scanning electron microscopy |
| SOC | state of charge |
| SR-PXRD | synchrotron radiation powder X-ray diffraction |

| | |
|---|---|
| STEM | scanning transmission electron microscopy |
| TGA | thermogravimetric analysis |
| TM | transition metal |
| TM-O | transition metal-oxygen |
| TOF-SIMS | time-of-flight secondary ion mass spectrometry |
| TVR | Taylor Vortex Reactor |
| V | volt |
| VOC | open circuit voltage |
| XANES | X-ray absorption near edge spectroscopy |
| XPS | X-ray photoelectron spectroscopy |
| XRD | X-ray diffraction |

*For my family.*

TABLE OF CONTENTS

ABSTRACT ..... 3

ACKNOWLEDGMENTS ..... 5

LIST OF ABBREVIATIONS ..... 12

LIST OF FIGURES ..... 23

LIST OF TABLES ..... 34

CHAPTER 1 : INTRODUCTION ..... 35

1.1 Motivation and Thesis Statement ..... 36

1.2 Lithium-Ion Batteries ..... 38

1.2.1 Lithium-Ion Battery Fabrication ..... 39

1.2.2 Cathode Materials for Lithium-Ion Batteries ..... 40

1.3 Degradation in Lithium-Ion Batteries ..... 47

1.3.1 Electrolyte Decomposition and SEI Formation ..... 48

1.3.2 Transition Metal Dissolution ..... 51

1.3.3 Gas Evolution ..... 54

1.3.4 Lithium Impurities ..... 57

1.3.5 Surface Phase Formation ..... 60

1.3.6 Chemomechanical Degradation ..... 62

1.3.6.1 Primary Particle Level ..... 63

1.3.6.2 Secondary Particle Level ..... 66

1.3.6.3 Electrode Level ..... 68

1.4 Mitigating Interfacial Degradation ..... 70

1.4.1 Oxide Coatings ..... 70
1.4.2 Doping ..... 70
1.4.3 Grain Boundary Engineering ..... 72
1.4.4 Two-Dimensional Materials: Graphene ..... 74
1.5 Thesis Organization and Roadmap ..... 78
CHAPTER 2 : ENHANCING NANOSTRUCTURED NICKEL-RICH LITHIUM-ION BATTERY CATHODES VIA SURFACE STABILIZATION ..... 81
2.1 Overview ..... 82
2.2 Background ..... 82
2.3 NCA Surface Impurity Characterization ..... 86
2.4 Assessing Graphene Coatings on NCA ..... 90
2.5 Comparative Electrochemical Characterization ..... 93
2.6 Experimental Methods ..... 99
2.6.1 NCA Synthesis ..... 99
2.6.2 Graphene Exfoliation ..... 100
2.6.3 Electrode Fabrication ..... 101
2.6.4 Electrochemical Testing ..... 102
2.6.5 Materials Characterization ..... 103
2.7 Summary ..... 104
CHAPTER 3 : ELUCIDATING AND MITIGATING HIGH-VOLTAGE INTERFACIAL CHEMOMECHANICAL DEGRADATION OF NICKEL-RICH LITHIUM-ION BATTERY CATHODES VIA CONFORMAL GRAPHENE COATING ..... 106

3.1 Overview ..... 107
3.2 Background ..... 107
3.3 Materials Characterization ..... 110
3.4 Electrochemical Characterization ..... 114
3.4.1 Galvanostatic Cycling ..... 114
3.4.2 Electrochemical Impedance Spectroscopy ..... 118
3.5 Postmortem Characterization ..... 126
3.5.1 High-Resolution X-Ray Diffraction ..... 126
3.5.2 X-Ray Photoelectron Spectroscopy ..... 129
3.5.3 Scanning Transmission Electron Microscopy (STEM) Analysis ..... 132
3.5.4 Inductively Coupled Plasma Mass Spectrometry ..... 134
3.5.5 Scanning Electron Microscopy ..... 135
3.5.6 Discussion ..... 139
3.6 Summary ..... 144
3.7 Experimental Methods ..... 145
3.7.1 NMC Synthesis ..... 145
3.7.2 Graphene Exfoliation ..... 145
3.7.3 Electrode Fabrication ..... 146
3.7.4 Electrochemical Characterization ..... 148
3.7.5 Raman Spectroscopy ..... 148
3.7.6 X-Ray Diffraction ..... 148
3.7.7 Inductively Coupled Plasma Mass Spectrometry ..... 149

3.7.8 X-Ray Photoelectron Spectroscopy ..... 150
3.7.9 Scanning Electron Microscopy ..... 150
3.7.10 Scanning Transmission Electron Microscopy ..... 151
CHAPTER 4 : ENABLING AMBIENT STORAGE OF $LiNiO_2$ LITHIUM-ION BATTERY CATHODES VIA A CONFORMAL, HYDROPHOBIC GRAPHENE-ETHYL CELLULOSE COATING ..... 152
4.1 Overview ..... 153
4.2 Background ..... 153
4.3 Impact of Humid $CO_2$ Exposure ..... 154
4.4 Behavior of Graphene-Coated LNO ..... 163
4.5 Summary ..... 174
4.6 Experimental Methods ..... 176
4.6.1 LNO Synthesis ..... 176
4.6.2 Graphene-Ethyl Cellulose Production ..... 176
4.6.3 Humidity Exposure ..... 177
4.6.4 Electrode Fabrication ..... 177
4.6.5 Electrochemical Characterization ..... 178
4.6.6 Scanning Electron Microscopy ..... 180
4.6.7 X-Ray Photoelectron Spectroscopy ..... 180
4.6.8 Fourier Transform Infrared Spectroscopy ..... 180
4.6.9 Raman Spectroscopy ..... 181
4.6.10 Thermogravimetric Analysis ..... 181

CHAPTER 5 : FUTURE WORK ..... 183

5.1 Introduction to Future Work ..... 184

5.2 Stabilizing Anionic Redox in Next-Generation Cathode Materials ..... 184

5.3 Graphene-Cellulose Lithium Metal Composite Anodes ..... 185

5.4 Understanding Electrode-Level State-of-Charge Heterogeneity ..... 186

5.5 Improving Beyond-Li Chemistries ..... 187

CHAPTER 6 : CONCLUSIONS ..... 190

REFERENCES ..... 194

VITA ..... 233

## LIST OF FIGURES

**Figure 1.1**. Schematic of the operation of a lithium-ion battery. Electrons and lithium ions flow from the anode towards the cathode during discharge, and flow from the cathode towards the anode during charge. Reproduced with permission from ref [8]. Copyright 2013 Royal Society of Chemistry. ..... 39

**Figure 1.2.** Structure and electrochemical properties of prototypical cathode materials for lithium-ion batteries. (a-c) Schematic of (a) layered, (b) spinel, and (c) olivine crystal structures. The green spheres in (a-c) represent lithium, while transition metal octahedra are blue in (a) purple in (b), and in brown (c). Phosphate tetrahedra are shown in purple in (c). Reproduced with permission from ref [13]. (d-g) Voltage-capacity profiles for (d) layered $LiCoO_2$, (e) layered $LiNiO_2$, (f) spinel $LiMn_2O_4$, and (g) olivine $LiFePO_4$. Reproduced with permission from ref [14], ref [15], ref [16], and ref [17], respectively. Copyrights 2019 Royal Society of Chemistry, 2019 Wiley, 1999 IOP Publishing, and 2001 IOP Publishing, respectively. ..... 42

**Figure 1.3.** Electrochemical properties of NMCs. (a-d) Soft X-ray absorption spectroscopy of NMC532 reveals that Ni initially mediates redox, followed by the $Co^{3+/4+}$ redox couple at high SOCs. (a) Ni-$L_3$ and (b) Co-$L_3$ sXAS spectra of NMC532 in total fluorescence yield mode (top), with calculated TFY reference spectra (bottom). (c) Calculated average Ni oxidation state from sXAS spectra as a function of charging voltage. (d) Position of the Co sXAS main peak as a function of charging voltage. Reprinted (adapted) with permission from ref [33]. Copyright 2017 Elsevier. (e) Thermal stability, discharge capacity, and capacity retention for various NMC chemistries. Reproduced with permission from ref [34]. Copyright 2013 Elsevier. (f) Voltage-capacity profiles for various multicomponent NMC cathodes, showing higher Ni compositions achieve higher capacities at the same cutoff voltage. Reproduced with permission from ref [35]. Copyright 2019 American Chemical Society. ..... 44

**Figure 1.4.** Energy band diagram for the anode, cathode, and electrolyte in a lithium-ion battery. The difference between the voltages of the anode and cathode is the operating voltage of the cell ($V_{OC}$), while the difference between the operating voltages of the electrodes and the stability

window of the electrolyte can drive the formation of the SEI and CEI. Reproduced with permission from ref [60]. Copyright 2021 IOP Publishing. ..... 48

**Figure 1.5.** Driving forces and reaction products of electrolyte decomposition reactions. (a-b) Electrolyte decomposition reactions are driven by ethylene carbonate dissociation, which varies as a function of (a) state of charge and (b) transition metal content. Reprinted (adapted) with permission from ref [63]. Copyright 2017 American Chemical Society. (c) XPS C 1s and (d) O 1s spectra reveal increased spectral intensities associated with electrolyte decomposition products formed during cycling, including oligomers and fluorophosphate compounds. Reprinted (adapted) with permission from ref [61]. Copyright 2015 American Chemical Society. (e) The resulting decomposition layer is posited to have a mosaic structure composed of various solvent and salt degradation products. Reproduced with permission from ref [70]. Copyright 2017 Springer Nature. ..... 50

**Figure 1.6.** Evidence and origins of gas evolution in high-energy cathode materials. (a) *In-situ* gas evolution measurement during high-voltage cathode operation of layered materials. Dark blue: $CO_2$; yellow: $O_2$; light blue: CO. Adapted with permission from ref [52]. Copyright 2018 Elsevier. (b) Schematic of the electronic band structure of overlithiated layered oxides before (left) and after cycling (right). Adapted with permission from ref [89]. Copyright 2018 Springer Nature. (c) Oxygen vacancy formation energy for various layered lithium transition metal oxides. Adapted with permission from ref [90]. Copyright 2018 Wiley. (d) In-situ DEMS provides evidence of $O_2$ and $CO_2$ evolution that are coincident with structural phase transformations as LNO is electrochemically cycled. Reproduced with permission from ref [15]. Copyright 2019 Wiley. (e) Temperature- and Ni composition-dependent mass spectroscopy show that higher-Ni NMCs are more susceptible to gas evolution. Reproduced with permission from ref [91]. Copyright 2014 American Chemical Society. ..... 53

**Figure 1.7.** Ni-rich layered oxides are susceptible to the formation of lithium impurities. (a) Lithium impurities can cause slurry gelation, compromising subsequent electrode fabrication procedures. Adapted with permission from ref [104]. Copyright 2020 Wiley. (b-c) Bare NMC811 secondary particle (b) before storage and (c) after storage in humid CO2 for 1 day. Adapted with

permission from ref [105]. Copyright 2019 American Chemical Society (d) XPS O 1s spectra shows an increase in carbonate spectral intensities after NMC811 is stored in ambient conditions for 1 year. (e) Cycle life results of NMC811-graphite full cells made with fresh NMC powder, NMC powder stored in ambient conditions for 3 months, and powder stored for 1 year. (f) Mean discharge voltage vs. cycle number shows significant changes in the NMC discharge potential and no changes in the graphite discharge potential, indicating that the full-cell degradation was due to cathode degradation. Reproduced with permission from ref [106]. Copyright 2018 IOP Publishing. ..... 56

**Figure 1.8.** Surface phases in LIB cathode materials. (a) Annular dark field-STEM images of NMC taken along the R-3m[100] zone axis reveals the presence of surface rocksalt phases, which are further verified using local fast Fourier transform analysis of the (b) surface and of the (c) bulk. (d) STEM image of the scanning pathway for electron energy loss spectroscopy. (e) Mn L-edge EELS spectra acquired along the scanning pathway reveals that the TM surface chemistry is more reduced than the bulk. Adapted with permission from ref [85]. Copyright 2014 Springer Nature. (f) Relationship between oxygen evolution and stacking structural change of LNO. (g) Stacking structural changes in layered LNO near the surface. (h) High-resolution image of the region boxed in (g). Adapted with permission from ref [56]. Copyright 2021 Wiley. (i) Schematic showing that surface phases compromise the long-term cycling performance of stoichiometric NMC due to "pinning" of Li layers, which limits the cyclability of the material.[64] Adapted with permission from ref [116]. Copyright 2020 Springer Nature. (j) HAADF-STEM image taken along the R-3m[110] zone axis reveals the presence of a surface phase on $Li[Ni_{1/5}Li_{1/5}Mn_{3/5}]O_2$. Reproduced with permission from ref [117]. Copyright 2011 Royal Society of Chemistry. ..... 59

**Figure 1.9.** Primary particle level degradation. Lattice parameter changes of the (a) *a*-lattice parameter and (b) *c*-lattice parameter for various compositions of NCM cathodes. Reproduced with permission from ref [35]. Copyright 2019 American Chemical Society. (c,d) Cracks along (003) planes for a NMC622 cathode after 100 cycles at 2.7–4.8 V as imaged by high angle annular dark field scanning transmission electron microscopy (HAADF-STEM). The scale bars are 10 nm in (c) and 2 nm in (d). Adapted with permission from ref [54]. (e) Schematic of cracking pathways induced by a (003) rock salt platelet. Green arrow: formation of rock salt phase along the (003)

plane. Purple arrow: formation of rock salt phase on the particle surface. Adapted with permission from ref [131]. Copyright 2017 American Chemical Society. (f) Bending induced by the local O1 stacking transition in $LiNiO_2$ as characterized by transmission electron microscopy. Adapted with permission from ref [56]. Copyright 2021 Wiley. ..... 63

**Figure 1.10.** Nonuniform lithium distributions at the particle level lead to particle fracture. (a-d) Spatially resolved Ni K-edge X-ray absorption near edge spectroscopy (XANES) mapping shows that NCM-622 exhibits SOC heterogeneity under (a) pristine, (b) chemically delithiated, (c) electrochemically charged, and (d) electrochemically discharged conditions. Adapted with permission from ref [138]. Copyright 2019 Wiley. (e) Schematic showing that intergranular fracture originates from the accumulation of cycling-induced stress among aggregates of randomly oriented primary particles. Reproduced with permission from ref [57]. Copyright 2017 American Chemical Society. (f,g) Finite element modeling (FEM) of an NCM secondary particle (f) without and (g) with electrolyte penetration into intergranular cracks shows that liquid percolation promotes further chemomechanical damage. Adapted with permission from ref [139]. (h-i) High-voltage cycling promotes (h) electrochemical creep and particle fracture after high-voltage cycling for primary particles of NCM-523 (scale bar is 2 μm) and (i) intergranular fracture in secondary particles of $LiNi_{0.8}Co_{0.15}Al_{0.05}O_2$ (NCA). Adapted with permission from refs [140] and [141], respectively. Copyright 2021 American Chemical Society and 2018 Royal Society of Chemistry, respectively. ..... 65

**Figure 1.11.** Compositional heterogeneity at the electrode level. (a-d) Depth-dependent mapping of cracked NCM-622 particles after 10 cycles at 5C. (a,c) X-ray phase contrast tomographic images and (b,d) color-coded images that demonstrate cracking probabilities for particles near the separator and near the current collector, respectively. Adapted with permission from ref [144]. Copyright 2019 Wiley. (e) Phase contrast hard X-ray nano-tomography enables discrimination between NCM-811, the carbon-binder domain, and void space. (f,g) Renderings of the calculated distribution of electrical resistance superimposed onto the rendering of the NCM particle (f) with and (g) without visualization of the void space. Adapted with permission from ref [58]. Copyright 2019 Wiley. ..... 68

**Figure 1.12.** Strategies to mitigate chemomechanical degradation in layered oxide materials. (a) DFT screening of dopant elements shows that appropriate surface doping can reduce the oxygen evolution capability during charging in Li-rich oxide systems, shown here for (001) and (010) facets. Yellow and purple colors indicate improved and reduced oxygen retention compared to the undoped structure, respectively. Reproduced with permission from ref [151]. Copyright 2018 Springer Nature. (b) Infused grain boundary coatings, such as poly(3,4-ethylenedioxythiophene) (PEDOT) deposited by an oxidative chemical vapor deposition process, can also improve cycle life by minimizing intergranular cracking. Adapted with permission from ref [132]. Copyright 2019 Springer Nature. (c-d) At the secondary particle level, (c) an NMC-900505 particle possessing a core-shell structure that utilizes radially oriented grains and compositional gradients with lower surface Ni content exhibits reduced cycling-induced intergranular cracking compared to (d) a traditional secondary particle structure. Adapted with permission from ref [155]. Copyright 2019 Wiley. ..... 72

**Figure 1.13.** Two-dimensional materials exhibit a wide range of optoelectronic properties as a function of their bandgap values, including graphene (metallic), various mono- and dichalcogenides (semiconducting) and hexagonal boron nitride (insulating). Reproduced with permission from ref [161]. Copyright 2016 Springer Nature. ..... 75

**Figure 1.14.** Liquid-phase exfoliation of 2D materials. (a) Schematic of ultrasonic graphene exfoliation assisted by the presence of a sodium cholate surfactant. (b) Image of an aqueous graphene dispersion with sodium cholate that remains stable six weeks after exfoliation. Adapted with permission from ref [174]. Copyright 2009 American Chemical Society. (c) Schematic of centrifugation-based isolation of thin nanoflakes. (d-e) Average flake (d) length and (e) thickness after dispersions were subjected to various g-forces during centrifugation. Adapted with permission from ref [175]. Copyright 2016 American Chemical Society. (f) Photograph of a vial of graphene-ethyl cellulose powder after solvent removal. Reproduced with permission from ref [176]. Copyright 2020 American Chemical Society. ..... 77

**Figure 2.1.** Characterization and control of nanoscale NCA (nNCA) surface chemistry. (a) XRD patterns of nNCA and commercial NCA powder. (b,c) SEM images of as-synthesized NCA at

different magnifications. (d) Schematic showing removal of impurities at the NCA particle surface during heat treatment, yielding nanoscale NCA with a refined surface (R-nNCA). (e) C 1s spectra and (f) O 1s spectra of nNCA and R-nNCA powders obtained via XPS. (g) Voltage-capacity plot showing the activation cycles of nNCA and R-nNCA at 0.1C. ..... 86

**Figure 2.2**. Scanning electron microscope image of commercial NCA powder (Toda America) showing a large, micron-scale secondary particle morphology. ..... 87

**Figure 2.3.** X-ray diffraction pattern of the refined nNCA particles, showing negligible change in the bulk layered structure. ..... 88

**Figure 2.4.** Results for conformal graphene coatings. (a) Schematic showing that a conformal graphene coating will encapsulate surface impurities on nNCA (Gr-nNCA), in contrast to a conformal graphene coating on a refined, impurity-free surface (Gr-R-nNCA). (b,c) TEM images showing the surface of the Gr-R-nNCA particles. (d) Half-cell rate capability test of nNCA, R-nNCA, Gr-nNCA, and Gr-R-nNCA electrodes. (e) Raman spectra for Gr-nNCA and Gr-R-nNCA. (f) C 1s spectra and (g) O 1s spectra of Gr-nNCA and Gr-R-nNCA obtained via XPS. ..... 91

**Figure 2.5.** Graphene-coated nanoscale NCA exhibits improved cycle life compared to the control. (a) Half-cell cycle life test at 1C. (b) O 1s, (c) Ni 2p, and (d) Co 2p postmortem XPS spectra show significant evidence of degradation for the uncoated nNCA electrode. ..... 93

**Figure 2.6.** Ni 2p (left) and Co 2p (right) X-ray photoelectron spectra showing minimal changes in the transition metal oxidation states after the refining step and the graphene coating process. 94

**Figure 2.7.** Postmortem XPS C 1s spectra for the Gr-R-nNCA electrode and the nNCA electrode. ..... 95

**Figure 2.8.** Postmortem Raman spectrum of the Gr-R-nNCA electrode showing that the graphene coating is preserved after 200 charge-discharge cycles. ..... 97

**Figure 2.9.** Electrochemical testing shows that graphene-coated Gr-R-nNCA electrodes enable comprehensive performance improvements compared to the nNCA control. (a) Half-cell volumetric rate capability test. (b) Nyquist plot of the electrodes at room temperature. (c) Full-cell rate capability test at 0°C. (d) Nyquist plot of the full cells at 0°C. (e) Ragone plot showing the

improved power and energy density of the Gr-R-nNCA electrode. (f) Plot showing the power density competitive advantage of Gr-R-nNCA electrodes compared to literature precedent. The numbers indicate the references for previously reported results. ..... 97

**Figure 3.1**. Synchrotron radiation powder X-ray diffraction pattern of the as-synthesized NMC. The magnitude of the scattering vector is $q = 4\pi\sin\theta/\lambda$, where $2\theta$ is the scattering angle and $\lambda$ is the X-ray wavelength. ..... 111

**Figure 3.2.** Scanning electron microscope images showing the morphology of the as-synthesized NMC powder. Higher magnification is shown in (b). Scale bars are (a) 10 μm and (b) 2 μm. . 112

**Figure 3.3.** Morphology and electrochemical performance of graphene-coated NMC. (a) Top-down scanning electron microscopy images of the NMC-GrEC electrode. (b) Higher magnification scanning electron microscopy image of the region outlined in yellow. (c) Bright-field transmission electron microscopy image of the NMC-GrEC electrode..... 112

**Figure 3.4.** Raman spectra of the NMC-GrEC electrodes before and after the thermal decomposition of the ethyl cellulose polymer. ..... 114

**Figure 3.5.** Electrochemical performance of NMC-GrEC and NMC-CBPVDF electrodes performed at 0.5C. (a) Cycle life test; (b) Coulombic efficiency; (c,d) Voltage-capacity plots showing the evolution of electrode polarization for the (c) NMC-GrEC and (d) NMC-CBPVDF electrodes. ..... 116

**Figure 3.6.** Nyquist plots of the NMC-CBPVDF and NMC-GrEC electrodes before cycling. Panel (a) shows a zoomed-in view of the high-frequency response in panel (b). ..... 119

**Figure 3.7.** DRT spectra for the NMC-CBPVDF and the NMC-GrEC electrodes acquired before cycling. ..... 119

**Figure 3.8.** The equivalent circuit models used to fit the EIS spectra for the NMC-CBPVDF and NMC-GrEC cells cycled versus Li metal (a) before cycling and after cycling between 2.0 V and 4.3 V vs. $Li/Li^+$. ..... 120

**Figure 3.9.** Nyquist plot of the NMC-CBPVDF and NMC-GrEC electrodes after 50 cycles to 4.8 V vs. $Li/Li^+$. The inset panel shows a zoomed-in view of the high-frequency response..... 121

**Figure 3.10.** DRT spectra from NMC-CBPVDF and NMC-GrEC electrodes after 50 cycles (a,c) between 2.0 V and 4.3 V vs. $Li/Li^+$ and (b,d) between 2.0 V and 4.8 V vs. $Li/Li^+$. Figures (c,d) are zoomed-in regions of Figures (a,b) to better show processes $P_1$, $P_2$, and $P_3$, which correspond to the electrode-current collector interface ($P_1$), Li metal-electrolyte interface ($P_2$) and electrode-electrolyte interface ($P_3$) processes, respectively. The gray region shows Li diffusion and high-voltage degradation processes ($P_4$). ..... 121

**Figure 3.11.** NMC-CBPVDF and NMC-GrEC electrodes cycled to 4.3 V vs. $Li/Li^+$ at 0.5C. (a) Galvanostatic cycling results. (b) Nyquist plot acquired after 50 cycles. Inset shows a zoomed-in view of the high-frequency response. To process the data for DRT and equivalent circuit modeling, the low-frequency data for the NMC-CBPVDF electrode were truncated after 20 mHz..... 123

**Figure 3.12.** The equivalent circuit models used to fit the EIS spectra for the NMC-CBPVDF and NMC-GrEC cells cycled versus Li metal after cycling between 2.0 V and 4.8 V vs. $Li/Li^+$. .... 125

**Figure 3.13.** Postmortem synchrotron radiation powder X-Ray diffraction patterns of the (a) NMC-CBPVDF electrode and (b) NMC-GrEC electrode. ..... 127

**Figure 3.14.** High-resolution powder X-Ray diffraction patterns near the vicinities of the (a) (003) peak and (b) (018)/(110) peaks for the pristine NMC powder and for samples that were cycled 50 times. ..... 128

**Figure 3.15.** XPS C 1s, O 1s, and P 2p spectra of the NMC-GrEC and NMC-CBPVDF electrodes before cycling (top) and after cycling (bottom). The P 2p spectra for the pristine samples were not taken since the phosphorous character should only be present after electrolyte contact. ..... 130

**Figure 3.16.** XPS Li 1s and F 1s spectra of the NMC-GrEC and NMC-CBPVDF electrodes before cycling (top) and after cycling (bottom). ..... 131

**Figure 3.17.** Postmortem STEM analysis of (a) NMC-CBPVDF and (b) NMC-GrEC electrodes after 50 cycles between 2.0 V and 4.8 V vs. $Li/Li^+$ at 0.5C. The inset FFT patterns show the

presence of layered (green, or L), spinel (red, or S), and rocksalt (yellow, or RS) phases. The zone axis is [1-10]. ..... 133

**Figure 3.18.** Postmortem scanning electron microscopy images of the (a) NMC-CBPVDF electrode surface and (b) NMC-GrEC electrode surface. Both scale bars are 2 μm. ..... 136

**Figure 3.19.** Additional postmortem SEM images showing intraparticle and interparticle fracture and electrochemical creep in the NMC-CBPVDF electrode. Unless noted, all scale bars are 2 μm. ..... 137

**Figure 3.20.** Additional postmortem SEM images showing limited evidence of intraparticle and interparticle fracture and electrochemical creep in the NMC-GrEC electrode. All scale bars are 2 μm. ..... 138

**Figure 3.21.** A schematic showing the proposed degradation mechanisms for the (a) NMC-CBPVDF electrode, which are mitigated in the (b) NMC-GrEC electrode due to the presence of the graphene coating. ..... 141

**Figure 3.22.** Cross-sectional SEM images of the pristine (a) NMC-CBPVDF electrode and (b) NMC-GrEC electrode, showing electrode compaction effects due to the use of graphene as the conductive additive rather than carbon black. Both scale bars are 20 μm. (c) Volumetric rate capability for the two electrodes between 2.0 V and 4.8 V vs. $Li/Li^+$. ..... 143

**Figure 4.1.** Scanning electron microscope image of pristine LNO. ..... 157

**Figure 4.2.** LNO exposed to humid $CO_2$ for 24 hours exhibits severe morphological and surface chemical changes. (a-b) Scanning electron microscopy images of (a) pristine LNO and (b) LNO after being exposed to humid $CO_2$ for 24 hours. (c) Raman, (d) DRIFTS-FTIR, (e) XPS C 1s, and (f) XPS O 1s spectra show the growth of surface carbonate species after exposure to humid $CO_2$. ..... 158

**Figure 4.3.** Scanning electron microscope images of LNO particles after exposure to humid $CO_2$ for 24 hours. ..... 159

**Figure 4.4.** Electrochemical performance of uncoated LNO before and after humid $CO_2$ exposure. (a-b) Activation cycles of (a) pristine LNO and (b) LNO exposed to humid $CO_2$. Activation was

performed at C/10 with a constant voltage hold at 2.8 V vs. $Li/Li^+$ until the current reached C/20. The inset in (b) shows a magnified view of the voltage peak present at the initial delithiation shoulder of LNO. (c-d) Nyquist plots (c) before cycling and (d) after activation for pristine LNO and LNO exposed to humid $CO_2$. ..... 161

**Figure 4.5.** The equivalent circuit model (Randles circuit) used to fit the impedance data. ..... 162

**Figure 4.6.** A hydrophobic GrEC coating protects the LNO surface from ambient degradation. ..... 163

**Figure 4.7.** Scanning electron microscopy images show no changes in the surface morphology of the GrEC-coated LNO after 24 hours of exposure to humid $CO_2$. (a) As-coated LNO-Gr-EC, (b) coated LNO-Gr-EC after 24 hours of exposure to humid $CO_2$, (c) LNO-Gr obtained by pyrolyzing LNO-Gr-EC, and (d) LNO-Gr obtained by pyrolyzing LNO-Gr-EC after 24 hours of exposure to humid $CO_2$. ..... 165

**Figure 4.8.** SEM images of the LNO-Gr sample showing a uniform graphene coating on the LNO particles. Prior to obtaining these images, ethyl cellulose was pyrolyzed at 300°C for 1 hour in flowing $O_2$. ..... 166

**Figure 4.9.** SEM images of the LNO-Gr sample after exposure to humid $CO_2$ for 24 hours, showing no evidence of surface morphological changes. Prior to obtaining these images, the ethyl cellulose was pyrolyzed at 300°C for 1 hour in flowing $O_2$. ..... 167

**Figure 4.10.** Raman spectra of the LNO-Gr-EC (top) and LNO-Gr (bottom) show a clear decrease in the D/G ratio after thermal pyrolysis of the EC at 300°C for 1 hour in flowing $O_2$, thus confirming decomposition of EC. ..... 168

**Figure 4.11.** SEM images of LNO powder after exposure to humid $CO_2$ for 24 hours and subsequently heated to 300°C for 1 hour in flowing $O_2$. These images show that the EC pyrolysis conditions do not remove lithium impurities from the surface of LNO. ..... 169

**Figure 4.12.** Raman spectrum of LNO powder after exposure to humid $CO_2$ for 24 hours and then heated to 300°C for 1 hour in flowing $O_2$. This spectrum confirms that the EC pyrolysis conditions do not remove lithium impurities from the surface of LNO. ..... 170

**Figure 4.13.** XPS C 1s and O 1s spectra of LNO after exposure to humid $CO_2$ for 24 hours and then heated to 300°C for 1 hour in flowing $O_2$. These spectra confirm that the EC pyrolysis conditions do not remove lithium impurities from the surface of LNO. ..... 170

**Figure 4.14.** LNO-Gr shows minimal evidence of degradation after 24 hours of exposure to humid $CO_2$. (a) XPS C 1s spectrum, (b) XPS O 1s spectrum, (c) Raman spectroscopy, (d) DRIFTS-FTIR, and (e) thermogravimetric analysis show that the surface impurity species on LNO-Gr do not significantly increase despite 24 hours of exposure to humid $CO_2$. ..... 171

**Figure 4.15.** Thermogravimetric analysis of GrEC powder showing that the decomposition of residual GrEC begins below 400°C. The Gr-EC powder here was compositionally identical to the GrEC in the LNO-Gr electrode (i.e., 1:3 Gr:EC). Prior to TGA, this GrEC powder was heated to 300°C for 1 hour in flowing $O_2$ to pyrolyze the ethyl cellulose, leaving behind graphene and carbonaceous residue. ..... 173

**Figure 4.16.** Electrochemical performance of LNO-Gr before and after exposure to humid $CO_2$ shows no discernable signatures of degradation. (a-b) Activation cycles of (a) pristine LNO-Gr and (b) LNO-Gr exposed to humid $CO_2$. Activation was performed at C/10 with a constant voltage hold at 2.8 V vs. $Li/Li^+$ until the current reached C/20. The inset in (b) shows a magnified view of the initial delithiation shoulder of LNO-Gr without any voltage spike present. (c-d) Nyquist plots (c) before cycling and (d) after activation for pristine LNO-Gr and LNO-Gr exposed to humid $CO_2$..... 173

# LIST OF TABLES

**Table 1.1.** Properties of selected LIB cathode material chemistries.[4,9-12] ..... 41

**Table 3.1.** Rietveld refinement results for the pristine NMC powder. ..... 111

**Table 3.2.** Transition metal ratio of the synthesized NMC powder determined via inductively coupled plasma mass spectrometry, confirming the target composition of 50% nickel, 30% manganese, and 20% cobalt. ..... 112

**Table 3.3.** Comparison of first cycle efficiencies among various reported strategies to stabilize the high-voltage cycling of NMC532. ..... 117

**Table 3.4.** Equivalent circuit model fitting results for the NMC-CBPVDF and NMC-GrEC electrodes before cycling. ..... 120

**Table 3.5.** Equivalent circuit model fitting results for the NMC-CBPVDF and NMC-GrEC electrodes after cycling between 2.0 V and 4.3 V vs. $Li/Li^+$ and after cycling between 2.0 V and 4.8 V vs. $Li/Li^+$. ..... 126

**Table 3.6.** Rietveld refinement results for the cycled NMC-CBPVDF electrode and the cycled NMC-GrEC electrode. ..... 128

**Table 3.7.** Concentrations of dissolved transition metal ions for the NMC-CBPVDF control electrode and the NMC-GrEC electrode as determined by ICP-MS. ..... 135

# CHAPTER 1:

# INTRODUCTION

This chapter is adapted in part from:

**Luu, N. S.,*** Park, K. Y.,* Hersam, M.C. Characterizing and Mitigating Chemomechanical Degradation in High-Energy Lithium-Ion Battery Cathode Materials. Acc. Mater. Res. (2022), 3, 5, 511–524.

(* indicates equal contribution)

## 1.1 Motivation and Thesis Statement

Lithium-ion batteries (LIBs) are ubiquitous energy storage tools that power technologies across modern society. Initially developed in the late 1970s,[1] LIBs played a key role in the growth of consumer electronics in the 1990s after materials and chemistry innovations improved battery safety and cycling stability.[2] Today, LIBs can be found in sectors across society, including modern consumer electronics, power tools, and medical devices – but most critically, battery technologies underpin nearly all discussions surrounding strategies to address climate change. Across the board, fossil fuel infrastructure is now increasingly being displaced by renewable electricity generation and transportation solutions. At the center of these discussions are technologies such as grid-level energy storage systems that enable consistent electricity distribution from intermittent energy sources (e.g., solar and wind), as well as the increasing market penetration of battery electric vehicles to replace the fleet of internal combustion engine vehicles. The importance of LIBs in revolutionizing modern society was recognized in 2019, when the Nobel Prize in Chemistry was awarded to M. Stanley Whittingham, John B. Goodenough, and Akira Yoshino for their roles in the developing the lithium-ion battery.[3]

The anticipated adoption of LIBs across many sectors of society has placed increased focus on battery materials. Broadly, the primary engineering goals for lithium-ion batteries are to:

- Possess high energy densities
- Have extended cycle life
- Charge and discharge quickly while delivering high capacity
- Operate safely

- Deliver high performance under various operational conditions, such as varying temperature and humidity

Many of these goals are closely tied to material chemistry and are governed by factors such as the intrinsic lithium content and material stability. Most current commercial LIBs are manufactured using graphite-based anodes and lithium transition metal oxide-based or phosphate-based cathodes, where transition metals such as Ni, Co, Mn, or Fe mediate redox.[2,4] This material choice was grounded in the research conducted over the last three decades that investigated how these materials degrade during electrochemical cycling, as well as engineering strategies to mitigate this degradation. Despite these advancements, many questions about LIBs are still under investigation, including optimized electrical contact, charge transfer processes, chemical and phase stabilities, and interfacial evolution.

Around the same time as major developments in LIB technology, the field of nanoscience also experienced exponential growth. Nanomaterials were first investigated for their novel properties that emerge at the atomically thin limit. In 2004, graphene was isolated for the first time by micromechanical exfoliation,[5] enabling subsequent studies that explored its electronic properties, including its anomalous quantum Hall effect and charge transport behavior that is characteristic of Dirac fermions.[6,7] Driven by the potential to utilize these noteworthy material properties in charge transport and electrochemical devices, various methods to isolate related two-dimensional materials were also explored. The parallel development of scalable nanomaterial processing schemes and electrochemical materials research opened the door for the application of nanomaterials in LIBs, enabling a rich research area that is still being explored today.

This thesis will focus on controlling and mitigating degradation in Ni-rich cathode materials using graphene coatings. The remainder of this chapter summarizes the current landscape of lithium-ion battery materials and introduces two-dimensional materials – notably, graphene – as a materials-level solution that has potential to address degradation in these systems. Chapters 2 through 4 outline three research projects that demonstrate the applicability of graphene to addressing issues in Ni-rich cathode materials, including improving cycling performance, decreasing chemomechanical degradation, and suppressing ambient degradation. Finally, this thesis will outline future research directions for graphene in energy storage devices.

## 1.2 Lithium-Ion Batteries

Lithium-ion batteries are electrochemical energy storage devices that operate by shuttling lithium ions and electrons between an anode and a cathode (**Figure 1.1**). At open circuit, the driving force for charge transport between the two electrodes is governed by the intrinsic electrochemical redox potentials of the two materials. The anode, which possesses a higher electrochemical potential than the cathode, releases $Li^+$ ions during discharge. These $Li^+$ are then transported through the ionically conducting electrolyte, react with the cathode surface, and are stored. To maintain electroneutrality, electrons flow in the same direction through an external circuit, where they can be harnessed to perform useful work. Charging the cell can be accomplished by imposing a current or bias to induce charge transport against the electrochemical potential gradient, sending $Li^+$ and electrons from the cathode towards the anode. In the absence of degradation, this process allows for safe, reliable, and on-demand energy storage.

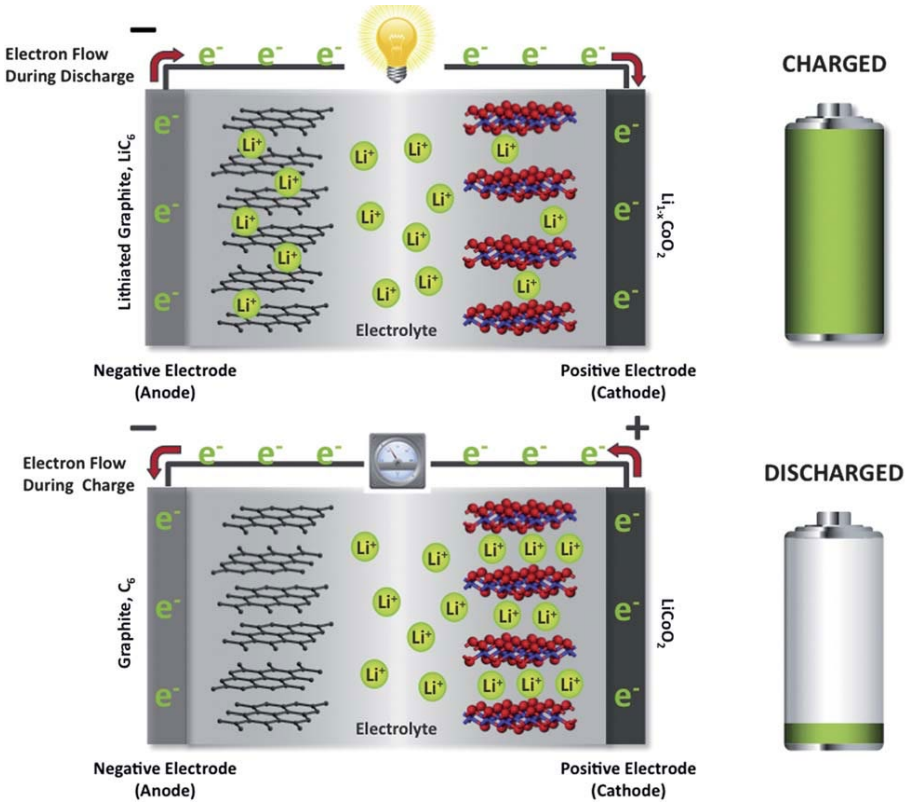


**Figure 1.1**. Schematic of the operation of a lithium-ion battery. Electrons and lithium ions flow from the anode towards the cathode during discharge, and flow from the cathode towards the anode during charge. Reproduced with permission from ref [8]. Copyright 2013 Royal Society of Chemistry.

### *1.2.1 Lithium-Ion Battery Fabrication*

Traditionally, LIB electrodes are fabricated using the following steps. First, active materials, conductive carbon, polymeric binder, and solvent are homogenously mixed to create a slurry. In cathode electrodes, the polymeric binder is often polyvinylidene fluoride (PVDF) or polytetrafluoroethylene (PTFE), while the solvent is often N-methyl-2-pyrrolidone (NMP). Using doctor blading or slot die coating techniques, the slurry is then uniformly deposited onto a metallic foil, which serves as the current collector. Copper foil is commonly used for the anode, while

aluminum is used for the cathode. The entire electrode sheet is dried to remove the solvent, calendered to compress the film, and then sent to subsequent assembly steps for packaging.

After drying, electrode sheets can be cut down to size that is appropriate for the desired cell form factor. Coin cells are often used for materials-level testing due to their small form factor and since electrodes of interest can be assembled versus a lithium metal counter electrode, which is referred to a "half-cell" geometry. In contrast to "full-cells" made with non-lithium containing electrode materials (such as graphite or silicon anodes), using a lithium metal anode ensures that $Li^+$ is always available, enabling direct assessment of the working electrode material. Nonetheless, cell assembly proceeds by creating a stack consisting of an anode sheet, a porous polyolefin separator, and a cathode sheet that is placed inside the exterior cell packaging. The polymeric separator (commonly polypropylene or polyethylene) is inserted between the two electrodes to prevent cell shorting. In contrast to coin cells and pouch cells, where the electrode stack lies parallel to the flat packaging, cylindrical cell fabrication involves winding the stack into a jelly roll, which is then inserted into the exterior casing. The cell is then filled with liquid electrolyte, sealed shut, and is ready for formation and cycling.

### *1.2.2 Cathode Materials for Lithium-Ion Batteries*

Nearly all commercially relevant LIB cathode materials store lithium via intercalation reactions. Categorized by crystal structure, these materials include layered structures (e.g., $LiCoO_2$ and $LiNiO_2$, or LCO and LNO), spinel-based structures (e.g., $LiMn_2O_4$, or LMO), and olivine structures (e.g., $LiFePO_4$, or LFP). Examples of notable cathode chemistries are listed in **Figure 1.2** and **Table 1.1**, which includes other materials that are actively being studied at the research

level. Layered materials such as LCO and LNO are redox-active at voltages near 5.0 V vs. $Li/Li^+$ and can simultaneously deliver high capacities at moderate voltage windows (**Figure 1.2d-e**). In contrast, the prototypical cathode materials with spinel and olivine frameworks (LMO and LFP) have redox windows limited to below 4.3 V vs. $Li/Li^+$, which constrains their achievable power performance (**Figure 1.2f-g)**. For these reasons, layered oxides were established as the cathode materials of choice for energy-dense cells used in high-performance applications.

**Table 1.1.** Properties of selected LIB cathode material chemistries.[4,9-12]

| **Crystal Structure** | **Chemistry** | **Abbreviation** | **Practical Capacity (mAh $g^{-1}$)** | **Operating Potential (V vs. $Li/Li^+$)** | **Level of development** |
|---|---|---|---|---|---|
| Layered | $LiCoO_2$ | LCO | 148 | 3.8 | Commercialized; consumer electronics |
| Layered | $LiNiO_2$ | LNO | 150 | 3.8 | Research |
| Layered | $LiNi_xMn_yCo_{1-x-y}O_2$ | NMC | 200 | 3.7 | Commercialized; electric vehicles and stationary storage |
| Layered | $LiNi_xCo_yAl_{1-x-y}O_2$ | NCA | 200 | 3.7 | Commercialized; electric vehicles and stationary storage |
| Layered | $LiNi_xMn_yAl_{1-x-y}O_2$ | LNMA | 216 | 3.7 | Research |
| Spinel | $LiMn_2O_4$ | LMO | 120 | 4.1 | Commercialized |
| Spinel | $LiMn_{1.5}Ni_{0.5}O_4$ | LMNO | 155 | 4.7 | Research |
| Olivine | $LiFePO_4$ | LFP | 165 | 3.4 | Commercialized; electric vehicles and stationary storage |
| Quasi-layered | $xLi_2MnO_3 \cdot (1-x)LiTMO_2$ TM = Ni, Mn, Co, etc. | LMR-NMC; Li-rich | 250-300 | 3.7 | Research |

| | | | | | |
|---|---|---|---|---|---|
| Disordered rocksalt | Various | DRX | 210 - 350 | 2.1-3.4 | Research |

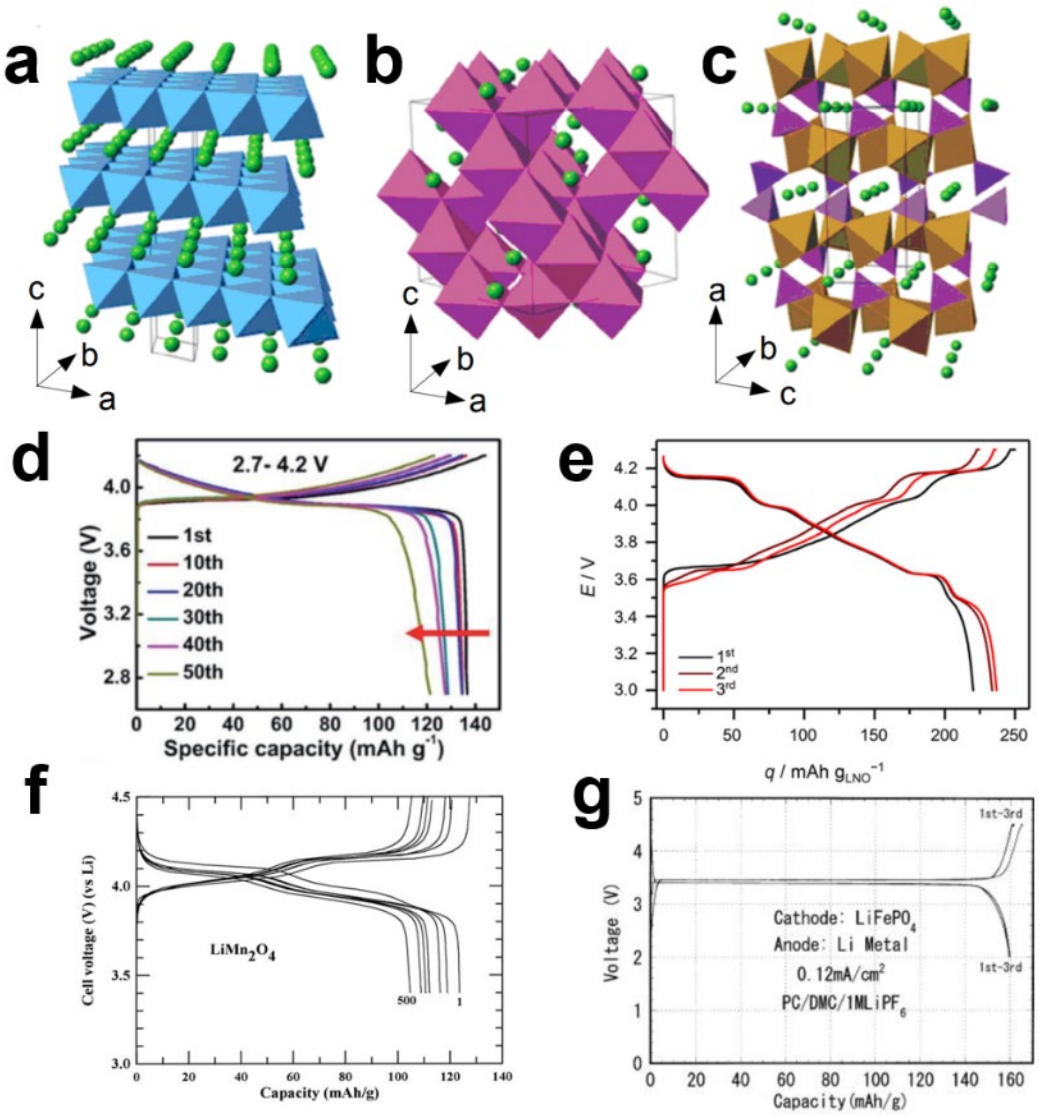


**Figure 1.2.** Structure and electrochemical properties of prototypical cathode materials for lithium-ion batteries. (a-c) Schematic of (a) layered, (b) spinel, and (c) olivine crystal structures. The green spheres in (a-c) represent lithium, while transition metal octahedra are blue in (a) purple in (b), and in brown (c). Phosphate tetrahedra are shown in purple in (c). Reproduced with permission from ref [13]. (d-g) Voltage-capacity profiles for (d) layered $LiCoO_2$, (e) layered $LiNiO_2$, (f) spinel $LiMn_2O_4$, and (g) olivine $LiFePO_4$. Reproduced with permission from ref [14], ref [15], ref [16], and ref [17], respectively. Copyrights 2019 Royal Society of Chemistry, 2019 Wiley, 1999 IOP Publishing, and 2001 IOP Publishing, respectively.

Layered oxides were first explored as LIB cathode materials in the 1980s by Goodenough et al., who established $LiCoO_2$ (LCO) as a stable and reversible lithium host.[18] LCO possesses an α-$NaFeO_2$-type crystal structure (*R-3m* space group) with alternating planes of cobalt and lithium atoms along the *c*-axis of the unit cell. The Li and Co cations are octahedrally coordinated by oxygen atoms, which themselves occupy a close-packed structure. This atomic configuration allows for $Li^+$ transport in two dimensions (**Figure 1.2a**) and promotes high electronic conductivity due to close Co-Co interactions.[19] Mediated by $Co^{3+/4+}$ redox, approximately 50% of the Li in this structure can be reversibly deintercalated, which corresponds to operating voltages of approximately 4.3 V vs. $Li/Li^+$ and a practical capacity of approximately 148 mAh $g^{-1}$ (**Figure 1.2d**).[4,14]

$LiNiO_2$ (LNO), an isostructural compound to LCO, was also explored in the 1990s.[20] Due to the lower toxicity, higher material abundance, and lower costs of Ni, as well as first-cycle discharge capacities exceeding 245 mAh $g^{-1}$ via $Ni^{3+/4+}$ redox (**Figure 1.2e**),[21,22] LNO showed promise as a complementary material candidate for LIB cathodes. However, investigations of various synthetic methods[20,23-25] identified the difficulty of achieving stoichiometric LNO since the cations in the Li-Ni-O system can easily form a solid solution. Consequently, $LiNiO_2$ can thermally decompose into $Li_{1-x}Ni_{1+x}O_2$ with Li/Ni antisite defects.[26,27] which are favorable due to the magnetic frustration of $Ni^{3+}$ in the TM layer that can easily be resolved by cation mixing. After $Ni^{3+}$ and $Li^+$ have swapped positions, the subsequent antiferromagnetic coupling between $Ni^{3+}$ across layers further stabilizes the $Li^+$ in Ni sites.[28,29] Beyond sequestering lithium in TM sites and rendering Li sites inactive, the accumulated effect of Li/Ni antisite defects is an overall decrease in the interlayer spacing, which further increases the barrier to $Li^+$ diffusion by ~20-30 meV.[30,31]

Moreover, LNO is known to evolve $O_2$ gas at high potentials, which compromises the crystal structure and results in safety problems due to the highly flammable electrolyte used in many LIBs.[32] For these reasons, pure LNO was largely abandoned for commercial applications.

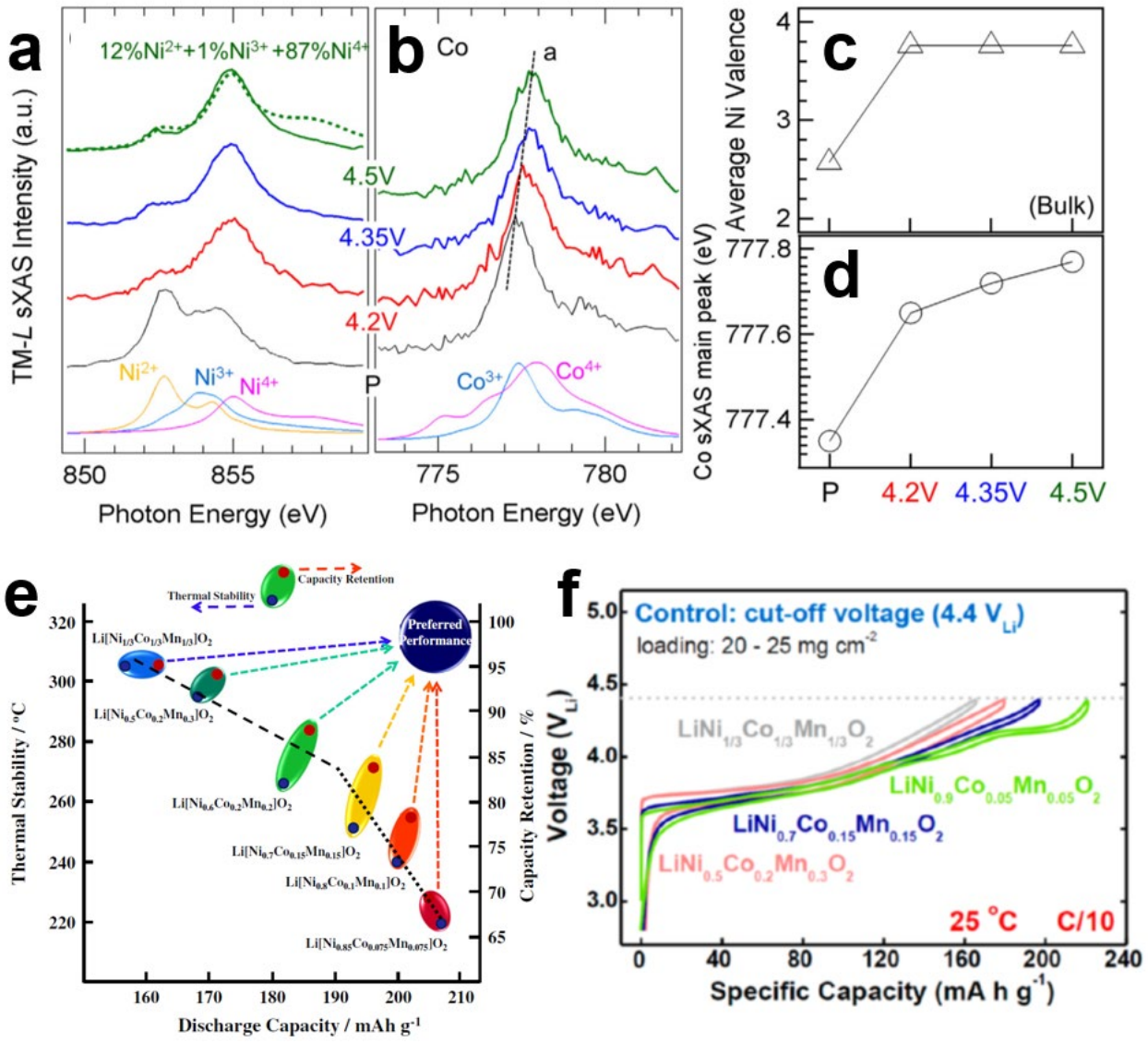


**Figure 1.3.** Electrochemical properties of NMCs. (a-d) Soft X-ray absorption spectroscopy of NMC532 reveals that Ni initially mediates redox, followed by the $Co^{3+/4+}$ redox couple at high SOCs. (a) Ni-$L_3$ and (b) Co-$L_3$ sXAS spectra of NMC532 in total fluorescence yield mode (top), with calculated TFY reference spectra (bottom). (c) Calculated average Ni oxidation state from sXAS spectra as a function of charging voltage. (d) Position of the Co sXAS main peak as a

function of charging voltage. Reprinted (adapted) with permission from ref [33]. Copyright 2017 Elsevier. (e) Thermal stability, discharge capacity, and capacity retention for various NMC chemistries. Reproduced with permission from ref [34]. Copyright 2013 Elsevier. (f) Voltage-capacity profiles for various multicomponent NMC cathodes, showing higher Ni compositions achieve higher capacities at the same cutoff voltage. Reproduced with permission from ref [35]. Copyright 2019 American Chemical Society.

Fortunately, LNO can be stabilized via the addition of transition metal dopants, which achieves a compromise between the cyclability of LCO and the supply chain and cost advantages of LNO. In these structures, a fraction of the Ni sites are filled by substitutional transition metals (TMs), such as Co, Mn, and Al. The resulting multicomponent lithium transition metal oxides, with compositions such as $LiNi_xMn_yCo_{1-x-y}O_2$ (NMC), exploit the electrochemical advantages of each constituent transition metal. Ni mediates redox through a majority of the voltage window (**Figure 1.3a-d**), while the dopant TMs provide structural, chemical, and thermal stability.

The structural similarities between LNO and LCO suggest that Co would be an excellent dopant candidate. Indeed, the small size of $Co^{3+}$ compared to $Ni^{3+}$ increases its stability in octahedral TM sites, decreasing the propensity for TM-Li antisite defect generation during synthesis or electrochemical cycling. In a similar manner as in LCO, $Co^{3+}$ can also participate in redox and therefore presents no significant detriment to capacity upon doping.[33] Despite the crystallographic advantages of Co doping, major ethical issues with the cobalt supply chain, combined with the higher natural abundance of Ni compared to Co, prompted an industrial shift in favor of decreasing the Co content in layered oxides.[36,37]

Another major dopant element in Ni-based layered oxides is Mn. When introduced alone, Mn doping was shown to promote $Ni^{2+}/Mn^{4+}$ charge separation rather than the formation of $Ni^{3+}/Mn^{3+}$, which precludes solid solution formation among the TM sites.[38] This charge separation

ultimately increases the degree of Li-Ni cation mixing and decreases the achievable capacity.[39] However, this issue can be circumvented when Mn and Co act as co-dopants together. Mn remains electrochemically inert as $Mn^{4+}$, stabilizing the structure against thermal and cycling-induced degradation.[2,34,40,41] In addition, due to its abundance and supply chain advantages, Mn substitution also helps decrease the overall cathode cost.[42]

Other substitutional elements, such as Al, have been integrated with Ni and Co to form $LiNi_{0.8}Co_{0.15}Al_{0.05}O_2$ (NCA) cathodes.[43] These cathodes possess a rhombohedral (layered) structure and are therefore isostructural to LCO, LNO, and NMC. In NCA, the redox-inactive $Al^{3+}$ plays a similar role as Mn in NMCs. At the slight expense of capacity, the addition of substitutional Al significantly improves thermal and structural stability by promoting a quasi-monophase oxygen stacking phase transition at high states of charge (SOCs), minimizing lattice distortion and therefore suppressing molecular oxygen release.[44-48]

Importantly, the properties of these multicomponent transition metal oxides can be tuned via the ratio of the constituent TMs (**Figure 1.3e**). For example, lower-Ni chemistries such as $LiNi_{0.5}Mn_{0.3}Co_{0.2}O_2$ (NMC532), or $LiNi_{0.8}Mn_{0.1}Co_{0.1}O_2$ (NMC111) have good capacity retention due to the presence of stabilizing Mn and Co. High capacities can be achieved by increasing the Ni content beyond 50% due to the redox activity of Ni in typical operating voltage windows (**Figure 1.3f**). However, these high-Ni stoichiometries, such as $LiNi_{0.8}Mn_{0.1}Co_{0.1}O_2$ (NMC811), are susceptible to serious thermal, electrochemical, and mechanical stability issues, implying that solutions to stabilize these degradation mechanisms are required for long-lasting operation.[34,49]

## 1.3 Degradation in Lithium-Ion Batteries

Recent research efforts have revealed various degradation phenomena in high-energy cathode materials that occur across multiple length scales. At the nanoscale, the most well-known initiators of degradation are the appearance of new phases on particle surfaces,[50] electrolyte decomposition,[51] gas evolution,[52] and transition metal (TM) dissolution.[53] Upon electrochemical cycling, this atomic-level chemomechanical degradation accelerates particle-level failure mechanisms, resulting in cracking,[54] electrochemical creep,[55] or bending.[56] The origins of chemical and mechanical degradation are highly intertwined and often accelerate one another, resulting in positive feedback loops that lead to widespread loss of electrochemical activity. At larger length scales, structural characteristics and kinetic limitations within and between particles can act as additional sites for chemomechanical degradation. For example, volumetric changes to the active material during cycling can induce pulverization of secondary particles[57] or detachment from the carbon-binder matrix.[58] As LIB engineering trends toward thicker electrodes with low-carbon and low-binder content to enable high cell-level energy densities, these electrode-scale problems will likely become even more pronounced.[59] Therefore, a broad understanding of the degradation mechanisms in emerging high-energy LIB cathode materials across multiple length scales is critical to inform strategies for next-generation materials design, materials synthesis, and advanced electrode fabrication.

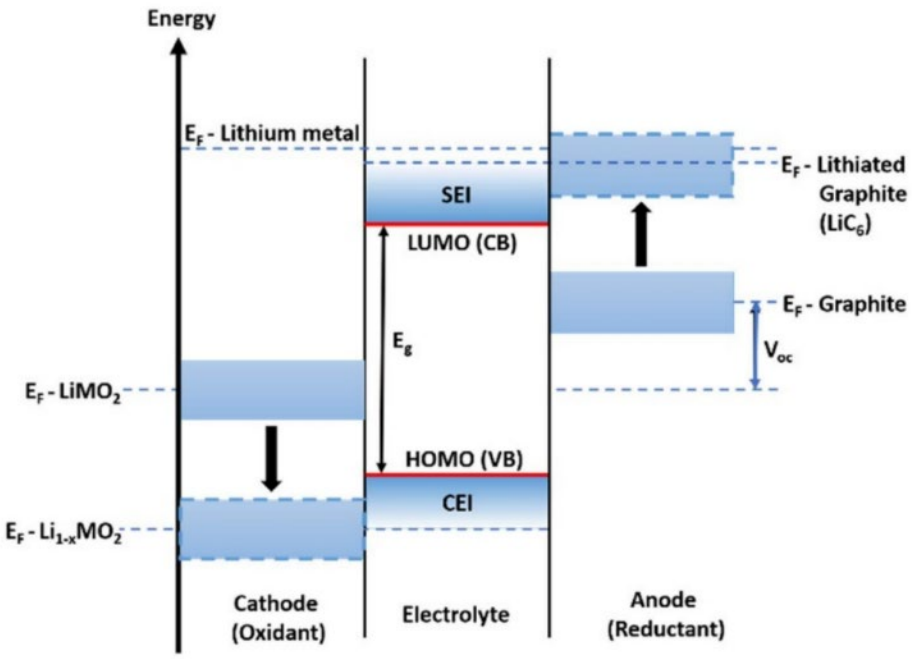


**Figure 1.4.** Energy band diagram for the anode, cathode, and electrolyte in a lithium-ion battery. The difference between the voltages of the anode and cathode is the operating voltage of the cell ($V_{OC}$), while the difference between the operating voltages of the electrodes and the stability window of the electrolyte can drive the formation of the SEI and CEI. Reproduced with permission from ref [60]. Copyright 2021 IOP Publishing.

### *1.3.1 Electrolyte Decomposition and SEI Formation*

Electrolytes that are most used in LIBs are composed of lithium salts dissolved in organic solvents. By design, LIB electrolytes should ideally have HOMO and LUMO levels that are outside the redox windows of the cathode and anode to eliminate the thermodynamic driving force for electrolyte decomposition onto electrode surfaces (**Figure 1.4**).[61] However, local variations in the electrode potential and band bending can promote electrolyte degradation, resulting in the deposition of chemical decomposition products on the electrode surface.[51] This process is known as cathode-electrolyte interphase (CEI) formation when occurring at the cathode and solid-electrolyte interphase (SEI) formation when occurring at the anode interface. Most aprotic

electrolytes are thermodynamically unstable at anode interfaces and are easily reduced, forming SEIs that passivate the anode interface and prevent further electrolyte decomposition. However, there is no analogous thermodynamic driving force for electrolyte oxidation at the cathode interface.[62] Instead, electrolyte oxidation is driven by the interaction between transition metals with high oxidation states and the carbonate solvents. Density functional theory calculations showed that the increasing covalency of the TM-O bond at higher SOCs increases the reactivity of oxygen sites, which can easily react with carbonate solvents in the electrolyte[63-65] and facilitate degradation processes such as nucleophilic attack,[66] ethylene carbonate dissociation,[63] and carbonate dehydrogenation (**Figure 1.5a-b**).[63,67] Correspondingly, charge transfer reactions between the electrode and electrolyte components result in transition metal reduction and oxide decomposition,[68] while surface protic species can further react with $LiPF_6$ electrolyte salts to form fluorophosphates and HF.[67]

Noninvasive methods such as X-ray photoelectron spectroscopy (XPS), Raman spectroscopy, and Fourier transform infrared spectroscopy (FTIR) in diffuse reflectance mode (DRIFTS) have been frequently employed to identify interfacial chemical decomposition products.[67,69] These compounds include organic species such as $Li_2CO_3$, alkyl carbonates ($ROCO_2Li$), and polycarbonates, which form during the oxidation of carbonate species (**Figure 1.5c-d**).[67] In addition, inorganic compounds such as $Li_2O$, LiF, $Li_xPF_yO_z$, and transition metal fluorides have been reported on oxide surfaces, which can parasitically form due to reactions with the $LiPF_6$ electrolyte salt.[70,71] Other methods, such as time-of-flight secondary ion mass spectrometry (TOF-SIMS),[70,72] have been employed to investigate spatial and depth distribution

of these reaction products. These studies posited that the SEI forms a mosaic structure (**Figure 1.5 e**), suggesting that the surface chemical environment strongly impacts the species that form.

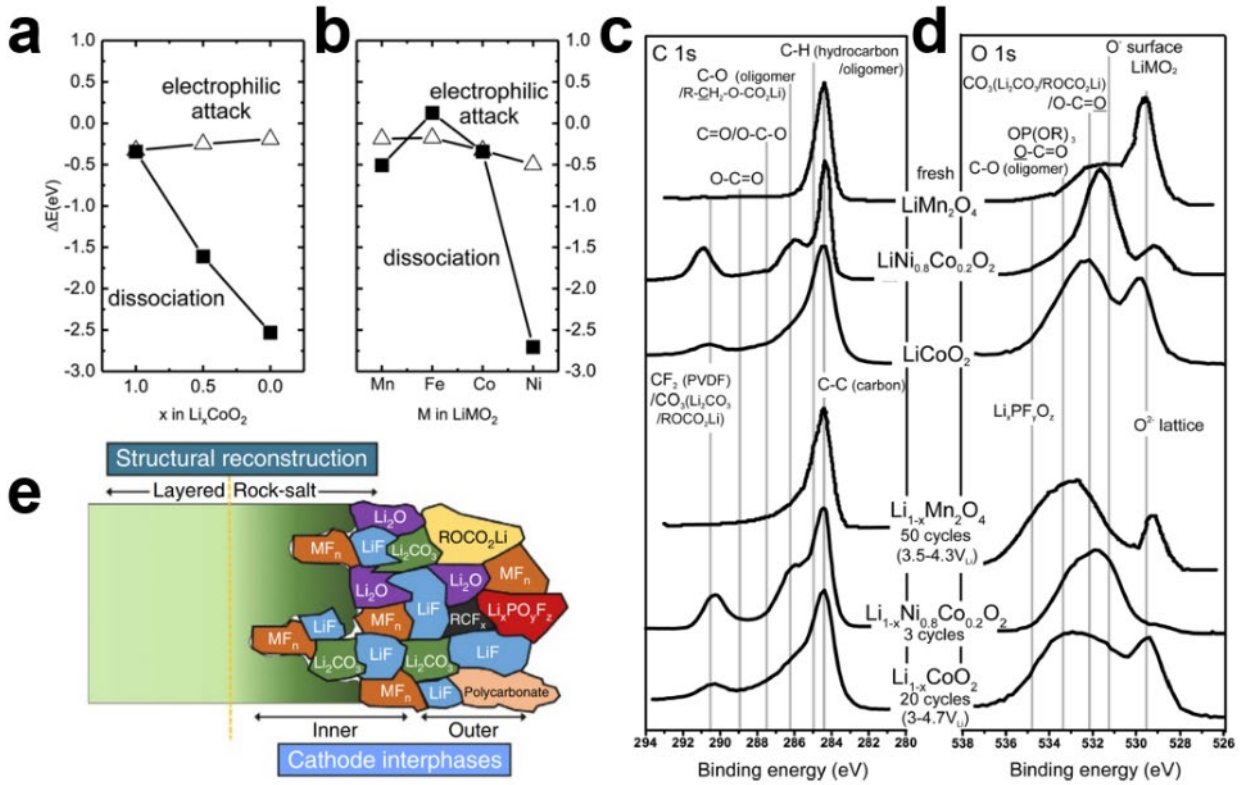


**Figure 1.5.** Driving forces and reaction products of electrolyte decomposition reactions. (a-b) Electrolyte decomposition reactions are driven by ethylene carbonate dissociation, which varies as a function of (a) state of charge and (b) transition metal content. Reprinted (adapted) with permission from ref [63]. Copyright 2017 American Chemical Society. (c) XPS C 1s and (d) O 1s spectra reveal increased spectral intensities associated with electrolyte decomposition products formed during cycling, including oligomers and fluorophosphate compounds. Reprinted (adapted) with permission from ref [61]. Copyright 2015 American Chemical Society. (e) The resulting decomposition layer is posited to have a mosaic structure composed of various solvent and salt degradation products. Reproduced with permission from ref [70]. Copyright 2017 Springer Nature.

The health of the cathode-electrolyte interface has strong implications on cycling performance. For example, a thicker interfacial layer composed of decomposition products can

hinder ionic and electronic charge transfer, resulting in large overpotentials that can artificially limit capacity and rate performance. Reaction products can also act as surface intermediates which react with other electrolyte components like $LiPF_6$ to form HF, further accelerating electrode degradation.[73] Subsequent kinetic studies have shown that such surface films are detrimental to cycling performance.[74] Therefore, the impact of CEI formation on cycling performance is often analyzed via electrochemical techniques, including electrochemical impedance spectroscopy (EIS),[75] leakage current measurements,[74] and galvanostatic cycling.

### *1.3.2 Transition Metal Dissolution*

TM dissolution is a phenomenon that is intimately tied to cycle life degradation since it irreversibly removes key redox couples in the cathode structure, thereby deactivating the portions of the cathode material. A notable example is Mn dissolution, which has been widely studied in the LMO system. Surface $Mn^{3+}$ ions are known to undergo disproportionation reactions, forming $Mn^{2+}$ ions which are soluble in the electrolyte.[76] Another driver of dissolution is the generation of HF in the electrolyte due to the decomposition of the $LiPF_6$ salt in the presence of water.[77] Trace amounts of HF can easily etch transition metals in layered oxide systems such as LCO,[78,79] NCA,[80] and NMC,[81] which all become more reactive above 4.6 V vs. $Li/Li^+$.[53] Li-rich structures are similarly susceptible to disproportionation- and HF-driven TM dissolution,[72,82,83] although direct TM loss was not observed to the same degree as Ni-rich layered oxides or spinel structures.[78] Nonetheless, the loss of active material can also induce structural changes, forming surface phases that further contribute to capacity fade.[84,85]

In full-cell geometries, the loss of transition metal redox centers is responsible for not only the deactivation of the cathode material, but also degradation of the anode electrode due to the crossover of $TM^{2+}$ ions. In this case, the dissolved transition metal ions deposit on the anode, compromising the solid-electrolyte interphase (SEI), and degrading full-cell performance.[86,87] Moreover, dendrite formation on anode surfaces preferentially occurs at sites with high concentrations of deposited transition metals, presenting additional challenges for the high-voltage operation of emerging cathode chemistries in full-cell configurations.[88]

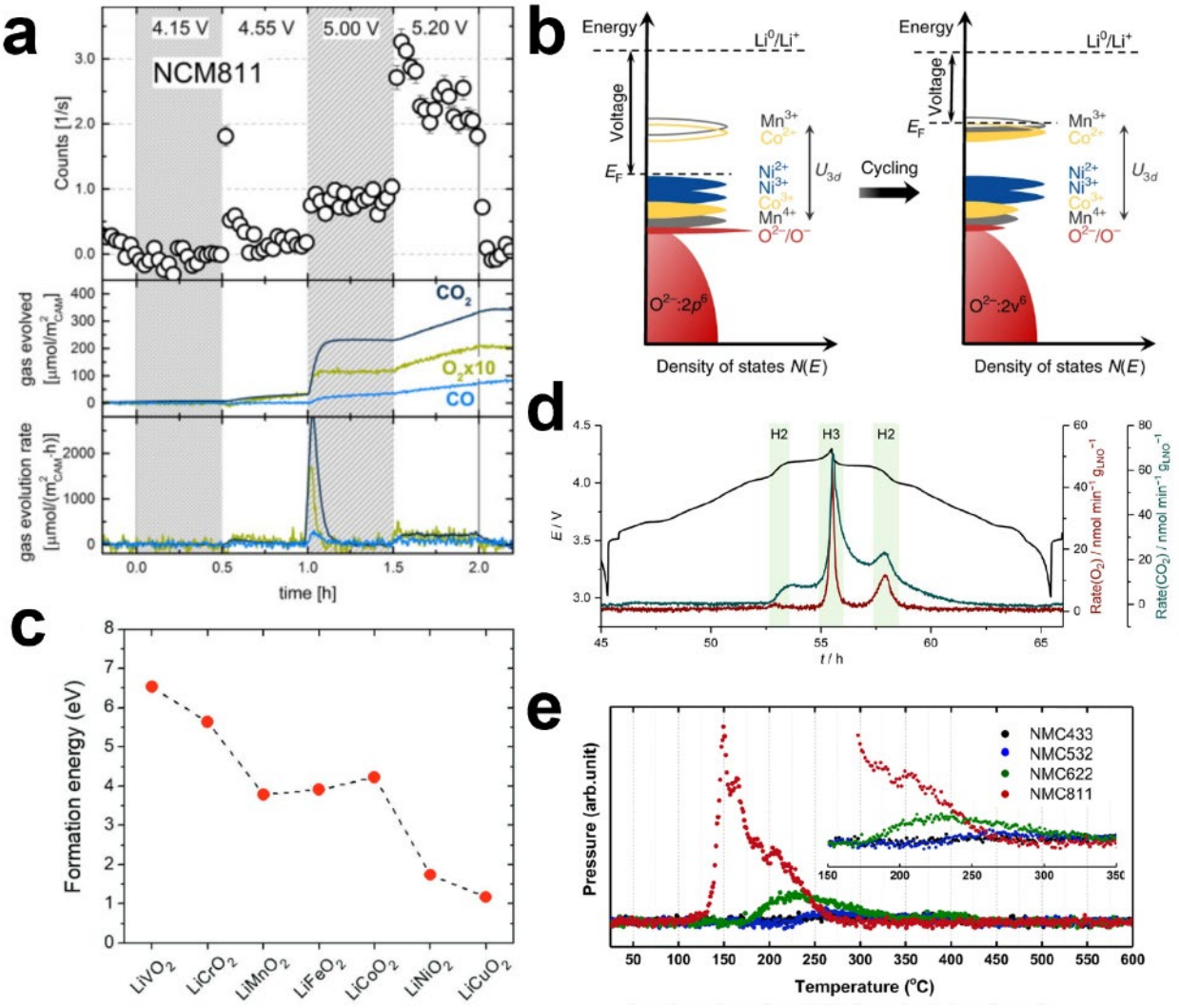


**Figure 1.6.** Evidence and origins of gas evolution in high-energy cathode materials. (a) *In-situ* gas evolution measurement during high-voltage cathode operation of layered materials. Dark blue: $CO_2$; yellow: $O_2$; light blue: CO. Adapted with permission from ref [52]. Copyright 2018 Elsevier. (b) Schematic of the electronic band structure of overlithiated layered oxides before (left) and after cycling (right). Adapted with permission from ref [89]. Copyright 2018 Springer Nature. (c) Oxygen vacancy formation energy for various layered lithium transition metal oxides. Adapted with permission from ref [90]. Copyright 2018 Wiley. (d) In-situ DEMS provides evidence of $O_2$ and $CO_2$ evolution that are coincident with structural phase transformations as LNO is electrochemically cycled. Reproduced with permission from ref [15]. Copyright 2019 Wiley. (e) Temperature- and Ni composition-dependent mass spectroscopy show that higher-Ni NMCs are more susceptible to gas evolution. Reproduced with permission from ref [91]. Copyright 2014 American Chemical Society.

### *1.3.3 Gas Evolution*

Most transition metal oxide cathode materials, including layered structures (e.g., Co-based, Ni-rich, and Li-rich), spinel structures, and disordered rock salt structures, release oxygen gas from their lattice upon electrochemical cycling.[92-94] Since this gas evolution is directly linked with the safety of battery packs and can initiate chemomechanical degradation of the active material, investigations on gas evolution and their mitigation methods have been critical research topics in these material systems. As an example, **Figure 1.6a** shows a typical *in-situ* gas evolution result using NMC811 cathodes.[52] In particular, online electrochemical mass spectrometry of pouch cells reveals significant $O_2$, $CO_2$, and CO evolution above 4.55 V (vs. $Li/Li^+$), which increases further as the operating voltage is raised to 5.2 V (vs. $Li/Li^+$). Moreover, simultaneous *in-operando* emission spectroscopy suggests the formation of reactive singlet oxygen, as evidenced by photon emission at 633 nm (**Figure 1.6a, top**). Singlet oxygen can promote $CO_2$ and CO evolution via chemical reactions with carbon additives or electrolyte compounds, causing further cell degradation.[95-97]

During redox, changes in the electronic band structure of the transition metal oxide promotes greater metal-oxygen covalency, which decreases the oxygen binding strength.[15,90,98] An example of the electronic band structure of the overlithiated $Li_{1.2}Ni_{0.15}Co_{0.1}Mn_{0.55}O_2$ is shown in **Figure 1.6b**.[89] During charging, electron extraction occurs via the oxidation of transition metals, including the 3*d* orbital of $Ni^{2+}$, $Ni^{3+}$, and $Co^{3+}$. However, since some of the TM 3*d* states overlap with the lattice oxygen 2*p* band, delithiation can also oxidize lattice oxygen ($O^{2-}$), resulting in oxygen dimerization and subsequent gas evolution.[99,100] This mechanism illustrates the

dependence of oxygen gas evolution on the transition metal oxidation state in cathode materials. Moreover, the identity of the TM in the $LiTMO_2$ structure sets the baseline for the oxygen evolution driving force in the fully lithiated state. Calculations of the oxygen vacancy formation energy show an inverse relationship with the TM-O covalency for various $LiTMO_2$ structures (**Figure 1.6c**), which can increase further during delithiation.

Gas evolution is also linked to changes in local atomic and electronic environments triggered by electrochemical cycling or thermal changes (**Figure 1.6d-e**).[91,101] Layered structures are known to experience changes in the oxygen stacking sequence at high states of charge, suggesting that crystallographic changes are tied to influence oxygen evolution. Indeed, density functional theory (DFT) calculations showed that the O1 stacking sequence (AB AB AB), which appears in layered oxides at high states of charge, is more susceptible to oxygen release than the O3 sequence (AB CA BC).[56] Moreover, gas release mainly occurs at the surface of active materials since oxygen migration from the bulk requires overcoming high activation barriers, up to 2.4 eV for bulk $LiNiO_2$.[90] Lattice oxygen vacancies are generally observed at surface regions that are in direct contact with the electrolyte, rather than at grain boundaries or interior surfaces.[102] Consequently, many electrode materials whose surfaces are coated or post-treated exhibit noticeable reductions in evolved gas amounts.[103]

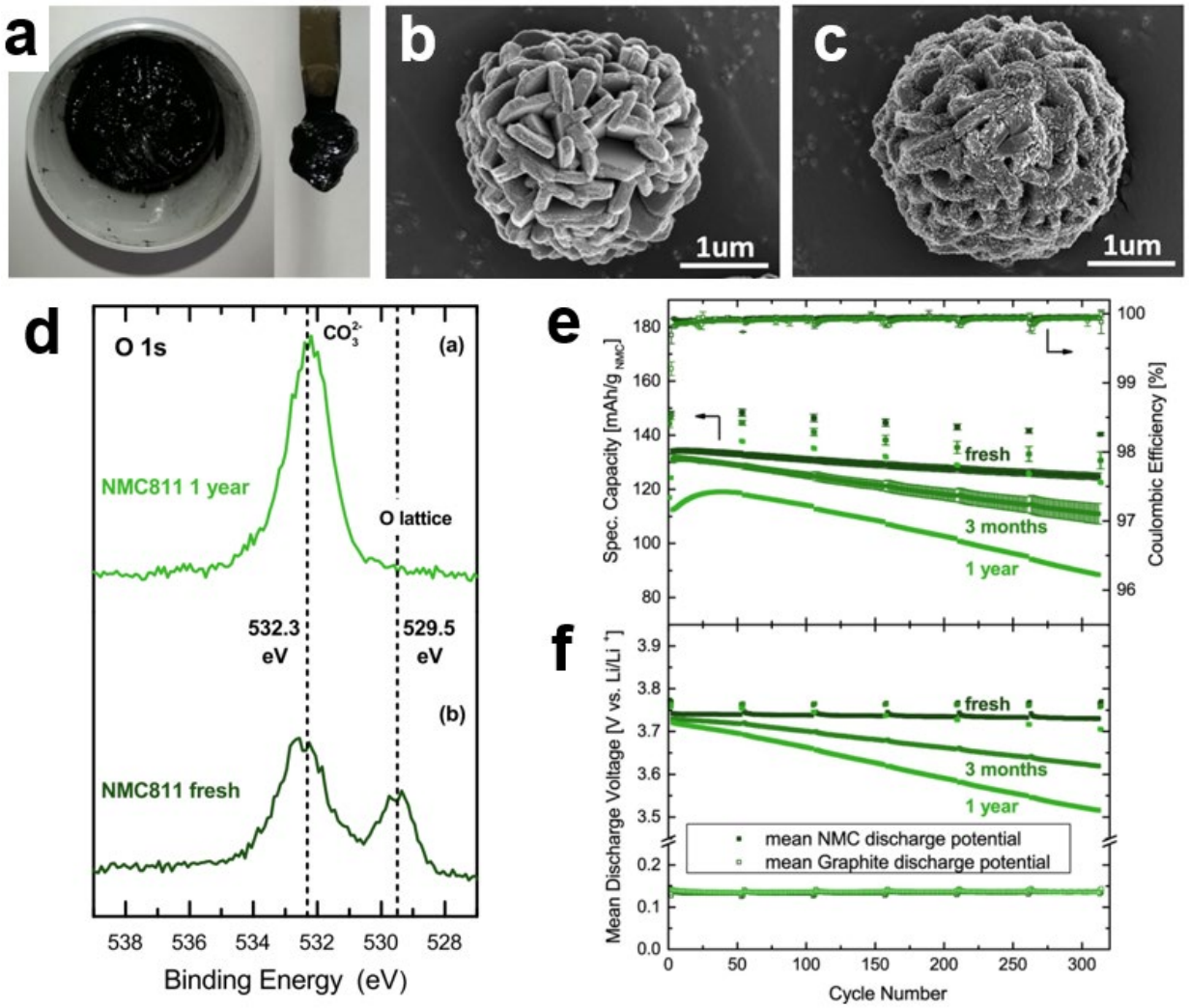


**Figure 1.7.** Ni-rich layered oxides are susceptible to the formation of lithium impurities. (a) Lithium impurities can cause slurry gelation, compromising subsequent electrode fabrication procedures. Adapted with permission from ref [104]. Copyright 2020 Wiley. (b-c) Bare NMC811 secondary particle (b) before storage and (c) after storage in humid CO2 for 1 day. Adapted with permission from ref [105]. Copyright 2019 American Chemical Society (d) XPS O 1s spectra shows an increase in carbonate spectral intensities after NMC811 is stored in ambient conditions for 1 year. (e) Cycle life results of NMC811-graphite full cells made with fresh NMC powder, NMC powder stored in ambient conditions for 3 months, and powder stored for 1 year. (f) Mean discharge voltage vs. cycle number shows significant changes in the NMC discharge potential and no changes in the graphite discharge potential, indicating that the full-cell degradation was due to cathode degradation. Reproduced with permission from ref [106]. Copyright 2018 IOP Publishing.

### *1.3.4 Lithium Impurities*

Lithium impurities, which are also referred to as lithium residues, are any lithium-containing species that are present on the cathode surface that are not part of the layered oxide, such as lithium hydroxides, carbonates, and bicarbonates. During cell operation, these species are known to electrochemically decompose in side reactions, generating undesirable gas reaction products.[107,108] The presence of lithium residues also decreases first-cycle efficiency, increases cell impedance, can induce slurry gelation (**Figure 1.7a**),[104] and is detrimental to long-term cycle life.[106]

There are two often-cited mechanisms for the presence of lithium impurities. The first mechanism originates during the synthesis of Ni-rich layered oxides. During synthesis, a mixture of lithium and transition metal precursors are uniformly mixed and heated. However, many reports have noted that lithium precursors are easily lost, leading to non-stoichiometry in the layered oxide. For example, lithium carbonate will not readily react with the nickel oxide structure until the temperature exceeds 600°C,[109] which is close to its thermal decomposition temperature at 640°C.[110] To compensate for this lithium loss, a small percentage of excess lithium source is typically added during synthesis.[109,111] The synthetic challenge is to add enough additional lithium to obtain the desired stoichiometry while avoiding excess lithium source to minimize the amount of lithium that does not react with the nickel oxide. Since it is difficult to precisely predict the variation in the excess lithium uptake between batches, the unreacted excess lithium typically remains on the cathode surface as lithium residues.

Second, Ni-rich layered oxides are known to readily react with ambient conditions to generate lithium impurities on the cathode surface (**Figure 1.7b-c**). Layered oxides with higher Ni content are known to be more susceptible to ambient degradation.[106] The known reaction pathway between environmental moisture and carbon dioxide with Ni-rich layered oxides is as follows:[112-114]

$$LiNiO_2 + H_2O \rightarrow Li_{1-x}H_xNiO_2 + xLiOH + (1-x)H_2O$$

$$LiNiO_2 + CO_2 \rightarrow NiO + \frac{1}{2}Li_2CO_3 + \frac{1}{4}O_2$$

These reactions sequester lattice lithium into surface LiOH and $Li_2CO_3$ deposits, which decreases the overall capacity. Lithium hydroxide can continue to react to terminally form lithium carbonate:[113-115]

$$2LiOH + CO_2 \rightarrow Li_2CO_3 + H_2O$$

$$LiOH + CO_2 \rightarrow LiHCO_3$$

$$LiOH + LiHCO_3 \rightarrow Li_2CO_3 + H_2O$$

Spectroscopic techniques such as X-ray photoelectron spectroscopy (XPS) have detected carbonate spectral intensities on the surface of NMC powders stored in ambient conditions (**Figure 1.7d**), providing strong evidence for this reaction pathway.[106] Moreover, three-electrode cells with a lithium reference electrode have shown not only that cells made with ambient-stored NMC exhibits poorer cycle life than cells made with fresh NMC, but also that the generation of lithium impurities at the cathode is uniquely responsible for this performance decrease (**Figure 1.7e-f)**.[106]

Therefore, even if the synthesis conditions are carefully tuned to obtain powders with a highly layered structure, improper handling and storage can still introduce degradation.

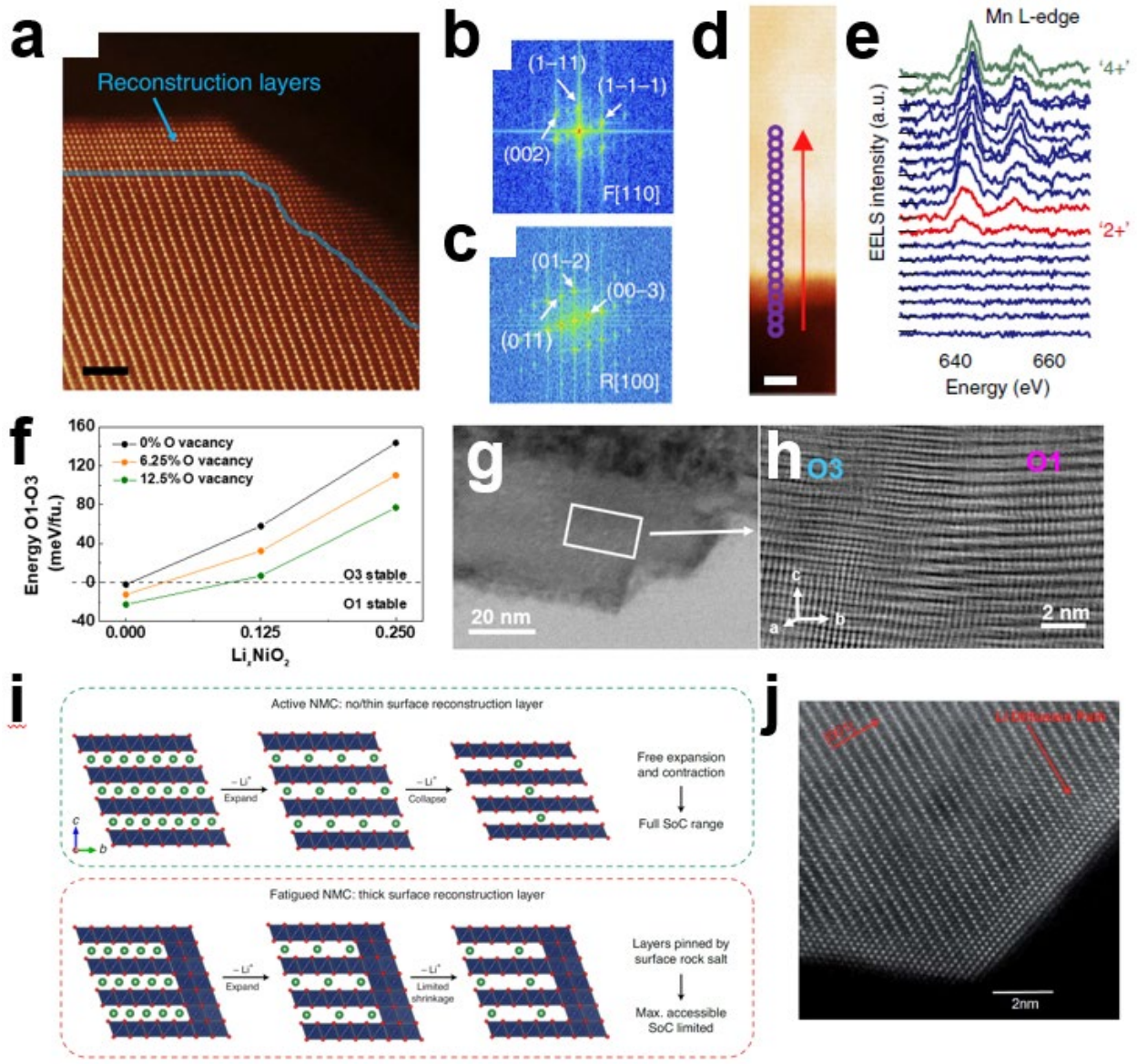


**Figure 1.8.** Surface phases in LIB cathode materials. (a) Annular dark field-STEM images of NMC taken along the R-3m[100] zone axis reveals the presence of surface rocksalt phases, which are further verified using local fast Fourier transform analysis of the (b) surface and of the (c) bulk. (d) STEM image of the scanning pathway for electron energy loss spectroscopy. (e) Mn L-edge EELS spectra acquired along the scanning pathway reveals that the TM surface chemistry is more reduced than the bulk. Adapted with permission from ref [85]. Copyright 2014 Springer Nature. (f)

Relationship between oxygen evolution and stacking structural change of LNO. (g) Stacking structural changes in layered LNO near the surface. (h) High-resolution image of the region boxed in (g). Adapted with permission from ref [56]. Copyright 2021 Wiley. (i) Schematic showing that surface phases compromise the long-term cycling performance of stoichiometric NMC due to "pinning" of Li layers, which limits the cyclability of the material.[64] Adapted with permission from ref [116]. Copyright 2020 Springer Nature. (j) HAADF-STEM image taken along the R-3m[110] zone axis reveals the presence of a surface phase on $Li[Ni_{1/5}Li_{1/5}Mn_{3/5}]O_2$. Reproduced with permission from ref [117]. Copyright 2011 Royal Society of Chemistry.

### *1.3.5 Surface Phase Formation*

In addition to interfacial chemical degradation, the surface transformation of layered structures to rocksalt and spinel phases is well-known for layered lithium transition metal oxides.[50,85,118-122] These phases are frequently analyzed via electron microscopy, including scanning transmission electron microscopy (STEM) paired with electron energy loss spectroscopy (EELS) analysis, which can together provide structural and chemical information with atomic resolution. High-angle annular dark field (HAADF STEM) may also be used to provide Z-contrast, allowing visualization of transition metals in lithium sites.

During extended cycling, the layered structure found in the bulk reconstructs into spinel and rocksalt phases due to the formation of Li-Ni antisite defects (**Figure 1.8a-c**).[50] The severities of such reconstructions are linked to the surface chemical environment, which include interactions between the cathode and the electrolyte that promote transition metal reduction near the surface (**Figure 1.8d-e**).[85,123-125] Although a direct correlation between the CEI and surface phase reconstruction is not yet well-understood, the oxidation state of the TM may provide a link between the two mechanisms as it plays a major role in the active material dissolution behavior near the surface. Due to changes in the TM oxidation state as a function of SOC, there is likely a strong

relationship between the nature of surface reconstructions and the cell upper cutoff voltage. As a representative example, Jung *et al.* revealed that a majority of the NMC532 surface transitions into a spinel phase when cycled to 4.5 V vs. $Li/Li^+$, while a mixture of spinel and rock salt phases were found when cycling to 4.8 V vs. $Li/Li^+$.[50]

The presence of other degradation mechanisms can also influence surface phase formation. Atomic-level reconstruction requires local transition metal migration from an original metal octahedral site to a vacant Li octahedral site. If oxygen vacancies are present due to gas evolution, there is a lower activation barrier inhibiting transition metal migration. Therefore, oxygen evolution can strongly influence the severity of these surface reconstructions.[90] Subsequent crystallographic shear along the (003) plane and cation migration can then result in the formation of rock salt phases.[126] Furthermore, the oxygen stacking sequence is affected by lattice oxygen vacancies. **Figure 1.8f** shows the thermodynamic relationship between oxygen stacking (O3-O1) and oxygen vacancy concentration in $Li_xNiO_{2-2y}$ ($y$ = 0, 0.125, and 0.25), where the O1 structure becomes more stable with increasing oxygen vacancy concentration. Accordingly, regions with O1 stacking can be found more easily near the surface than in the bulk following electrochemical cycling (**Figure 1.8g-h**).[56]

Although such surface structural reconstructions are typically thin (only about 3 to 20 nm), they have been implicated as a major degradation mechanism in high-energy cathode materials since these phases possess poor electrochemical activity.[116,127,128] For example, a recent study by Xu *et al.* revealed that surface rock salt phases can inhibit lattice changes in layered oxides (**Figure 1.8i**). Specifically, rock salt phases pin Li layers together, which limits the extractable capacity of Ni-rich layered materials and initiates intergranular cracking.[116] In disordered rock salt materials,

gas evolution is associated with surface densification,[129,130] leading to poor charge transfer kinetics. Similarly, in lithium-rich materials, surface structural changes (**Figure 1.8j**) can also induce other degradation phenomena, such as voltage fading. As oxygen loss is charge compensated by transition metal reduction, the main redox-active components switch from $O^{2-}/O^{-}$ and $Ni^{2+}$ to $Mn^{3+}$ and $Co^{2+}$ after cycling (**Figure 1.6b, right**).[89] Since these phases present barriers to Li migration, surface structural changes into rock salt or densified phases have been reported to significantly increase the charge transfer resistance of the active material.[129,130]

### *1.3.6 Chemomechanical Degradation*

Most LIB applications require cells that can be cycled hundreds to thousands of times. Under such long-term cycling, cathode particles experience inter-particle and intra-particle fracture due to accumulated chemomechanical degradation. Particle-level degradation stems from the accumulation of local structural changes and resulting strains, which are exacerbated by spatially inhomogeneous lithiation dynamics across primary and secondary particle structures. Ultimately, these degradation events can generate sites of electrochemical deactivation within the electrode.

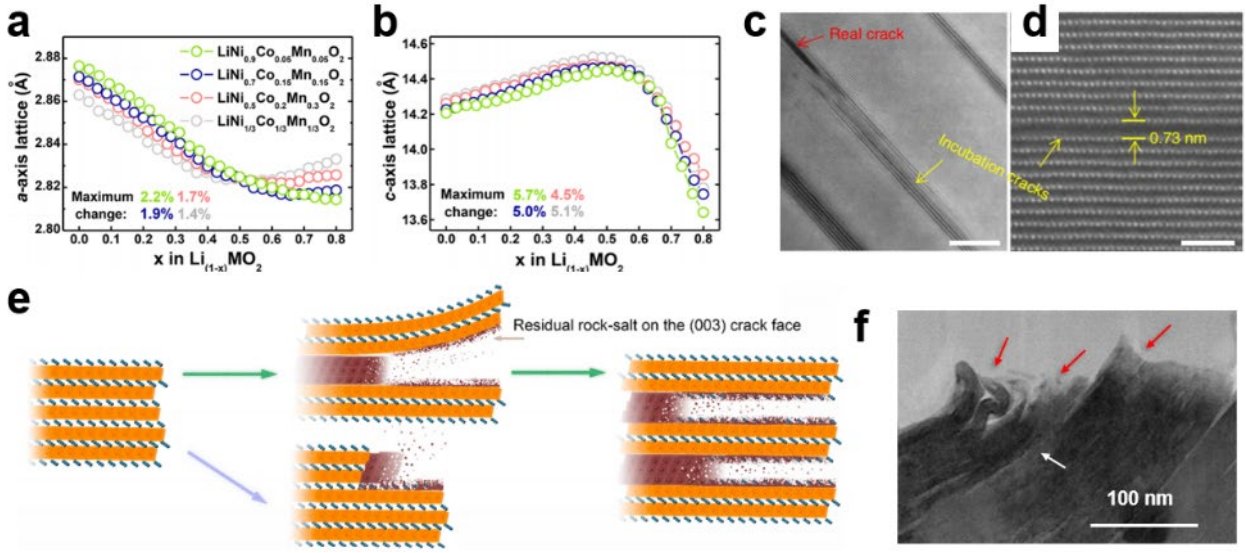


**Figure 1.9.** Primary particle level degradation. Lattice parameter changes of the (a) *a*-lattice parameter and (b) *c*-lattice parameter for various compositions of NCM cathodes. Reproduced with permission from ref [35]. Copyright 2019 American Chemical Society. (c,d) Cracks along (003) planes for a NMC622 cathode after 100 cycles at 2.7–4.8 V as imaged by high angle annular dark field scanning transmission electron microscopy (HAADF-STEM). The scale bars are 10 nm in (c) and 2 nm in (d). Adapted with permission from ref [54]. (e) Schematic of cracking pathways induced by a (003) rock salt platelet. Green arrow: formation of rock salt phase along the (003) plane. Purple arrow: formation of rock salt phase on the particle surface. Adapted with permission from ref [131]. Copyright 2017 American Chemical Society. (f) Bending induced by the local O1 stacking transition in $LiNiO_2$ as characterized by transmission electron microscopy. Adapted with permission from ref [56]. Copyright 2021 Wiley.

#### 1.3.6.1 Primary Particle Level

Layered oxides, which contain anisotropic unit cells, are susceptible to mechanical degradation at the primary particle level.[35,121,132,133] In general, the *a*-lattice parameter of layered materials continuously decreases with increasing SOC due to the reduced electrostatic repulsion associated with transition metal oxidation (**Figure 1.9a**). Meanwhile, the *c*-lattice parameter expands with increasing SOC due to greater oxygen-oxygen repulsion between slabs. However, a sudden *c*-lattice parameter collapse is observed beyond ~60 % SOC regardless of the transition

metal composition of NMC as shown in **Figure 1.9b**, initiating severe mechanical degradation during long-term cycling.[35] Notably, the intraparticle mechanical degradation is mainly observed along the (003) planes in layered structures (**Figure 1.9c-d**), owing to the relatively weak bonding nature between neighboring transition metal ($MO_2$) slabs.[54,134]

The origins of particle fracture have been attributed to various factors. Surface reconstructions into spinel or rock salt phases is an often-cited culprit due to the lattice mismatch and corresponding stress discontinuities between the bulk layered structure and surface phases.[54,131] For example, as illustrated in **Figure 1.9e**, oxygen evolution can promote the formation of rock salt phases. If rock salt phases form along (003) surfaces, severe fracture can follow, generating the formation of multiple parallel (003) platelets. Otherwise, a dramatic stepped layered structure can appear when the rock salt phase is developed along the other planes as shown in the purple-colored path of **Figure 1.9e**.[131] In addition, Liu *et al.* recently showed that particle cracking is strongly linked with the transition metal composition. Although Co presents advantages in suppressing the formation of Li/Ni antisite defects in layered materials, greater inclusion of Co also exacerbates oxygen release and lattice changes, inducing more serious intragranular microcracks.[134] Furthermore, particles possessing nonuniform distributions of Li-ions are more susceptible to reversible planar gliding and cracks along (003) planes in Ni-rich layered cathodes.[135] The newly exposed surface then undergoes additional chemical degradation, further compromising electrochemical performance.

Another notable origin of chemomechanical degradation is the oxygen stacking transition. Layered transition metal oxides nominally possess O3 oxygen stacking (AB CA BC). However, highly delithiated layered cathodes, including lithium-rich NMC, $LiCoO_2$, NMC, and Ni-rich

layered oxides, tend to transition into O1 type stacking (AB AB) in order to minimize repulsion between oxygen atoms, thus generating stacking faults, dislocations, or O1-O3 mixed phases (also called H1-H3)[55,136,137]. This local stacking transition causes an oxygen framework mismatch with the original O3 stacking, inducing cracking along the (003) plane or serious bending of layers as shown in **Figure 1.9f**.[56] Also, since cyclic stacking changes between O1-O3 structures can induce electrochemical creep,[55] this oxygen stacking transition at high SOCs degrades the activity of active particles.

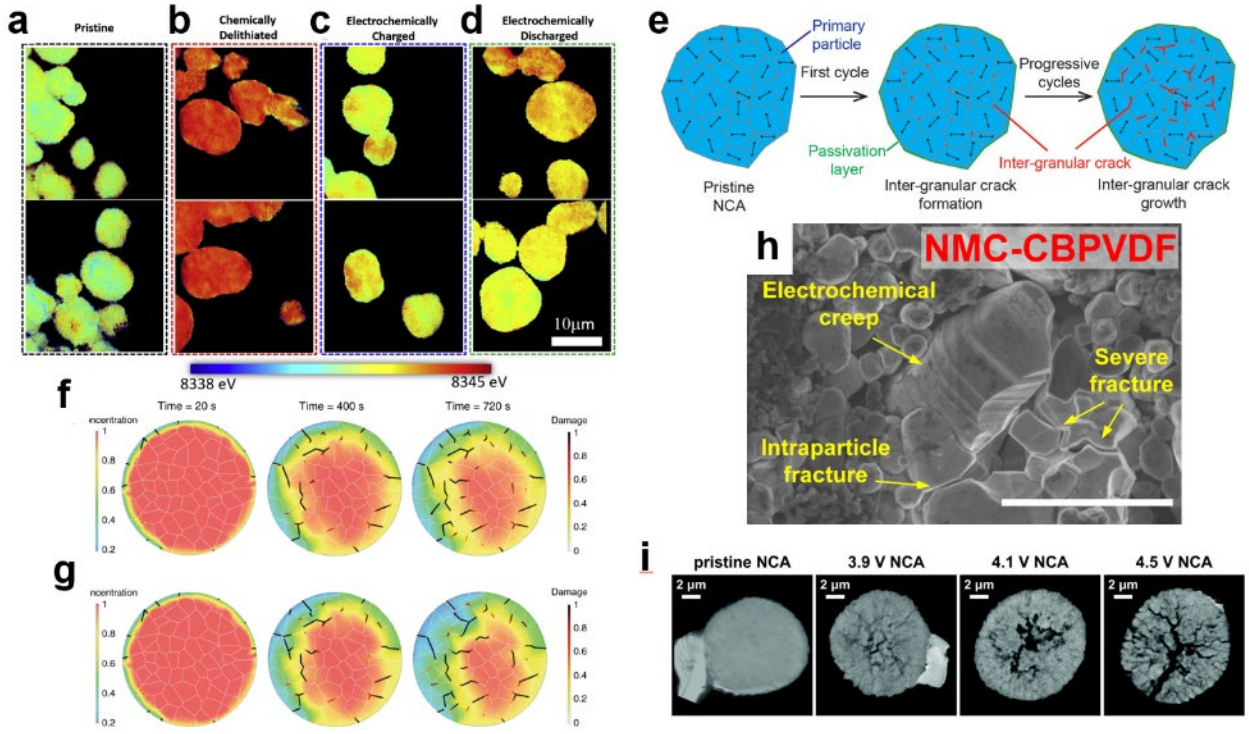


**Figure 1.10.** Nonuniform lithium distributions at the particle level lead to particle fracture. (a-d) Spatially resolved Ni K-edge X-ray absorption near edge spectroscopy (XANES) mapping shows that NCM-622 exhibits SOC heterogeneity under (a) pristine, (b) chemically delithiated, (c) electrochemically charged, and (d) electrochemically discharged conditions. Adapted with permission from ref [138]. Copyright 2019 Wiley. (e) Schematic showing that intergranular fracture originates from the accumulation of cycling-induced stress among aggregates of randomly oriented primary particles. Reproduced with permission from ref [57]. Copyright 2017 American

Chemical Society. (f,g) Finite element modeling (FEM) of an NCM secondary particle (f) without and (g) with electrolyte penetration into intergranular cracks shows that liquid percolation promotes further chemomechanical damage. Adapted with permission from ref [139]. (h-i) High-voltage cycling promotes (h) electrochemical creep and particle fracture after high-voltage cycling for primary particles of NCM-523 (scale bar is 2 μm) and (i) intergranular fracture in secondary particles of $LiNi_{0.8}Co_{0.15}Al_{0.05}O_2$ (NCA). Adapted with permission from refs [140] and [141], respectively. Copyright 2021 American Chemical Society and 2018 Royal Society of Chemistry, respectively.

1.3.6.2 Secondary Particle Level

Multicomponent Ni-rich layered oxides exhibit a sloping voltage profile, indicating solid-solution behavior during lithiation and delithiation. However, postmortem spectromicroscopy on individual secondary particles have revealed local differences in the SOC within individual particles, implying that kinetic effects can inhibit the charge-discharge process and prevent the overall particle SOC from changing uniformly (**Figure 1.10a-d**). One explanation for this observation is limited access to electronic or ionic current paths, which can cause charge transfer reactions to progress at different rates across the particle surface. This spatial heterogeneity in composition persists after long relaxation times[142] and can even be generated by chemical delithiation (**Figure 1.10b**).[138] Such heterogeneity is detrimental to long-term stability since it can promote the formation of locally overcharged or undercharged regions during cycling. Since properties such as electronic conductivity, ionic conductivity, lattice parameter, and stability with the electrolyte are highly dependent on the SOC, these regions can act as sites for additional chemomechanical degradation.

A predominant degradation mechanism in secondary particles is intergranular fracture, which is driven by randomly oriented primary particles that experience anisotropic volume expansion during cycling (**Figure 1.10e**).[57,133] As individual primary particles expand and contract

relative to each other, the high hoop stress and the local lattice mismatch near grain boundaries can cause connections with neighboring particles to break.[139] If the electrolyte is unable to percolate into the interior of the particle (for example, if interior cracking is more severe than surface cracking), contact loss can cause particles to become electrochemically isolated and deactivated as electrical and ionic conduction pathways are severed.[143] Conversely, if the electrolyte can percolate into the particle and wet newly exposed surfaces formed from intergranular fracture, these faces can become additional sites for surface phase formation or electrolyte decomposition. Additionally, electrolyte penetration acts as a positive feedback loop for further SOC heterogeneity and chemomechanical degradation since cracked surfaces become pathways for fast lithium transport, as illustrated in **Figure 1.10f** (without electrolyte penetration) and **Figure 1.10g** (with electrolyte penetration).[139]

The extent of chemomechanical degradation is also tied to the operating voltage of the cell. High SOCs can induce severe volumetric changes to the unit cell of layered oxides,[35] which exacerbates the stress buildup that precedes particle fracture in both primary (**Figure 1.10h**)[140] and secondary particles (**Figure 1.10i**).[141] Moreover, at high SOCs, the partially filled Li layers present a lower energetic barrier to TM slab sliding,[55] suggesting that electrochemical creep and secondary particle fracture may become more facile when materials are overcharged.

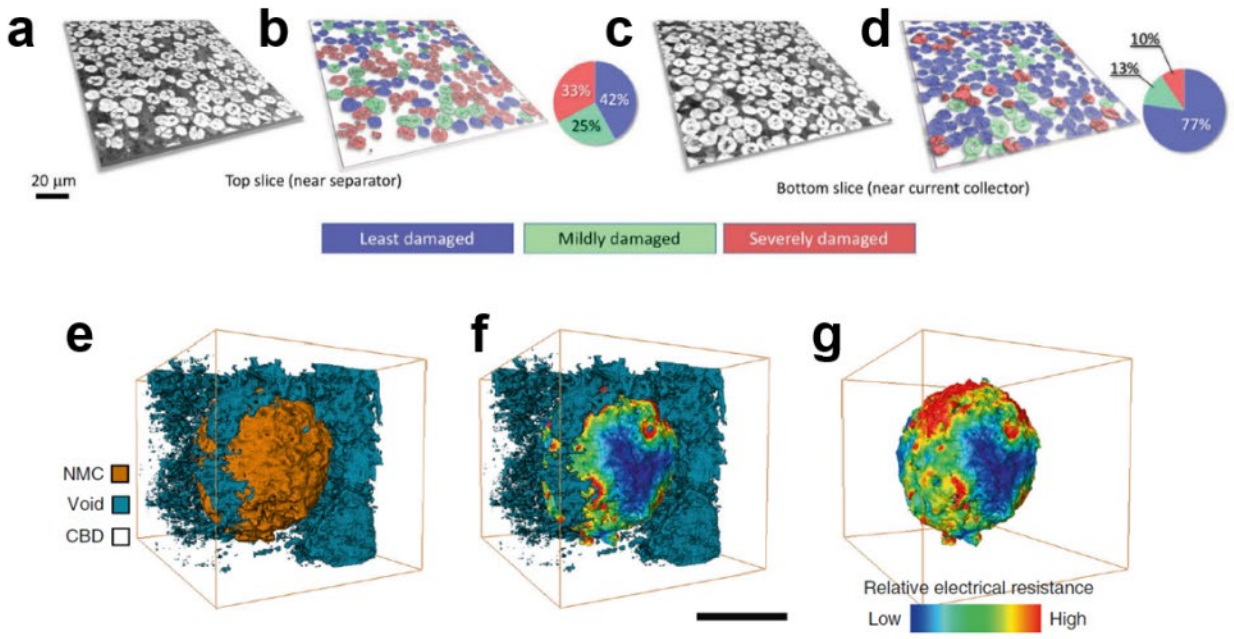


**Figure 1.11.** Compositional heterogeneity at the electrode level. (a-d) Depth-dependent mapping of cracked NCM-622 particles after 10 cycles at 5C. (a,c) X-ray phase contrast tomographic images and (b,d) color-coded images that demonstrate cracking probabilities for particles near the separator and near the current collector, respectively. Adapted with permission from ref [144]. Copyright 2019 Wiley. (e) Phase contrast hard X-ray nano-tomography enables discrimination between NCM-811, the carbon-binder domain, and void space. (f,g) Renderings of the calculated distribution of electrical resistance superimposed onto the rendering of the NCM particle (f) with and (g) without visualization of the void space. Adapted with permission from ref [58]. Copyright 2019 Wiley.

1.3.6.3 Electrode Level

Signs of compositional heterogeneity have been observed for aggregates of layered oxides that undergo fast delithiation. X-ray spectromicroscopy, X-ray diffraction, and electrochemical analysis have shown that the exchange current density for layered oxides increases with decreasing lithium composition. Since the changes in the exchange current density accelerate during charge and slow during discharge, changes in compositional variations are correspondingly autocatalytic and autoinhibitory. Delithiation can therefore drive a collection of particles with slight initial

compositional heterogeneity to a final state possessing further compositional separation, provided that the reaction rate is sufficiently fast.[145]

Thick electrodes can also induce gradients of varying composition within the electrode. *In-situ* microfocused X-ray diffraction has shown that particles closest to the separator react faster than the prescribed cycling rate, while particles buried in the interior of the electrode lag behind.[146] Correspondingly, X-ray phase contrast tomography shows that the particles closer to the separator exhibit greater evidence of cracking than those closer to the current collector (**Figure 1.11a-d**).[144] This difference was ascribed to the poor ionic conduction paths generated by pockets of trapped electrolyte in the electrode.[144,147] Compositional heterogeneity within an electrode has also been observed in non-layered systems, such as $LiFePO_4$. For example, Liu *et al.* observed both thickness-dependent and radially-dependent charge heterogeneity, suggesting the presence of laterally inhomogeneous reaction rates.[148] At larger length scales, compositional variations appear to be dependent on ionic and electronic conduction paths within the electrode rather than the properties of the material. Therefore, strategies that can alleviate compositional heterogeneity at the electrode length scale will likely be highly impactful since they can universally provide benefits across many material systems.

Although compositional heterogeneity may arise due to suboptimal electrode engineering, the resulting chemomechanical degradation will be a function of atomic-level and particle-level degradation. For NMC622, cycling-induced volumetric changes have been shown to induce particle detachment from the carbon-binder domain, which could render a particle electrochemically inactive (**Figure 1.11e-f**).[58,149] Partial detachment can also lead to locally high electrical resistance, promoting hotspots on the particle that are more prone to overcharge (**Figure**

**1.11g**).[58] Since particle detachment can occur anywhere within the electrode, measures should be taken to optimize electrical conduction paths within the electrode to minimize local hotspots.

## 1.4 Mitigating Interfacial Degradation

### *1.4.1 Oxide Coatings*

To improve the cycle life of layered cathode materials, coating layers such as $Al_2O_3$,[60,68,86] MgO,[87] $ZrO_2$,[60,88] $TiO_2$,[89] $LiBO_2$,[90] and $Li_2TiO_3$[91] have been extensively explored. Coatings can act as interfacial buffer layers that scavenge HF from the electrolyte and shield the cathode from electrolyte decomposition reactions. While these layers are advantageous since they can be incorporated on the cathode surface via simple methods such as atomic layer deposition[60,68,86–88] or wet chemical routes,[90,91] they often possess low ionic conductivity,[92] which can be detrimental for high-rate cycling. Additionally, since these coating layers are often directly bonded to the active material surface, changes in the unit cell volume during cycling can generate mechanical incompatibilities with the coating, inducing delamination of the surface coating and rendering it ineffective for future cycles.[93]

### *1.4.2 Doping*

To mitigate chemomechanical degradation at the atomic level, strategies typically aim to reduce the thermodynamic favorability of interfacial changes, such as oxygen evolution or surface phase formation, or to kinetically inhibit such reactions. One of the primary approaches is to incorporate dopant elements to the active material by adding foreign precursors during synthesis. Appropriately chosen dopants then segregate to the interface without significantly generating

undesired structural defects. Parameters such as the dopant oxidation state, atomic radius, and bonding nature with the active material dictate the extent and type of electrochemical improvement.[150,151] DFT calculations of the surface oxygen release energies for doped $Li_2MnO_3$, a representative Li-rich cathode chemistry, predict that dopant elements that can easily hybridize with lattice oxygen promote improved oxygen retention (**Figure 1.12a**).[151] Doping can also stabilize delithiated phases by inducing $Ni^{2+}$ ordering in Li layers,[152] and can suppress the H2-H3 transition in Ni-rich layered oxides.[153] Anionic dopants have also been employed for DRX systems, where F substitution resulted in greater $Ni^{2+}$ content and ultimately increased the average discharge voltage and improved cycle life and rate capability.[154] In excess, dopants can also generate interfacial layers during synthesis that limit the growth of charge transfer impedance and protect the active material from HF etching.[153] Nonetheless, since the degradation mechanisms for Ni-rich and Li-rich cathodes can sensitively vary with composition, the dopant selection for each active material chemistry must be carefully considered.

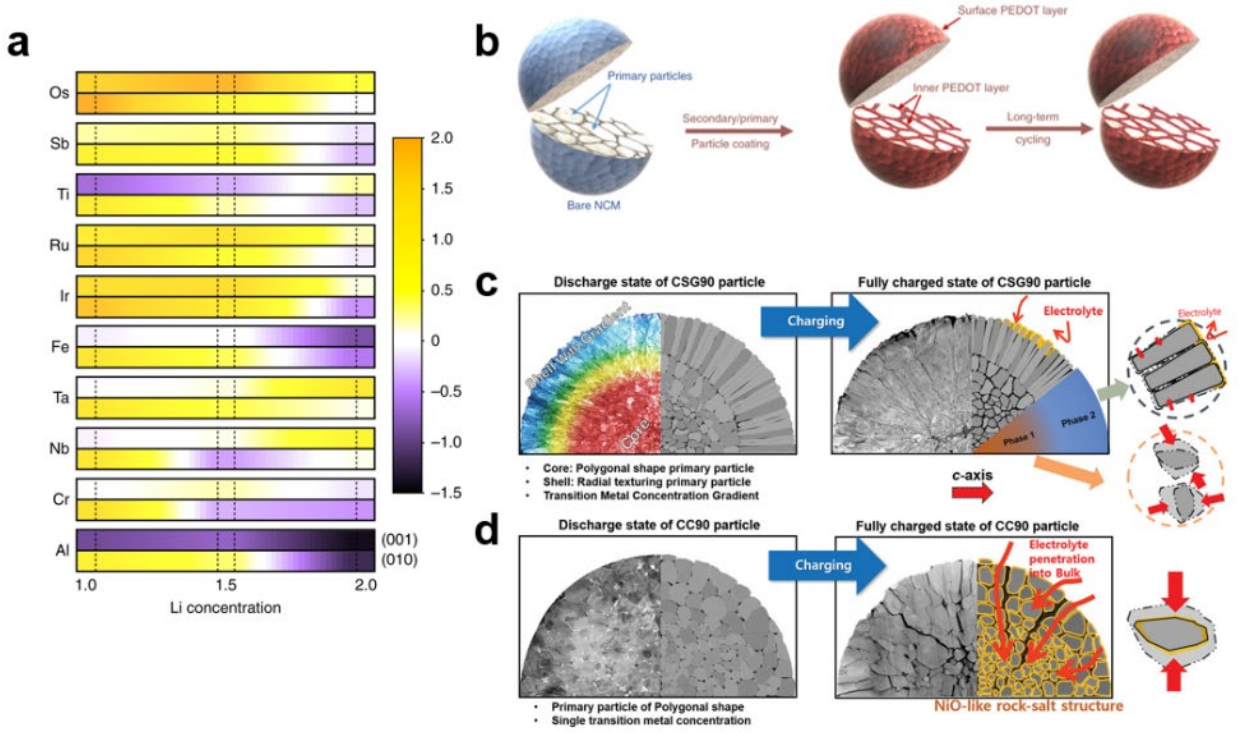


**Figure 1.12.** Strategies to mitigate chemomechanical degradation in layered oxide materials. (a) DFT screening of dopant elements shows that appropriate surface doping can reduce the oxygen evolution capability during charging in Li-rich oxide systems, shown here for (001) and (010) facets. Yellow and purple colors indicate improved and reduced oxygen retention compared to the undoped structure, respectively. Reproduced with permission from ref [151]. Copyright 2018 Springer Nature. (b) Infused grain boundary coatings, such as poly(3,4-ethylenedioxythiophene) (PEDOT) deposited by an oxidative chemical vapor deposition process, can also improve cycle life by minimizing intergranular cracking. Adapted with permission from ref [132]. Copyright 2019 Springer Nature. (c-d) At the secondary particle level, (c) an NMC-900505 particle possessing a core-shell structure that utilizes radially oriented grains and compositional gradients with lower surface Ni content exhibits reduced cycling-induced intergranular cracking compared to (d) a traditional secondary particle structure. Adapted with permission from ref [155]. Copyright 2019 Wiley.

### *1.4.3 Grain Boundary Engineering*

Grain boundary engineering strategies can also provide benefits at the secondary particle level. One approach to minimize the impact of intergranular cracking is to employ nanowelding, whereby nanoparticles grow within the grain boundaries in secondary particles to effectively pin

neighboring grains together.[156] Infused coatings, shown in **Figure 1.12b**, can also provide protection against chemomechanical degradation and are therefore highly desirable for high electrochemical performance. Like particle-level coatings, these layers protect against electrolyte decomposition reactions and surface phase formation but provide additional benefits at grain boundaries.[132,157] Furthermore, infused coatings can reduce intergranular cracking during cycling since they provide additional bonding between individual primary particles.[132,157,158] Similarly, if volumetric changes cause neighboring particles to be in compression, these layers can provide mechanical compliance to accommodate cycling-induced strains. The benefits imparted by infused coatings are therefore highly dependent on the mechanical properties of the coating material.

Significant effort has also been dedicated to engineering the grain structure within secondary particles. During traditional synthesis procedures, primary particles nucleate and randomly sinter together, causing interfacial incompatibilities during volume expansion or contraction during cycling. In contrast, radially oriented grains can dissipate strain buildup circumferentially and promote radially uniform expansion and contraction, thereby reducing intergranular cracking and improving cycle life. These microstructures can be achieved by incorporating appropriate dopant elements (such as B, W, Ta, Sb, Mn, and Al), which lower the surface energy of certain facets upon substitution. These facets will therefore preferentially form during particle growth. Finally, coarsening can be controlled using carefully chosen synthetic temperatures and times, resulting in radially oriented, high aspect ratio grains.[152,159,160]

The chemical composition of secondary particles can also be radially segmented to form concentration-gradient structures, which further provide resistance against intergranular cracking. These types of particles are synthesized by gradually introducing Ni-deficient precursors during

coprecipitation. In this manner, Ni-rich domains are found in the core of the particle and are surrounded by an exterior shell possessing lower Ni content that is comparatively chemically stable and can better dissipate strain (**Figure 1.12c-d**).[155,160]

### *1.4.4 Two-Dimensional Materials: Graphene*

Two-dimensional (2D) materials are crystalline solids that are one atomic layer thick. Due to quantum confinement effects at the atomically thin limit, 2D materials exhibit unique optoelectronic properties that differ from their bulk counterparts. For example, graphene exhibits a linear dispersion relation that results in ballistic electron transport, while $MoS_2$ transitions from an indirect bandgap in the bulk to a direct bandgap at the monolayer limit.[6,7,161,162] The wide library of 2D materials enables access to a wide range of optoelectronic properties as a function of composition, phase, and thickness (**Figure 1.13**). These effects can be exploited for next-generation devices with applications in memory, quantum computing, and energy storage.

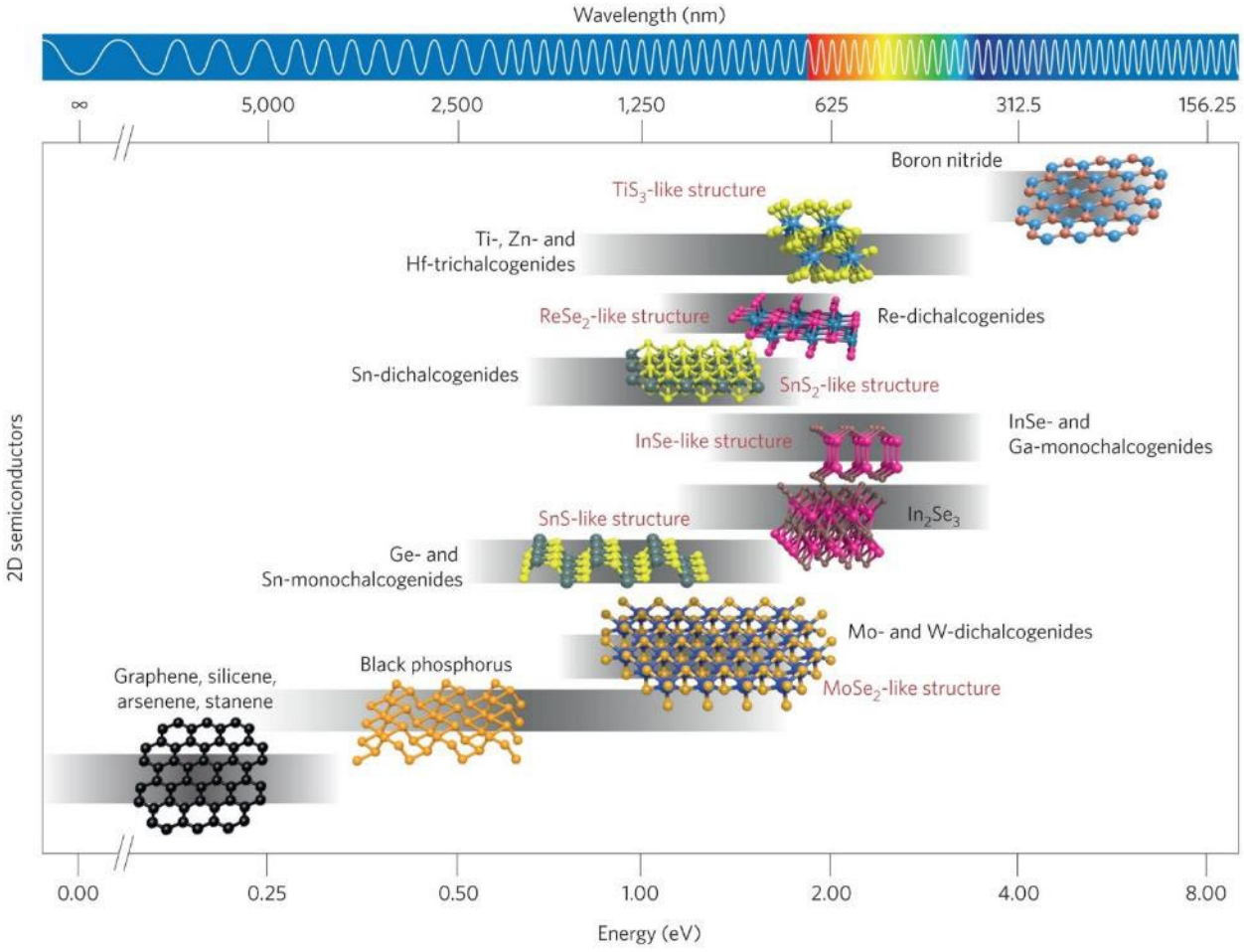


**Figure 1.13.** Two-dimensional materials exhibit a wide range of optoelectronic properties as a function of their bandgap values, including graphene (metallic), various mono- and dichalcogenides (semiconducting) and hexagonal boron nitride (insulating). Reproduced with permission from ref [161]. Copyright 2016 Springer Nature.

Despite their attractive properties, scalable manufacturing of 2D materials remains a practical challenge. Two-dimensional materials can be synthesized using a bottom-up approach, using direct growth methods such as chemical vapor deposition[163,164] or molecular beam epitaxy,[165,166] or extracted from bulk solids using top-down methods such as mechanical exfoliation[5] or liquid-phase exfoliation (LPE).[167-171] While bottom-up synthesis can yield 2D

materials with low defect densities, materials must be grown on a substrate, which can encumber subsequent processing steps. For applications with greater tolerances to material defects, and where throughput is a higher priority, top-down methods are more appropriate. Of these methods, liquid-phase exfoliation is an excellent processing scheme for producing large quantities of 2D materials in a scalable manner. LPE involves immersing a bulk layered solid in a solvent and applying shear forces[172,173] or ultrasonic cavitation[167-171] to tear apart the crystal into nanosheets (**Figure 1.14a-b**). Since exfoliated sheets can easily reaggregate, surfactants or polymers may be added as auxiliary dispersing agents to improve flake suspension and improve processing yields.[169-171] The resulting exfoliated material can be postprocessed using techniques such as filtration or centrifugation to select exfoliated nanosheets with appropriate thicknesses and lateral sizes for desired applications (**Figure 1.14c-e**).

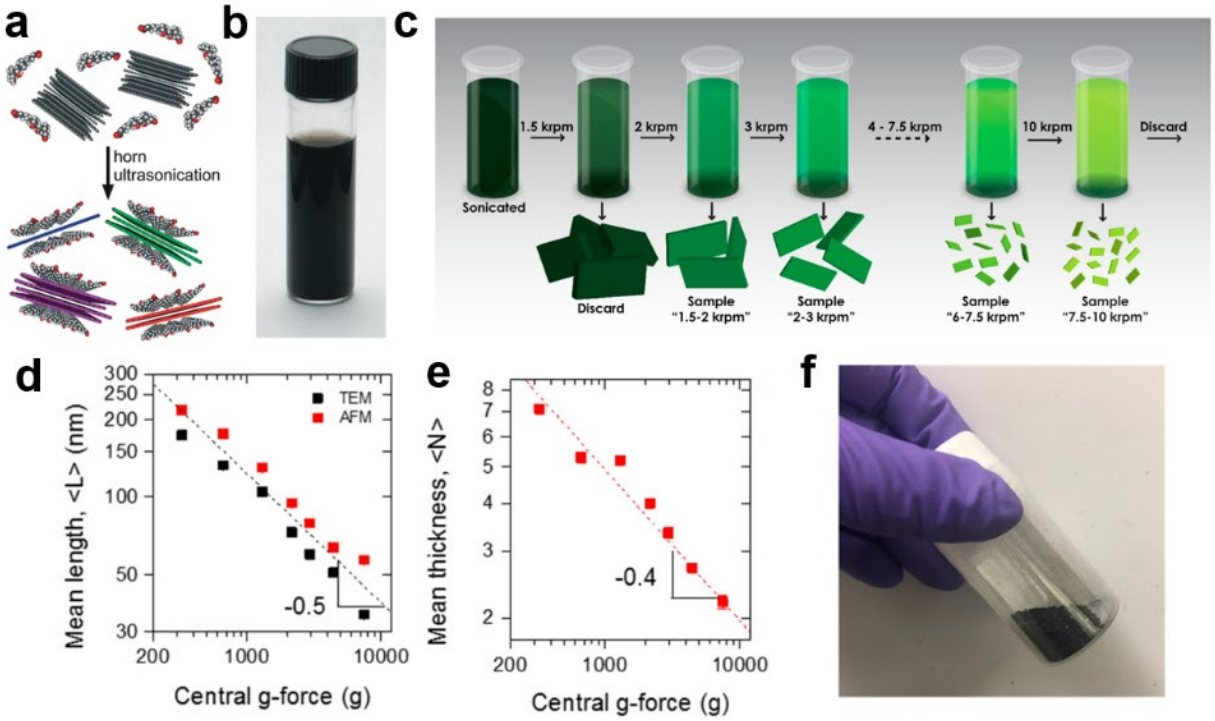


**Figure 1.14.** Liquid-phase exfoliation of 2D materials. (a) Schematic of ultrasonic graphene exfoliation assisted by the presence of a sodium cholate surfactant. (b) Image of an aqueous graphene dispersion with sodium cholate that remains stable six weeks after exfoliation. Adapted with permission from ref [174]. Copyright 2009 American Chemical Society. (c) Schematic of centrifugation-based isolation of thin nanoflakes. (d-e) Average flake (d) length and (e) thickness after dispersions were subjected to various g-forces during centrifugation. Adapted with permission from ref [175]. Copyright 2016 American Chemical Society. (f) Photograph of a vial of graphene-ethyl cellulose powder after solvent removal. Reproduced with permission from ref [176]. Copyright 2020 American Chemical Society.

Once processed, two-dimensional materials provide significant opportunities to tune interfacial reaction kinetics in LIBs.[177] In particular, graphene is of great interest since it possesses high electron mobility ($2 \times 10^6$ cm$^2$ V$^{-1}$s$^{-1}$ under ideal conditions),[178] which is useful for boosting rate capability in composite electrodes.[179,180] Moreover, since graphene layers can screen direct interactions between reactive oxide surfaces and carbonate electrolytes, they inhibit interfacial chemical degradation reactions and promote stable interphase growth.[181-186] Schemes to

incorporate graphene or reduced graphene oxide (rGO) have been employed in the literature, including encapsulation,[56,182,183,187,188] compositing,[103,140,179,180,189-192] and scaffolding.[193-196] For these applications, graphene can be obtained via liquid phase exfoliation, yielding graphene sheets with higher pristineness and fewer chemical defects compared to other synthetic methods such as chemical reduction of graphene oxide.[197-199] As a notable example, graphene can be exfoliated with ethyl cellulose (EC) as an auxiliary dispersing agent that envelops exfoliated flakes and ensuring that they stay suspended in solution.[171,200,201] Postprocessing steps thoroughly remove the solvent, producing graphene-ethyl cellulose powder that can then be easily incorporated into battery electrode architectures (**Figure 1.14f**).[56,140,176,179,180,188,190]

Nonetheless, the use of 2D materials in lithium-ion batteries is becoming increasingly widespread as both fields experience rapid growth. A broad understanding of LIB use cases and degradation pathways, combined with a thorough exploration of the impact of 2D material incorporation, can help establish a path forward for the use of 2D materials in next-generation energy storage devices.

## 1.5 Thesis Organization and Roadmap

This thesis investigates the role of graphene coatings in comprehensively improving the performance of Ni-based lithium-ion battery cathode materials across wide operational regimes. Each chapter will focus on an individual Ni-rich layered oxide chemistry, identify inherent materials issues within that system, and explore how graphene coatings can address those limitations.

Chapter 2 explores the power performance of nanoparticle $LiNi_{0.8}Co_{0.15}Al_{0.05}O_2$ (NCA) cathodes. In comparison to traditional secondary particle-based cathodes, nanoparticle-based cathodes are attractive for power performance since their high surface areas increase the number of charge transfer sites and shorten solid-state lithium-ion diffusion lengths. However, their large surface areas increase their susceptibility to surface degradation. This chapter describes a facile thermal procedure to remove surface lithium impurities, which was verified using spectroscopic methods. Subsequently, the NCA nanoparticles were uniformly coated with a graphene layer, which substantially improved the rate performance, electrode packing density, and low-temperature performance in half-cell and full-cell geometries. This work also identified that a pristine cathode surface is critical for successful graphene encapsulation strategies.

Chapter 3 investigates high-voltage degradation mechanisms in $LiNi_{0.5}Mn_{0.3}Co_{0.2}O_2$ (NMC532). At high states of charge, chemomechanical degradation is responsible for the extremely poor cycle life in Ni-based layered oxides. In this work, NMC532 particles were coated with graphene and subjected to electrochemical cycling to 4.8 V vs. $Li/Li^+$. The graphene coating extended the cycle life of the NMC, decreased cell impedance, and enabled record coulombic efficiencies at high operating voltages. Through a suite of materials characterization, including spectroscopy, microscopy, and X-ray diffraction, the graphene coating was found to decrease high-voltage chemomechanical degradation, which ultimately improved the cycle life. This work proposes that the electronic wiring within the LIB electrode likely plays a key role in delocalizing cycling-induced strains that contribute to particle fracture and electrochemical creep, which is highly relevant for LIB electrode designs.

Chapter 4 establishes a scheme to address the ambient surface degradation in $LiNiO_2$ (LNO). Ni-rich layered oxides, including LNO, are susceptible to reaction with atmospheric moisture and carbon dioxide, which react with the lattice to form lithium residues on the cathode surface. This work exploits the hydrophobic properties of graphene and ethyl cellulose to prevent direct contact between the LNO surface and ambient moisture. Spectroscopy, microscopy, and electrochemical methods confirm that the graphene-EC coating suppresses the formation of lithium impurities and preserves ideal electrochemical behavior. Importantly, this scheme is demonstrated on the Ni-rich limit and therefore has broad applicability for addressing ambient stability of NMC and NCA materials that are widely used in cells for electric vehicles.

Chapter 5 broadly explores future research opportunities for graphene in energy storage systems, including lithium-ion and beyond-lithium batteries. Based on the work presented in this dissertation, this chapter posits that graphene can play a role in improving the electrochemical performance of emerging electrode materials and architectures, with compositional and morphological control as further knobs to tune the level of improvement.

Chapter 6 summarizes the work presented in this thesis and provides an outlook on the prospects for the intersection of 2D materials and lithium-ion battery development.

# CHAPTER 2:

# ENHANCING NANOSTRUCTURED NICKEL-RICH LITHIUM-ION BATTERY CATHODES VIA SURFACE STABILIZATION

This chapter is adapted from:

Lim, J.-M.,* **Luu, N. S.,*** Park, K. Y., Tan, M. T. Z., Kim, S., Downing, J.R., He, K. Dravid, V. P., Hersam, M.C. Enhancing Nanostructured Nickel-Rich Lithium-Ion Battery Cathodes via Surface Stabilization. *J. Vac. Sci. Technol. A.* (**2020**) A 38, 063210.

(* indicates equal contribution)

## 2.1 Overview

Layered, nickel-rich lithium transition metal oxides have emerged as leading candidates for lithium-ion battery (LIB) cathode materials. High-performance applications for nickel-rich cathodes, such as electric vehicles and grid-level energy storage, demand electrodes that deliver high power without compromising cell lifetimes or impedance. Nanoparticle-based nickel-rich cathodes seemingly present a solution to this challenge due to shorter lithium-ion diffusion lengths compared to micron-scale active material particles. However, since smaller particle sizes imply that surface effects become increasingly important, particle surface chemistry must be well characterized and controlled to achieve robust electrochemical properties. Moreover, residual surface impurities can disrupt commonly used carbon coating schemes, which results in compromised cell performance. X-ray photoelectron spectroscopy was utilized to characterize the surface chemistry of $LiNi_{0.8}Al_{0.15}Co_{0.05}O_2$ (NCA) nanoparticles, ultimately identifying surface impurities that limit LIB performance. With this chemical insight, annealing procedures were developed that minimized these surface impurities, thus improving electrochemical properties and enabling conformal graphene coatings that reduce cell impedance, maximize electrode packing density, and enhance cell lifetime fourfold. Overall, this chapter demonstrates that controlling and stabilizing surface chemistry enables the full potential of nanostructured nickel-rich cathodes to be realized in high-performance LIB technology.

## 2.2 Background

As society transitions towards a renewable energy infrastructure, lithium-ion batteries (LIBs) have emerged as attractive power sources for key applications such as electric vehicles and consumer electronics. By tailoring the electrode materials, LIBs can be rationally designed to

possess electrochemical properties that are customized for specific commercial technologies. For example, electric vehicles require high-power performance for fast acceleration, high-energy performance for long drivable range, and long cell lifetimes to minimize the need for cumbersome battery replacement.[37] Consequently, significant efforts in LIB research have been focused on developing stable, high-capacity, and high-rate electrode materials.

Layered lithium transition metal oxides, especially nickel-rich chemistries such as $LiNi_{0.8}Al_{0.15}Co_{0.05}O_2$ (NCA), have emerged as leading LIB cathode material candidates due to their high operating potentials, high capacities, smooth voltage profiles, and facile synthesis.[37,202,203] However, the adoption of these materials in high-power commercial applications has been hindered by poor rate performance, which can partially be attributed to relatively slow lithium-ion bulk diffusivities. Therefore, to achieve the high electrode power density and rate performance demanded by electric vehicles, a seemingly attractive strategy is to shrink the active material particle size to both decrease lithium-ion bulk diffusion lengths and increase the number of charge transfer sites.[204]

Despite the apparent advantages of nanoparticle-based LIB electrodes, this approach introduces its own unique challenges. In addition to the difficulty in packing nanoparticles and conventional carbon black conductive additives into dense electrodes, the increased surface area associated with smaller particle sizes increases the severity of degradation mechanisms driven by surface impurities, which can be found as byproducts of materials synthesis or are generated as components of interfacial layers that form during electrochemical cycling. Indeed, the surface chemistries of electrochemically active materials are well-known to have significant implications for long-term stability.[108,179,205-209] Residual surface impurities are especially problematic for

nickel-rich layered oxides,[208] suggesting that the active material surface chemistry needs to be carefully characterized and controlled in order to achieve high-performance nanoparticle-based LIB cathodes. For example, lithium carbonates and hydroxides left over from materials synthesis often contaminate nickel-rich oxide surfaces, which leads to high electrode polarization, reduced first-cycle efficiency, and compromised cell lifetimes.[108,207-209] Furthermore, during cycling, electrolyte decomposition products, including solvent and salt components from the liquid electrolyte, deposit on and react with the active material surface, forming a solid-electrolyte interphase (SEI).[61,63,67] Upon repeated cycling, the accumulation of these compounds increases the impedance of the SEI, which is detrimental to electrochemical properties and cyclic stability.

To address the surface impurities formed during materials synthesis, methods such as acid rinsing,[210] aqueous treatments,[107] treatments under vacuum[211] or electrochemical regeneration[207] have been employed to improve the long-term cycle life of LIBs. Although these methods are effective for research-scale studies on nickel-rich cathode microparticles, they are cumbersome for large-scale materials production and are often ineffective for nanoparticle systems that possess high surface areas, and therefore, greater amounts of impurity species. Additionally, to mitigate the formation of surface degradation products *in operando*, thin surface coating layers have been employed to further stabilize nickel-rich cathode particle surfaces by preventing direct electrode-electrolyte contact while remaining electrochemically inert within the operating voltage window of the cell. In particular, coatings such as $Al_2O_3$,[124] $TiO_2$,[124,212] $SiO_2$,[213] and $Co_3O_4$[214] can be deposited via facile, scalable techniques such as atomic layer deposition or wet chemical methods. However, these strategies are inherently limited by the poor electrical conductivity of the deposited oxide layers.[203] In contrast, a thin, conductive carbon coating (e.g., graphene) can limit the

formation of a thick SEI layer and improve charge-discharge kinetics.[179,180] Moreover, since graphene coating schemes minimize the need for additional conductive additives, they are known to increase electrode tap density, which is particularly helpful in overcoming packing density limitations that have traditionally plagued nanoparticle-based electrodes.[188]

Here, we employ surface chemical characterization as a strategy for identifying and minimizing residual hydroxide and carbonate impurities from the synthesis of NCA nanoparticles. Using this surface chemical insight, post-synthetic processing methods are developed to minimize surface impurities and thus improve electrochemical properties. Furthermore, the improved pristineness of the NCA surface facilitates the conformal coating of the NCA nanoparticles with ultrathin conductive and chemically inert graphene. The resulting graphene-coated NCA nanoparticles are then formulated into LIB cathodes, which show superlative electrochemical properties, including low impedance, high rate performance, high volumetric energy and power densities, and long cycling lifetimes. In addition to being directly applicable to emerging nickel-rich LIB cathodes, the methodology presented here can likely be generalized to other LIB electrode materials that are synthesized with hydroxide-based or carbonate-based lithium sources, including oxide-based cathode, anode, and solid-state electrolyte materials.

## 2.3 NCA Surface Impurity Characterization

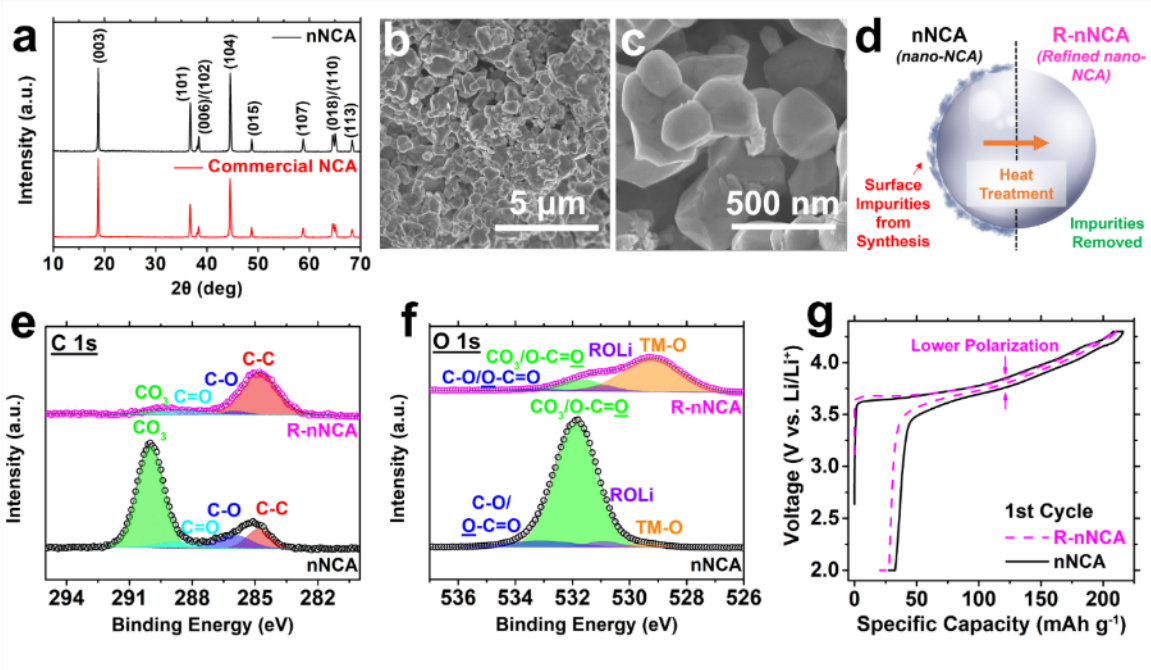


**Figure 2.1.** Characterization and control of nanoscale NCA (nNCA) surface chemistry. (a) XRD patterns of nNCA and commercial NCA powder. (b,c) SEM images of as-synthesized NCA at different magnifications. (d) Schematic showing removal of impurities at the NCA particle surface during heat treatment, yielding nanoscale NCA with a refined surface (R-nNCA). (e) C 1s spectra and (f) O 1s spectra of nNCA and R-nNCA powders obtained via XPS. (g) Voltage-capacity plot showing the activation cycles of nNCA and R-nNCA at 0.1C.

Nanoparticles of NCA (hereafter referred to as nNCA) were synthesized using a solid-state method.[215] To validate the quality of the synthesized nNCA, X-ray diffraction (XRD) was performed to confirm that the solid-state method yielded NCA with a layered crystal structure (**Figure 2.1a**). The XRD pattern of the synthesized nNCA closely matched the reference pattern obtained from commercial NCA powder and showed no evidence of impurity phases. Furthermore, the splitting of the (006)/(102) peaks and the (018)/(110) peaks provided additional confirmation that the nNCA powder possessed a layered structure. Scanning electron microscopy (SEM) was

used to analyze the particle morphology. In contrast to the commercial micron-scale powders, the nNCA powder was comprised of primary NCA nanoparticles less than 500 nm in diameter (**Figure 2.1b-c and Figure 2.2**). Together, the XRD and SEM results verified that the solid-state synthesis scheme successfully yielded crystalline NCA nanoparticles.

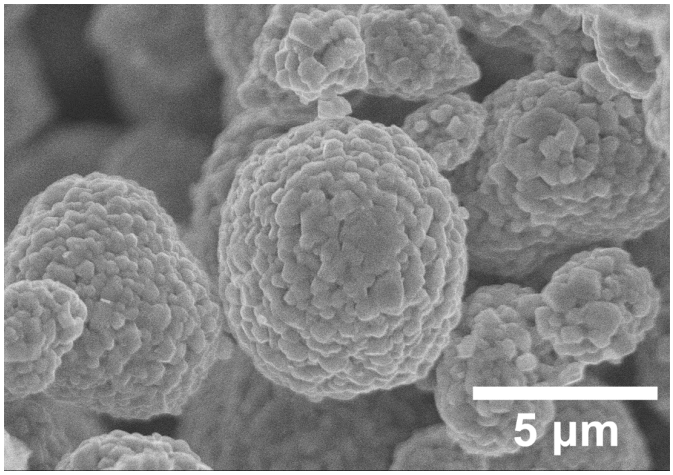


**Figure 2.2**. Scanning electron microscope image of commercial NCA powder (Toda America) showing a large, micron-scale secondary particle morphology.

Although the nNCA powder possessed the desired crystal structure and particle size, a careful analysis of the surface chemistry via X-ray photoelectron spectroscopy (XPS) revealed that impurity compounds were still present on the surface after synthesis. To deconvolute the XPS C 1s spectra, four peaks were assigned: C-C bonds at 284.8 eV, C-O bonds at 286.0 eV, C=O bonds at 288.5 eV, and $CO_3$ bonds at 290.7 eV. Similarly, the XPS O 1s spectra was also deconvoluted with four peaks: lattice transition metal oxygen bonds at 529.2 eV, ROLi species at 530.9 eV, $CO_3$/O-C=O bonds at 531.7 eV, and C-O/O-C=O bonds at 533.1 eV.[67,216] The C-C bonding nature likely originated from adventitious carbon, while the various carbon-oxygen bond signals can be

attributed to the acetate and oxalate precursors used for nNCA synthesis. On the other hand, the carbonate and ROLi signals are evidence of impurity compounds formed during synthesis.[108]

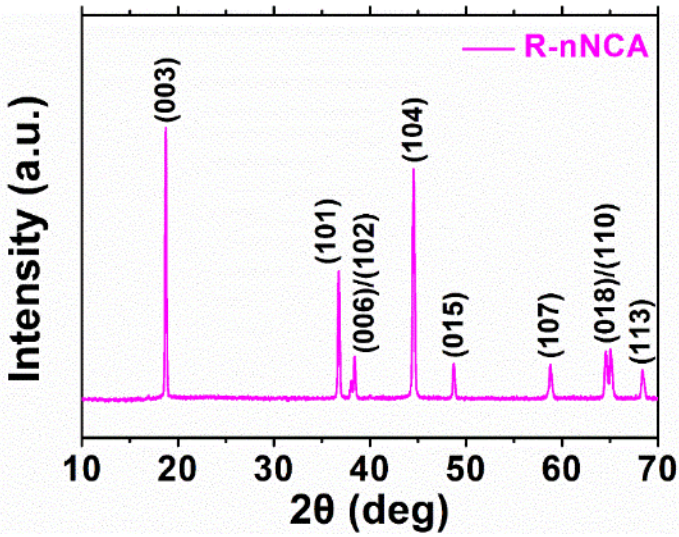


**Figure 2.3.** X-ray diffraction pattern of the refined nNCA particles, showing negligible change in the bulk layered structure.

Since XPS revealed evidence for surface impurity species that can likely be removed through mild heating in an oxidizing environment, post-synthetic annealing treatments were explored to produce a more pristine nNCA surface. In particular, annealing at 250°C under flowing oxygen gas for 1 hour effectively refined the nNCA surface (hereafter referred to as R-nNCA, **Figure 2.1d**). Because heat treatment steps are commonly employed in existing cathode powder synthesis procedures, this refining step can more easily be implemented in practice compared to other reported strategies for removing surface impurities.[107,207,210,211] Importantly, this surface refinement step did not lead to any measurable changes to the bulk structure of the nNCA (**Figure 2.3**). XPS analysis of the original synthesized nNCA suggested that the surface possessed significant carbonate character (**Figure 2.1e-f**), as evidenced by the peaks at 290.7 eV and 532.1

eV, which is consistent with prior reports.[108,207-209] In contrast, after the surface refinement step, the XPS C 1s and O 1s spectra of the R-nNCA powder revealed that the intensity of the carbonate peaks decreased dramatically. Additionally, the XPS O 1s spectrum of the R-nNCA powder showed an increase in the peak intensity assigned to lattice transition metal-oxygen bonds at 529.8 eV. This intensity increase is consistent with the removal of a surface layer that would otherwise attenuate the transition metal oxide intensity originating in the particle bulk.

To probe the effect of surface impurities on the electrochemical properties of nNCA, electrochemical cycling measurements were performed on nNCA and R-nNCA samples. **Figure 2.1g** shows that the R-nNCA electrodes experienced lower electrode polarization during activation than the nNCA electrodes. Since a sample with high electrode polarization reaches its upper cutoff voltage with a higher lithium content than expected, a constant voltage hold allows the electrode to finish delithiating close to its thermodynamically defined lithium content. Therefore, a comparison of the capacity gained during the hold steps at constant voltage serves as a measurement of electrode polarization. In particular, the nNCA electrode gained an additional 7.5 mAh $g^{-1}$ of capacity during the constant voltage hold at 4.3 V, corresponding to 3.5% of its charge capacity. In contrast, the R-nNCA electrode only gained 1.6 mAh $g^{-1}$ during the voltage hold, corresponding to 0.75% of its charge capacity, which confirms that the surface refinement step did indeed lower the electrode polarization. Moreover, the first cycle efficiency (FCE) for the R-nNCA electrode was 90.4%, whereas the FCE for the nNCA electrode was 87.3%, which shows that the R-nNCA electrode possessed better electrochemical reversibility than the nNCA electrode. This analysis is consistent with prior work, which found that the presence of surface $Li_2CO_3$ species impedes local reaction kinetics near the carbonate deposits.[209] Overall, these results highlight the

importance of carefully assessing and controlling the surface chemistry of nickel-rich cathode materials.

## 2.4 Assessing Graphene Coatings on NCA

Surface conductive carbon coating schemes (e.g., conformal graphene coatings) are commonly employed strategies to reduce cell impedance and increase high-rate performance. A solution-phase coating scheme was used to encapsulate the nNCA and R-nNCA particles with a conformal graphene-ethyl cellulose (EC) layer, yielding Gr-nNCA and Gr-R-nNCA, respectively (**Figure 2.4a**). The thermal decomposition of the EC polymer leaves behind a carbonaceous residue on the active material surface that possesses high $sp^2$ character, thus reinforcing the graphitic character of the carbon coating.[171,180] In addition, this residue is highly electrically conductive, thereby improving the electrical contact between adjacent graphene flakes and enhancing electrochemical cycling.[171,176,179,180,188,200,217]

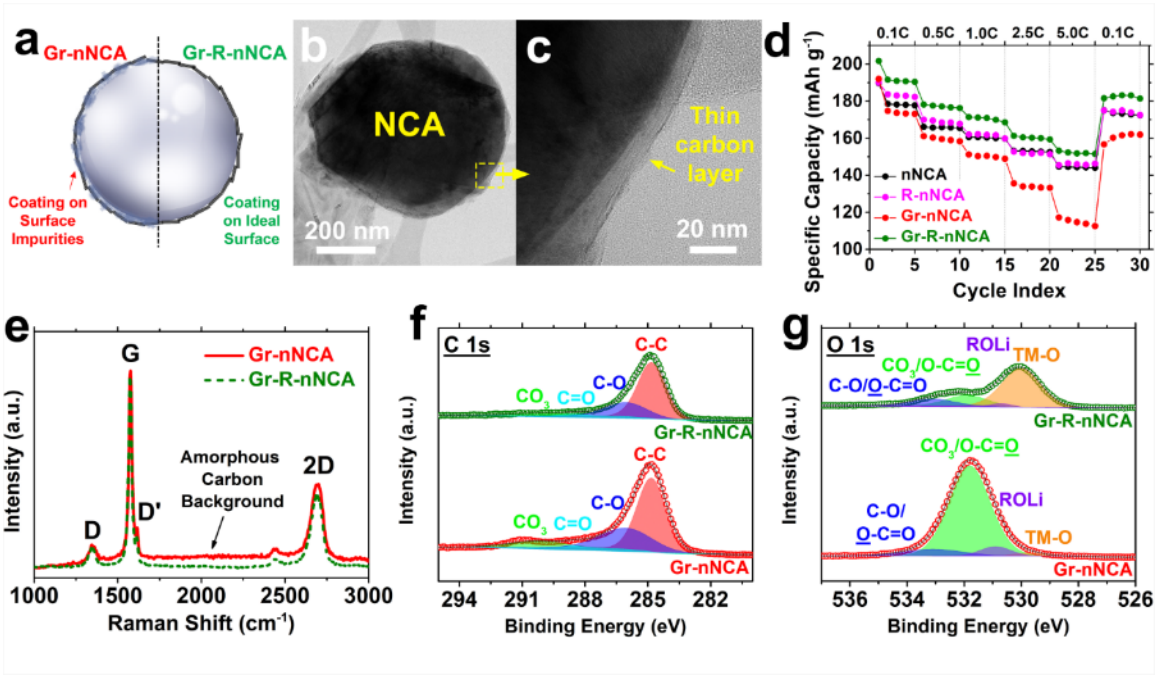


**Figure 2.4.** Results for conformal graphene coatings. (a) Schematic showing that a conformal graphene coating will encapsulate surface impurities on nNCA (Gr-nNCA), in contrast to a conformal graphene coating on a refined, impurity-free surface (Gr-R-nNCA). (b,c) TEM images showing the surface of the Gr-R-nNCA particles. (d) Half-cell rate capability test of nNCA, R-nNCA, Gr-nNCA, and Gr-R-nNCA electrodes. (e) Raman spectra for Gr-nNCA and Gr-R-nNCA. (f) C 1s spectra and (g) O 1s spectra of Gr-nNCA and Gr-R-nNCA obtained via XPS.

Following the coating process, transmission electron microscopy (TEM) confirmed the presence of a thin carbon layer on the surface of the NCA particles (**Figure 2.4b-c**). Since this conformal graphene coating scheme yields a highly percolating, electrically conductive network between the NCA particles, the graphene-coated nNCA (Gr-nNCA) and graphene-coated R-nNCA (Gr-R-nNCA) electrodes were expected to outperform the respective nNCA and R-nNCA control electrodes fabricated with traditional carbon black additives. However, while the Gr-R-nNCA electrode possessed higher initial capacity and better rate capability than the R-nNCA control sample, the Gr-nNCA electrode surprisingly performed considerably worse than the nNCA control

electrode (**Figure 2.4d**). This result suggests that an active material surface that is rich in impurity species, such as carbonates, undermines the effectiveness of carbon coating schemes.

Raman spectroscopy and XPS analysis of the pristine electrode surfaces after thermal decomposition of the EC polymer further corroborated that the quality of the electrode coating depends on the cleanliness of the active material surface. The Raman spectra for the Gr-nNCA and Gr-R-nNCA electrodes revealed a large G/D ratio for both samples, which indicated that both electrodes possessed graphene-like character (**Figure 2.4e**). However, the Gr-nNCA electrode showed greater evidence of an amorphous carbon background than the Gr-R-nNCA electrode, implying that the presence of the carbonate impurities hindered the formation of the $sp^2$-rich carbonaceous residue during the EC thermal decomposition process. Since EC contains many carbon-based and oxygen-based functional groups, evidence of this bonding character in the graphene-coated electrodes would provide further evidence that surface impurities have adverse impact on EC volatilization.[180] Indeed, the higher relative intensity of the C-O peak in the XPS C 1s spectrum of the Gr-nNCA electrode compared to the Gr-R-nNCA electrode confirms the difference in amorphous carbon signals between the two electrodes (**Figure 2.4f**). Furthermore, the XPS C 1s and O 1s spectra (**Figure 2.4f-g**) of the Gr-nNCA electrode showed a much higher carbonate signal than the Gr-R-nNCA electrode, suggesting that that these species persisted through the second heat treatment step where the EC polymer is supposed to be decomposed. Since the carbonate species are detrimental to electrochemical cycling, these spectroscopic data are consistent with the electrochemical results that showed the poorest performance for the Gr-nNCA electrode.

## 2.5 Comparative Electrochemical Characterization

To further assess the combined advantages of surface refinement and conformal graphene coating, additional electrochemical characterization was undertaken. For example, **Figure 2.5a** shows that surface refinement coupled with the conformal graphene coating significantly improved the cycle life of the NCA material. After 200 cycles at a 1C cycling rate, the Gr-R-nNCA electrode possessed a capacity of 91.8 mAh $g^{-1}$, corresponding to 60.5% capacity retention. In contrast, the nNCA control electrode degraded quickly within the first 100 cycles, ultimately resulting in a capacity of 21.2 mAh $g^{-1}$ after 200 cycles, corresponding to 15.9% capacity retention.

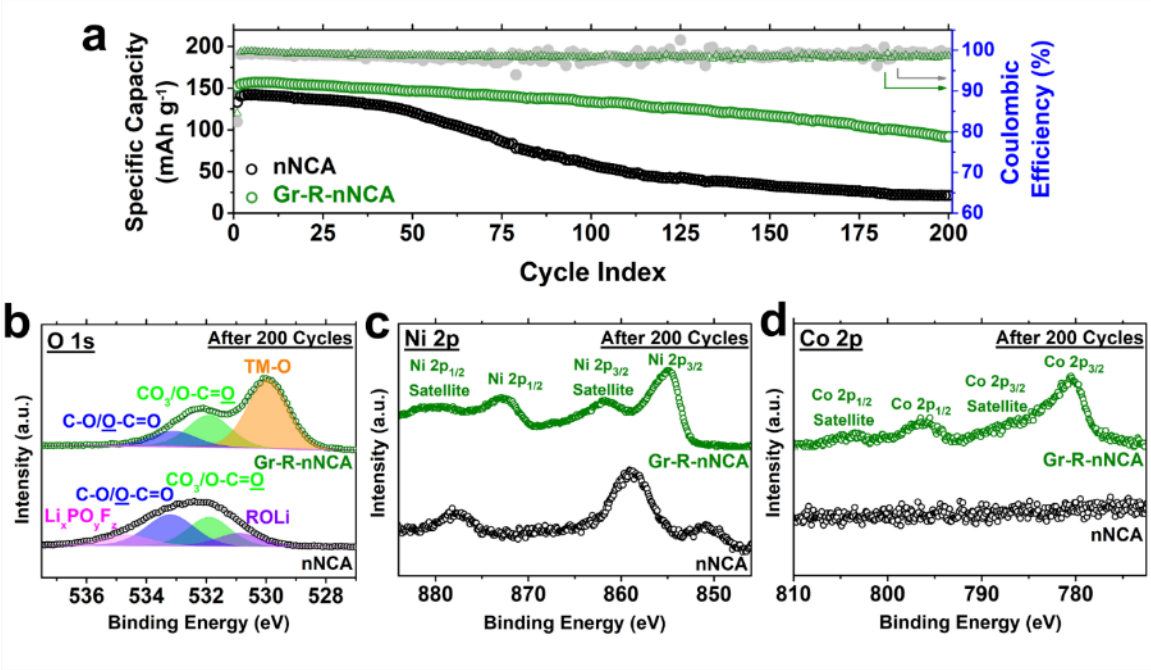


**Figure 2.5.** Graphene-coated nanoscale NCA exhibits improved cycle life compared to the control. (a) Half-cell cycle life test at 1C. (b) O 1s, (c) Ni 2p, and (d) Co 2p postmortem XPS spectra show significant evidence of degradation for the uncoated nNCA electrode.

Over 200 cycles, the nNCA electrode possessed an average coulombic efficiency of 98.56%, which was marginally higher than the 98.52% average efficiency for the Gr-R-nNCA

electrode. Although these average values were similar in magnitude, the coulombic efficiency for the Gr-R-nNCA electrode was significantly more stable than that of the nNCA electrode (**Figure 2.5a**). The large fluctuations in the nNCA coulombic efficiency values suggested variations in lithium consumption during each cycle, which could be a byproduct of unstable interfacial layers on the nNCA particle surface. If the SEI is fragile and breaks down with each cycle, additional lithium must be consumed to reform the interphase. In contrast, the coulombic efficiency evolution for the Gr-R-nNCA electrode remains stable throughout 200 cycles, which is consistent with the superior cycle life observed for the Gr-R-nNCA electrode.

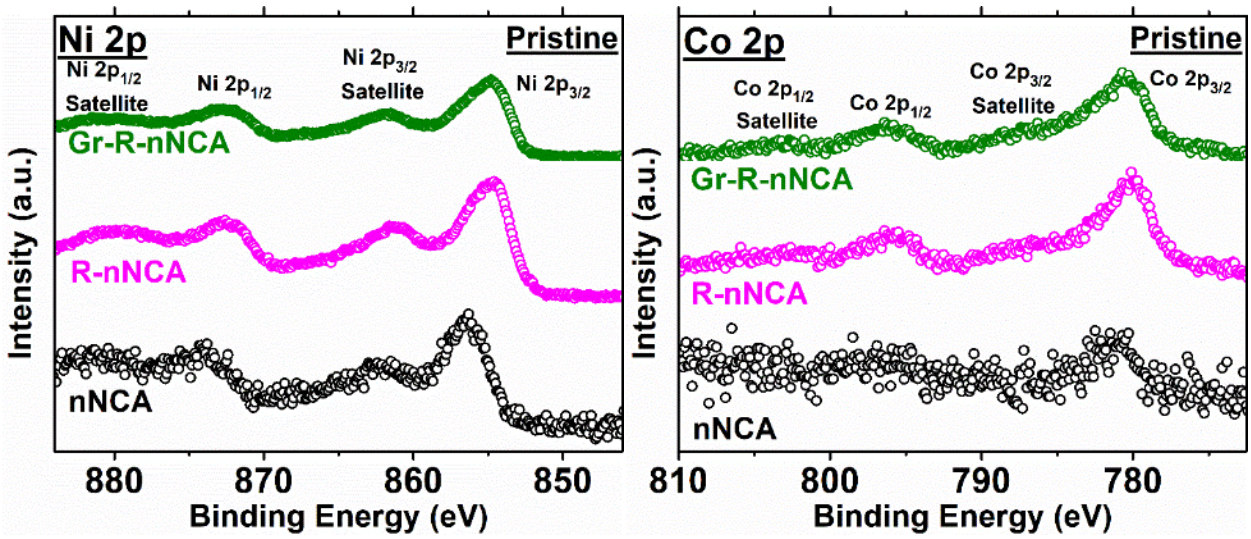


**Figure 2.6.** Ni 2p (left) and Co 2p (right) X-ray photoelectron spectra showing minimal changes in the transition metal oxidation states after the refining step and the graphene coating process.

To elucidate the origins of the observed cycle life improvement, postmortem XPS analysis of the cathode surfaces was performed. The XPS O 1s spectra for the Gr-R-nNCA and nNCA samples were fit with the same four component spectra as the pristine electrodes, as well as an

additional peak at 534.7 eV that was assigned to $Li_xPO_yF_z$ species formed *in operando* due to electrolyte decomposition (**Figure 2.5b**).[67,69] For the nNCA electrode after cycling, the increase in the C-O and C=O spectral peaks, the clear presence of $Li_xPO_yF_z$ species, the changes in the Ni 2p spectrum compared to the pristine electrode (**Figure 2.5c and Figure 2.6**), and the absence of any discernable Co 2p signal (**Figure 2.5d and Figure 2.6**) together suggest that the nNCA surface was coated with a layer during cycling that is rich in organic and fluorophosphate components. The formation of this layer is well known and has been attributed to a ring-opening reaction of the ethylene carbonate solvent, which is assisted by transition metal ions on the cathode surface.[67] Other reported degradation reactions, such as transition metal etching by trace amounts of HF in the electrolyte,[80] may also contribute to the surface degradation in the nNCA electrode.

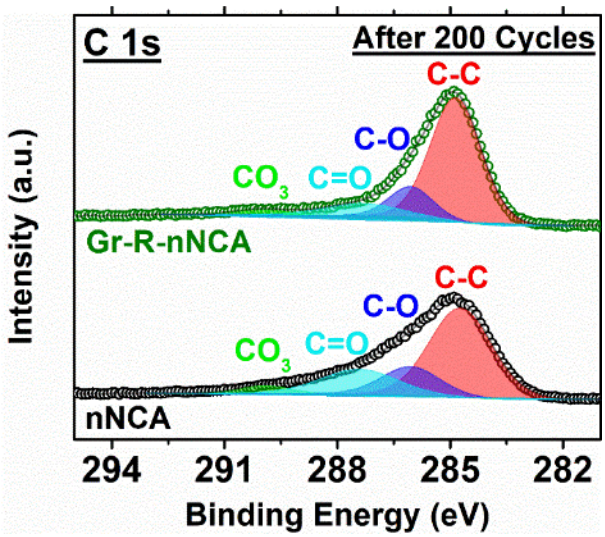


**Figure 2.7.** Postmortem XPS C 1s spectra for the Gr-R-nNCA electrode and the nNCA electrode.

In contrast, fewer changes were observed for the Gr-R-nNCA electrode after cycling. Although some slight increases in the carbon-oxygen bond intensities are observed in the XPS C

1s and O 1s spectra, little evidence exists for fluorophosphate degradation products (**Figure 2.5b and Figure 2.7**). Furthermore, the transition metal oxide signal and the minimal changes in the Ni 2p and Co 2p spectral features for the pristine and postmortem electrodes (**Figure 2.5c-d and Figure 2.6**) suggest that the Gr-R-nNCA surface did not significantly degrade during cycling. Postmortem Raman spectroscopy of the Gr-R-nNCA electrode also corroborated this conclusion (**Figure 2.8**). If electrochemical cycling had altered the integrity of the graphene coating, then the increased defect density in the graphene coating would have resulted in a decrease of the G/D ratio. Even after 200 charge-discharge cycles, the Raman spectrum for the Gr-R-nNCA electrode continues to exhibit a large G/D ratio, which confirms that the electrode maintained its graphene-like character throughout the cycle life test. Small changes in the amorphous carbon background are likely due to organic electrolyte degradation products, which are also present in the XPS C 1s spectrum. Similar to other electrode coating schemes,[124,212-214] the conformal graphene coating in the Gr-R-nNCA electrode apparently acts as a barrier layer that minimizes the interaction between the transition metals in the active material and the electrolyte, effectively mitigating the severity and extent of electrolyte decomposition. Additionally, the graphene coating may act as a scavenger for HF, which would otherwise etch the transition metals near the surface and degrade interfacial charge transport.

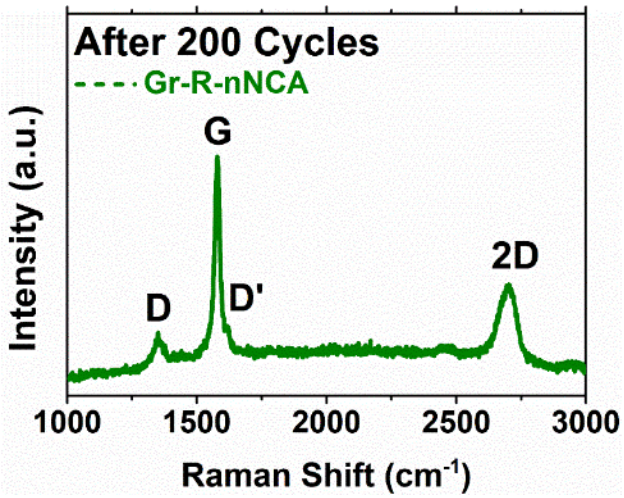


**Figure 2.8.** Postmortem Raman spectrum of the Gr-R-nNCA electrode showing that the graphene coating is preserved after 200 charge-discharge cycles.

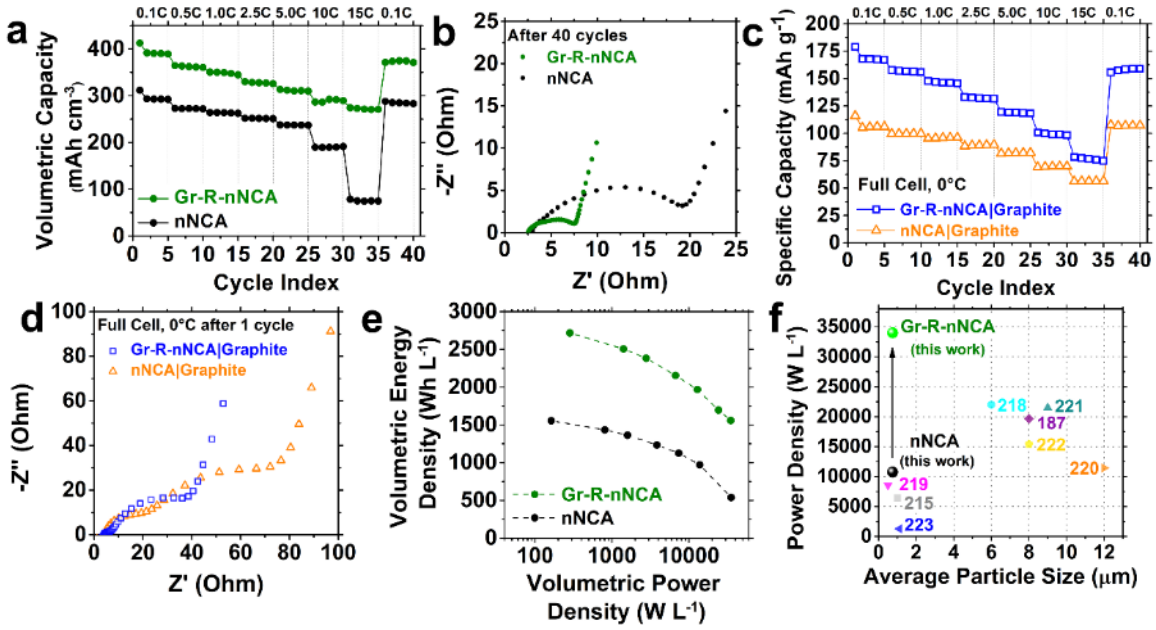


**Figure 2.9.** Electrochemical testing shows that graphene-coated Gr-R-nNCA electrodes enable comprehensive performance improvements compared to the nNCA control. (a) Half-cell volumetric rate capability test. (b) Nyquist plot of the electrodes at room temperature. (c) Full-cell rate capability test at 0°C. (d) Nyquist plot of the full cells at 0°C. (e) Ragone plot showing the improved power and energy density of the Gr-R-nNCA electrode. (f) Plot showing the power density competitive advantage of Gr-R-nNCA electrodes compared to literature precedent. The numbers indicate the references for previously reported results.

The combination of surface refinement and conformal graphene coating enabled substantial enhancements in numerous other electrochemical performance metrics. Prior work has shown that graphene-coated microparticle electrodes experienced large improvements in volumetric capacity due to the replacement of low-density carbon black with a percolating graphene network.[188] Here, the initial volumetric capacities again reflected this phenomenon for nickel-rich nanoparticles. Specifically, the Gr-R-nNCA electrode reached an initial volumetric discharge capacity of 412.6 mAh $cm^{-3}$, while the nNCA electrode only reached an initial volumetric discharge capacity of 311.7 mAh $cm^{-3}$ (**Figure 2.9a**). The high electrical conductivity of the graphene network also promotes fast electronic transport, while the nanoparticle NCA morphology provides short Li-ion diffusion lengths into the bulk and increases the number of charge transfer reaction sites. Together, these factors significantly improved the high-rate performance of the Gr-R-nNCA electrode compared to the nNCA control sample. When discharged at 15C, the Gr-R-nNCA electrode possessed a volumetric capacity of 273 mAh $cm^{-3}$, while the volumetric capacity of the nNCA control electrode dramatically dropped to 78.5 mAh $cm^{-3}$. Electrochemical impedance spectroscopy was also performed on the electrodes after cycling at different current rates to confirm the enhancement in charge transport behavior. The Nyquist plots showed that the Gr-R-nNCA electrode possessed substantially lower cell impedance (~5 Ω) than the nNCA electrode (~15 Ω), thereby corroborating the rate capability results (**Figure 2.9b**).

To test the limits of the Gr-R-nNCA electrode, full cells were assembled and subjected to galvanostatic cycling at 0°C. Under these conditions, the amount of lithium in the full cell is restricted to the capacity possessed by the cathode, implying that parasitic side reactions that irreversibly consume lithium become even more deleterious. Furthermore, ionic charge transport

is more sluggish at low temperatures, which reduces discharge capacities, particularly at high applied current rates. Despite these harsh testing conditions, the Gr-R-nNCA|Graphite full cell showed impressive electrochemical performance. Specifically, at all current rates, the Gr-R-nNCA|Graphite full cell possessed higher capacities than the nNCA|Graphite full cell (**Figure 2.9c**). The Nyquist plot further showed that the lower impedance observed in the half-cell geometry tested at room temperature was again evident for the full cell at 0°C (**Figure 2.9d**). The smaller high-frequency arcs for the Gr-R-nNCA|Graphite sample suggest that both the surface film and charge transfer impedances were lower than the nNCA control sample, indicating that interfacial charge transport was significantly improved by the graphene coating.

The high volumetric capacity and superlative rate capability enabled by the surface refinement and subsequent conformal graphene coating correspondingly led to substantial improvements in the energy and power densities. These enhancements are evident on a Ragone plot (**Figure 2.9e**), which shows that the Gr-R-nNCA sample clearly outperformed the nNCA control sample. Additionally, the exceptionally high volumetric power density for the Gr-R-NCA sample compares favorably to literature precedent for NCA-based cathodes (**Figure 2.9f**).[187,215,218-223] Overall, these results establish that Gr-R-nNCA cathodes enable high-performance LIBs with long cell lifetimes, high rate capability, and wide operating temperature windows.

## 2.6 Experimental Methods

### *2.6.1 NCA Synthesis*

NCA nanoparticles (nNCA) were synthesized via a solid-state method. Initially, stoichiometric amounts of nickel (II) acetate tetrahydrate, cobalt (II) acetate tetrahydrate, and

aluminum (II) acetate tetrahydrate (Millipore Sigma) were dissolved in deionized water to form a 0.1 M precursor solution. Oxalic acid dihydrate (Millipore Sigma) was simultaneously dissolved in deionized water to form a 0.2 M solution. To precipitate the transition metal precursors, the oxalic acid solution was added dropwise to the precursor solution while stirring at 300 RPM to ensure homogeneous mixing. After further stirring for 3 hours, the water was evaporated using a rotary evaporator (Buchi Rotavapor R-300 System), yielding the precipitate powder. This powder was then heated in a tube furnace (Thermo Scientific Lindberg Blue M) at 450°C for 8 hours under flowing oxygen. Using a mortar and pestle, the calcined powder was then mixed with lithium hydroxide monohydrate (Millipore Sigma) at a 3% mol excess until a homogeneous mixture was formed. The combined powder was calcined at 550°C for 8 hours and then 750°C for 24 hours under flowing oxygen. The refined nanoparticle NCA powder (hereafter referred to as R-nNCA) was obtained by a final heat treatment step at 250°C under flowing oxygen for 1 hour. All furnace ramp rates used were 5°C/min.

### *2.6.2 Graphene Exfoliation*

Graphene-ethyl cellulose (EC) powder was produced by shear mixing 150 mesh flake graphite (Millipore Sigma), ethyl cellulose (4 cP, Millipore Sigma), and ethanol (200-proof, Decon Labs) for 2 hours at 10,230 RPM using a Silverson L5M-A high shear mixer. The dispersion was then centrifuged for 2 hours at 7,500 RPM in a Beckman Coulter J26 XPI centrifuge to sediment out large, unexfoliated graphite flakes. The supernatant dispersion was flocculated with a 1 M sodium chloride solution at a 9:16 weight ratio (NaCl solution:graphene dispersion), and then centrifuged again at 7,500 RPM for 6 minutes to crash out the graphene-EC powder. These solids

were washed with deionized water, vacuum filtered, and dried under an infrared lamp. The final graphene fraction in the graphene-EC powder was 33% as determined by thermogravimetric analysis in air.

### *2.6.3 Electrode Fabrication*

The nNCA electrodes were fabricated by mixing nNCA powder, carbon black (Alfa Aesar), and polyvinylidene fluoride (MTI Corporation) at a 90:5:5 ratio in a mortar and pestle. N-methyl pyrrolidone (NMP, Millipore Sigma) was added to form a viscous and homogeneous slurry. The slurry was cast on aluminum foil using a doctor blade, initially dried in a convection oven at 120°C for 30 minutes, and subsequently dried in a vacuum oven at 80°C overnight. This process yielded electrodes with an active material loading of 3 mg/cm$^2$. Electrode discs with 1 cm diameter were cut using a disc cutter and then pressed using a 6 MPa applied pressure prior to coin cell assembly. The R-nNCA electrodes were fabricated using the same method, with the R-nNCA powder serving as the active material. The graphite electrodes for the full cell testing were fabricated using identical methods but used natural graphite powder (Alfa Aesar) as the active material. The graphite slurry was cast on copper foil and dried at 80°C in the convection oven prior to overnight drying for the full cell experiments.

To form the graphene-coated electrodes, graphene-EC powder and multiwalled carbon nanotubes (MWCNT, Sigma) were dispersed in ethanol using a horn sonicator (Fisher Scientific Sonic Dismembrator Model 500) equipped with a 1/8” tip at 40 W for 1 hour. Solvent exchange was performed by adding NMP to this dispersion and evaporating the ethanol using a hot plate set at 80°C, yielding a dispersion of graphene, ethyl cellulose, MWCNT, and NMP. R-nNCA powder

was added to this dispersion to form a viscous slurry, which was mixed homogeneously using a mortar and pestle. The final ratio of solids in this slurry was 95% active material, 4.5% graphene, and 0.5% MWCNT. This ratio was chosen to keep the conductive carbon fraction consistent with the control electrodes made with carbon black. After mixing, the slurry was cast onto aluminum foil and dried in a convection oven set at 120°C for 30 minutes, and then dried again in a vacuum oven at 80°C overnight, yielding Gr-R-nNCA electrodes. Electrode discs with a diameter of 1 cm and an active material loading of 3 mg/cm$^2$ were cut and heated to 250°C for 1 hour to decompose the EC. Following thermal decomposition, the electrodes were compressed with a 6 MPa applied pressure prior to coin cell assembly. The Gr-nNCA electrodes were produced using the same method but instead using nNCA powder as the active material.

Electrode thicknesses were measured using a Mitutoyo micrometer. 2032-type coin cells were assembled in an argon glovebox (OMNI-LAB, Vacuum Atmospheres Company) with less than 0.2 ppm of oxygen. For room-temperature testing, Celgard 2325 was used as the separator, and 1 M $LiPF_6$ in 1:1 v/v ethylene carbonate/ethyl methyl carbonate (Millipore Sigma) was used as the electrolyte. For low-temperature testing, a polyethylene separator (single-layer PE, Asahi Kasei) and 1 M $LiPF_6$ in 1:1 v/v ethylene carbonate/dimethyl carbonate (Millipore Sigma) electrolyte were used. Lithium metal (Alfa Aesar) was used as the counter electrode for half-cell testing. For full-cell testing, graphite electrodes were used as the counter electrode.

### *2.6.4 Electrochemical Testing*

Room-temperature galvanostatic cycling was performed using an Arbin LBT-20084 64-channel battery cycler. For half-cell testing, the NCA electrodes were activated with a constant-

current constant-voltage (CCCV) protocol, where the electrode was cycled once at 0.1C with constant-voltage holds at the upper and lower cutoff voltages until the current reached C/20. Here, 1C was set at 200 mAh $g_{NCA}^{-1}$. For full-cell testing, the graphite anode was activated with 3 cycles between 0.01 V and 2 V vs. $Li/Li^+$ using the same CCCV protocol to form a stable solid-electrolyte interphase on the anode. The graphite electrode was then harvested and assembled in a full cell against an activated NCA cathode. The negative to positive electrode areal capacity ratio (N:P ratio) was set at 1.1:1. Rate capability tests were performed using a charging current rate of 0.1C, and then discharging at the desired current rate. Cycle life tests were performed at 1C charge and discharge. Low-temperature testing was performed by cycling the coin cells in an environmental chamber (ESPEC BTX-475) set at 0°C. Electrochemical impedance spectroscopy tests were conducted in a fully charged state using a Biologic VSP potentiostat between 1 MHz and 100 mHz. Power density was calculated based on the total volume of the electrode and the measured energy at the highest C-rate.

### *2.6.5 Materials Characterization*

X-ray diffraction (XRD) was conducted on the synthesized powders using a Scintag XDS2000 with Cu Kα (λ=1.5046 Å) radiation from 10° to 70°. The same analysis was performed on commercially available NCA powder (BASF Toda America). Scanning electron microscopy (SEM) was performed using a Hitachi SU8030 Field Emission SEM at a 5 kV accelerating voltage. SEM samples were prepared by depositing the NCA powder directly onto carbon tape mounted on an SEM stub. Transmission electron microscopy (TEM) samples were prepared by a direct application of the Gr-R-nNCA powder on a lacey carbon supported TEM grid. The TEM imaging

was performed using a JEOL ARM 300CF. Raman spectroscopy was conducted using a Horiba Scientific XploRA PLUS Raman microscope with a laser excitation of 532 nm and a laser grating with 1800 grooves/mm. The signal was collected by a 50x LWD Olympus objective (NA = 0.5). X-ray photoelectron spectroscopy (XPS) was performed using a Thermo Scientific ESCALAB 250Xi with Al Kα radiation (~1486.6 eV). Spectra were acquired after the analysis chamber reached a base pressure of $5 \times 10^{-8}$ Torr. The samples were mounted using copper tape and were charge compensated with a flood gun during acquisition. All spectra were charge corrected to adventitious carbon at 284.8 eV. Postmortem analysis of the battery electrodes was conducted by disassembling the coin cells in an argon glovebox. The harvested electrodes were rinsed with anhydrous dimethyl carbonate (Millipore Sigma) and dried at 120°C on a hot plate in the glovebox. Postmortem XPS and Raman spectra were acquired using the aforementioned methods.

## 2.7 Summary

In summary, this chapter explored the surface chemistry of nanoscale nickel-rich cathode particles to identify and remove residual contaminants from solid-state synthesis. The resulting chemically pristine nanoparticles were more amenable to a conformal graphene coating, ultimately resulting in a nanoparticle-based electrode with exceptional electrochemical properties. Specifically, the surface refinement and conformal graphene coating enabled superlative performance in LIBs including high rate capability, low impedance, high volumetric energy and power densities, and long cycle life. In addition, these nanostructured cathode materials widened the LIB operating range, particularly at low temperatures. While demonstrated here for nickel-rich LIB cathodes, this methodology can likely be generalized to other energy storage electrodes, such as sodium-ion or magnesium-ion batteries, that incorporate nanostructured materials possessing

high surface area. Therefore, this work establishes a clear path forward for the realization of high-performance, nanoparticle-based energy storage devices.

# CHAPTER 3:

# ELUCIDATING AND MITIGATING HIGH-VOLTAGE INTERFACIAL CHEMOMECHANICAL DEGRADATION OF NICKEL-RICH LITHIUM-ION BATTERY CATHODES VIA CONFORMAL GRAPHENE COATING

This chapter is adapted from:

**Luu, N.S.**, Lim, J.-M., Torres, C. G., Park, K. Y., Moazzen, E., He, K. Meza, P. L., Li, W., Downing, J. R., Dravid, V. P., Barnett, S., Bedzyk, M. J., Hersam, M. C. Elucidating and Mitigating High-Voltage Chemomechanical Degradation of Nickel-Rich Lithium-Ion Battery Cathodes via Conformal Graphene Coating. *ACS Appl. Energy Mater.* (**2021**), 4, 10, 11069–11079.

## 3.1 Overview

Lithium nickel manganese cobalt oxides (NMCs) are promising cathode materials for high-performance lithium-ion batteries (LIBs). Although these materials are commonly cycled within mild voltage windows (up to 4.3 V vs. $Li/Li^+$), operation at high voltages (> 4.7 V vs. $Li/Li^+$) to access additional capacity is generally avoided due to severe interfacial and chemomechanical degradation. At these high potentials, NMC degradation is caused by exacerbated electrolyte decomposition reactions and non-uniform buildup of chemomechanical strains that result in particle fracture. This chapter describes a conformal graphene coating applied to the surface of NMC primary particles, which significantly enhances the high-voltage cycle life and coulombic efficiency during electrochemical cycling. Postmortem X-ray diffraction, X-ray photoelectron spectroscopy, and electron microscopy indicate that the graphene coating mitigates electrolyte decomposition reactions and reduces particle fracture and electrochemical creep. These results suggest a relationship between the spatial uniformity of lithium flux and particle-level mechanical degradation. Moreover, this work demonstrates that a conformal graphene coating is well-suited to address these issues. Overall, these results delineate a pathway for rationally mitigating high-voltage chemomechanical degradation of nickel-rich cathodes that can be applied to existing and emerging classes of battery materials.

## 3.2 Background

Lithium-ion batteries (LIBs) have emerged as the preeminent energy storage devices for renewable energy technologies. High-performance applications, including electric vehicles, often utilize cathode chemistries based on nickel-rich layered lithium nickel manganese cobalt oxides such as NMC532 ($LiNi_{0.5}Mn_{0.3}Co_{0.2}O_2$), NMC622 ($LiNi_{0.6}Mn_{0.2}Co_{0.2}O_2$), and NMC811

($LiNi_{0.8}Mn_{0.1}Co_{0.1}O_2$).[37] Although these nickel-rich cathode materials possess intrinsically high energy densities, they suffer from severe cyclic stability issues due to chemical, structural, and mechanical deterioration of the active material during electrochemical cycling. For these reasons, the practical operating window for layered cathodes has been empirically limited to an upper cutoff voltage of 4.3 V vs. $Li/Li^+$.[37] Nonetheless, since additional capacity and energy density can be obtained by operating LIBs over wider electrochemical voltage windows, the ability to safely and reliably utilize nickel-rich cathode materials at higher states of charge (SOCs) is greatly desired.

LIB cathode material degradation is severely exacerbated at high operating potentials (> 4.7 V vs. $Li/Li^+$). For example, electrolyte decomposition reactions such as ethylene carbonate dehydrogenation or $PF_6^-$ decomposition become increasingly favorable at higher voltages due to the increased reactivity of lattice oxygen.[63,67] The resulting organic and lithium fluorophosphate reaction products form a solid-electrolyte interphase (SEI), which irreversibly consumes the lithium inventory and impedes subsequent ionic transport. These compounds are known to react with other electrolyte salt components to form HF, which etches the active material and further accelerates capacity fade.[68] Structurally, charging layered oxides to high SOCs also induces severe anisotropic volumetric changes in the NMC unit cell as the *c* lattice parameter collapses after 50% of the lithium is extracted.[35,224] Moreover, delithiation results in compositional heterogeneity throughout the active material particle, which is known to be a consequence of non-uniform distributions of interfacial chemical products, surface phases, and reaction sites.[138,225,226] The resulting spatial gradients in lithium concentration induce internal strains, which can be relieved through particle cracking and intergranular fracture.[57,227,228] Beyond forming additional interfacial

degradation sites, these cracks can also contribute to capacity fade as active material fragments become electrically isolated and electrochemically inactive.

To improve the cycle life of nickel-rich cathode materials, coating layers such as $Al_2O_3$,[124,229,230] MgO,[231] $ZrO_2$,[124,232] $TiO_2$,[233] $LiBO_2$,[234] and $Li_2TiO_3$[235] have been explored as interfacial buffers that scavenge HF from the electrolyte and shield the cathode surface from electrolyte decomposition reactions. However, these layers often possess low ionic and/or electronic conductivity,[236] which is detrimental to high-rate cycling. Moreover, since these coating layers are often directly bonded to the active material surface, changes in the cathode unit cell volume at high SOCs can induce mechanical delamination, irreversibly compromising the coating for future cycles.[237] Amorphous carbon coatings possessing weak carbon-carbon bonds are similarly prone to mechanical failure.[182] Therefore, a thin, conductive, conformal coating that acts as an interfacial buffer layer while accommodating mechanical changes is likely to be more effective at enabling reliable high-voltage operation of nickel-rich cathodes.

This chapter demonstrates a strategy to enhance the high-voltage cycle life and coulombic efficiency of NMC cathodes via a conformal, conductive graphene coating. Although graphene coatings have been widely employed to improve the cycle life of Ni-rich cathode materials, most reports explored the effect of graphene coatings under mild operating voltage windows that avoided severe degradation mechanisms.[187,188,190] In this work, we used a high upper cutoff voltage not only to accelerate interfacial degradation, including electrolyte decomposition reactions, but also to drive chemomechanical degradation at high SOCs, such as particle fracture or electrochemical creep. Additionally, by utilizing submicron primary particles in this study, we circumvented issues of strain buildup within large secondary particle structures and ensured that

exposed NMC surfaces can be uniformly coated with graphene. This strategy enabled a direct investigation into the role of optimized electronic conduction pathways. Additionally, the choice to use relatively small active material particles also enabled a facile morphological assessment of chemomechanical degradation since fracture and electrochemical creep events appeared on the same length scale as the particles themselves. Postmortem analysis using X-ray diffraction (XRD), X-ray photoelectron spectroscopy (XPS), and electron microscopy revealed that the graphene coating reduces the accumulation of interfacial electrolyte decomposition products and the severity of particle-level chemomechanical degradation. We proposed that the graphene coating promoted spatially uniform charge transfer reactions across the electrode surface, which delocalized cycling-induced stress and reduced the propensity for particle fracture. Moreover, the graphene coating was mechanically compliant towards unit cell volume changes at high SOCs and maintained electrical contact throughout cycling. Graphene-coated NMC cathodes therefore achieved substantially improved cycle life and coulombic efficiencies under high-voltage operation.

### 3.3 Materials Characterization

NMC532 particles were synthesized using a solid-state co-precipitation method. Synchrotron radiation powder X-ray diffraction (SR-PXRD) verified the synthesis of NMC532 (*R-3m*) and showed no significant evidence of impurity phases (**Figure 3.1**). Additional features in the SR-PXRD pattern, including the (006)/(102) peak splitting, confirmed the synthesis of a layered structure. Rietveld refinement indicated that the lattice parameters of the as-synthesized NMC agreed well with prior reports (**Table 3.1**).[35] Inductively coupled plasma mass spectrometry (ICP-MS) was used to quantify the NMC transition metal ratio, which confirmed the target composition of 50% nickel, 30% manganese, and 20% cobalt (**Table 3.2**). Scanning electron

microscopy (SEM) showed that the synthesized powder was composed of primary particles with sizes ranging from hundreds of nanometers to 1 micron in diameter (**Figure 3.2**), with no evidence of well-defined secondary particle agglomerates.

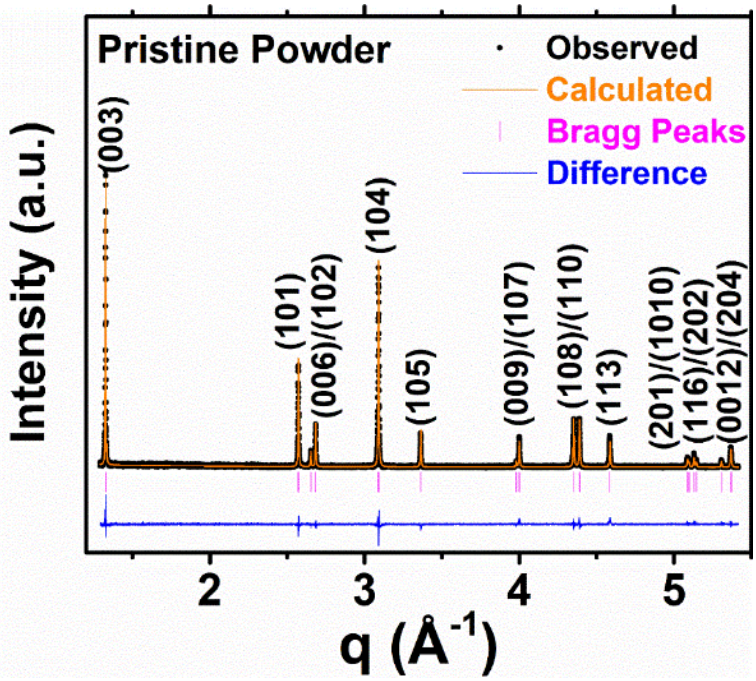


**Figure 3.1**. Synchrotron radiation powder X-ray diffraction pattern of the as-synthesized NMC. The magnitude of the scattering vector is $q = 4\pi\sin\theta/\lambda$, where $2\theta$ is the scattering angle and $\lambda$ is the X-ray wavelength.

**Table 3.1.** Rietveld refinement results for the pristine NMC powder.

| Sample | Lattice parameters (Å) | | Li/Ni mixing | Domain size (μm) | Microstrain | RF, $RF^2$ (%) |
|---|---|---|---|---|---|---|
| | *a* | *C* | | | | |
| Pristine NMC powder | 2.8659(3) | 14.224(1) | 3.56% | 0.7082 | 2027.5 | 8.89, 15.10 |

**Table 3.2.** Transition metal ratio of the synthesized NMC powder determined via inductively coupled plasma mass spectrometry, confirming the target composition of 50% nickel, 30% manganese, and 20% cobalt.

| | Ni | Mn | Co |
|---|---|---|---|
| Average ICP Sample (ppb) | 23109 | 13801 | 9898 |
| Percentages | 49.37% | 29.48% | 21.15% |
| Target for NMC532 | 50% | 30% | 20% |

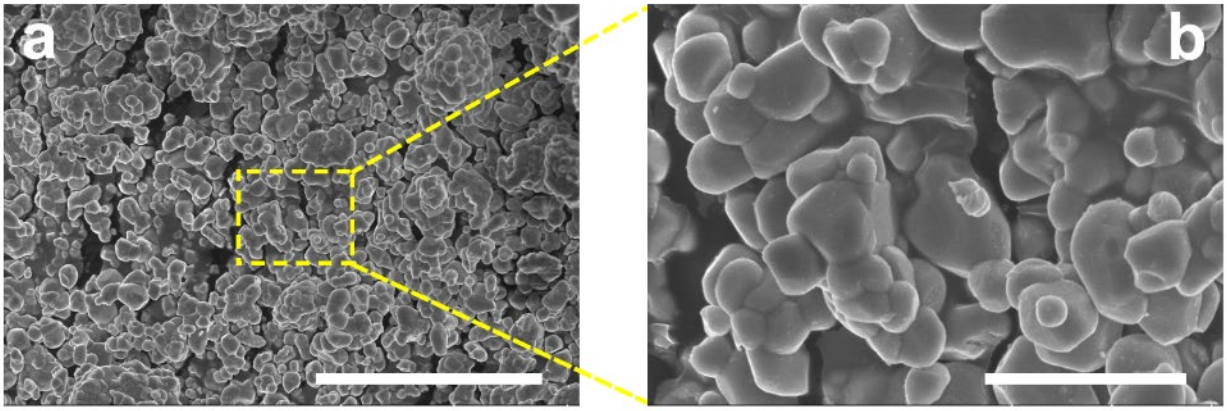


**Figure 3.2.** Scanning electron microscope images showing the morphology of the as-synthesized NMC powder. Higher magnification is shown in (b). Scale bars are (a) 10 µm and (b) 2 µm.

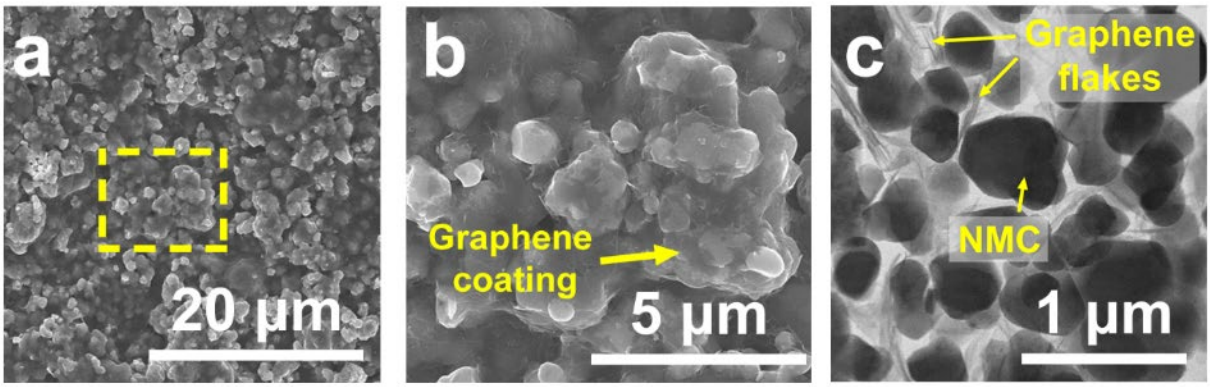


**Figure 3.3.** Morphology and electrochemical performance of graphene-coated NMC. (a) Top-down scanning electron microscopy images of the NMC-GrEC electrode. (b) Higher magnification scanning electron microscopy image of the region outlined in yellow. (c) Bright-field transmission electron microscopy image of the NMC-GrEC electrode.

Following synthesis, the NMC particles were uniformly coated with graphene and ethyl cellulose (GrEC) using a previously established solution-phase method.[180,190] The coating conformality was confirmed using SEM and TEM (**Figure 3.3**), which revealed the presence of a percolating network of graphene flakes throughout the electrode and was consistent with prior work.[179,180,190] After fabricating electrodes with the GrEC powder (NMC-GrEC), the electrode was heated to pyrolyze the ethyl cellulose (EC) polymer, which largely volatilized the EC, compacted the electrode, and generated a carbon residue that helped form a percolating, electrically conductive network among the graphene-coated NMC particles.[171,179,180,188,190,238] Subsequent Raman spectroscopy of the electrode confirmed that the ratio of the D and G peaks decreased (at 1350 $cm^{-1}$ and 1580 $cm^{-1}$, respectively) (**Figure 3.4**), suggesting that EC decomposition resulted in a more graphitic carbon network that facilitated efficient charge transfer. The uncoated NMC powder was also mixed with carbon black (CB) and polyvinylidene fluoride (PVDF) to fabricate control electrodes (NMC-CBPVDF).

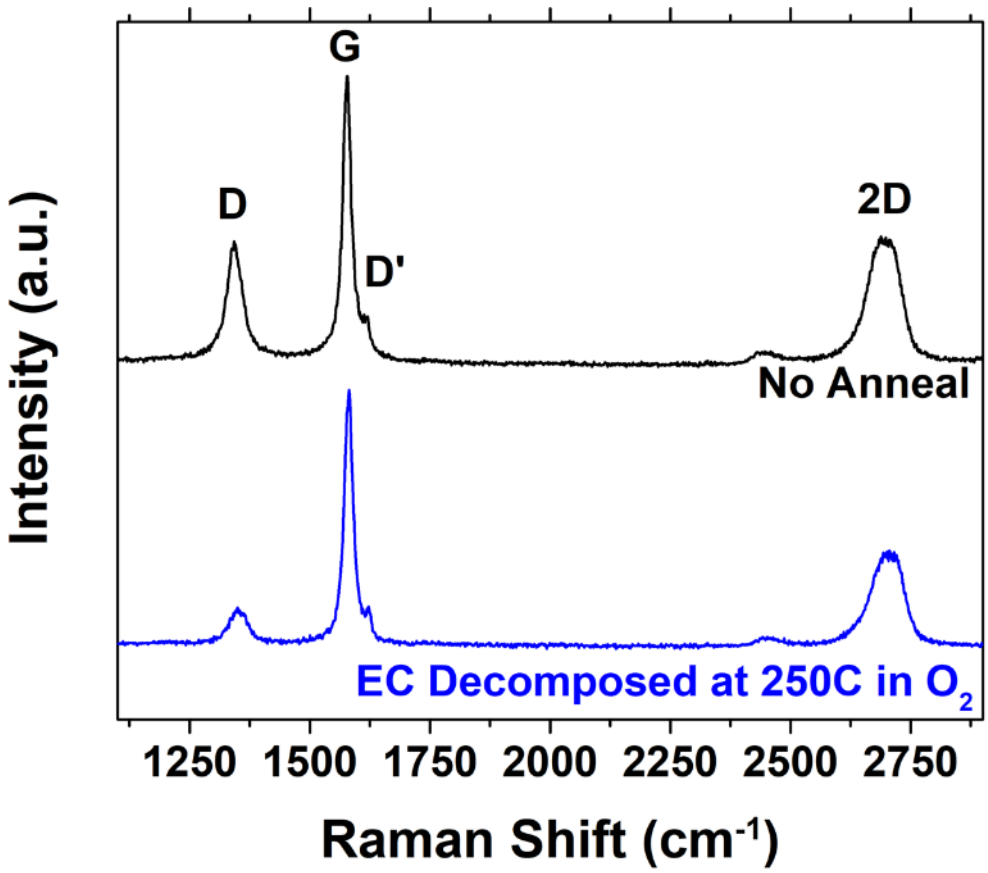


**Figure 3.4.** Raman spectra of the NMC-GrEC electrodes before and after the thermal decomposition of the ethyl cellulose polymer.

## 3.4 Electrochemical Characterization

### *3.4.1 Galvanostatic Cycling*

The cycle life behaviors of the NMC-GrEC and the NMC-CBPVDF electrodes were investigated using galvanostatic cycling to an upper cutoff voltage of 4.8 V vs. $Li/Li^+$ (**Figure 3.5a**). During the activation cycle, the NMC-GrEC electrode achieved a discharge capacity of 203.1 mAh $g^{-1}$, whereas the NMC-CBPVDF control electrode discharge capacity reached only

188.1 mAh $g^{-1}$, suggesting that the graphene coating enabled increased lithium utilization from the NMC lattice. After 50 charge-discharge cycles at 0.5C, the NMC-GrEC electrode retained 70.9% of its original capacity, which was far superior to the 20.7% capacity retention observed for the NMC-CBPVDF control electrode. The extremely poor cycle life observed for the NMC-CBPVDF control electrode was attributed to two factors. First, the high primary particle surface area provided ample surfaces upon which electrolyte decomposition reactions or surface phase formation could have occurred.[63,67,85,239] Since electrodes composed of smaller particles should possess significantly greater surface area, the NMC-CBPVDF electrode, which utilized submicron particles with no surface protection, exhibited a precipitous decline in cycle life. This behavior was consistent with trends for other reports utilizing comparatively larger single-crystal NMC particles.[239] Second, the high upper cutoff voltage exacerbated the severity of these interfacial chemical degradation mechanisms and promoted additional bulk chemomechanical degradation associated with layered oxides at high SOCs.[35,55] Nonetheless, the observed capacity fading reinforced the need for mitigation strategies that could enable improved high-voltage operation.

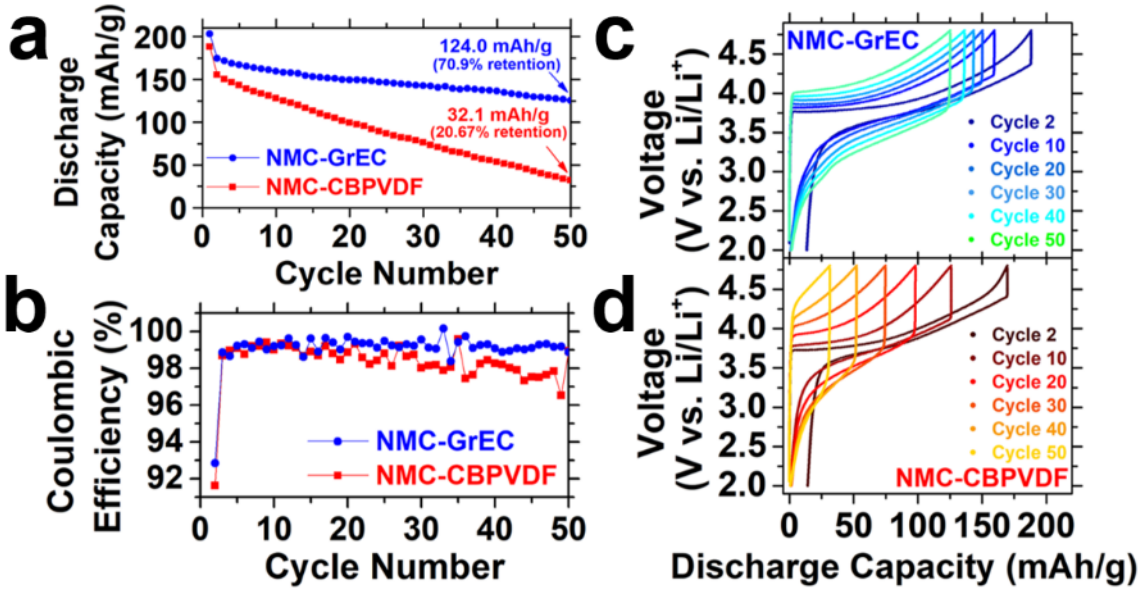


**Figure 3.5.** Electrochemical performance of NMC-GrEC and NMC-CBPVDF electrodes performed at 0.5C. (a) Cycle life test; (b) Coulombic efficiency; (c,d) Voltage-capacity plots showing the evolution of electrode polarization for the (c) NMC-GrEC and (d) NMC-CBPVDF electrodes.

The coulombic efficiency results (**Figure 3.5b**) also highlighted the improved charge-discharge behavior of the NMC-GrEC electrodes. The first cycle coulombic efficiency (FCE) was higher for the NMC-GrEC electrode (94.49%) than for the NMC-CBPVDF electrode (92.9%), which implied that the NMC-GrEC electrode lost fewer lithium ions to parasitic side reactions as the solid-electrolyte interphase (SEI) formed during the first cycle. This FCE was the highest reported among the many coating and doping strategies attempted for NMC532 half cells at voltages beyond 4.6 V vs. $Li/Li^+$ (**Table 3.3**). With additional cycling, the coulombic efficiency of the NMC-GrEC electrode remained consistent after 50 cycles, while the coulombic efficiency of the NMC-CBPVDF electrode declined after the $30^{th}$ cycle. As a result, the average coulombic efficiency of the NMC-GrEC electrode (99.68%) remained considerably higher than the average coulombic efficiency of the NMC-CBPVDF electrode (98.57%).

**Table 3.3.** Comparison of first cycle efficiencies among various reported strategies to stabilize the high-voltage cycling of NMC532.

| Strategy | Type | C-rate | Lower Cutoff Voltage (vs. $Li/Li^+$) | Upper Cutoff Voltage (vs. $Li/Li^+$) | Active Material Fraction in Electrode | Particle Size (um) | Loading (mg $cm^{-2}$) | FCE |
|---|---|---|---|---|---|---|---|---|
| $LiTiO_3$ coating (8%)[240] | Coating | 0.2 | 2.8 | 4.6 | 80% | 5 | 2.5-3.5 | 85.5% |
| $LiTiO_3$ coating (6%)[240] | Coating | 0.2 | 2.8 | 4.6 | 80% | 5 | 2.5-3.5 | 86.1% |
| $LiTiO_3$ coating (3%)[240] | Coating | 0.2 | 2.8 | 4.6 | 80% | 5 | 2.5-3.5 | 86.1% |
| $Li_3VO_4$[241] | Coating | 0.1 | 2.8 | 4.6 | 80% | -- | -- | 96.1% |
| ALD $Al_2O_3$[230] | Coating | 0.1 | 3 | 4.6 | 93% | 10-15 | 2.5 | 84.2% |
| $LiAlO_2$ 1 mol%[242] | Coating | 1 | 2.7 | 4.6 | 85% | 5 | 2 | 84.6% |
| $LiAlO_2$ 2 mol%[242] | Coating | 1 | 2.7 | 4.6 | 85% | 5 | 2 | 87.0% |
| $LiAlO_2$ 3 mol%[242] | Coating | 1 | 2.7 | 4.6 | 85% | 5 | 2 | 78.7% |
| $NaTi_2(PO_4)_3$[243] | Coating | 0.2 | 3 | 4.6 | 80% | 10-15 | 15 | 86.7% |
| Zr doping and polypyrrole coating[244] | Coating and Doping | 1 | 3 | 4.6 | 80% | 10-20 | -- | 84.1% |
| Nano-LFP coating with carbon nanotubes[245] | Core-Shell | 0.1 | 3 | 4.6 | 80% | 10-15 | -- | 87.0% |
| Nd-doping (0.4%)[246] | Doping | 0.2 | 2.8 | 4.6 | 80% | 10 | 3-4 | 82.3% |
| Nd-doping (0.8%)[246] | Doping | 0.2 | 2.8 | 4.6 | 80% | 10 | 3-4 | 84.4% |
| Nd-doping (1.2%)[246] | Doping | 0.2 | 2.8 | 4.6 | 80% | 10 | 3-4 | 82.2% |
| Zr doping[244] | Doping | 1 | 3 | 4.6 | 80% | 10-20 | -- | 84.3% |
| $LiBF_4$ (0.93 mol/kg)[247] | Electrolyte salt | 0.1 | 3 | 4.6 | 80% | 10-15 | -- | 82.6% |
| $LiBF_4$ (3.7 mol/kg)[247] | Electrolyte salt | 0.1 | 3 | 4.6 | 80% | 10-15 | -- | 86.5% |
| $LiBF_4$ (8.67 mol/kg)[247] | Electrolyte salt | 0.1 | 3 | 4.6 | 80% | 10-15 | -- | 88.9% |
| ALD $Al_2O_3$[4] | Coating | 1 | 2 | 4.8 | 93% | 10-15 | 2.5 | 88.2% |
| CNT 5%, filtered[248] | Composite | 0.1 | 3 | 4.8 | 80% | 5-10 | -- | 77.1% |
| CNT 5%[248] | Composite | 0.1 | 3 | 4.8 | 80% | 5-10 | -- | 78.3% |
| Nd-doping (1.2%)[246] | Doping | 1 | 2.8 | 4.8 | 80% | 10 | 3-4 | 58.0% |

| | | | | | | | | |
|---|---|---|---|---|---|---|---|---|
| 0.5 wt% p-toluenesulfonyl isocyanate (PTSI)[249] | Electrolyte additive | 1 | 3 | 4.8 | 80% | 10-15 | 1.2 | 71.1% |
| **Graphene-EC (this work)** | **Coating** | **0.1** | **2** | **4.8** | **95%** | **< 1 um** | **3** | **94.5%** |

The voltage-capacity plots indicated that the charge-discharge behavior was relatively stable for the NMC-GrEC electrode (**Figure 3.5c**), with only a mild polarization increase over 50 cycles. This polarization growth was again attributed to the high primary particle surface area and high cutoff voltage. On the other hand, the sudden increase in the position of the voltage shoulder (initially at ~3.7 V vs. $Li/Li^+$) and the increasing magnitude of the Ohmic drop between charge and discharge indicated that the inferior cycle life for the NMC-CBPVDF electrode was related to a significant increase in electrode polarization (**Figure 3.5d**). These results suggest that as the NMC-CBPVDF electrode was charged, fewer lithium ions than expected were extracted before the cutoff voltage was reached, limiting the overall per-cycle reversible capacity.

### *3.4.2 Electrochemical Impedance Spectroscopy*

To investigate the observed improvements in the high-voltage cycling and charge-discharge behavior for graphene-coated NMC, electrochemical impedance spectroscopy (EIS) and corresponding equivalent circuit modeling were utilized to quantify the observed changes in cell impedance. Distribution function of relaxation times (DRT) analysis was also performed to accurately determine the polarization processes and the corresponding frequencies in the EIS response. The Nyquist plots for the NMC-CBPVDF and NMC-GrEC cells before cycling both showed one semicircle followed by the diffusion region (**Figure 3.6**). Using the corresponding

DRT data (**Figure 3.7**), the semicircle was deconvoluted with three processes occurring at high and medium frequencies, which corresponded to the electrode-current collector interface ($P_1$ at ~105 Hz), lithium metal-electrolyte interface ($P_2$ at ~102 Hz), and electrode-electrolyte interface ($P_3$ at ~5 Hz), respectively.[75] To fit the EIS spectra, an equivalent circuit model was used that contained an inductor (L), ohmic resistance ($R_0$), two RQ elements that modeled $P_1$ and $P_2$, and a Randles circuit that modeled $P_3$ and Li-ion solid-state diffusion (**Figure 3.8**).

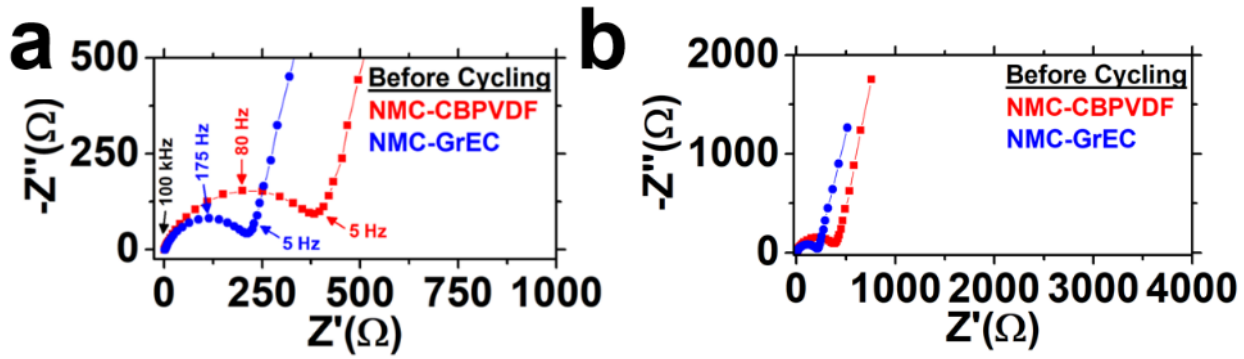


**Figure 3.6.** Nyquist plots of the NMC-CBPVDF and NMC-GrEC electrodes before cycling. Panel (a) shows a zoomed-in view of the high-frequency response in panel (b).

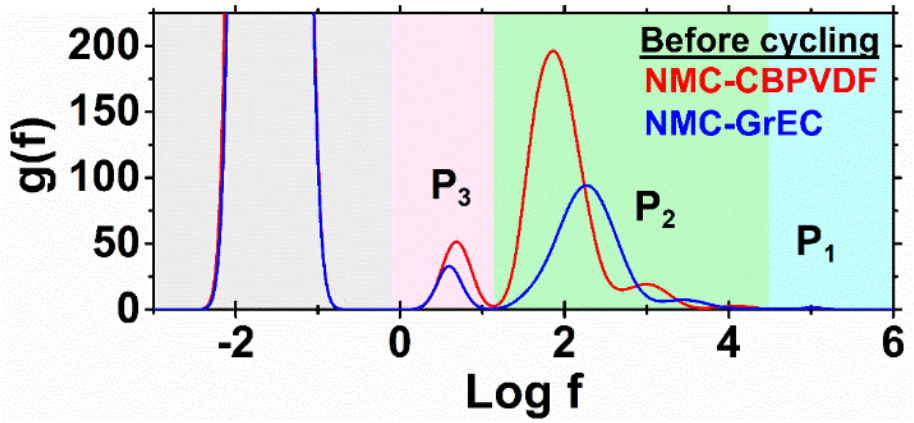


**Figure 3.7.** DRT spectra for the NMC-CBPVDF and the NMC-GrEC electrodes acquired before cycling.

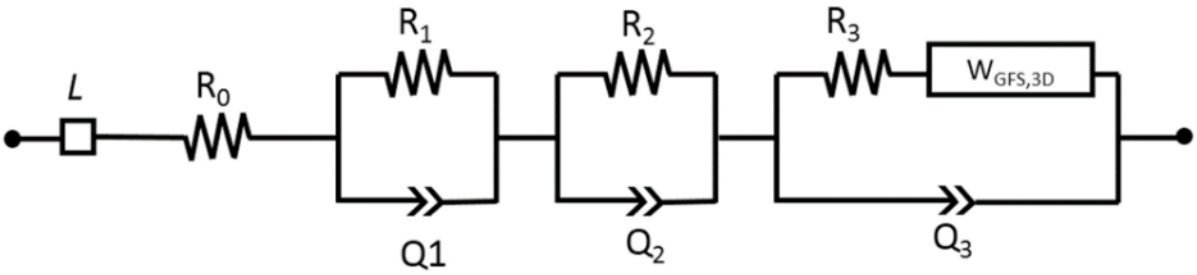


**Figure 3.8.** The equivalent circuit models used to fit the EIS spectra for the NMC-CBPVDF and NMC-GrEC cells cycled versus Li metal (a) before cycling and after cycling between 2.0 V and 4.3 V vs. $Li/Li^+$.

**Table 3.4.** Equivalent circuit model fitting results for the NMC-CBPVDF and NMC-GrEC electrodes before cycling.

| | | **Electrode/ Current Collector ($P_1$)** | | **Lithium Metal/ Electrolyte ($P_2$)** | | **Electrode/ electrolyte charge transfer ($P_3$)** | | **High-Voltage ($P_4$)** | | **D ($cm^2$ $S^{-1}$)** |
|---|---|---|---|---|---|---|---|---|---|---|
| | | **$R_1$ (Ω)** | **$C_1$ (μF $cm^{-2}$)** | **$R_2$ (Ω)** | **$C_2$ (μF $cm^{-2}$)** | **$R_3$ (Ω)** | **$C_3$ (mF $cm^{-2}$)** | **$R_4$ (Ω)** | **$C_4$ (mF $cm^{-2}$)** | |
| Before cycling | NMC-CBPVDF | 3 | 0.46 | 370 | 1.97 | 118 | 0.11 | - | - | $1.09 \times 10^{-7}$ |
| | NMC-GrEC | 2.5 | 0.56 | 200 | 1.78 | 85 | 0.22 | - | - | $1.24 \times 10^{-7}$ |

According to the results in **Table 3.4**, the NMC-GrEC electrode showed lower charge transfer impedance ($R_3$ of 85 Ω) than the NMC-CBPVDF electrode ($R_3$ of 118 Ω) before cycling. This result was consistent with expectations gleaned from the NMC-GrEC electrode microstructure. Since the NMC particles were conformally coated with a percolating carbon network possessing intrinsically high electronic conductivity (~$10^4$ S/m),[171] electrons and holes could be immediately supplied to charge compensate near sites where lithium (de)intercalation occurs. This mechanism enabled efficient charge transfer across the surfaces of the active material particles.[179,188] In contrast, carbon black particles, which possess lower intrinsic electrical

conductivities,[250] acted as point contacts between active material particles, thereby permitting only localized charge transfer.

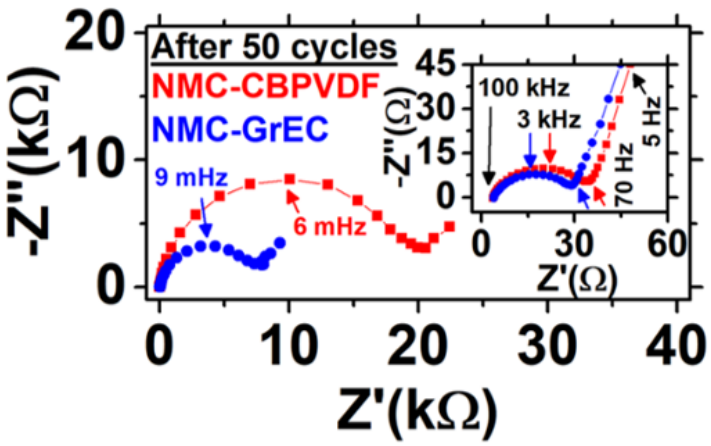


**Figure 3.9.** Nyquist plot of the NMC-CBPVDF and NMC-GrEC electrodes after 50 cycles to 4.8 V vs. Li/Li$^+$. The inset panel shows a zoomed-in view of the high-frequency response.

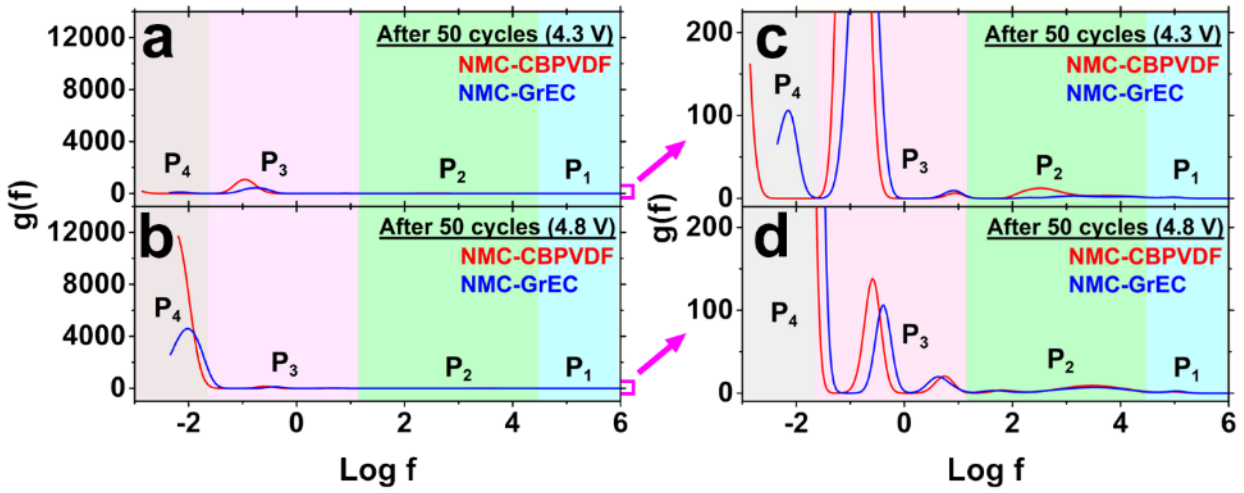


**Figure 3.10.** DRT spectra from NMC-CBPVDF and NMC-GrEC electrodes after 50 cycles (a,c) between 2.0 V and 4.3 V vs. Li/Li$^+$ and (b,d) between 2.0 V and 4.8 V vs. Li/Li$^+$. Figures (c,d) are zoomed-in regions of Figures (a,b) to better show processes $P_1$, $P_2$, and $P_3$, which correspond to the electrode-current collector interface ($P_1$), Li metal-electrolyte interface ($P_2$) and electrode-electrolyte interface ($P_3$) processes, respectively. The gray region shows Li diffusion and high-voltage degradation processes ($P_4$).

After 50 cycles between 2.0 V and 4.8 V vs. $Li/Li^+$, the Nyquist plots for both electrodes each contained two semicircles and a diffusion line (**Figure 3.9**). The DRT analysis for the samples after 50 cycles suggested that the high-frequency semicircle in the Nyquist plot (**Figure 3.9-inset**) was composed of impedances associated with the electrode-current collector ($P_1$) and lithium metal-electrolyte ($P_2$) interfaces. The process assigned to charge transfer at the electrode-electrolyte interface ($P_3$), which occurred at medium frequencies, increased in magnitude and shifted to lower frequencies with cycling (**Figure 3.9 and Figure 3.10b,d**). The DRT analysis implied that the $P_3$ process comprised only a small portion of the large semicircle in the Nyquist plot of the cells after 50 cycles (**Figure 3.9**). The remainder of the second semicircle corresponded to a fourth process at lower frequencies ($P_4$ at ~9 mHz) and was assigned to degradation processes at high voltage.

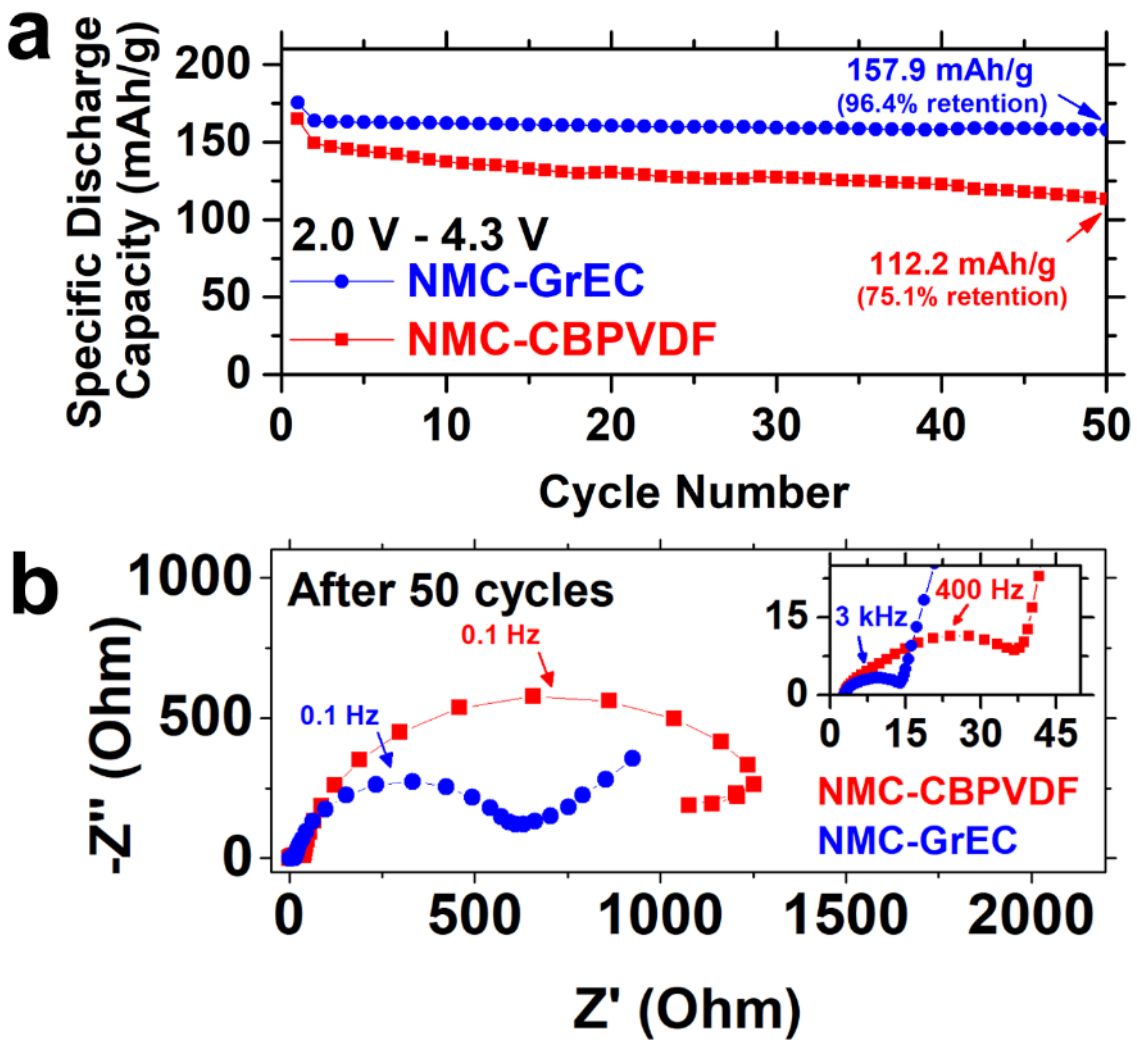


**Figure 3.11.** NMC-CBPVDF and NMC-GrEC electrodes cycled to 4.3 V vs. Li/Li$^+$ at 0.5C. (a) Galvanostatic cycling results. (b) Nyquist plot acquired after 50 cycles. Inset shows a zoomed-in view of the high-frequency response. To process the data for DRT and equivalent circuit modeling, the low-frequency data for the NMC-CBPVDF electrode were truncated after 20 mHz.

To confirm that the $P_4$ process was indeed related to high-voltage degradation, replicate NMC-CBPVDF and NMC-GrEC cells were fabricated and cycled at a narrower voltage window (2.0 V to 4.3 V vs. Li/Li$^+$) to identify the $P_4$ behavior under these cycling conditions. After 50

cycles at 0.5 C within this voltage window, the NMC-CBPVDF retained 75.1 % of its original capacity, while the NMC-GrEC electrode exhibited excellent cycle life and retained 96.4% of its original capacity (**Figure 3.11a**). EIS, equivalent circuit modeling, and DRT were subsequently performed. Based on the DRT results (**Figure 3.10a,c**), the small semicircle in the high-frequency region of the Nyquist plot (**Figure 3.11b**) contained $P_1$ and $P_2$, which again originated from the electrode-current collector interface and the lithium metal-electrolyte interface, respectively. The second semicircle in the Nyquist plot (**Figure 3.11b**) corresponded to a third process representing charge transfer at the electrode-electrolyte interface ($P_3$), which occurred at medium frequencies (~0.1 Hz) and shifted to lower frequencies with cycling (**Figure 3.10a,c**). Importantly, although the $P_4$ process was present in the DRT response for the samples cycled to 4.3 V vs. $Li/Li^+$, it was much lower in magnitude than for samples cycled to 4.8 V vs. $Li/Li^+$, suggesting that this process was indeed tied to high-voltage operation.

Since the DRT response of replicate cells cycled at lower cutoff voltages showed a $P_4$ process with a negligible magnitude when compared to the DRT response of the cells cycled at high voltage, there was strong evidence for a relationship between the cutoff voltage and the magnitude of the $P_4$ polarization (**Figure 3.10**). The voltage-dependent activation of this process suggested that it could have been related to degradation mechanisms at high voltages, such as chemomechanical changes in the active material or the formation of a thick chemical interphase. Correspondingly, another RQ element was added to the equivalent circuit model and used to fit the high-voltage EIS data after cycling (**Figure 3.12**).

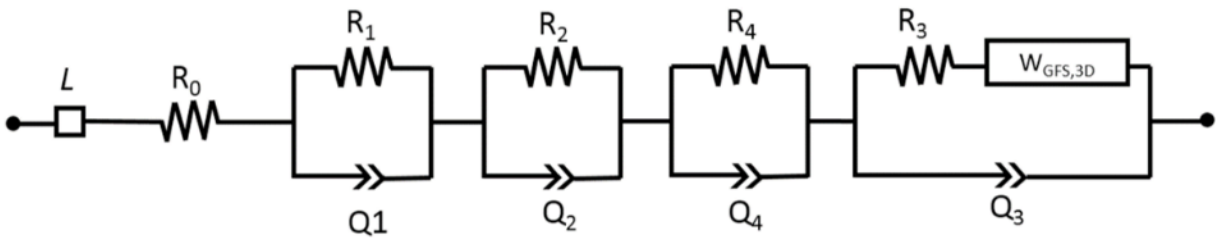


**Figure 3.12.** The equivalent circuit models used to fit the EIS spectra for the NMC-CBPVDF and NMC-GrEC cells cycled versus Li metal after cycling between 2.0 V and 4.8 V vs. $Li/Li^+$.

According to the fit results (**Table 3.5**), the charge transfer impedance ($R_3$) for both electrodes increased after 50 cycles. This increase was greater for the NMC-CBPVDF electrode (180 **Ω**, corresponding to a 153% increase) compared to the NMC-GrEC electrode (120 **Ω**, corresponding to a 141% increase). Moreover, the magnitude of the surface film impedance ($P_4$) at low frequencies was significantly higher in the NMC-CBPVDF (18500 **Ω**) electrode compared to the NMC-GrEC electrode (6850 **Ω**). These EIS results, coupled with the galvanostatic cycling data, suggest that active material degradation accumulated in a manner that increased the electrode charge transfer impedance. However, since these impedance values were lower for the NMC-GrEC electrode, the graphene coating apparently mitigated NMC degradation and ensured a more efficient charge-discharge process. Finally, the improved electrochemical performance of the NMC-GrEC electrode was likely related to the significantly lower $R_4$ impedance associated with high-voltage degradation.

**Table 3.5.** Equivalent circuit model fitting results for the NMC-CBPVDF and NMC-GrEC electrodes after cycling between 2.0 V and 4.3 V vs. $Li/Li^+$ and after cycling between 2.0 V and 4.8 V vs. $Li/Li^+$.

| | | **Electrode/ Current Collector ($P_1$)** | | **Lithium Metal/ Electrolyte ($P_2$)** | | **Electrode/ electrolyte charge transfer ($P_3$)** | | **High-Voltage ($P_4$)** | | **D ($cm^2$ $S^{-1}$)** |
|---|---|---|---|---|---|---|---|---|---|---|
| | | **$R_1$ (Ω)** | **$C_1$ (μF $cm^{-2}$)** | **$R_2$ (Ω)** | **$C_2$ (μF $cm^{-2}$)** | **$R_3$ (Ω)** | **$C_3$ (mF $cm^{-2}$)** | **$R_4$ (Ω)** | **$C_4$ (mF $cm^{-2}$)** | |
| After 50 cycles (4.3 V) | NMC-CBPVDF | 2.9 | 0.47 | 36 | 2.8 | 1290 | 0.79 | - | - | |
| | NMC-GrEC | 2.2 | 0.51 | 11 | 2 | 595 | 0.88 | - | - | $2.00 \times 10^{-10}$ |
| After 50 cycles (4.8 V) | NMC-CBPVDF | 2 | 0.79 | 31 | 0.62 | 180 | 3.55 | 18500 | 1.13 | $4.00 \times 10^{-10}$ |
| | NMC-GrEC | 2 | 0.71 | 24 | 0.98 | 120 | 1.71 | 6850 | 1.64 | $2.2 \times 10^{-10}$ |

## 3.5 Postmortem Characterization

### *3.5.1 High-Resolution X-Ray Diffraction*

To further explain the electrochemical results, high-resolution SR-PXRD was performed on fully discharged samples to investigate cycling-induced structural changes (**Figure 3.13**). Since the NMC unit cell dimensions are known to be highly dependent on the SOC, discharging the electrodes to the same voltage and then measuring the (110) and the (003) peak positions can elucidate differences between the lithium content of the two samples. As NMC is charged to moderate SOCs, lithium is removed from the NMC structure, causing the unit cell to contract in the $a = b$ directions and expand in the $c$ direction, since unoccupied sites in the lithium layer promote oxygen-oxygen repulsion across the resulting van der Waals gap. Therefore, during charging, the NMC (110) peak shifts to higher angles, while the (003) peak shifts to lower angles.[35,224]

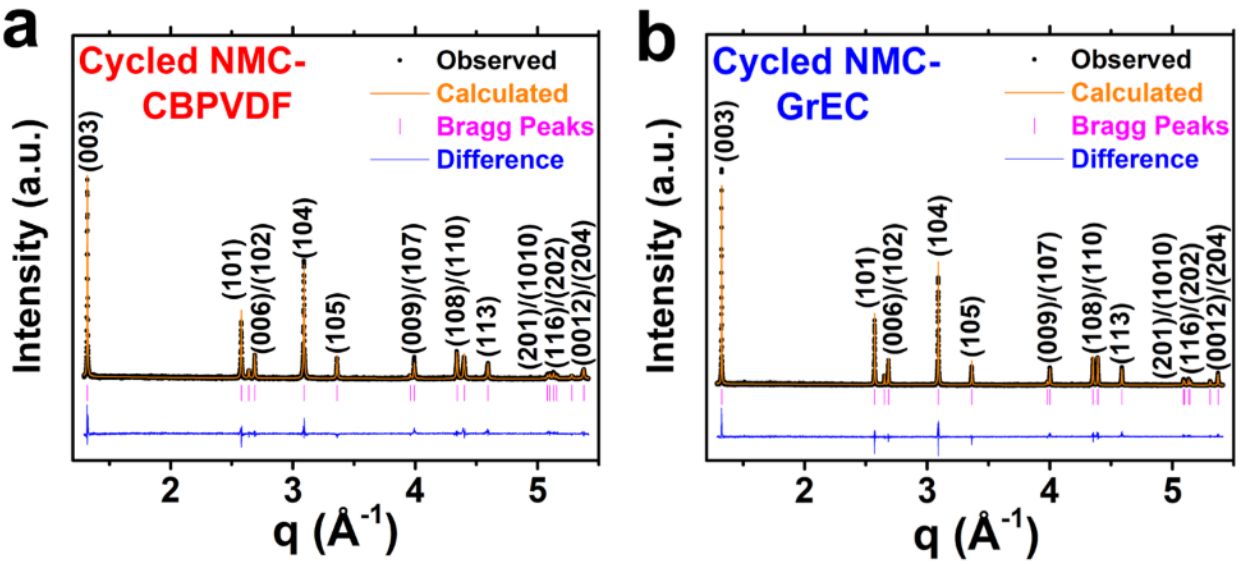


**Figure 3.13.** Postmortem synchrotron radiation powder X-Ray diffraction patterns of the (a) NMC-CBPVDF electrode and (b) NMC-GrEC electrode.

Although these peaks are expected to return to their original positions at the end of discharge, the postmortem diffraction patterns showed that this trend was not the case for the (110) and the (003) peaks in the cycled samples (**Figure 3.14**). The deviations in the diffraction peak positions were more severe for the NMC-CBPVDF electrode, suggesting that a large population of NMC was not re-lithiated during the 50th cycle discharge step. This result could have occurred for multiple reasons, including the formation of interfacial electrolyte decomposition products that kinetically limited charge transfer reactions or cycling-induced volumetric changes that caused cracking, particle fracture, or detachment from the conductive path to the current collector.[35,251,252]

Furthermore, the changes in the (003) and the (110) full-width half maxima (**Figure 3.14**) after cycling indicated that the domain sizes and microstrain amounts evolved differently between the two samples. Rietveld refinement of the SR-PXRD patterns was used to quantify these changes

and showed an increase in the domain size and a decrease in the microstrain for the NMC-CBPVDF sample after cycling. This result would be consistent with particle fracture induced by cycling at high SOCs. In contrast, no significant changes were found between the NMC-GrEC sample and the pristine NMC powder (**Table 3.1** and **Table 3.6**). Nonetheless, the SR-PXRD results corroborated the galvanostatic cycling and EIS results, further suggesting that the graphene-coated electrode experienced reduced material degradation compared to the control sample.

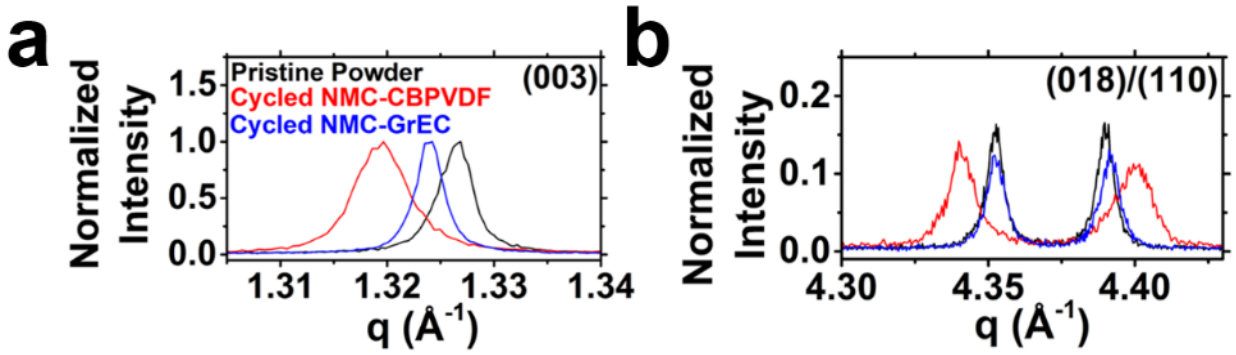


**Figure 3.14.** High-resolution powder X-Ray diffraction patterns near the vicinities of the (a) (003) peak and (b) (018)/(110) peaks for the pristine NMC powder and for samples that were cycled 50 times.

**Table 3.6.** Rietveld refinement results for the cycled NMC-CBPVDF electrode and the cycled NMC-GrEC electrode.

| **Sample** | **Lattice parameters (Å)** | | **Li/Ni mixing** | **Domain size (μm)** | **Microstrain** | **RF, RF$^2$ (%)** |
|---|---|---|---|---|---|---|
| | ***a*** | ***C*** | | | | |
| NMC-CBPVDF after 50 cycles | 2.8595(7) | 14.298(2) | 1.17% | 0.4237 | 3285.7 | 5.94, 11.26 |
| NMC-GrEC after 50 cycles | 2.8626(5) | 14.214(2) | 1.93% | 0.7613 | 1827.2 | 6.64, 9.77 |

### *3.5.2 X-Ray Photoelectron Spectroscopy*

XPS was used to investigate the differences between the surface chemistries of the two electrodes before and after cycling. The C 1s spectra for both electrodes before cycling showed an intense peak at 284.8 eV, corresponding to C-C bonds from adventitious carbon and the conductive carbon additives (**Figure 3.15**). The NMC-CBPVDF electrode also exhibited spectral intensities in the range of reported values for C-O bonds (286.1 eV) and C=O/O-C-O bonds (287.4 eV), which likely originated from carbon-oxygen surface functional groups on carbon black.[253] In contrast, the C 1s spectrum for the pristine NMC-GrEC electrode surface was dominated by C-C bonding character, which was consistent with previous reports for pyrolyzed graphene-ethyl cellulose films.[171,190,200,201] The difference in the C-F bond intensities near 290.7 eV was attributed to the absence of polyvinylidene fluoride binder in the NMC-GrEC electrode.

After electrochemical cycling to 4.8 V vs. $Li/Li^+$, the C 1s and O 1s XPS spectra for both electrodes exhibited increased spectral intensities at binding energies corresponding to carbon-oxygen bonds (C=O at 531.8 eV and C-O at 533.2 eV), which was likely due to the formation of interfacial organic decomposition products (**Figure 3.15**). This conclusion was supported by the corresponding decrease in transition metal-oxygen bond intensities (529.1 eV) in the O 1s spectra. Similarly, the Mn 3p and the Co 3p peaks were initially prominent in the Li 1s XPS spectra for both pristine samples, but significantly decreased in intensity after cycling (**Figure 3.16**). These trends suggested that an organic-rich SEI layer formed during cycling that attenuated the transition metal-oxygen signal from the NMC bulk. Importantly, the cycling-induced increase in carbon-oxygen spectral intensities was greater in the NMC-CBPVDF electrode than the NMC-GrEC

electrode, suggesting that less decomposition products were present the NMC-GrEC electrode. While carbon black is known to react with electrolyte components to form organic decomposition products,[70] the absence of out-of-plane dangling bonds on graphene likely minimized its chemical reactivity with the electrolyte. Indeed, the C 1s spectrum for the NMC-GrEC electrode after cycling was still dominated by C-C spectral intensities, suggesting that the graphene coating successfully maintained a highly conductive surface over the operating lifetime of the cell.

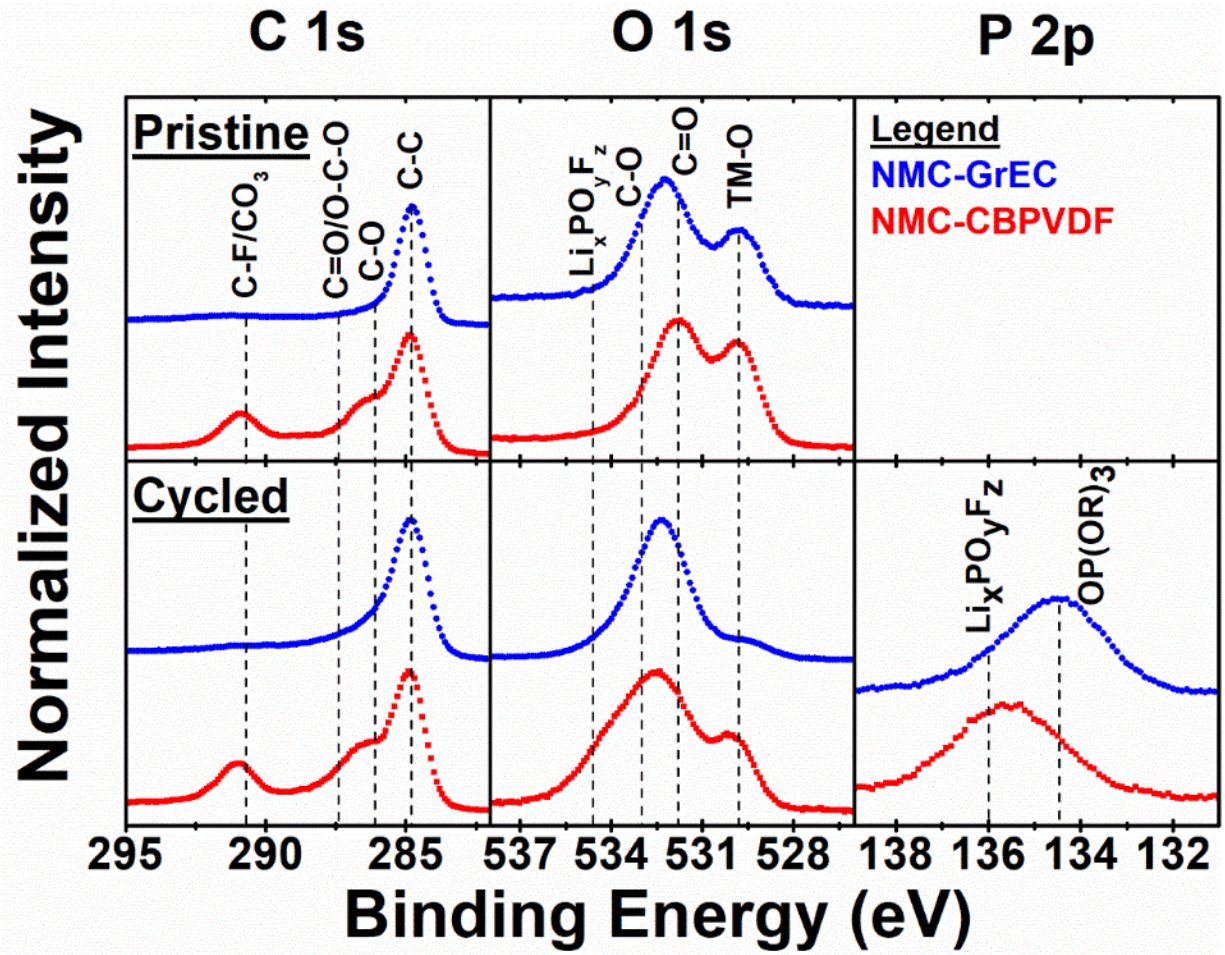


**Figure 3.15.** XPS C 1s, O 1s, and P 2p spectra of the NMC-GrEC and NMC-CBPVDF electrodes before cycling (top) and after cycling (bottom). The P 2p spectra for the pristine samples were not taken since the phosphorous character should only be present after electrolyte contact.

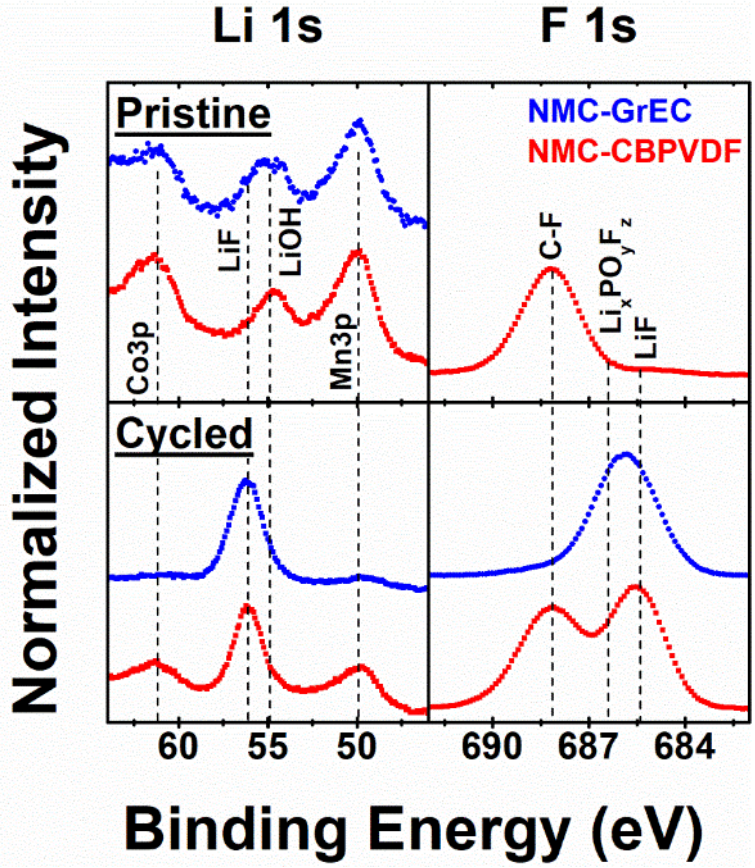


**Figure 3.16.** XPS Li 1s and F 1s spectra of the NMC-GrEC and NMC-CBPVDF electrodes before cycling (top) and after cycling (bottom).

The chemical natures of the inorganic degradation products differed between the two cycled electrodes. The Li 1s and the F 1s spectra (**Figure 3.16**) indicated that LiF (56.1 eV and 685.4 eV), a $LiPF_6$ salt decomposition product,[80] were present in both cycled samples. Additional salt degradation reactions are known to generate phosphate compounds, which can subsequently react with lattice lithium to form $Li_xPO_yF_z$ species.[67] Significantly, the P 2p spectrum (**Figure 3.15**) for the cycled NMC-CBPVDF electrode showed prominent spectral intensities at binding energies close to reported values for $Li_xPO_yF_z$ (136.0 eV), whereas the NMC-GrEC electrode

exhibited greater intensities close to the binding energies reported for phosphates (134.5 eV). These results implied that fewer fluorophosphate degradation products were present on the NMC-GrEC electrode. Since the graphene coating presumably limited the amount of electrolyte that could have contacted the active material surface, it likely reduced interactions between charged oxide surfaces and electrolyte solvent molecules, kinetically suppressing dissociation reactions such as ethylene carbonate dehydrogenation.[63,67] Moreover, the coating also limited the contact between the electrode surface and phosphate-based reaction intermediates, which can generate surface protic species that form HF and $Li_xPO_yF_z$. Together, these benefits likely resulted in preserved lithium inventory, reduced active material etching, and ultimately improved coulombic efficiency and cycle life.

### *3.5.3 Scanning Transmission Electron Microscopy (STEM) Analysis*

NMC is known to experience surface phase transformations at the electrode-electrolyte interface. The bulk layered structure changes to spinel and rocksalt phases due to the accumulation of Li-Ni antisite defects,[50,116] a phenomenon which is linked to the surface chemical environment.[85,123-125,254] Since the XPS analysis suggested that the graphene coating suppressed chemical interactions between the oxide surface and the electrolyte, the relationship between the presence of the graphene-EC coating and surface phase transformation was investigated using high-angle annular dark-field scanning transmission electron microscopy (HAADF-STEM) (**Figure 3.17**). In the interior of the NMC particle, regions with bright and dark contrast were observed, corresponding to regions with high and low atomic numbers, respectively. This observation was consistent with a *R-3m* layered structure containing alternating transition metal

and lithium layers along the *c* direction.[85] Near the particle edge, transition metals were observed in the lithium layer, which was consistent with the presence of Li-Ni antisite defects.

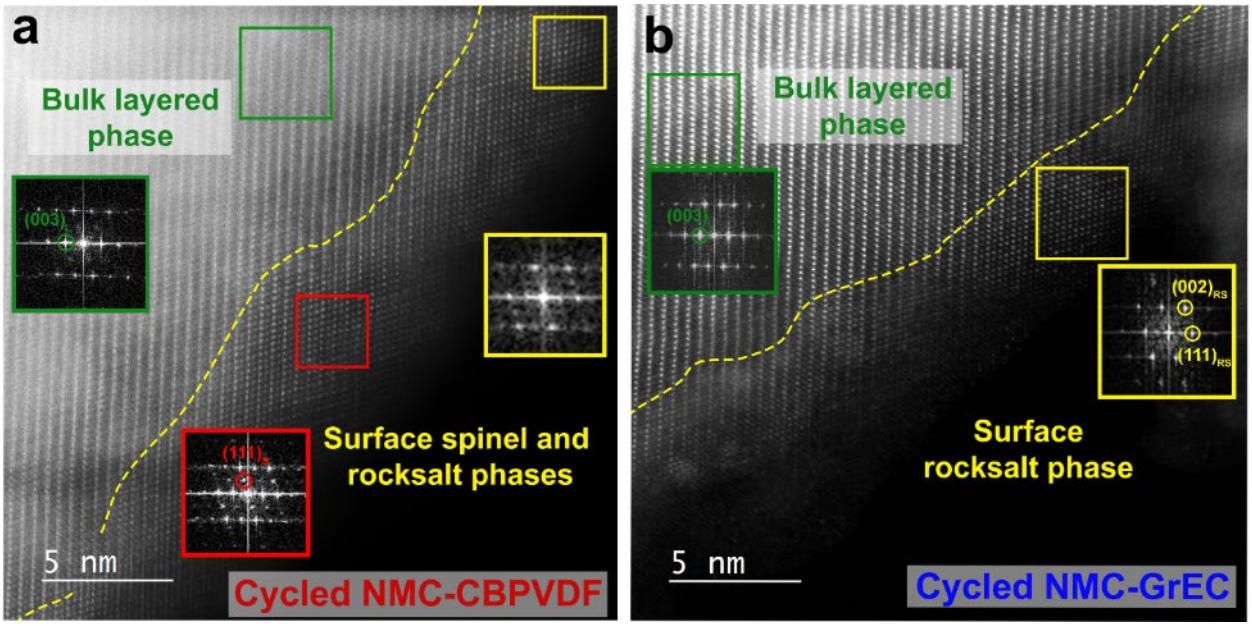


**Figure 3.17.** Postmortem STEM analysis of (a) NMC-CBPVDF and (b) NMC-GrEC electrodes after 50 cycles between 2.0 V and 4.8 V vs. $Li/Li^+$ at 0.5C. The inset FFT patterns show the presence of layered (green, or L), spinel (red, or S), and rocksalt (yellow, or RS) phases. The zone axis is [1-10].

Fast Fourier transform (FFT) analysis was used to identify layered (L), spinel (S), and rocksalt (RS) phases (insets in **Figure 3.17**). The FFT analysis showed spots indexed to the $(003)_L$ planes in the layered phase, the $(111)_{RS}$ and the $(002)_{RS}$ planes in the rocksalt phase, and the $(111)_S$ planes in the spinel phase. All three phases were found in the NMC-CBPVDF electrode (consistent with the findings of Jung *et al.*[50]), whereas the spinel phase was not observed in the NMC-GrEC sample. Previous reports posited that the spinel phase serves as a bridge between the bulk layered phase and the rocksalt phase.[70,85] Using the HAADF-STEM images, the thicknesses of the surface reconstruction layers on the NMC-CBPVDF and the NMC-GrEC samples were both found to be

approximately 5 nm. The similarity between these measurements suggested that the graphene coating did not significantly impact the formation of new phases near the particle surface and therefore was unlikely to have played a significant role in the improved cycle life of the NMC-GrEC electrode.

### *3.5.4 Inductively Coupled Plasma Mass Spectrometry*

Since earlier reports on NMC concluded that dangling bonds on surface phases are susceptible to transition metal dissolution into the electrolyte,[85] this possibility was probed via inductively coupled plasma-mass spectroscopy (ICP-MS). In prior work, graphene was used to prevent the dissolution of Mn into carbonate-based electrolytes since its basal plane presents a high diffusion barrier to Mn ions.[179,184] A conformal graphene-EC coating could therefore provide similar benefits for the NMC system. However, analysis of the transition metal dissolution behavior in the pristine electrodes (**Table 3.7**) showed no significant differences between the NMC-GrEC and the NMC-CBPVDF electrodes. Although the transition metal concentrations between the two samples varied by approximately ± 10%, the measured amount was low (< 1 ppm of dissolved transition metal per milligram of active material), suggesting that the improved cycle life of the NMC-GrEC electrode was unlikely due to a change in the transition metal dissolution behavior induced by the graphene coating.

**Table 3.7.** Concentrations of dissolved transition metal ions for the NMC-CBPVDF control electrode and the NMC-GrEC electrode as determined by ICP-MS.

| | ***Concentration (ppb/mg active material)*** | | |
|---|---|---|---|
| **Sample** | **Ni** | **Mn** | **Co** |
| NMC-CBPVDF | 320.62 | 677.31 | 68.86 |
| NMC-GrEC | 314.76 | 615.27 | 71.33 |

### *3.5.5 Scanning Electron Microscopy*

Finally, postmortem SEM was performed on the cycled electrodes to investigate morphological changes that occurred during cycling. First, interparticle cracking was observed (**Figure 3.18**), which likely originated from anisotropic changes in the unit cell volume at high SOCs or spatially non-uniform charge transfer reactions between particles, both of which could generate strain energy that drive particle fracture. Second, intraparticle cracking was observed in primary particles. The NMC-CBPVDF electrode showed significant signs of both failure modes, with wide gaps forming between individual primary particles (**Figure 3.18a and Figure 3.19**). In contrast, fewer and thinner intraparticle and interparticle cracks were found on particles in the NMC-GrEC electrode (**Figure 3.18b and Figure 3.20**). Third, electrochemical creep was observed, as evidenced by a terrace-like surface morphology on primary particles. This phenomenon is consistent with lattice-invariant shear associated with the O3 to O1 phase transformation for layered cathode materials[55] such as $LiCoO_2$,[14,121,137,255] $LiNiO_2$,[21,256,257] and NMC.[251,258] Significantly, the severity of electrochemical creep was much lower in the NMC-

GrEC electrode (**Figure 3.18b and Figure 3.20**). To confirm that this observation was consistent across different areas on the electrodes, over 2,000 primary particles on each electrode were analyzed via SEM to identify signs of electrochemical creep. Approximately 18% of the primary particles evaluated for the NMC-CBPVDF electrode showed terracing, compared to only 6% of the primary particles evaluated for the NMC-GrEC electrode. Therefore, postmortem SEM provided a morphological confirmation of chemomechanical degradation after cycling to high SOCs, corroborating the SR-PXRD and Rietveld refinement results.

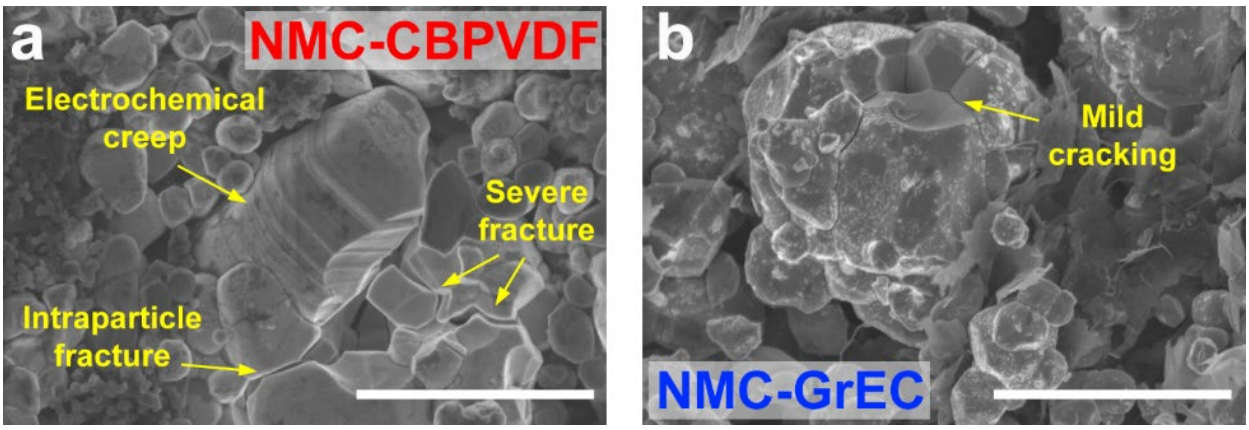


**Figure 3.18.** Postmortem scanning electron microscopy images of the (a) NMC-CBPVDF electrode surface and (b) NMC-GrEC electrode surface. Both scale bars are 2 μm.

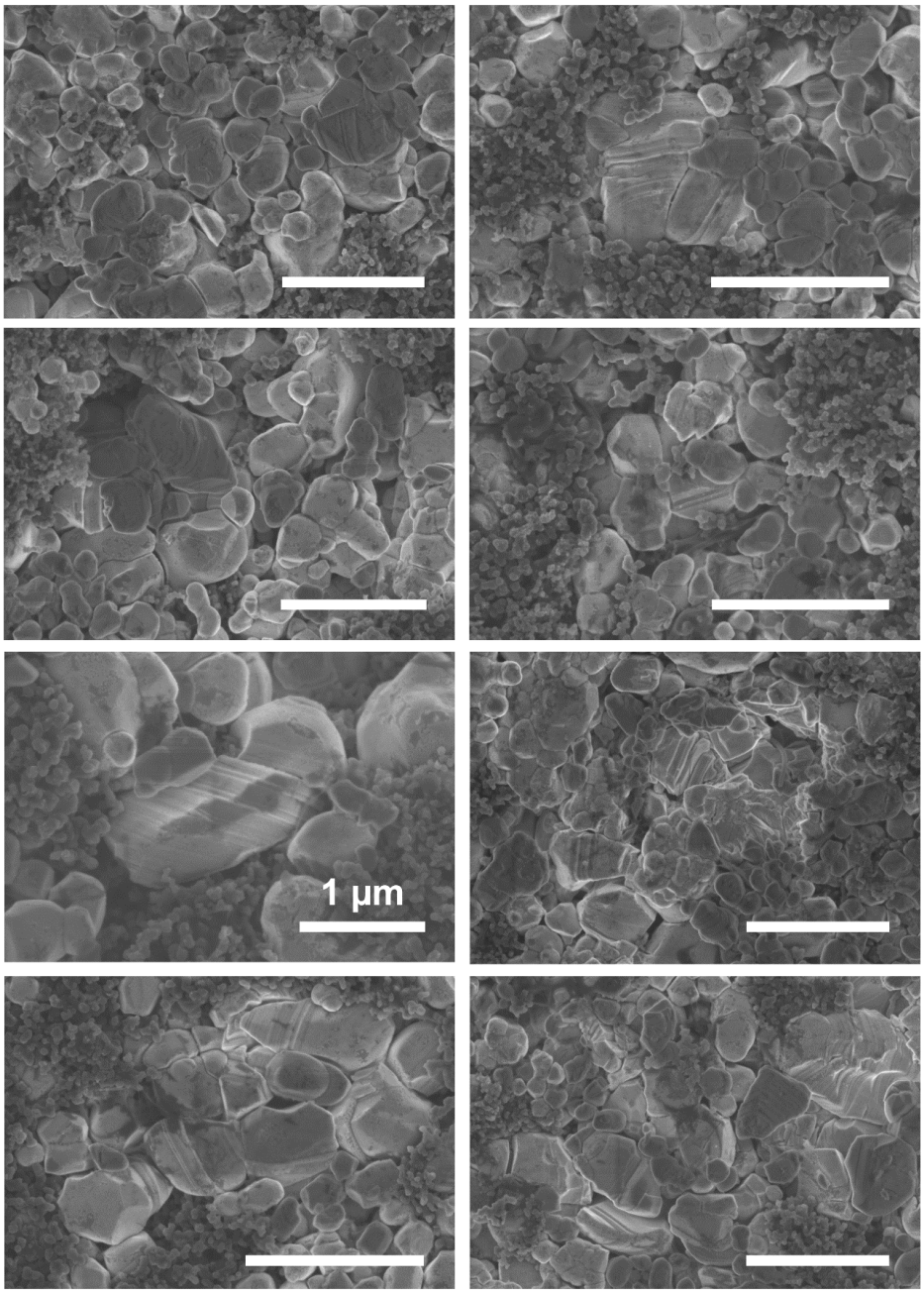


**Figure 3.19.** Additional postmortem SEM images showing intraparticle and interparticle fracture and electrochemical creep in the NMC-CBPVDF electrode. Unless noted, all scale bars are 2 µm.

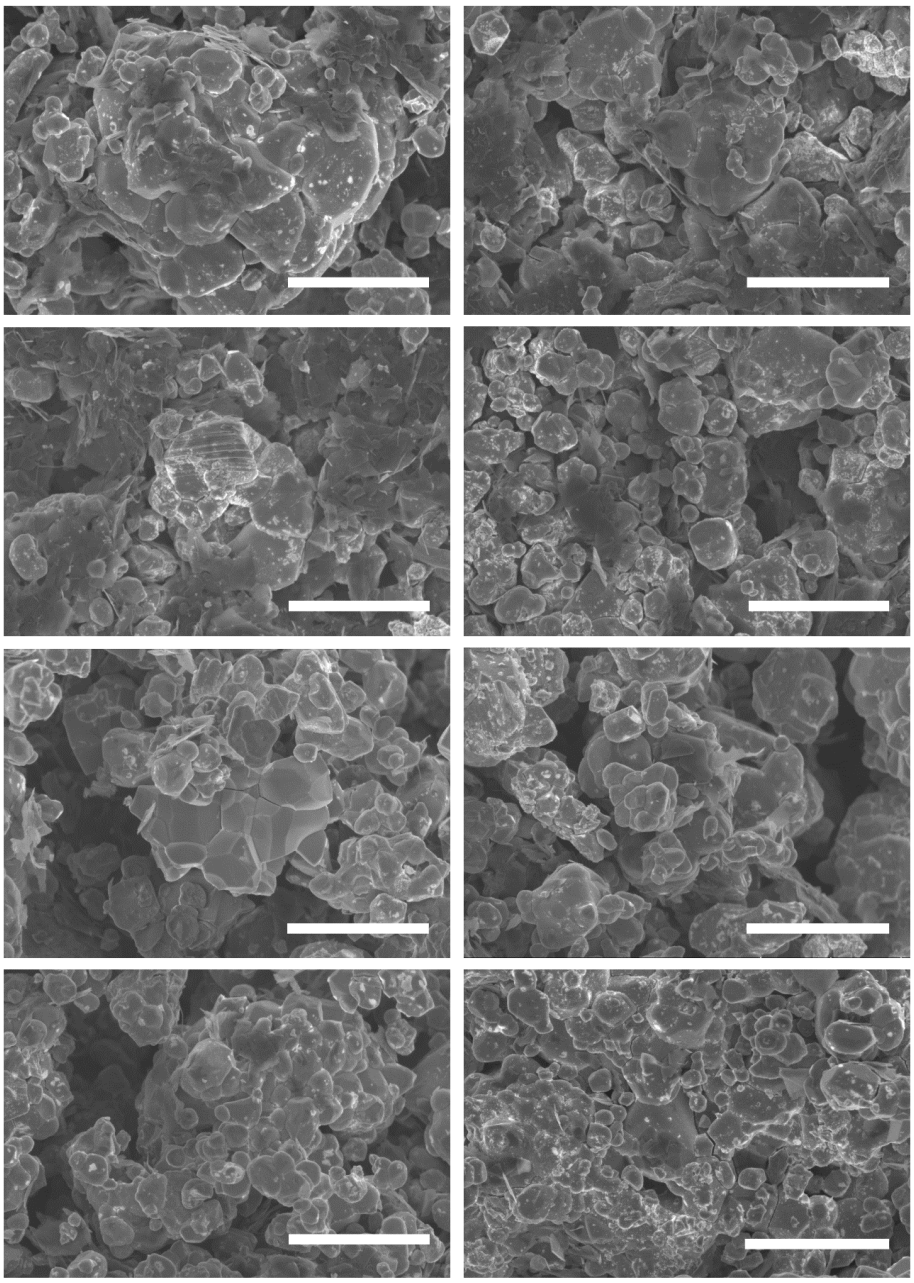

**Figure 3.20.** Additional postmortem SEM images showing limited evidence of intraparticle and interparticle fracture and electrochemical creep in the NMC-GrEC electrode. All scale bars are 2 μm.

### *3.5.6 Discussion*

The observed electrochemical performance enhancement in the NMC-GrEC electrodes was likely related to the improved lithiation dynamics enabled by a conformal carbon coating. Prior work identified compositional heterogeneity across active material particle surfaces during cycling.[138,142,225,226] In secondary particle-based electrodes, reaction non-uniformity is related to the contact between adjacent primary particles, which can change as a result of cycling-induced anisotropic strains, as well as the electrolyte penetration into the interior of the agglomerate.[138,139,144,228] In these structures, intergranular fracture is a well-known failure mechanism that underlies capacity fading due to the loss of electrical contact between individual grains. The use of primary particles in this work ensured that all NMC surfaces that could be exposed to the electrolyte were coated by a conductive carbon layer, enabling an investigation into the relationship between surface electronic conductivity and charge-transfer-induced chemomechanical degradation. For primary particles, other factors can also contribute to reaction non-uniformity, such as crystallographically anisotropic lithium diffusivities or the presence of high-impedance surface phases.[138] The graphene coating demonstrated in this work was unlikely to affect these sources of compositional heterogeneity since they should be inherent to the material system. However, a surface coating nonetheless presented an opportunity to engineer the dynamics of interfacial charge transfer reactions in the context of electronic connectivity within the electrode, which is highly important irrespective of the particle size or composition.[138]

Since intercalation reactions depend on electrically conductive pathways for charge compensation, a conductive network based on non-uniformly distributed carbon black particles

results in high spatial variations in surface electrical resistance,[58] promoting hotspots with high lithium-ion current densities on the particle surface. During charging, regions neighboring these current hotspots would be delithiated first, with two implications for mechanical degradation. First, lithium-poor and lithium-rich regions with different molar volumes would exist simultaneously within a particle, generating a corresponding stress field that varies with lithium content. Non-uniform stress and strain distributions are likely precursors to intraparticle and interparticle fracture.[252,259,260] Second, highly delithiated regions can act as nucleation sites for the high-voltage O3 to O1 phase transition that induces electrochemical creep.[55] In contrast, a layer that can supply or accept electrons anywhere on the particle surface, such as a graphene coating, delocalizes these hotspots and thereby promotes more spatially uniform compositional and volumetric changes during cycling (**Figure 3.21**). We anticipate that future studies will continue to explore the relationship between surface conduction and reaction uniformity, utilizing techniques such as scanning transmission X-ray microscopy that allow visualization of the SOC within a single particle via Ni K-edge mapping. It is also important to consider the possibility that delithiation induces changes in the NMC electrical conductivity, which could generate new electrical conduction pathways at high SOCs. However, since the electrical conductivity of GrEC films is 3 orders of magnitude greater than that of layered lithium transition metal oxides ($10^4$ S/m vs. $10^1$ S/m),[171,261,262] electrons are likely to continue to conduct along the graphene network even if the NMC bulk electrical conductivity changes.

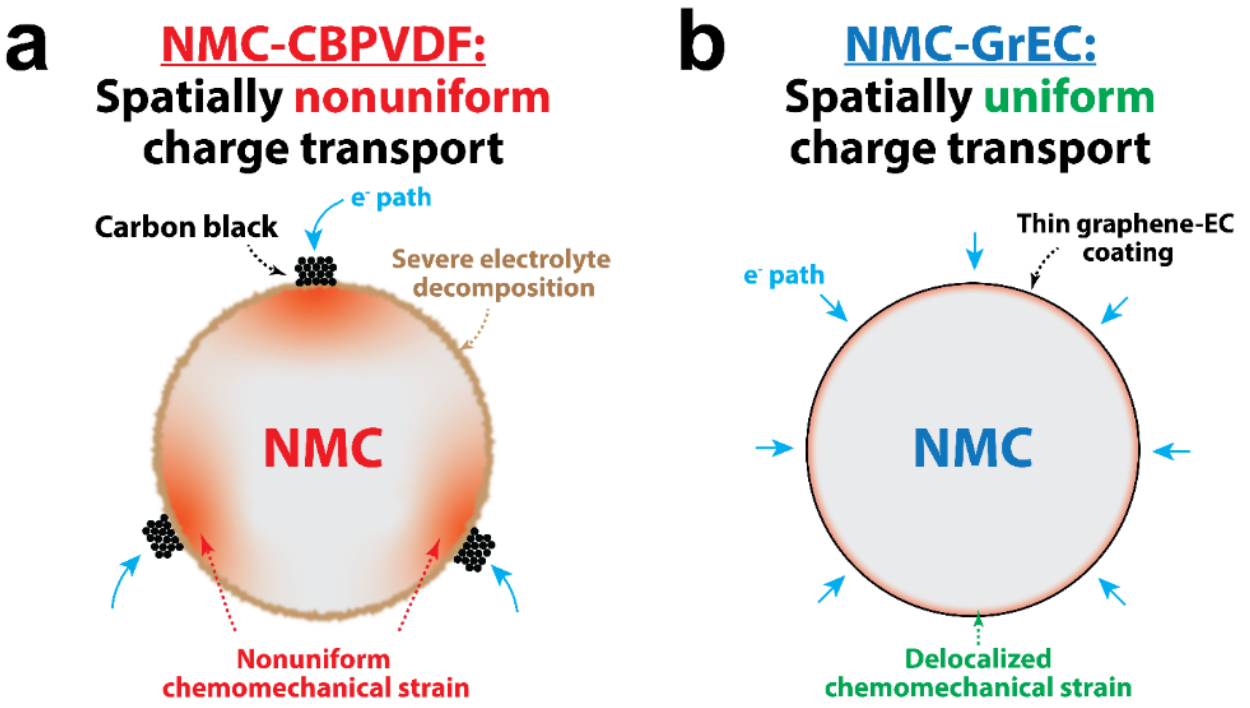


**Figure 3.21.** A schematic showing the proposed degradation mechanisms for the (a) NMC-CBPVDF electrode, which are mitigated in the (b) NMC-GrEC electrode due to the presence of the graphene coating.

A feedback loop exists between particle-level mechanical degradation and changes in interfacial chemistry, crystallography, and electrochemical activity. Cracking and lattice-invariant shear both generate new surfaces that quickly react with the electrolyte, which can lead to additional SEI or rocksalt phase formation. Effective mitigation of particle-level mechanical degradation could address these issues, therefore decreasing electrode polarization and increasing coulombic efficiency during long-term cycling. In addition, although fracture-initiated particle detachment can significantly contribute to capacity fade,[58] this negative effect can be reduced by engineering the electronic conduction path within an electrode. Here, the conformal graphene network played this role since it acted as a conductive network that captured particle fragments

generated via intraparticle and interparticle fracture, ensuring that fragments remained electrochemically active. This mechanism has been proposed to explain cycle life improvements in other systems that undergo volume expansion during lithiation, such as graphene-coated silicon microparticles.[182]

Finally, the conductive graphene coating possesses electrode engineering advantages over other inorganic coating layers that have been employed to stabilize the electrode-electrolyte interface.[236,237] To overcome the low electrical conductivity of these materials, one approach is to increase the fraction of conductive carbon in the electrode. However, this strategy results in compromised electrode-level energy densities. In contrast, electrodes utilizing graphene-coated NMC possessed intrinsically higher packing densities than electrodes fabricated with an equivalent fraction of carbon black (**Figure 3.22a-b**), resulting in high volumetric capacities even at high applied current rates (**Figure 3.22c**). These positive impacts across multiple length scales were enabled by the intrinsically robust mechanical, chemical, and electronic properties of graphene that present distinct advantages over other surface coating schemes.

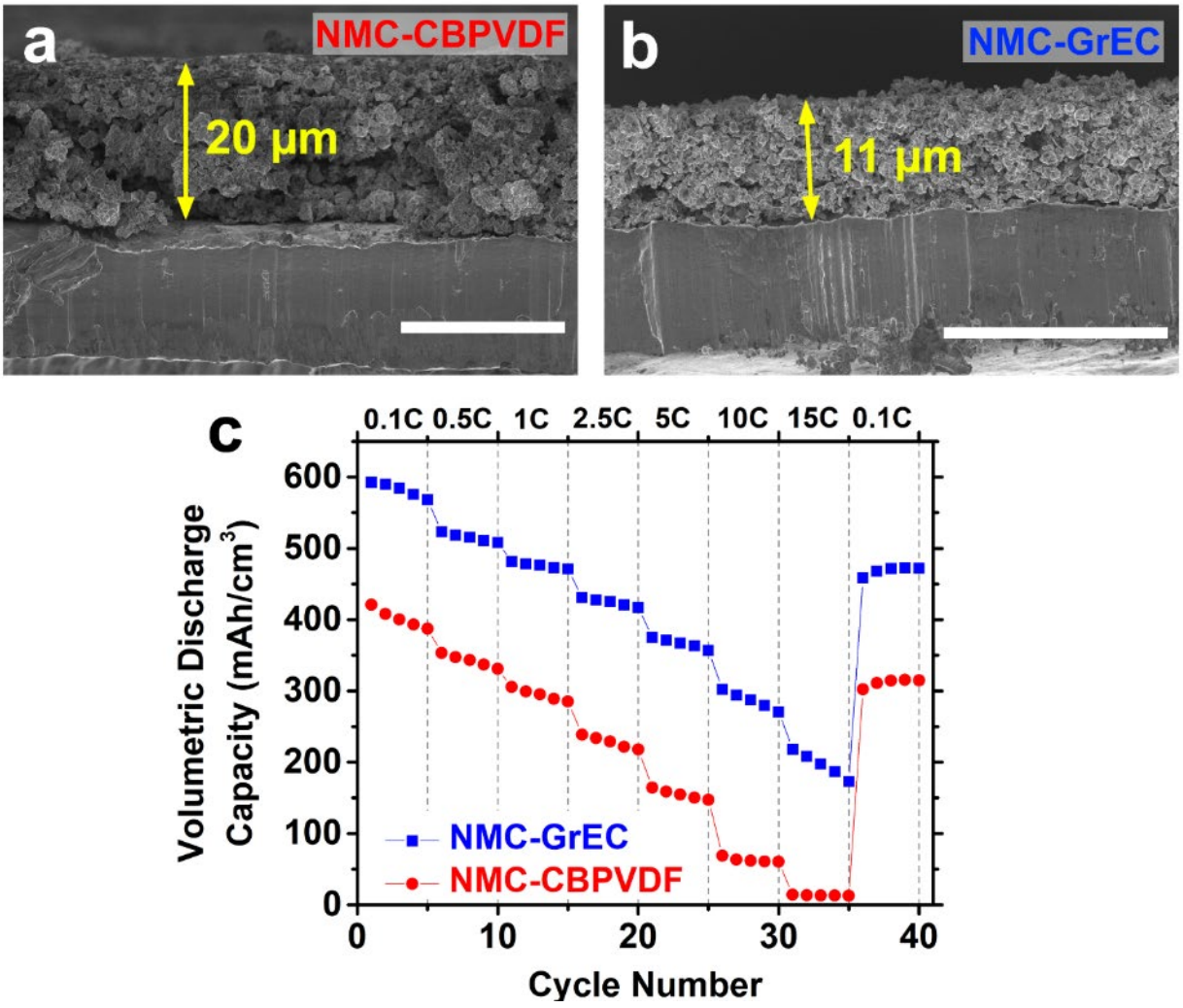


**Figure 3.22.** Cross-sectional SEM images of the pristine (a) NMC-CBPVDF electrode and (b) NMC-GrEC electrode, showing electrode compaction effects due to the use of graphene as the conductive additive rather than carbon black. Both scale bars are 20 µm. (c) Volumetric rate capability for the two electrodes between 2.0 V and 4.8 V vs. $Li/Li^+$.

## 3.6 Summary

This chapter described how a conformal graphene coating comprehensively enhanced the high-voltage electrochemical performance of NMC cathode materials, including significantly improved cycle life, increased coulombic efficiency, and slower impedance growth. XPS analysis revealed that graphene-coated NMC electrodes exhibited reduced spectral intensities corresponding to electrolyte decomposition products, suggesting that the interfacial graphene layer minimized parasitic interactions between the electrode and electrolyte. Postmortem electron microscopy showed that the cycling improvements were also related to suppressed mechanical degradation, evidenced by fewer signs of cracking and electrochemical creep for the graphene-coated NMC particles. This observation was consistent with fewer changes in the crystallite size and microstrain values obtained from Rietveld refinement following high-resolution SR-PXRD. Therefore, the conformal graphene coating likely enabled spatially uniform charge transfer reactions across the particle surface, delocalizing cycling-induced stress that can initiate mechanical degradation. Overall, this chapter highlighted the importance of the relationships among interfacial coating layers, lithiation dynamics, and chemomechanical degradation of the active material, which is highly relevant for the development of systematic engineering strategies aimed at improving the performance of high-voltage LIB electrode materials.

## 3.7 Experimental Methods

### *3.7.1 NMC Synthesis*

A solid-state co-precipitation method was used to synthesize the NMC532 active material. Ni (II) acetate tetrahydrate, Mn (II) acetate tetrahydrate, and Co (II) acetate tetrahydrate precursors (MilliporeSigma) were dissolved in deionized water in a 5:3:2 molar ratio, yielding a 0.2 M transition metal precursor solution. At the same time, oxalic acid dihydrate (MilliporeSigma) was dissolved in deionized water to form a 0.1 M solution of oxalic acid. After 10 minutes of stirring at 300 RPM, the oxalic acid solution was added dropwise to precipitate the precursors from the solution. The mixture was then further stirred at 300 RPM for 3 hours before the water was evaporated using a rotary evaporator (Buchi Rotavapor R-300 System). The resulting powder was dried overnight under dynamic vacuum at 80°C, and then subsequently calcined at 450°C under 50 sccm of flowing oxygen for 6 hours using a tube furnace (Thermo Scientific Lindberg Blue M). After the powder cooled to room temperature, lithium hydroxide monohydrate (MilliporeSigma) was added in 3 mol% excess and uniformly mixed into the powder using a mortar and pestle. The final powder mixture was calcined under flowing oxygen at 550°C for 8 hours, and then was subsequently heated to 850°C for 12 hours, ultimately yielding stoichiometric NMC532. All ramp rates used were 5°C/min.

### *3.7.2 Graphene Exfoliation*

The graphene/ethyl cellulose (graphene/EC) powder was prepared by mixing 100 g of 150 mesh flake graphite (MilliporeSigma), 6 g of ethyl cellulose powder (4 cP, MilliporeSigma), and

1 L of 200-proof ethanol (Decon Labs) using a Silverson L5M-A shear mixer for 2 hours at 10,230 RPM. Large, unexfoliated graphite flakes were removed from the dispersion by centrifuging at 7,500 RPM for 20 minutes using a Beckman Coulter J26 XPI centrifuge. Following centrifugation, the supernatant was harvested and flocculated by adding a solution of NaCl in water (0.04 g/mL) to reach a final ratio of 1.74:1 graphene dispersion:sodium chloride solution. This mixture was then centrifuged again at 7,500 RPM for 7 minutes to sediment the graphene/ethyl cellulose powder. The powder was collected, thoroughly rinsed with deionized water to remove residual sodium chloride, vacuum filtered, and dried under an infrared lamp overnight. Thermogravimetric analysis revealed that the resulting powder possessed a graphene fraction of approximately 33 wt.%.

### *3.7.3 Electrode Fabrication*

The NMC-CPBVDF electrode slurry was prepared by homogeneously mixing a 90:5:5 weight ratio of NMC, Super P (Alfa Aesar), and polyvinylidene fluoride (PVDF, MTI Corporation) with N-Methyl 2-pyrrolidone (NMP, MilliporeSigma) using a centrifugal mixer (Thinky USA). To promote better homogeneity and viscosity in the electrode slurry, PVDF was first mixed with NMP at 80°C overnight to form a 6 wt.% solution. To fabricate the graphene electrodes (NMC-GrEC), graphene/EC powder and multiwalled carbon nanotubes (MWCNT, MilliporeSigma) were dispersed in ethanol for 1 hour using a Fisher Scientific Sonic Dismembrator Model 500 set at a power output of 40 W. To match the carbon content of the control electrode (i.e., 5% conductive carbon), a 95:4.5:0.5 ratio of NMC, graphene, and MWCNT was used. Here, a small amount of MWCNT was added to improve the mechanical integrity of the

binder-free electrode. Additionally, since prior work found that only 0.5 wt% of graphene is needed to conformally coat $LiNi_{0.8}Co_{0.15}Al_{0.05}O_2$ secondary particles,[188] 4.5 wt% of graphene was used in this work to ensure that all primary particle surfaces were coated. Any remaining graphene flakes formed a composite with the graphene-coated NMC particles that promoted charge transport within the electrode.

To promote better homogeneity and slurry stability during electrode casting, a solvent exchange with NMP was performed. NMP was added to the graphene/EC-MWCNT-ethanol dispersion, and the ethanol was subsequently removed by stirring the graphene/EC-MWCNT-NMP-ethanol solution on a hot plate set at 70°C. Following the solvent exchange, NMC powder was annealed at 250°C for 1 hour in flowing oxygen, and then mixed with the exfoliated graphene/EC-MWCNT solution using a centrifugal mixer (Thinky, USA). Both slurries were cast onto aluminum foil and dried at 120°C in a convection oven, followed by a second drying step at 80°C under dynamic vacuum. Although the NMC-GrEC electrode contained no additional polymeric binder, the MWCNTs and the conductive carbon residue formed by the decomposition of the ethyl cellulose together acted as the binding components in the electrode. Consequently, no film delamination was observed during casting and drying, which was consistent with previous reports.[180,190] The average active material loadings for both the NMC-CBPVDF and the NMC-GrEC electrodes were maintained at ~3 mg $cm^{-2}$. Electrode discs were punched out and calendered with approximately 6 MPa applied pressure. A micrometer (Mituyo) was used to measure the thickness of the electrodes. For NMC-GrEC electrodes, ethyl cellulose was removed from the electrodes via thermal annealing at 250°C in flowing oxygen for 1 hour. 2032-type two-electrode coin cells were assembled in an Ar glovebox (VAC Omni-Lab) versus a lithium (Alfa Aesar)

counter electrode and 1 M $LiPF_6$ in 1:1 vol/vol ethylene carbonate/ethyl methyl carbonate (EC/EMC, MilliporeSigma) as the electrolyte. The separator used was Celgard 2325.

### *3.7.4 Electrochemical Characterization*

Galvanostatic cycling was performed between 2.0 V and 4.8 V vs. Li/Li+ using an Arbin LBT-20084 battery cycler. Prior to cycling at 0.5C, electrodes were activated using a 0.1C constant current-constant-voltage (CCCV) protocol. Specifically, after a galvanostatic step, cells were held at the respective cutoff voltage until the current reached C/20. Rate capability tests were performed using a constant charge-fast discharge protocol. Electrochemical impedance spectroscopy measurements were performed on fully charged electrodes using a Bio-Logic VSP potentiostat between 1 MHz and 1 mHz. Distribution of relaxation times analysis was performed using the DRTtools MATLAB toolbox.[263]

### *3.7.5 Raman Spectroscopy*

Raman spectra were collected with a Horiba Scientific XploRA PLUS Raman microscope with a 532 nm laser excitation wavelength at 16.75 mW laser power and an 1800 g/mm grating for 20 seconds.

### *3.7.6 X-Ray Diffraction*

Synchrotron radiation powder X-ray diffraction (SR-PXRD) experiments were carried out on Beamline 5-BMC at the Advanced Photon Source (APS) at an energy of 19.97 keV ($\lambda = 0.6208$ Å). After cycling, NMC powder was harvested from cycled electrodes inside an Ar glovebox. The

powders were then transferred into capillaries and sealed shut. During acquisition, the capillaries were continuously rotated about a horizontal axis. The incoming X-ray beam spot size was 2 × 8 $mm^2$. The powder diffractometer was employed in a high-resolution Bragg-Brentano geometry with a double bounce pseudo-channel-cut crystal configuration of two Si(111) crystals. In the detector arm, an anti-scatter flight tube followed by Soller slits with a vertical blade were employed to limit horizontal axial divergence. To improve resolution, a Ge(220) analyzer crystal was utilized before acquiring the signal with an Oxford Cyberstar scintillation counter. Rietveld analysis was performed with GSAS-II software.[264] The refined parameters were the lattice constants (*a* and *c*), sample displacement, crystallite size and microstrain (both isotropic), and the Ni in Li site fraction. The standard reference material $LaB_6$ was utilized to obtain the appropriate instrument profile parameters of the setup.

### *3.7.7 Inductively Coupled Plasma Mass Spectrometry*

To analyze the transition metal ratio of the synthesized NMC, a small amount of synthesized NMC powder was added directly into a 50/50 mixture of trace-grade nitric acid and hydrochloric acid. After complete digestion of the powder overnight at 65°C, ultrapure water was added to dilute the solution to a 4% (v/v) acid concentration in a sample volume of 10 mL. To quantify transition metal dissolution in pristine samples, NMC-GrEC and NMC-CBPVDF electrodes with the same active material mass loading were each immersed in 1 mL of 1 M $LiPF_6$ in 1:1 vol/vol ethylene carbonate/ethyl methyl carbonate (EC/EMC, MilliporeSigma), sealed under argon, and placed in an oven at 60°C. Two replicates were made for each sample. After seven days, the electrolyte was harvested and digested overnight using trace-grade nitric acid in a water

bath set at 65°C. Following digestion, the solution was diluted to a 3% (v/v) acid concentration in a 5 mL sample volume. All ICP analysis was performed using a ThermoFisher iCAP Q ICP-MS.

### *3.7.8 X-Ray Photoelectron Spectroscopy*

Postmortem X-Ray photoelectron spectroscopy measurements were performed using a Thermo Scientific ESCALAB 250 Xi+ system (Al Kα radiation, ~1486.6 eV) at a pressure of ~5 × $10^{-8}$ Torr. Acquisition was performed using a 900 μm spot size. Samples were charge compensated with a flood gun. To prepare samples for XPS analysis, coin cells were disassembled inside an Ar glovebox and thoroughly rinsed with dimethyl carbonate. After drying on a hot plate inside the glovebox at 120°C for 48 hours, the electrodes were transferred into the XPS analysis chamber using a sealed transfer vessel to prevent ambient exposure. All peaks were charge corrected to adventitious carbon at ~284.8 eV.

### *3.7.9 Scanning Electron Microscopy*

Scanning electron microscopy was performed using a Hitachi SU8030 SEM. Cross-sectional samples were prepared by immersing electrode discs in liquid nitrogen for 20 seconds prior to cleaving with a razor blade. The electrochemical creep and fracture analysis was performed at various points across the surfaces of the NMC-CBPVDF and NMC-GrEC electrodes to ensure that representative statistics were acquired. Approximately 2,000 particles were assessed for electrochemical creep and fracture in both electrode compositions. Particles were considered to be fractured if the gap distance formed by particle fracture was ~10 nm or greater. Similarly, particles were considered to have experienced electrochemical creep only if a terraced morphology was

evident on the surface. Since a thick layer of graphene flakes could obfuscate the NMC surface during SEM analysis, both electrodes were slightly scratched using a razor blade to allow imaging of particles buried in the interior of the electrode. Particle surfaces on both the NMC-CBPVDF and NMC-GrEC electrodes were then analyzed in various regions on the electrode surface and subsurface.

### *3.7.10 Scanning Transmission Electron Microscopy*

Electrodes were prepared for scanning transmission electron microscopy (STEM) analysis by focused ion beam (FIB) milling on a FEI Helios Nanolab SEM/FIB. STEM investigations were performed using a JEOL JEM ARM200CF aberration-corrected STEM that was operated at 200 kV.

# CHAPTER 4:

# ENABLING AMBIENT STABILITY OF $LiNiO_2$ LITHIUM-ION BATTERY CATHODE MATERIALS VIA GRAPHENE-CELLULOSE COMPOSITE COATINGS

This chapter is a preprint version of an article that has been submitted for publication in *Chemistry of Materials*.

## 4.1 Overview

Nickel-rich layered oxides are widely used as cathode materials for energy-dense lithium-ion batteries. These chemistries, based on the parent compound $LiNiO_2$ (LNO), are highly sensitive to ambient environments and are known to readily react with moisture and carbon dioxide. As a result, impurities such as lithium hydroxides and lithium carbonates are formed at the LNO surface, compromising electrochemical behavior. Here, we address this issue by coating LNO cathode particles with a hydrophobic barrier layer composed of graphene and ethyl cellulose (GrEC). This coating limits contact between atmospheric moisture and the LNO surface, which minimizes the generation of lithium impurities. This scheme is evaluated by exposing coated LNO to humidified $CO_2$ for 24 hours as an accelerated ambient degradation test. Subsequent spectroscopy, microscopy, and electrochemical characterization show no detectable signatures of carbonates on the LNO surface, thus verifying that the GrEC coating prevents ambient degradation. By demonstrating this methodology for the ultimate nickel-rich chemistry, this approach can likely be generalized to a wide range of ambient-sensitive battery materials.

## 4.2 Background

Lithium-ion batteries (LIBs) are playing a key role in the societal transition towards clean energy by serving as the technology of choice to power electric vehicles and grid-level energy storage.[37] Current and emerging engineering applications demand battery packs with increasingly higher energy densities and longer lifetimes, necessitating intelligent materials selection of electrochemically active materials. For LIB cathode materials, Ni-rich layered oxide chemistries provide a pathway to address this need since they possess intrinsically high energy

densities and lifetimes that can be tuned with careful control over transition metal content and operational states of charge.[35,265] Incumbent Ni-rich LIB cathode materials include $LiNi_{0.8}Mn_{0.1}Co_{0.1}O_2$ (NMC811), $LiNi_{0.6}Mn_{0.2}Co_{0.2}O_2$ (NMC622), and $LiNi_{0.8}Co_{0.15}Al_{0.05}O_2$ (NCA), which are isostructural to the parent compound $LiNiO_2$ (LNO). The addition of dopant elements in these multicomponent lithium transition metal oxides (e.g., Mn, Co, and Al) helps increase cycling longevity. Nevertheless, these materials still show instabilities that can be traced back to the chemical reactivity of Ni.

Beyond cycling stability, recent work on Ni-rich LIB cathode materials has sought to understand and mitigate their high sensitivity to ambient conditions. Ni-rich layered oxides are known to readily react with atmospheric moisture and $CO_2$,[106] forming LiOH on the oxide surface. The current understanding of this ambient degradation pathway involves two mechanisms, both requiring water as a reactant. One proposed mechanism involves moisture-catalyzed transition metal reduction reactions, which are favorable due to the inherent reactivity of $Ni^{3+}$ compared to $Ni^{2+}$.[113,266-268] This pathway results in partial delithiation near the surface, with lithium sequestered in hydroxide deposits. A second proposed mechanism for the formation of LiOH involves $H^+$-$Li^+$ site exchange upon exposure to water, which has been well-documented as a consequence of washing Ni-rich layered oxides to remove undesirable lithium residues after synthesis.[269-271] After LiOH forms, it then readily reacts with ambient $CO_2$, forming species such as $LiHCO_3$ or $Li_2CO_3$.[113] Lithium bicarbonates can further react with LiOH to form $H_2O$ and $Li_2CO_3$ byproducts in an autocatalytic feedback loop. Following prolonged exposure to ambient conditions, where the supply of $CO_2$ is effectively unlimited, lithium

carbonate impurities are continuously generated until the available cathode surface area is depleted of reaction sites.

Surface hydroxides and carbonates are highly undesirable since they are detrimental to both electrochemical performance and cell manufacturing. Lithium impurities reduce first-cycle capacity due to their low electronic and ionic conductivities, causing increased electrode polarization and charge transfer impedance.[113,272-274] Furthermore, lithium carbonates on cathode surfaces promote electrolyte oxidation reactions and generate gas products during cycling, which compromise long-term cycle life.[107,108,113,275-277] At sufficiently high concentrations, surface hydroxides and carbonates are also known to cause slurry gelation, compromising electrode coating procedures that require strict control of slurry viscosity.[104,114,278] Therefore, these surface species are typically removed from cathode powders prior to slurry mixing using methods such as acid treatments,[210,279,280] washing,[107,281] annealing,[113,190,276,282] and chemical conversion of lithium impurities.[280,283,284]

A more attractive strategy is to inhibit the formation of surface hydroxides and carbonates altogether. Consequently, industrial facilities employ large dry rooms with tight limits on internal dew points for the storage and handling of Ni-rich LIB cathode powders. Since the operation of these dry rooms are expensive and energy-intensive,[285] strategies for preserving high-quality cathode surfaces in ambient conditions are of high interest to ease the demand for strict environmental control. One promising approach is to utilize hydrophobic coatings that prevent direct contact between ambient moisture and Ni-rich oxide surfaces.[105,286] Since the coating layer must also be electrochemically inert and transparent to lithium ions, compatible coating materials are highly limited and rarely employed in practice. To circumvent these

restrictions, it would be ideal if LIB cathode surfaces could be protected with a barrier layer that could be removed on demand prior to electrochemical cycling.

This chapter describes a scheme to address the aforementioned issues of ambient-reactive Ni-rich layered oxides by utilizing a hydrophobic coating layer composed of graphene and ethyl cellulose (GrEC). This scheme is demonstrated for LNO since it represents the Ni-rich limit with the highest ambient sensitivity in the family of Ni-rich layered oxides.[106,287,288] Ethyl cellulose (EC) is an attractive materials choice since it is hydrophobic[289-292] and can be scalably coated onto cathode material surfaces via solution-phase methods. EC can also be pyrolyzed thermally[201] or photonically,[172] enabling its removal immediately preceding electrochemical cycling. Notably, when this pyrolysis occurs in the presence of graphene, EC is known to decompose into low molecular weight aromatic carbon products, yielding carbonaceous residues with high $sp^2$ content that improves charge transport.[56,140,171,179,180,188,190,238] GrEC coatings therefore enable both long-term ambient storage and exceptional electrochemical performance for Ni-rich LIB cathode powders.

## 4.3 Impact of Humid $CO_2$ Exposure

LNO powder was synthesized via a hydroxide co-precipitation and calcination method, yielding secondary particles of LNO approximately 10 μm in diameter (**Figure 4.1**). These agglomerates were composed of individual LNO grains, which each exhibited a smooth surface morphology (**Figure 4.2a**) immediately after particle synthesis. After 24 hours of exposure to humidified $CO_2$, the LNO surface became rough, with jagged features that rendered individual grains indistinguishable from one another (**Figure 4.2b** and **Figure 4.3**). This transformation was indicative of degradation induced by the humid $CO_2$ exposure and was consistent with surface

changes observed in other Ni-rich cathode systems.[105,207,281,282] To further investigate the chemical changes associated with this apparent surface morphological transformation, the degraded samples were interrogated with Raman spectroscopy, diffuse reflectance infrared Fourier transform spectroscopy (DRIFTS-FTIR), and X-ray photoelectron spectroscopy (XPS).

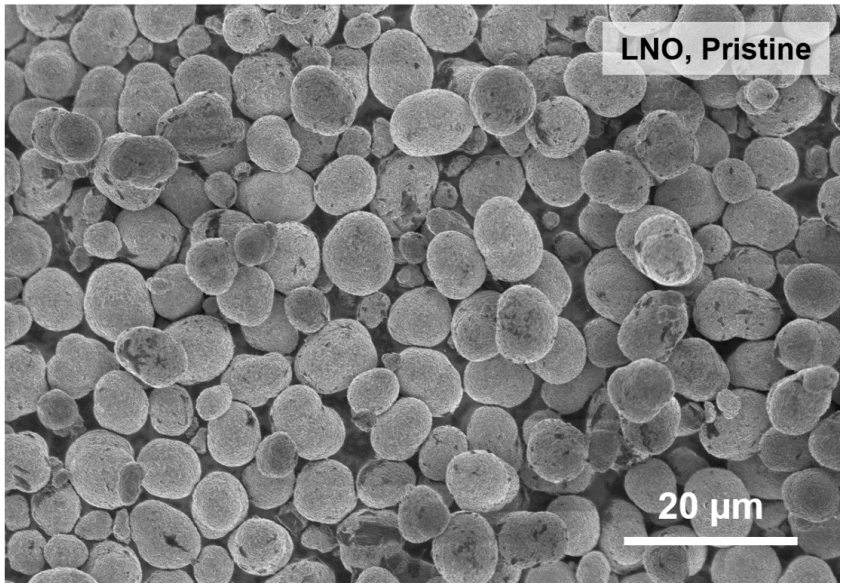


**Figure 4.1.** Scanning electron microscope image of pristine LNO.

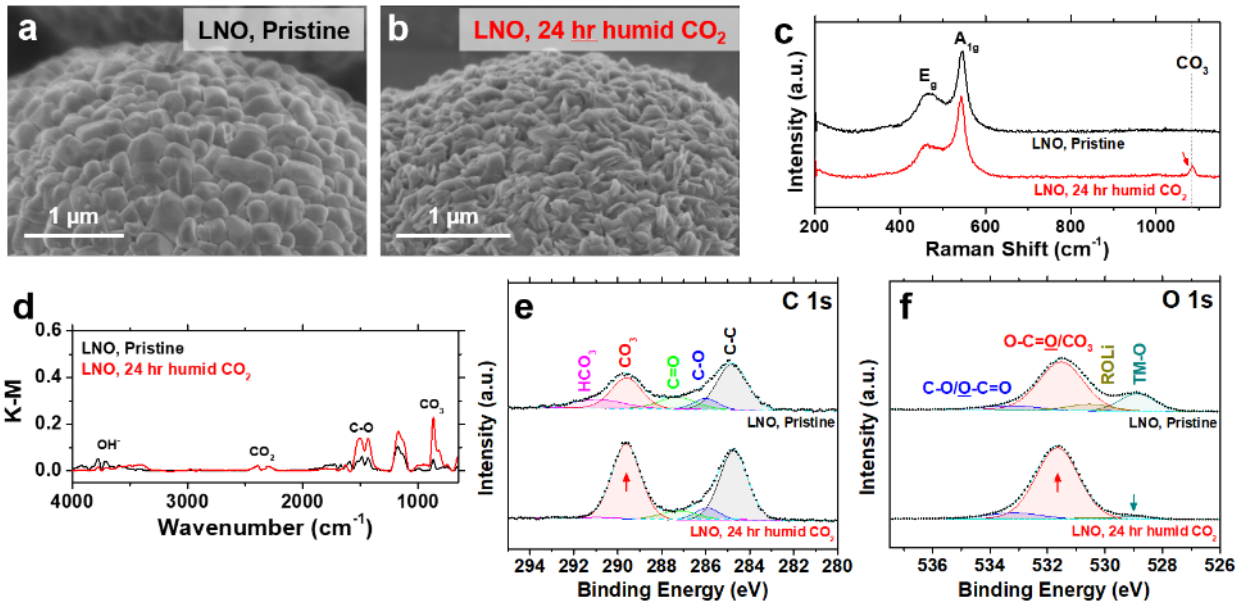


**Figure 4.2.** LNO exposed to humid $CO_2$ for 24 hours exhibits severe morphological and surface chemical changes. (a-b) Scanning electron microscopy images of (a) pristine LNO and (b) LNO after being exposed to humid $CO_2$ for 24 hours. (c) Raman, (d) DRIFTS-FTIR, (e) XPS C 1s, and (f) XPS O 1s spectra show the growth of surface carbonate species after exposure to humid $CO_2$.

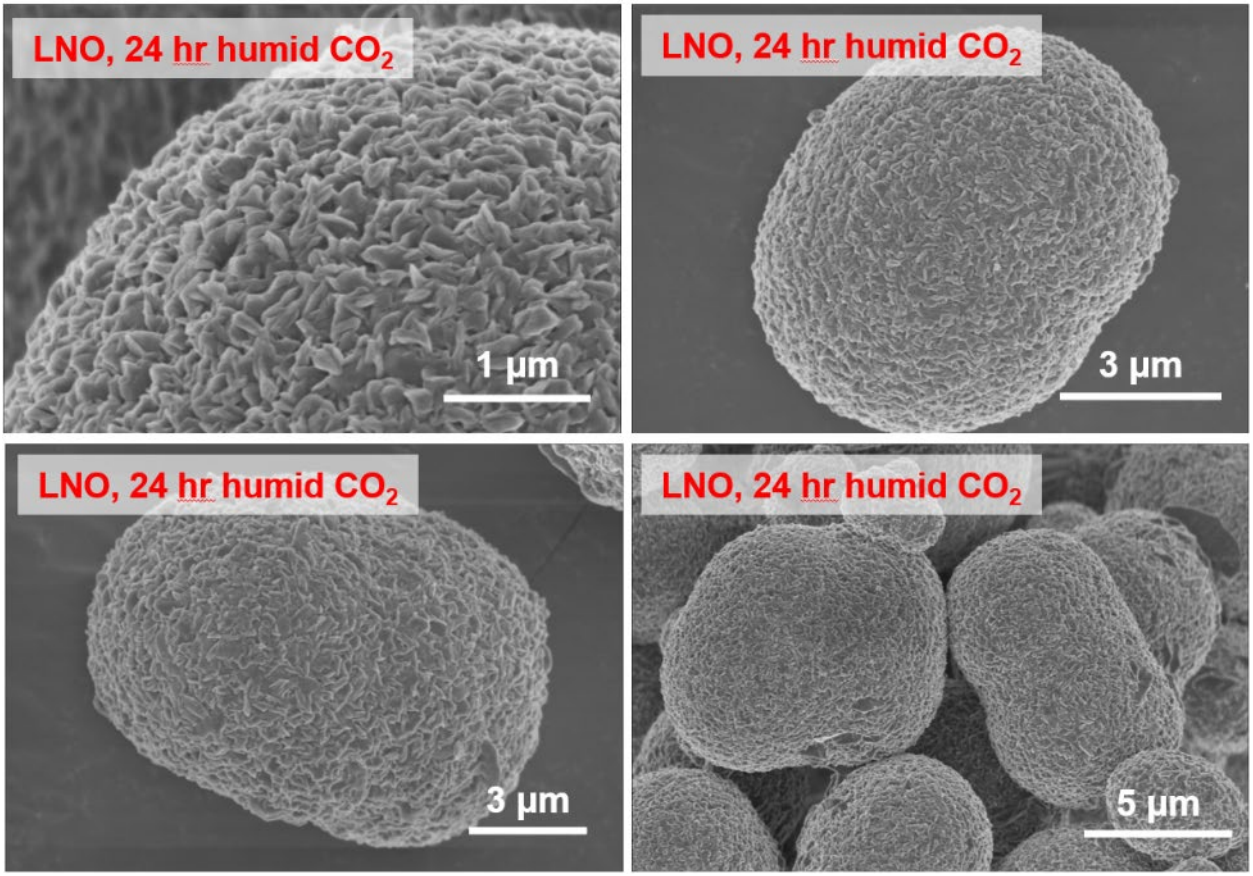


**Figure 4.3.** Scanning electron microscope images of LNO particles after exposure to humid $CO_2$ for 24 hours.

Raman spectroscopy of the pristine LNO showed peaks that were assigned to the Ni-O $A_{1g}$ (540 $cm^{-1}$) and the $E_g$ (460 $cm^{-1}$) vibrational modes (**Figure 4.2c, top**),[106,274,293] with no other peaks clearly present. Surface-sensitive DRIFTS-FTIR revealed spectral intensities at wavenumbers consistent with C-O stretching (1500 $cm^{-1}$ and 1435 $cm^{-1}$) and $CO_3$ bending (865 $cm^{-1}$) (**Figure 4.2d**), which suggest that organic species and lithium carbonate impurities were weakly present. To further interrogate these surface species, XPS was used to carefully identify the chemical nature of the pristine LNO surface. The XPS C 1s spectrum was fit with component peaks assigned to

adventitious C-C bonding at 284.8 eV, C-O bonding at 286 eV, and C=O at 287.3 eV (**Figure 4.2e, top**). At higher binding energies, spectral intensities were observed and fit to lithium impurities $CO_3$ and $HCO_3$ at 289.6 eV and 290.9 eV, respectively. Meanwhile, the O 1s spectrum was fit with component spectra assigned to Ni-O bonding at 528.9 eV, ROLi bonding at 530.5 eV, O-C=O/$CO_3$ bonding at 531.5 eV, and C-O/O-C=O bonding at 533.2 eV (**Figure 4.2f, top**). Taken together, these spectroscopic results suggested that the pristine LNO was relatively clean, containing surface organic species and carbonate impurities that are generally expected for Ni-rich layered oxides following synthesis.[276]

Exposure of the LNO to humid $CO_2$ induced significant spectroscopic changes, which allowed chemical identification of the morphological changes observed in SEM. First, Raman spectroscopy (**Figure 4.2c, bottom**) showed the emergence of a peak at 1080 $cm^{-1}$ that was spectrally consistent with prior reports of carbonate vibrations in Ni-rich cathodes.[106,274,293] Second, DRIFTS-FTIR (**Figure 4.2d**) revealed that spectral intensities assigned to C-O stretching (1500 $cm^{-1}$ and 1430 $cm^{-1}$) and out-of-plane $CO_3$ bending (865 $cm^{-1}$) increased following exposure to humid $CO_2$, which is consistent with an increase in carbonate species on the LNO surface.[207,209,274,276,286,293] Finally, the XPS C 1s spectrum revealed an increase in the carbonate spectral intensities after exposure to humid $CO_2$ (**Figure 4.2e, bottom**), while the XPS O 1s spectrum revealed that the carbonate spectral intensities increased simultaneously with decreased transition metal-oxygen (TM-O) bonding intensities (**Figure 4.2f, bottom**). Since these TM-O spectral intensities originate from Ni-O bonding in LNO, these results suggested that an additional carbonate-rich layer is formed on the LNO surface during exposure to humid $CO_2$.

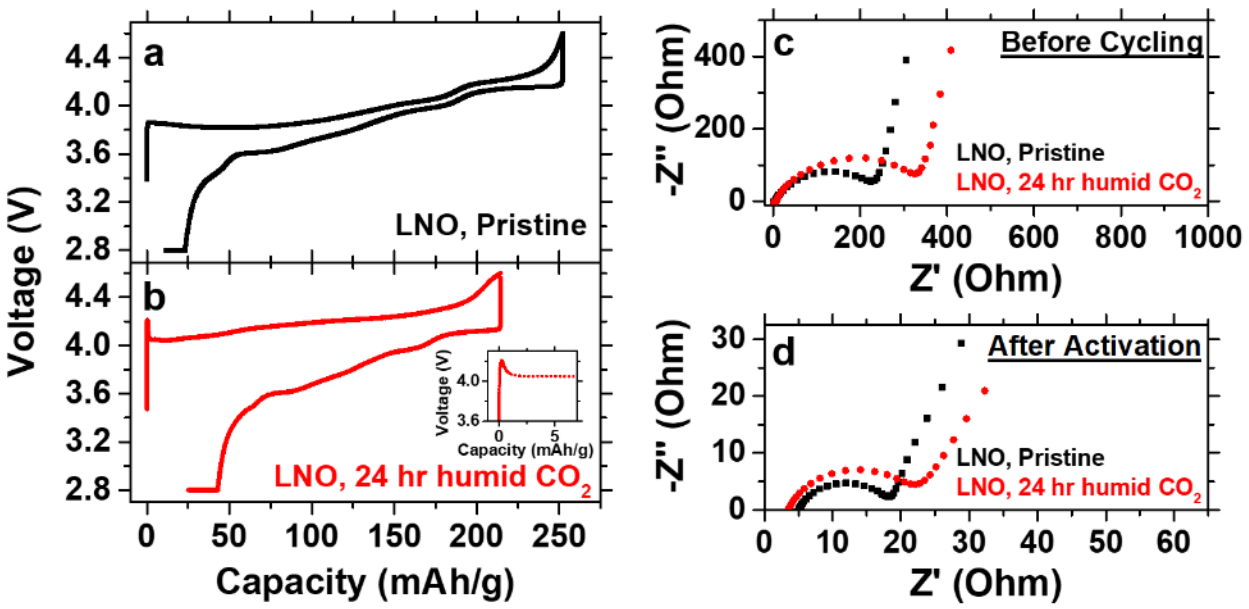


**Figure 4.4.** Electrochemical performance of uncoated LNO before and after humid $CO_2$ exposure. (a-b) Activation cycles of (a) pristine LNO and (b) LNO exposed to humid $CO_2$. Activation was performed at C/10 with a constant voltage hold at 2.8 V vs. $Li/Li^+$ until the current reached C/20. The inset in (b) shows a magnified view of the voltage peak present at the initial delithiation shoulder of LNO. (c-d) Nyquist plots (c) before cycling and (d) after activation for pristine LNO and LNO exposed to humid $CO_2$.

Humid $CO_2$ exposure severely degraded the electrochemical performance of uncoated LNO, which was evident in the initial activation cycle. As a baseline, the pristine LNO achieved an initial charge capacity of 252 mAh $g^{-1}$ and a discharge capacity of 240 mAh $g^{-1}$, with low polarization during the charge-discharge process (**Figure 4.4a**). In contrast, the LNO exposed to humid $CO_2$ exhibited severe charge-discharge polarization, resulting in a low charge capacity of 214 mAh $g^{-1}$ and a corresponding discharge capacity of 189 mAh $g^{-1}$ (**Figure 4.4b**), which were ~15% and ~21% lower than the pristine LNO charge and discharge capacities, respectively. The shape of the initial charge process provided an additional signature of the carbonate impurities that were generated during humid $CO_2$ exposure. The initial delithiation voltage for LNO is known to occur at approximately 3.7 V vs. $Li/Li^+$, which was observed for pristine LNO. However, the

voltage shoulder for LNO exposed to humid $CO_2$ was measured at approximately 4.0 V vs. $Li/Li^+$, corresponding to a ~300 mV overpotential. Moreover, above this voltage shoulder, a peak was evident (**Figure 4.4b, inset**), which has been observed previously and is characteristic of the electrochemical removal of impurity species on the LNO surface.[106,209,282] This feature was not present in the voltage profile for pristine LNO.

The increase in electrode polarization was also assessed via electrochemical impedance spectroscopy (EIS) and equivalent circuit modeling using a Randles circuit (**Figure 4.4c-d** and **Figure 4.5**). Before activation, the charge transfer resistance was higher for the cell fabricated with LNO exposed to humid $CO_2$ (313.2 Ω) compared to pristine LNO (213.8 Ω). These results indicated that the surface layer of impurities that formed during humid $CO_2$ exposure was detrimental to the initial electrochemical behavior and further corroborated the observed polarization increase in the voltage-capacity plots of the initial cycle. After activation, the cell fabricated with LNO exposed to humid $CO_2$ had a higher measured charge transfer resistance (17.2 Ω) compared to pristine LNO (12.1 Ω), suggesting that lithium impurities negatively impact cell behavior beyond the initial activation protocol.

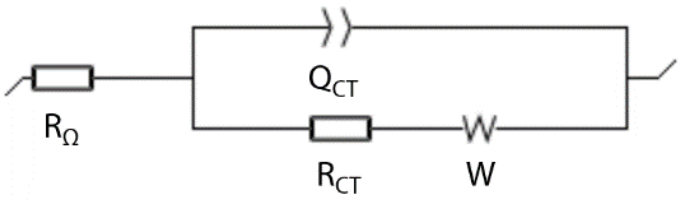


**Figure 4.5.** The equivalent circuit model (Randles circuit) used to fit the impedance data.

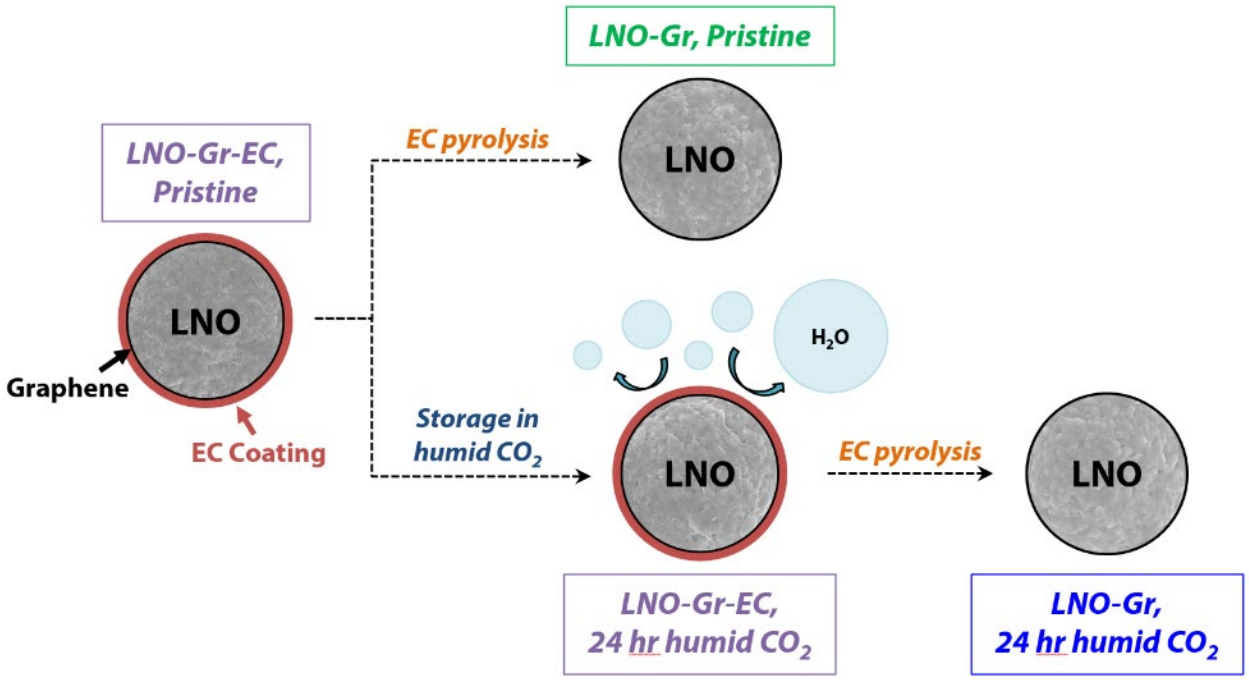


**Figure 4.6.** A hydrophobic GrEC coating protects the LNO surface from ambient degradation.

## 4.4 Behavior of Graphene-Coated LNO

To address the issue of ambient-induced degradation, LNO particles were encapsulated with a protective barrier layer to preserve the pristine surface state. Since the ambient degradation of Ni-rich layered oxides requires the presence of both moisture and $CO_2$,[113,276] limiting the availability of moisture via an external, hydrophobic barrier layer is a promising strategy for preventing the formation of surface carbonates and hydroxides.[105,286] Towards this end, LNO particles were encapsulated with a GrEC coating (**Figure 4.6**). Graphene and ethyl cellulose (EC) were selected in this context due to their inherent hydrophobic character[289-292] and combined ability to form a conformal coating on particles. In particular, the EC filled in gaps between the graphene nanoflakes, ensuring that the LNO particles were uniformly encapsulated and protected from ambient degradation. Since EC is electrically insulating, it is removed via a low-temperature

pyrolysis step prior to electrochemical testing, which decomposes the EC into low molecular weight aromatic carbon with high $sp^2$ character.[238] These carbonaceous residues bridge the graphene flakes, thus creating a percolating electronically conductive network throughout the electrode that aided charge transport as has been previously demonstrated for other Ni-rich cathodes such asNMC532,[140] NCA,[188,190] and LNO.[56]

Experimentally, LNO particles were coated by homogeneously combining a GrEC dispersion in N-methyl-2-pyrrolidone (NMP) with LNO powder using a centrifugal mixer. A subsequent solvent removal step yielded LNO-Gr-EC, where the graphene and EC formed a uniform coating on the LNO surface (**Figure 4.7a**). The LNO-Gr-EC was then subjected to 24 hours of exposure to humid $CO_2$ and examined for changes to the particle surface morphology. SEM showed that the GrEC coating successfully preserved the quality of the LNO surface during the humid $CO_2$ exposure, as evidenced by the lack of changes to the secondary particle shape (**Figure 4.7b**). Individual primary particles of LNO were visible below the thin coating layer and exhibited no discernable changes in surface morphology, in contrast to the uncoated LNO exposed to humid $CO_2$ (**Figure 4.2b**). Since any exposed LNO surfaces would rapidly react and form impurity species under these humid $CO_2$ exposure conditions, the SEM images suggested that the GrEC coating was conformal and free of pinhole defects.

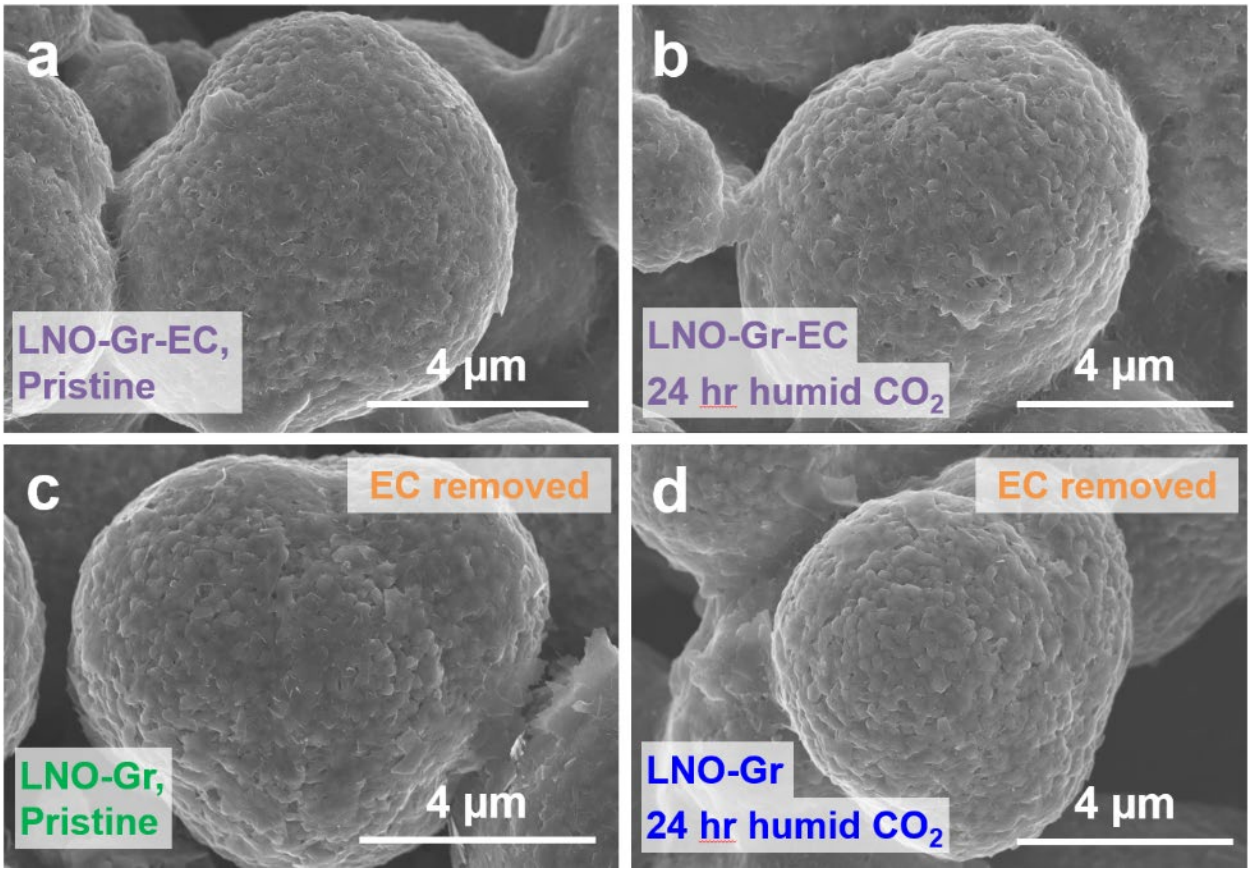


**Figure 4.7.** Scanning electron microscopy images show no changes in the surface morphology of the GrEC-coated LNO after 24 hours of exposure to humid $CO_2$. (a) As-coated LNO-Gr-EC, (b) coated LNO-Gr-EC after 24 hours of exposure to humid $CO_2$, (c) LNO-Gr obtained by pyrolyzing LNO-Gr-EC, and (d) LNO-Gr obtained by pyrolyzing LNO-Gr-EC after 24 hours of exposure to humid $CO_2$.

In preparation for electrochemical cycling and spectroscopic analysis, the EC layer was removed from the system by heating the LNO-Gr-EC in flowing $O_2$ to 300°C, yielding LNO-Gr. The EC pyrolysis was conducted on as-coated samples (LNO-Gr, **Figure 4.7c** and **Figure 4.8**), as well as samples that were coated and then exposed to humid $CO_2$ for 24 hours (LNO-Gr, 24 hr humid $CO_2$, **Figure 4.7d** and **Figure 4.9**). Raman spectroscopy indicated that the graphene D/G ratio decreased after this heating step, confirming decomposition of EC (**Figure 4.10**).[140,171,190] The coating uniformity and quality were invariant even after thermal pyrolysis of the EC,

demonstrating that this scheme was robust and yielded active materials that were compatible with subsequent electrode fabrication procedures.

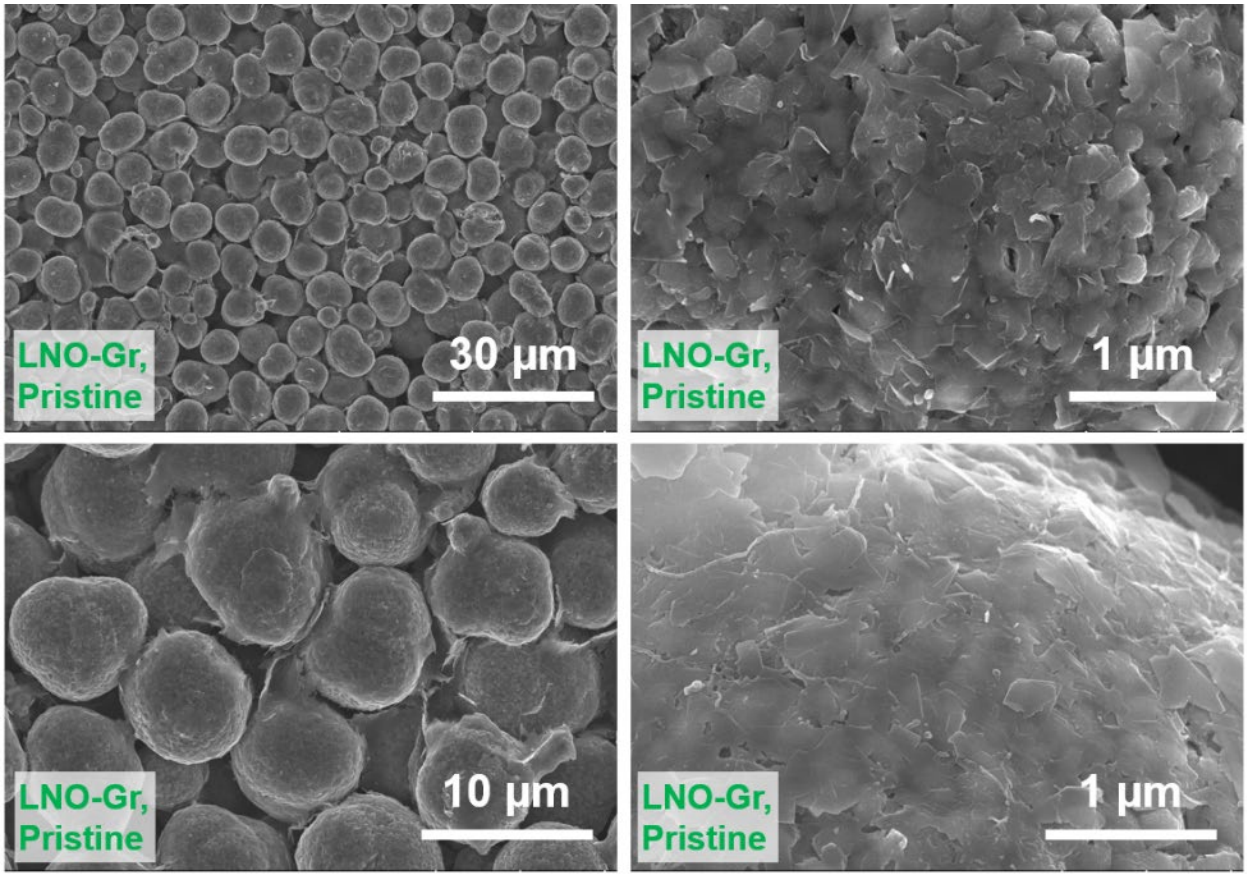


**Figure 4.8.** SEM images of the LNO-Gr sample showing a uniform graphene coating on the LNO particles. Prior to obtaining these images, ethyl cellulose was pyrolyzed at 300°C for 1 hour in flowing $O_2$.

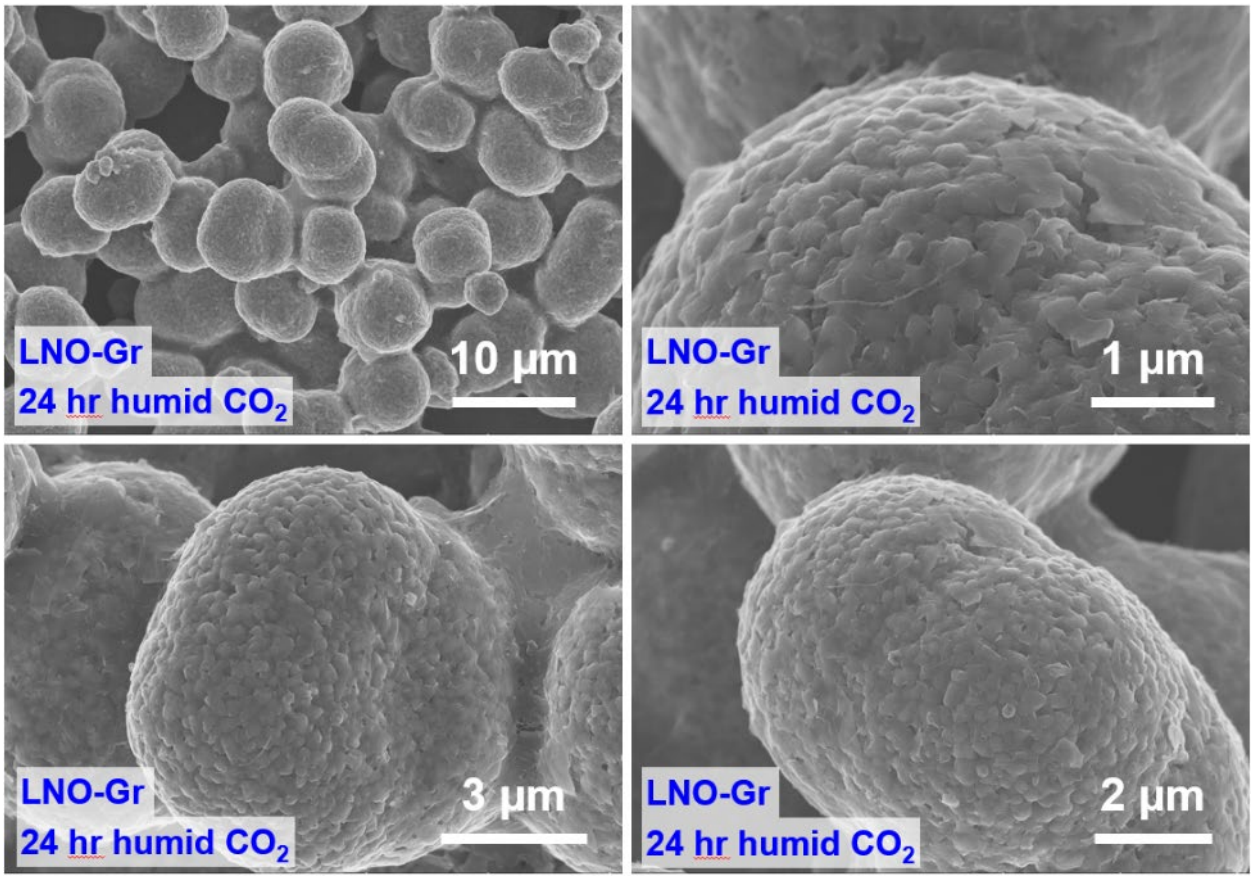


**Figure 4.9.** SEM images of the LNO-Gr sample after exposure to humid $CO_2$ for 24 hours, showing no evidence of surface morphological changes. Prior to obtaining these images, the ethyl cellulose was pyrolyzed at 300°C for 1 hour in flowing $O_2$.

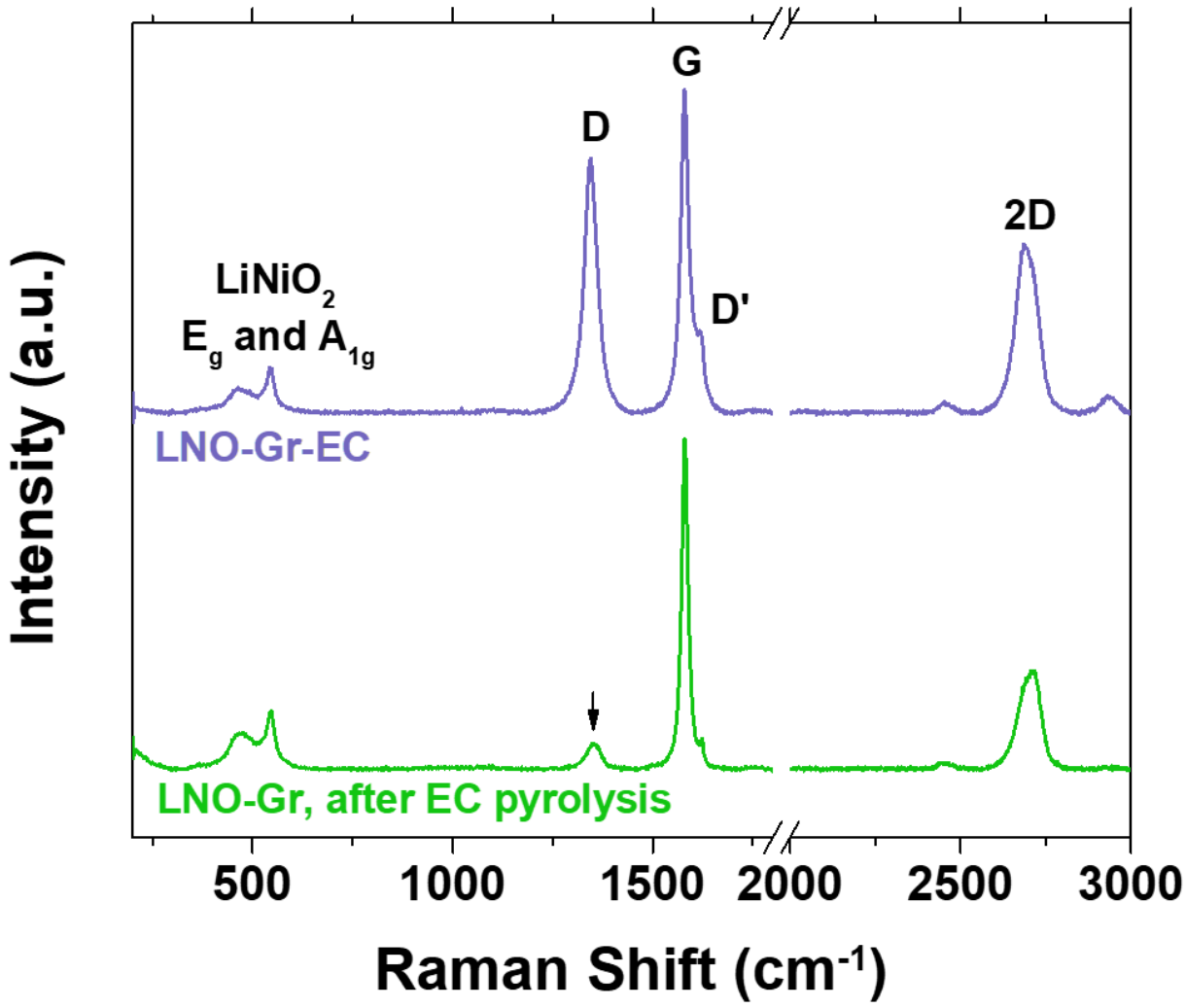


**Figure 4.10.** Raman spectra of the LNO-Gr-EC (top) and LNO-Gr (bottom) show a clear decrease in the D/G ratio after thermal pyrolysis of the EC at 300°C for 1 hour in flowing $O_2$, thus confirming decomposition of EC.

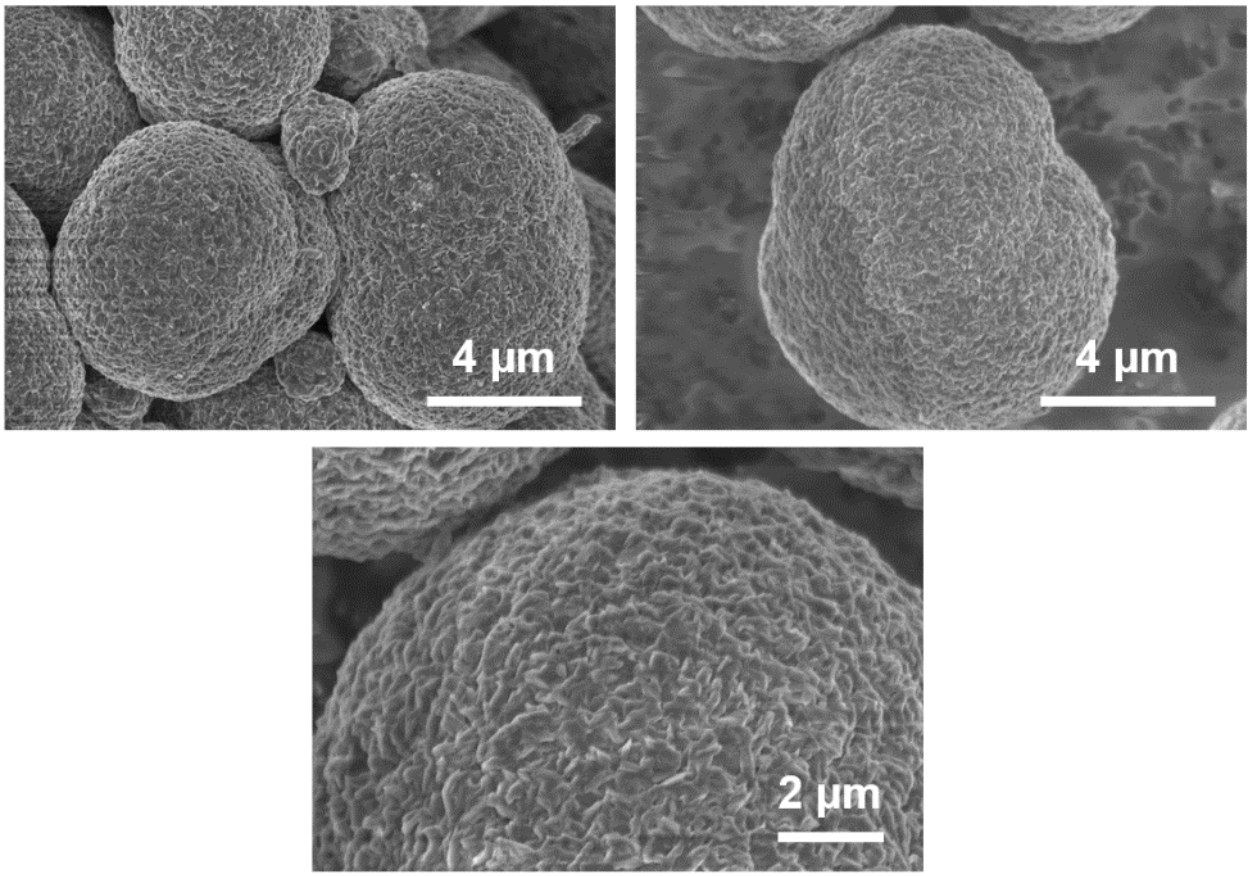


**Figure 4.11.** SEM images of LNO powder after exposure to humid $CO_2$ for 24 hours and subsequently heated to 300°C for 1 hour in flowing $O_2$. These images show that the EC pyrolysis conditions do not remove lithium impurities from the surface of LNO.

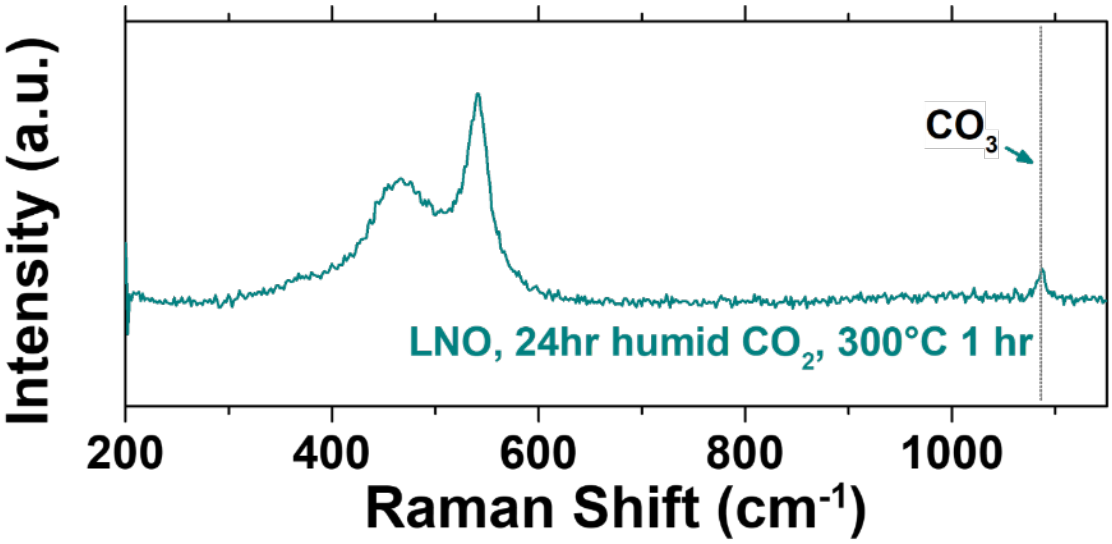

**Figure 4.12.** Raman spectrum of LNO powder after exposure to humid $CO_2$ for 24 hours and then heated to 300°C for 1 hour in flowing $O_2$. This spectrum confirms that the EC pyrolysis conditions do not remove lithium impurities from the surface of LNO.

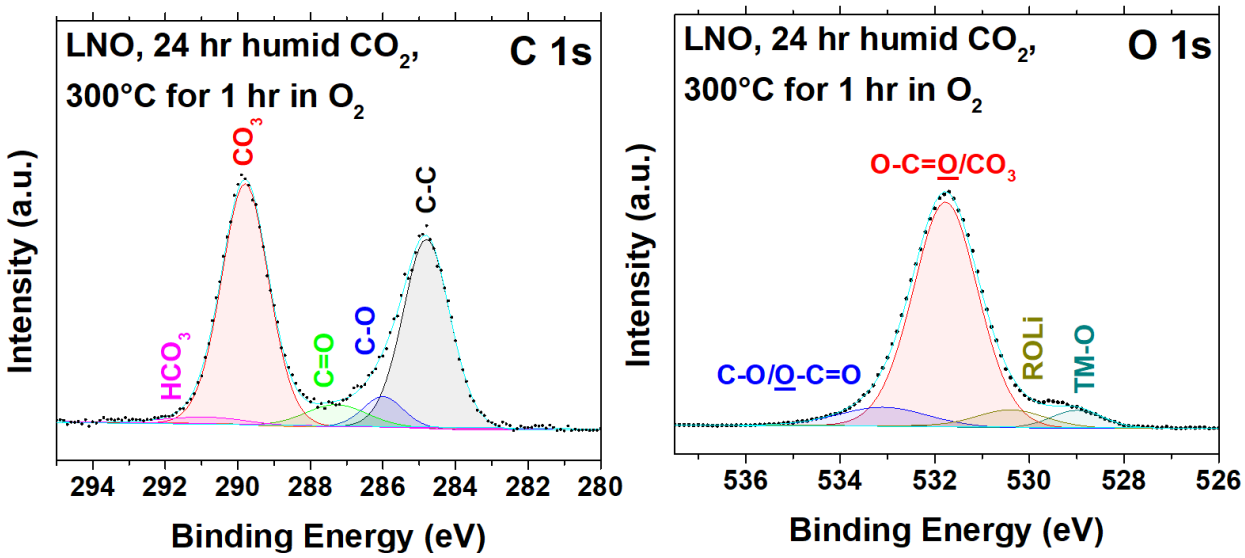


**Figure 4.13.** XPS C 1s and O 1s spectra of LNO after exposure to humid $CO_2$ for 24 hours and then heated to 300°C for 1 hour in flowing $O_2$. These spectra confirm that the EC pyrolysis conditions do not remove lithium impurities from the surface of LNO.

Since the pyrolysis temperature of EC[140,190] (300°C) is lower than the decomposition temperatures of $LiHCO_3$ (350°C), LiOH (400°C), or $Li_2CO_3$ (725°C),[113,276,282,293] surface impurities generated during exposure to humid $CO_2$ should be preserved following the EC removal step and thus detectable via subsequent spectroscopic analysis. To confirm whether the EC pyrolysis conditions were sufficient to induce changes in the surface morphology or chemistry, uncoated LNO that was exposed to humid $CO_2$ was subjected to the same thermal treatment. Subsequent SEM, Raman, and XPS analysis of this powder showed that the rough surface morphology and carbonate spectral intensities persisted through the heating procedure (**Figure**

**4.11**, **Figure 4.12**, and **Figure 4.13**). These results suggest that if lithium impurities formed on the LNO-Gr-EC during storage, the EC removal step would not remove them from the LNO surface.

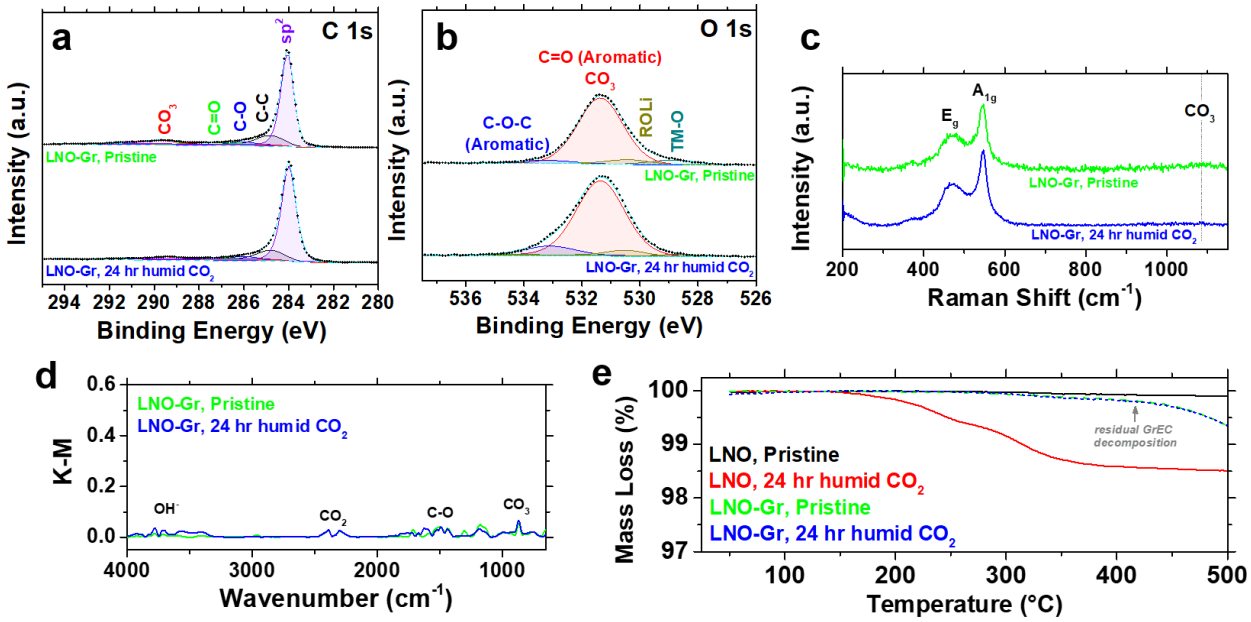


**Figure 4.14.** LNO-Gr shows minimal evidence of degradation after 24 hours of exposure to humid $CO_2$. (a) XPS C 1s spectrum, (b) XPS O 1s spectrum, (c) Raman spectroscopy, (d) DRIFTS-FTIR, and (e) thermogravimetric analysis show that the surface impurity species on LNO-Gr do not significantly increase despite 24 hours of exposure to humid $CO_2$.

Following the removal of the EC coating, spectroscopic and gravimetric methods that directly interrogated the LNO-Gr surface revealed that the GrEC coating indeed mitigated the formation of surface carbonates and hydroxides upon the exposure to humid $CO_2$. The XPS C 1s spectra were fit with the same component peaks as the uncoated LNO, with the addition of $sp^2$ bonding at 284.0 eV due to the presence of graphene. No significant changes were observed in the XPS C 1s spectra between the pristine and humid-$CO_2$ LNO-Gr samples (**Figure 4.14a**). In the O 1s spectra, component peaks corresponding to aromatic C=O/$CO_3$ and C-O-C were assigned at

533.2 eV and 531.5 eV to account for the carbonaceous residue produced by EC pyrolysis (**Figure 4.14b**), but again no significant changes were observed between the pristine and humid-$CO_2$ LNO-Gr samples. Similarly, the Raman spectra of the LNO-Gr samples before and after humid $CO_2$ exposure showed no appreciable differences, especially near the spectral vicinity of carbonate vibrational modes (1080 $cm^{-1}$, **Figure 4.14c**). This trend was also observed for the DRIFTS-FTIR spectra, which showed no substantial differences in the intensities corresponding to C-O stretching (1500 $cm^{-1}$ and 1435 $cm^{-1}$) and $CO_3$ bending (865 $cm^{-1}$, **Figure 4.14d**). Finally, since impurity species should desorb or decompose at high temperatures, thermogravimetric analysis (TGA) was performed to quantify the amount of impurity species present on the LNO (**Figure 4.14e**). Upon heating to 500°C, the pristine LNO showed minimal mass loss (less than 0.1 wt%), suggesting that the LNO was relatively impurity-free. In contrast, the uncoated LNO exposed to 24 hours of humid $CO_2$ lost 1.5% of its mass upon heating to 500°C, which was attributed to the decomposition of carbonate species near 350°C.[113,282]

Compared to the uncoated LNO, the mass loss behavior for the GrEC-coated LNO before and after exposure to humid $CO_2$ was nearly identical (0.7 wt% loss at 500°C), which suggested that the impurity levels on both samples were comparably low. Notably, both LNO-Gr samples exhibited a mass decrease beginning at approximately 300°C. Since other analytical techniques suggested that the LNO-Gr sample was largely free of impurities, this mass loss was attributed to the pyrolysis of the carbonaceous residue that remained after the initial EC removal.[171] To test this hypothesis, TGA was performed on GrEC powder that was pre-pyrolyzed under identical conditions as the LNO-Gr samples (**Figure 4.15**). The GrEC powder similarly showed mass loss

below 500°C, confirming that the mass loss observed for the LNO-Gr samples was due to the pyrolysis of residual carbon.

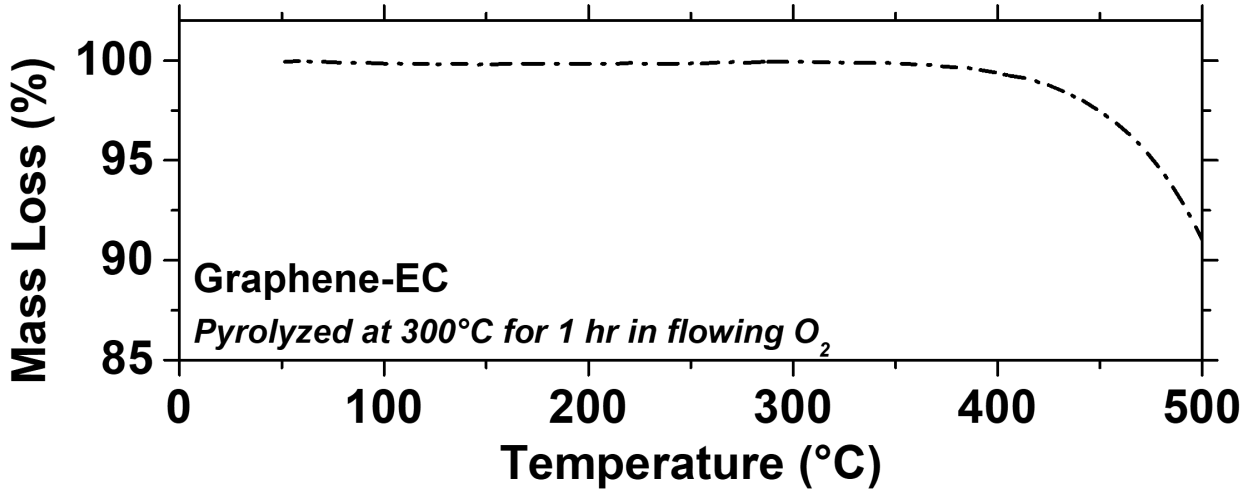


**Figure 4.15.** Thermogravimetric analysis of GrEC powder showing that the decomposition of residual GrEC begins below 400°C. The Gr-EC powder here was compositionally identical to the GrEC in the LNO-Gr electrode (i.e., 1:3 Gr:EC). Prior to TGA, this GrEC powder was heated to 300°C for 1 hour in flowing $O_2$ to pyrolyze the ethyl cellulose, leaving behind graphene and carbonaceous residue.

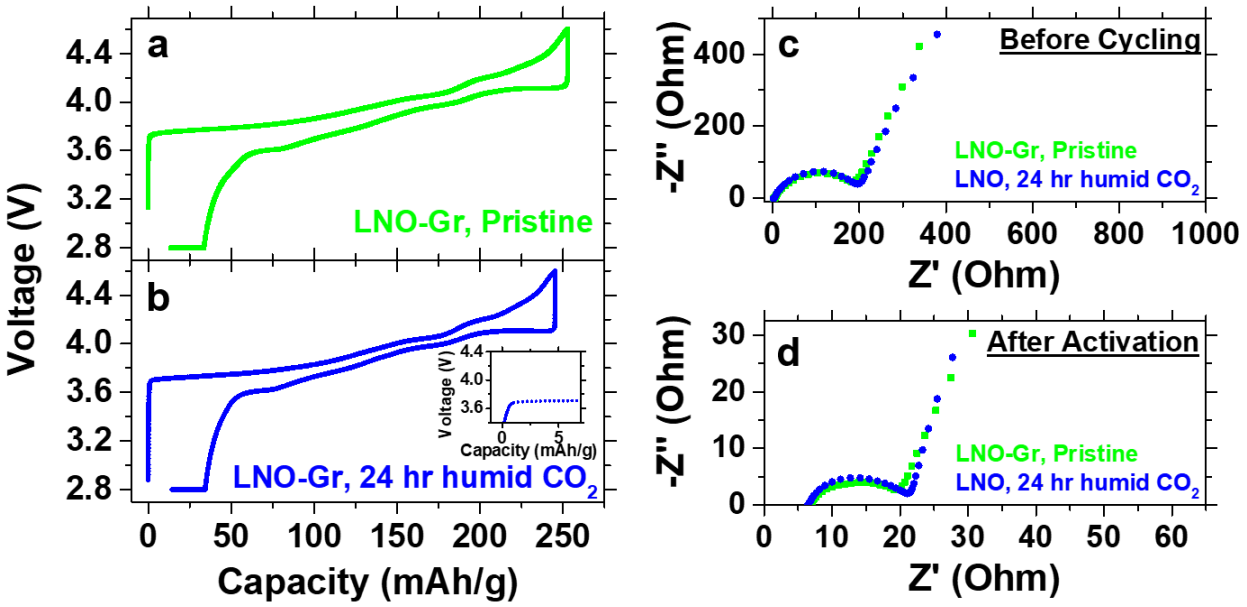


**Figure 4.16.** Electrochemical performance of LNO-Gr before and after exposure to humid $CO_2$ shows no discernable signatures of degradation. (a-b) Activation cycles of (a) pristine LNO-Gr

and (b) LNO-Gr exposed to humid $CO_2$. Activation was performed at C/10 with a constant voltage hold at 2.8 V vs. $Li/Li^+$ until the current reached C/20. The inset in (b) shows a magnified view of the initial delithiation shoulder of LNO-Gr without any voltage spike present. (c-d) Nyquist plots (c) before cycling and (d) after activation for pristine LNO-Gr and LNO-Gr exposed to humid $CO_2$.

Finally, the LNO-Gr electrodes were galvanostatically cycled to search for electrochemical signatures of impurity species. During the activation cycle, the pristine LNO-Gr sample exhibited no evidence of compromised electrochemical behavior, achieving a charge capacity of 253 mAh $g^{-1}$ and a discharge capacity of 240 mAh $g^{-1}$ (**Figure 4.16a**). Similarly, the LNO-Gr sample after exposure to humid $CO_2$ achieved a charge capacity of 245 mAh $g^{-1}$ and a discharge capacity of 230 mAh $g^{-1}$ without a discernable voltage peak at the shoulder near 3.7 V vs. $Li/Li^+$ (**Figure 4.16b**). The charge transfer resistances of the pristine LNO-Gr sample and the LNO-Gr sample after exposure to humid $CO_2$ were similar before cycling (176.9 Ω vs. 191 Ω, respectively; **Figure 4.16c**) and after activation (12.3 Ω vs. 13.2 Ω, respectively; **Figure 4.16d**). Altogether, the galvanostatic cycling and EIS results showed that the GrEC coating protected the LNO from degradation during exposure to humid $CO_2$ and had no deleterious effects on subsequent electrochemical behavior.

Overall, this work builds upon prior research that investigated the value imparted by GrEC coatings on a wide range of lithium-ion battery electrode chemistries in the context of cycling stability and electronic conductivity.[56,140,179,180,188,190] Although a long-term cycling performance assessment was not conducted in this study, prior research has already extensively explored the beneficial impacts of GrEC coatings on LNO[56] and related layered oxides due to reduced chemomechanical degradation, suppressed deleterious phase transitions near the top of charge, and improved rate capability.[140,188,190] This work demonstrates that the same coating technology can

further address the ambient sensitivity of LNO, which has extremely strict storage requirements among the family of Ni-rich layered oxides. Therefore, this work establishes a secondary material platform that can be broadly applied not only to lithium-ion battery cathode materials but also other ambient-reactive materials that can benefit from the additional electronic conductivity imparted by pyrolyzed GrEC coatings.

## 4.5 Summary

In this chapter, we addressed the ambient degradation of LNO by coating particles with a uniform, hydrophobic coating composed of graphene and ethyl cellulose. Compared to a control sample of bare LNO powder, which formed significant surface lithium impurities after 24 hours of exposure to humid $CO_2$, the coated LNO-Gr-EC was highly resistant to degradation. X-ray photoelectron, Raman, and DRIFTS-FTIR spectroscopies showed no spectral evidence of carbonate formation on LNO-Gr-EC after exposure to humid $CO_2$, corroborating the lack of surface morphological changes in SEM and mass changes in TGA. Moreover, the presence of lithium impurities is known to introduce greater electrode polarization, higher impedance, and a voltage peak near the delithiation shoulder in the activation cycle, indicating that the lithium impurities severely compromise electrochemical performance. These characteristics were clearly present for uncoated LNO following exposure to humid $CO_2$ but were absent for the coated LNO-Gr-EC electrode exposed to the same conditions. Overall, this study establishes a scalable strategy for improving the ambient stability of Ni-rich cathode materials. By demonstrating this scheme for the Ni-rich limit of the layered lithium transition metal oxide family (i.e., LNO), this work can also be applied to related Ni-rich chemistries such as NMC and NCA that are widely used in electric vehicles and related energy storage technologies.

## 4.6 Experimental Methods

### *4.6.1 LNO Synthesis*

LNO powder was synthesized at the Argonne National Laboratory (ANL) Materials Engineering Research Facility (MERF) using a procedure that was slightly modified from previous reports.[294,295] In particular, $Ni(OH)_2$ precursor powders were synthesized continuously in a 10 L Taylor Vortex Reactor (TVR) via the hydroxide co-precipitation method using $NiSO_4 \cdot 6H_2O$ as the starting material. Nickel sulfate salts were first dissolved in nitrogen-purged deionized water to obtain a 2 M solution. A 4 M solution of NaOH was employed as a co-precipitating agent, while the chelating agent was 4 M $NH_4OH$. The pH and temperature of the solution inside the reactor were maintained at 11.8 (± 0.02) and 50°C (± 0.2°C), respectively. The reactor was filled with nitrogen-purged deionized water before pumping in the reactants, and the inner cylinder was rotated at 900 RPM to create a Taylor vortex flow pattern inside the gap between two concentric cylinders where the reaction proceeded. The nickel sulfate solution was fed at ~17 mL $min^{-1}$, and $NH_4OH$ was introduced at ~8.5 mL $min^{-1}$. The NaOH flow was adjusted to maintain the pH of the solution. The final precursor powder was produced continuously with a yield of ~170 g $h^{-1}$. The precipitated product was washed thoroughly with nitrogen-purged deionized water until the conductivity of the solution was below 20 μS $cm^{-1}$. The washed powder was then dried overnight at 120°C under vacuum to obtain the hydroxide precursor with a tap density of 1.94 g $cm^{-3}$ and particle size (D50) of 9.36 μm. The final LNO powder was obtained after calcination with LiOH at 665°C for 12 h with a heating ramp of 2°C $min^{-1}$ under $O_2$ atmosphere in a modified box furnace. The LNO powder had a final tap density of 2.31 g $cm^{-3}$ and particle size (D50) of 9.66 μm. Prior to use, LNO powders were subjected to a low-temperature thermal cleaning process at 250°C for

1 h under flowing oxygen to remove weakly adsorbed impurity species. The ramp rate used for this step was 5°C $min^{-1}$. After cooling, the cleaned LNO powder was then immediately moved into an Ar glovebox (VAC Omni-Lab) with less than 0.5 ppm of oxygen for long-term storage.

### *4.6.2 Graphene-Ethyl Cellulose Production*

Graphene-ethyl cellulose powder was produced using a previously established liquid-phase exfoliation method.[56,140,171,180,188,190] Briefly, 100 g of 150 mesh flake graphite (Millipore Sigma) was mixed with 6 g of ethyl cellulose powder (4 cp, Millipore Sigma) and 1 L of 200-proof ethanol in a Silverson L5M-A shear mixer at 10,230 RPM for 2 h. The dispersion was retrieved and centrifuged for 20 min at 7,500 RPM in a Beckman Coulter J26 XPI centrifuge to remove unexfoliated graphite, which was discarded. The supernatant from this step was then flocculated with a 0.04 g/mL solution of NaCl in water until the final dispersion reached a 1.74:1 ratio of graphene dispersion:sodium chloride solution. After a final centrifugation step at 7,500 RPM for 7 min, the GrEC powder was harvested, rinsed with deionized water, vacuum filtered, and dried under infrared light overnight. The powder was analyzed using thermogravimetric analysis, which revealed that the GrEC powder was approximately 50 wt% graphene.

### *4.6.3 Humidity Exposure*

A chamber was used to expose LNO powders to humid $CO_2$ (99.9% purity). Specifically, incoming $CO_2$ (99.9% purity) was humidified prior to reaching the chamber by flowing through an Erlenmeyer flask that was filled halfway with deionized water, placed on a hotplate set at 100°C, and sealed with a rubber stopper. Two plastic tubes were inserted into the two holes in the rubber

stopper to supply incoming dry $CO_2$ and carry outgoing humidified $CO_2$, allowing the flask to function as a bubbler. A small hygrometer was left inside the chamber to measure the internal relative humidity, which was approximately 60% RH during gas flow. After humidity exposure, the powder was retrieved and dried in an 80°C vacuum oven (ThermoFisher Lindberg Blue M) overnight to desorb additional moisture prior to subsequent analysis and electrode fabrication. The powder was then moved into an Ar glovebox (VAC Omni-Lab) for long-term storage.

### *4.6.4 Electrode Fabrication*

Control electrodes were fabricated by mixing a 90:5:5 mass ratio of LNO, Super P conductive carbon black (MTI Corporation), and polyvinylidene fluoride (PVDF, MTI Corporation). To improve slurry homogeneity, the PVDF was dissolved in N-Methyl 2-pyrrolidone (NMP, anhydrous, Millipore Sigma) at 60°C overnight to form a 6 wt% solution. The PVDF solution and carbon black were first mixed with additional NMP such that the total solids percentage in the final slurry was approximately 45% by weight. Mixing was performed in a centrifugal mixer (Thinky USA) at 800 RPM for 3 min, 1200 RPM for 3 min, 1600 RPM for 3 min, 2000 RPM for 3 min, and 2000 RPM for 3 min. In between each mixing step, the slurry was allowed to rest for 1 min without agitation. After a homogeneous slurry of carbon black, PVDF, and NMP was obtained, LNO was added and mixed again using the same protocol. The slurry was then cast onto carbon-coated aluminum foil (MTI Corporation), dried in a convection oven set at 120°C for 15 min (BINDER GmbH), and followed by a final drying step under dynamic vacuum at 80°C overnight (ThermoFisher Lindberg Blue M). The resulting active material loading was

approximately 5 $mg_{LNO}$ $cm^{-2}$. Electrode discs were punched out and calendered to a final electrode porosity of approximately 40% using an electric cold roller press (MTI Corporation).

To coat LNO particles, GrEC powder was first dispersed in a 5.33:1 vol/vol mixture of ethanol and NMP (anhydrous, Millipore Sigma). The ratio of ethanol to graphene in the mixture was approximately 5 mg $mL^{-1}$. To impart mechanical stability to the coating, multiwalled carbon nanotubes (MWCNTs, Millipore Sigma) were also added such that the mass ratio of graphene to MWCNTs was approximately 8:1. These components were homogeneously dispersed using a Fisher Scientific Sonic Dismembrator Model 500 equipped with a ¼ inch tip for 1 h at a power output of 40 W. Next, the dispersion was placed on a hotplate set at 90°C to evaporate the ethanol. LNO powder was added to the dispersion at a 97.5:2 mass ratio of LNO to graphene and homogeneously incorporated into the dispersion using a centrifugal mixer (Thinky USA). The mixing protocol used was 800 RPM for 3 min, 1200 RPM for 3 min, 1600 RPM for 3 min, 2000 RPM for 3 min, and 2000 RPM for 3 min, with a 1 min rest period in between each mixing step. The dispersion was used for electrode preparation by casting onto aluminum foil, drying at 120°C for 15 min in a convection oven (BINDER GmbH) and a final step in an 80°C vacuum oven (ThermoFisher Lindberg Blue M) for overnight drying. LNO-GrEC electrodes with active material loadings of approximately 5 mg $cm^{-2}$ were punched out and calendered identically to the control electrodes. Ethyl cellulose (EC) pyrolysis was accomplished by heating samples under flowing $O_2$ in a tube furnace (ThermoFisher Lindberg Blue M) to 300°C for 1 h at a 5°C $min^{-1}$ ramp rate.

Coin cells (2032-type) were assembled in an Ar glovebox (VAC Omni-Lab). Cells were assembled with Celgard 2325 as the separator and lithium metal (China Energy Lithium, Co.) as

the counter electrode. In each coin cell, 100 μL of 1 M $LiPF_6$ in ethylene carbonate/ethyl methyl carbonate (EC/EMC, 50/50 v/v, Millipore Sigma) was used as the electrolyte.

### *4.6.5 Electrochemical Characterization*

Galvanostatic cycling was performed between 2.8 V and 4.6 V vs. $Li/Li^+$ with an Arbin LBT-20084 64-channel battery cycler. The cells were activated with 5 cycles at 0.1C using a constant-current constant-voltage protocol on discharge, where the voltage was held constant at the end of the discharge step until a cutoff value of C/20. Here, 1C is defined as the current required to fully discharge LNO in 1 h. Electrochemical impedance spectroscopy (EIS) measurements were performed on fully discharged cells using a Bio-Logic VSP potentiostat between 1 MHz and 10 mHz. Equivalent circuit modeling was performed using the EC-Lab software (Biologic).

### *4.6.6 Scanning Electron Microscopy*

A Hitachi SU8030 SEM was used for scanning electron microscopy. Powder was deposited onto double sided carbon tape adhered to an SEM stub. Prior to imaging, samples were also coated with 7 nm of Os using an Osmium Coater (SPI supplies). Imaging was performed at an accelerating voltage of 2 kV or 10 kV and a current of 10 mA.

### *4.6.7 X-Ray Photoelectron Spectroscopy*

X-Ray photoelectron spectroscopy analysis was performed using a Thermo Scientific ESCALAB 250 Xi+ (Al Kα radiation, ~1486.6 eV) at a base pressure of ~$2 \times 10^{-8}$ Torr and an analysis spot size of 900 μm. During the analysis, samples were charge compensated with a flood

gun. Depth profiling was performed with an $Ar^+$ gun at 2 keV, corresponding to an approximate etching rate of 0.11 nm $sec^{-1}$. To prepare samples for analysis, a spatula was used to press powder onto double-sided copper adhesive tape on the sample holder, which left an optically dense layer of LNO. The amount of ambient exposure time during this step was less than 30 s. Peak fitting was performed using the Thermo Scientific Avantage software, with charge calibration set to adventitious carbon at ~284.8 eV.

### *4.6.8 Fourier Transform Infrared Spectroscopy*

Fourier Transform Infrared Spectroscopy was performed in diffuse reflectance mode using a Nicolet iS50 spectrometer (Thermo Fisher) equipped with a DRIFTS module. To prepare samples for DRIFTS-FTIR, KBr powder was mixed with LNO at a ratio of 99:1 using a mortar and pestle inside an Ar glovebox. Spectra were acquired with an average of 64 scans at a resolution of 4 $cm^{-1}$. Since the scans were conducted in ambient conditions with $CO_2$ present, the spectra of the LNO powders were normalized using the intensities of the $CO_2$ doublet (located at 2330 $cm^{-1}$ and 2360 $cm^{-1}$) to allow for direct comparison between samples.

### *4.6.9 Raman Spectroscopy*

Raman spectroscopy was conducted using a HORIBA LabRAM HR Evolution Confocal Raman Microscope equipped with a 532 nm laser. 60 spectra were acquired and averaged using a 600 g/mm grating for 5 s.

### *4.6.10 Thermogravimetric Analysis*

Thermogravimetric analysis was performed using a Mettler Toledo TGA/DSC 3+ under flowing dry air. Prior to TGA, all powders were dried at 80°C under dynamic vacuum to desorb moisture and then loaded into alumina crucibles for data acquisition.

# CHAPTER 5:

# FUTURE WORK

This chapter is adapted in part from:

**Luu, N. S.,*** Park, K. Y.,* Hersam, M.C. Characterizing and Mitigating Chemomechanical Degradation in High-Energy Lithium-Ion Battery Cathode Materials. Acc. Mater. Res. (2022), 3, 5, 511–524.

(* indicates equal contribution)

## 5.1 Introduction to Future Work

This dissertation has discussed several ways that graphene-polymer coatings can expand the stability and performance of current lithium-ion battery materials. The work described in **Chapters 2 to 4** describe the application of graphene to various nickel-rich layered oxides, including NCA, NMC, and LNO. In these electrode architectures, graphene coatings minimizes electrolyte decomposition reactions, decreases high-voltage chemomechanical strain, and protects the layered oxides from ambient degradation. The remainder of this section will explore pathways for graphene to address issues within electrochemical energy storage technologies. This future work falls under several categories: stabilizing emerging lithium-ion cathode materials, improving lithium metal host anodes, serving as a platform for investigating electrode-level state-of-charge heterogeneity, and improving the performance of beyond-lithium battery chemistries.

## 5.2 Stabilizing Anionic Redox in Next-Generation Cathode Materials

Next-generation cathode materials, including Li-rich layered oxides and disordered rocksalt cathodes, are extremely attractive cathode material candidates due to their high capacities. These materials rely on both cationic and anionic redox to charge compensate for lithium insertion and extraction. However, when oxygen is oxidized in these structures, the formation of oxygen-oxygen dimers can occur, leading to gas evolution.[93] The degradation cascade then promotes formation of surface spinel phases and introduces an intolerable decay in both the cycle life and the average discharge voltage of these materials.[154,296] Beyond evolving $O_2$ gas, peroxide and superoxide ions formed by oxygen activity at high SOCs can easily donate electrons to catalyze ring-opening reactions of cyclic carbonates, leading to deposition of organic species on cathode surfaces.[67,71,297,298] Similarly, molecular oxygen can also react with electrolyte salt components to

form fluorophosphate degradation products.[299,300] The result is the formation of a thick SEI layer, which is uniquely attributed to anionic redox rather than the operating potential of the cell.[297]

A uniform graphene coating could be a facile pathway to resolving issues with SEI formation and oxygen evolution, enabling long-lasting electrochemical performance in emerging Li-rich and DRX cathodes. Although prior work exists incorporating graphene,[301,302] rGO,[185,192,303] and amorphous carbon coatings[304] onto these materials, such studies focus on rate capability enhancements and the chemical evolution of the CEI without discussion of oxygen evolution. Graphene coatings have been shown to kinetically suppress gas evolution in LNO[56] and LCO[103] cathodes, while separately suppressing electrolyte decomposition reactions (**Chapter 3**). Therefore, graphene coatings can be explored as a solution to address multiple critical degradation pathways in emerging cathode materials.

## 5.3 Graphene-Cellulose Lithium Metal Composite Anodes

A key engineering challenge precluding the successful adoption of lithium metal anodes is stable lithium plating and stripping. However, recent work has shown that host structures can control lithium plating behavior.[186,305,306] These structures are often highly porous and made from conductive materials, including metals,[307,308] amorphous carbon,[309] carbon nanofibers,[193,196,310] and graphene-based materials.[194,311,312] The high surface area of these scaffolds promotes delocalized $Li^+$ flux during plating, which subsequently suppresses $Li^+$ current hotspots and prevents dendrite growth. Importantly, since the pore sizes influence the surface area upon which lithium plating occurs, they have a large impact on lithium plating dynamics. The optimal pore size may also change as a function of applied current densities, suggesting that microstructures may need to be

tailored to the intended use case.[313] Fortunately, graphene-polymer scaffolds can be easily fabricated using a combination of phase inversion and combustion-assisted cellulose decomposition,[292] which allows for thorough investigation of optimized composite microstructures for lithium metal deposition. By dispersing nanomaterials and polymers in a solvent, mixing in a nonsolvent, and sequentially removing the liquid phases, a porous microstructure can be easily formed with precise microstructural control.[292,314] The larger pore sizes can be tuned by adjusting parameters relevant for phase inversion, including the ratio between solvent and nonsolvent components or solids loading. Similarly, the size of smaller pores can also be tuned by changing the conditions by which the polymeric dispersant is removed, such as thermal or photonic annealing.[172,217,292] Finally, to improve the affinity of lithium,[315] graphene can be functionalized or doped with various functional groups using plasma etching or chemical modification. These parameters create a wide phase space within which lithium deposition can be optimized.

## 5.4 Understanding Electrode-Level State-of-Charge Heterogeneity

As LIBs trend toward higher-loading electrodes, an improved understanding of the state-of-charge heterogeneity in the electrode is necessary to inform strategies that aim to minimize chemomechanical degradation. Examples of these solutions include conductive additives and binders since they can be utilized or modified to address degradation events such as particle fracture or detachment from the carbon-binder domain.

However, the incorporation of graphene into electrode architectures presents a unique opportunity to investigate the role of electronic conductivity on electrode-level state-of-charge heterogeneity and subsequent chemomechanical degradation. Local variations in the state of

charge depend heavily on the electronic wiring within the electrode.[58] Therefore, electrodes can be fabricated with graphene-coated active material particles, which possess greater surface electronic conductivity than bare particles, and electrochemically cycled to search for evidence of electrode-level SOC heterogeneity. The graphene content within the electrode, flake geometries, and chemical pristineness can serve as knobs to further tune film conductivity and determine the subsequent impact on SOC heterogeneity. Compatible mapping approaches include X-ray spectromicroscopy, microfocused X-ray diffraction, and Raman spectroscopy, which exploit measurable parameters, such as the unit cell lattice parameter or the absorption edge energies of elements responsible for charge compensation, as proxy measurements for the SOC. This investigation would be especially pertinent for encapsulation strategies that keep active material particles in electrical contact in the event of particle fracture, including segregated networks of carbon nanotubes[316] and graphene coatings.[56,140,182] Finally, since this method can be broadly applied to many active material systems, optimal electrode formulations and microstructures with minimized electrode-level chemomechanical degradation can be identified.

## 5.5 Improving Beyond-Li Chemistries

Due to mineral scarcity and comparatively higher prices of lithium, alternative energy storage solutions that do not rely on lithium chemistries are becoming increasingly attractive. Notably, Na-ion chemistries are incredibly attractive from a supply-chain perspective since sodium mineral precursors are more abundant than lithium precursors and present slight cost advantages.[317] Due to the larger ionic radius of $Na^+$ compared to $Li^+$, the main challenge for Na-ion batteries is to identify appropriate electrode materials that can provide high energy and power densities with good coulombic efficiencies. Current $Na^+$ host materials include hard carbons,[318,319]

metal oxides,[320-322] and metal sulfides,[323,324] which all suffer from low electrical conductivity. Graphene coatings, which can be combined with active material particle size modifications,[179,190] can easily be adopted to improve the rate capability of these materials. The atomically thin nature of graphene and its excellent electrical properties imply that only a small weight fraction is required in the architecture to significantly boost the film electrode conductivity. Furthermore, chalcogenide-based electrodes are known to suffer from volume expansion due to pulverization and loss of electrical conductivity.[324,325] Graphene can buffer volume expansion in these systems in an analogous manner as silicon anodes and can maintain electrical contact after fracture occurs.

Other van der Waals materials have also been used for energy storage applications, including phosphorene,[326-328] $MoS_2$,[323,325,329] $WS_2$,[330,331] and MXenes.[332,333] Like metal oxides and sulfides, semiconducting 2D materials are limited by their low electronic conductivities and large volume expansion upon ion intercalation.[334,335] Conveniently, 2D materials can be individually processed in large quantities via liquid phase exfoliation, yielding inks with highly tunable viscosities.[171,200,336-343] They can then be deposited onto arbitrary substrates using various deposition schemes, including vacuum filtration, inkjet printing,[171,339] screen printing,[340,341] aerosol jet printing,[338,342] and 3D printing.[343] To resolve the inherent limitations of 2D materials alone, graphene can be processed using the same solution-phase methods, enabling the fabrication of heterostructured 2D material-based electrodes for energy storage. For example, exfoliated $MoS_2$ and graphene can be combined in solution and deposited simultaneously for high-throughput electrode fabrication. Alternatively, inspired by microstructural morphology control as another knob to tune battery performance,[344] unary 2D material inks can be discretely printed to define electrodes with varying lateral or vertical compositions. Finally, the wide compatibility of these

inks with a library of various printing techniques enables the fabrication of microbatteries or flexible batteries, opening the door for 2D materials to augment or control electrochemical behavior in emerging electrode form factors.

# CHAPTER 6:

# CONCLUSIONS

The research presented in this dissertation expands the applications of graphene in improving the performance of lithium-ion battery electrode materials, focusing on addressing operational and ambient degradation in nickel-rich layered oxides. Although surface coatings are central to most LIB engineering solutions today, questions remain about their role in improving cycling stability, particularly at extreme operational regimes that are known to induce severe degradation. Using graphene as an example, the work explored in this dissertation provides valuable information for engineering strategies that explore the role of surface coatings in improving the performance of energy storage materials, from the particle- to the electrode-level.

Chapter 1 establishes a background in lithium-ion battery science, identifying the incumbent and commercially relevant cathode chemistries that underlie most lithium-ion batteries in consumer electronics and electric vehicles today. The degradation mechanisms of these chemistries were then discussed, including cycling-induced and ambient-induced degradation. Active material doping and coating were introduced as strategies to address these issues. This chapter also introduced two-dimensional materials, liquid-phase exfoliation as a platform to manufacture these materials in a scalable manner, and the potential applications of two-dimensional materials in lithium-ion batteries.

Chapter 2 explores the role of graphene coatings to simultaneously enhance the reaction kinetics and stability of nanoparticle-based NCA cathodes. Compared to secondary particles, nanoparticles offer shorter solid-state Li-ion diffusion lengths and increased charge transfer sites, which are ideal for rate performance. Unfortunately, Ni-rich cathode synthesis procedures often leave lithium residues on particle surfaces that reduce cycling efficiencies. These effects are exacerbated in nanoparticle systems with high surface areas. To address this issue, a post-synthetic

thermal treatment that removed these residues was developed and applied to NCA nanoparticles, priming the surface for subsequent surface coating procedures. Graphene was then coated onto the NCA to impart improved rate capability and cyclic stability, which was confirmed with half- and full-cell testing at room temperature and at low temperatures. This work indicates that careful control over surface chemistry is required for effective surface coating schemes, which has implications for electrode design across existing and emerging nanoparticle-based electrodes for energy storage.

Chapter 3 covers high-voltage chemomechanical degradation in NMC cathodes. Primary particles of NMC were synthesized and subsequently coated with graphene. Next, electrodes were fabricated using both coated and uncoated NMC particles and galvanostatically cycled to 4.8 V vs. $Li/Li^+$, where the graphene-coated electrodes show significantly improved capacity retention and record coulombic efficiencies under these operating conditions. Extensive postmortem materials characterization, including X-ray diffraction, spectroscopy, and microscopy, confirmed that the graphene-coated electrodes show reduced electrolyte decomposition reaction products, as well as reduced particle-level fracture and electrochemical creep. A scheme was proposed that explains how a conductive surface coating can delocalize lithium-ion flux and associated chemomechanical strain, which is most deleterious at high states of charge. This scheme established a new framework for addressing chemomechanical degradation at the particle level, which is highly relevant for incumbent and emerging energy storage materials.

Chapter 4 investigates the role of hydrophobic coatings in mitigating ambient degradation of Ni-rich layered oxides. These materials are known to degrade in ambient conditions as adsorbed moisture and carbon dioxide leach lithium from the structure, forming surface lithium hydroxides,

bicarbonates, and carbonates. To address this issue, a hydrophobic graphene-ethyl cellulose layer was coated onto LNO particles. The integrity of the coating was tested under accelerated degradation conditions by subjecting the particles to a stream of humidified $CO_2$ for 24 hours. Microscopy, spectroscopy, gravimetric analysis, and electrochemical data reveal no signatures of ambient-generated lithium impurities, indicating that the surface coating successfully preserved the pristineness of the LNO. This strategy, demonstrated for the Ni-rich limit, has immediate implications for easing strict dry room requirements in large-scale battery manufacturing. More broadly, this work also outlines a potential platform for alleviating the moisture sensitivity of ambient-reactive materials across electrical and electrochemical systems.

Battery science is a rapidly growing and evolving field. It is driven by a constant pace of materials development towards high-performance devices and is informed by fundamental studies that uncover detailed nanoscale chemical, mechanical, and phase phenomena. This dissertation adds to this conversation, drawing inspiration from both nanomaterials and energy storage to address critical materials issues that are highly relevant for incumbent lithium-ion battery cathodes. Grounded in extensive materials and electrochemical characterization, the work described here shows that graphene coatings can add value to Ni-rich layered oxides across wide operational regimes, including changes in temperature, humidity, and states of charge. By demonstrating such varied performance improvements for one cathode system, this dissertation establishes a platform that can be broadly applied to not only existing and emerging lithium-ion electrode systems, but also other beyond-lithium battery systems. In this way, this dissertation opens the door for future studies that can rationally utilize graphene and other 2D materials in electrode architectures across energy storage.

## REFERENCES


1 Whittingham, M. S. Electrical Energy Storage and Intercalation Chemistry. *Science* **192**, 1126-1127 (1976). https://doi.org:10.1126/science.192.4244.1126

2 Whittingham, M. S. Lithium Batteries and Cathode Materials. *Chemical Reviews* **104**, 4271-4302 (2004). https://doi.org:10.1021/cr020731c

3 Yoshino, A. The Lithium-ion Battery: Two Breakthroughs in Development and Two Reasons for the Nobel Prize. *Bulletin of the Chemical Society of Japan* **95**, 195-197 (2022). https://doi.org:10.1246/bcsj.20210338

4 Nitta, N., Wu, F., Lee, J. T. & Yushin, G. Li-ion battery materials: present and future. *Materials Today* **18**, 252-264 (2015). https://doi.org:10.1016/j.mattod.2014.10.040

5 Novoselov, K. S., Geim, A. K., Morozov, S. V., Jiang, D., Zhang, Y., Dubonos, S. V., Grigorieva, I. V. & Firsov, A. A. Electric Field Effect in Atomically Thin Carbon Films. *Science* **306**, 666-669 (2004). https://doi.org:10.1126/science.1102896

6 Novoselov, K. S., Geim, A. K., Morozov, S. V., Jiang, D., Katsnelson, M. I., Grigorieva, I. V., Dubonos, S. V. & Firsov, A. A. Two-dimensional gas of massless Dirac fermions in graphene. *Nature* **438**, 197-200 (2005). https://doi.org:10.1038/nature04233

7 Castro Neto, A. H., Guinea, F., Peres, N. M. R., Novoselov, K. S. & Geim, A. K. The electronic properties of graphene. *Reviews of Modern Physics* **81**, 109-162 (2009). https://doi.org:10.1103/RevModPhys.81.109

8 Thackeray, M. M., Wolverton, C. & Isaacs, E. D. Electrical energy storage for transportation—approaching the limits of, and going beyond, lithium-ion batteries. *Energy & Environmental Science* **5**, 7854-7863 (2012). https://doi.org:10.1039/C2EE21892E

9 Li, W., Lee, S. & Manthiram, A. High-Nickel NMA: A Cobalt-Free Alternative to NMC and NCA Cathodes for Lithium-Ion Batteries. *Advanced Materials* **32**, 2002718 (2020). https://doi.org:10.1002/adma.202002718

10 Zhong, Q., Bonakdarpour, A., Zhang, M., Gao, Y. & Dahn, J. R. Synthesis and Electrochemistry of $LiNi_xMn_{2-x}O_4$. *Journal of The Electrochemical Society* **144**, 205 (1997). https://doi.org:10.1149/1.1837386

11 Manthiram, A., Knight, J. C., Myung, S.-T., Oh, S.-M. & Sun, Y.-K. Nickel-Rich and Lithium-Rich Layered Oxide Cathodes: Progress and Perspectives. *Advanced Energy Materials* **6**, 1501010 (2016). https://doi.org:10.1002/aenm.201501010

12 Clément, R. J., Lun, Z. & Ceder, G. Cation-disordered rocksalt transition metal oxides and oxyfluorides for high energy lithium-ion cathodes. *Energy & Environmental Science* **13**, 345-373 (2020). https://doi.org:10.1039/C9EE02803J

13 Julien, C. M., Mauger, A., Zaghib, K. & Groult, H. Comparative Issues of Cathode Materials for Li-Ion Batteries. *Inorganics* **2**, 132-154 (2014).

14 Jiang, Y., Qin, C., Yan, P. & Sui, M. Origins of capacity and voltage fading of $LiCoO_2$ upon high voltage cycling. *Journal of Materials Chemistry A* **7**, 20824-20831 (2019). https://doi.org:10.1039/C9TA06579B

15 de Biasi, L., Schiele, A., Roca-Ayats, M., Garcia, G., Brezesinski, T., Hartmann, P. & Janek, J. Phase Transformation Behavior and Stability of $LiNiO_2$ Cathode Material for Li-Ion Batteries Obtained from In Situ Gas Analysis and Operando X-Ray Diffraction. *ChemSusChem* **12**, 2240-2250 (2019). https://doi.org:10.1002/cssc.201900032

16 Choa, J. & Thackeray, M. M. Structural Changes of $LiMn_2O_4$ Spinel Electrodes during Electrochemical Cycling. *Journal of The Electrochemical Society* **146**, 3577 (1999). https://doi.org:10.1149/1.1392517

17 Yamada, A., Chung, S. C. & Hinokuma, K. Optimized $LiFePO_4$ for Lithium Battery Cathodes. *Journal of The Electrochemical Society* **148**, A224 (2001). https://doi.org:10.1149/1.1348257

18 Mizushima, K., Jones, P. C., Wiseman, P. J. & Goodenough, J. B. $Li_xCoO_2$ ($0<x<-1$): A new cathode material for batteries of high energy density. *Materials Research Bulletin* **15**, 783-789 (1980). https://doi.org:10.1016/0025-5408(80)90012-4

19 Manthiram, A. & Goodenough, J. B. Layered lithium cobalt oxide cathodes. *Nature Energy* **6**, 323-323 (2021). https://doi.org:10.1038/s41560-020-00764-8

20 Ohzuku, T., Ueda, A. & Nagayama, M. Electrochemistry and Structural Chemistry of $LiNiO_2$ (R3m) for 4 Volt Secondary Lithium Cells. *Journal of The Electrochemical Society* **140**, 1862 (1993). https://doi.org:10.1149/1.2220730

21 Li, H., Zhang, N., Li, J. & Dahn, J. R. Updating the Structure and Electrochemistry of $Li_xNiO_2$ for $0 \leq x \leq 1$. *Journal of The Electrochemical Society* **165**, A2985 (2018). https://doi.org:10.1149/2.0381813jes

22 Kim, U. H., Jun, D. W., Park, K. J., Zhang, Q., Kaghazchi, P., Aurbach, D., Major, D. T., Goobes, G., Dixit, M., Leifer, N., Wang, C. M., Yan, P., Ahn, D., Kim, K. H., Yoon, C. S. & Sun, Y. K. Pushing the limit of layered transition metal oxide cathodes for high-

energy density rechargeable Li ion batteries. *Energy & Environmental Science* **11**, 1271-1279 (2018). https://doi.org:10.1039/C8EE00227D

23 Larcher, D., Palacín, M. R., Amatucci, G. G. & Tarascon, J. M. Electrochemically Active $LiCoO_2$ and $LiNiO_2$ Made by Cationic Exchange under Hydrothermal Conditions. *Journal of The Electrochemical Society* **144**, 408 (1997). https://doi.org:10.1149/1.1837424

24 Garcia, B., Pereira-Ramos, J. P., Caurant, D. & Baffier, N. Synthesis and Electrochemical Properties of $LiNiO_2$ Prepared via an Aqueous Solution Technique. *Chemistry Letters* **27**, 543-544 (1998). https://doi.org:10.1246/cl.1998.543

25 Chang, C.-C., Kim, J. Y. & Kumta, P. N. Influence of Crystallite Size on the Electrochemical Properties of Chemically Synthesized Stoichiometric $LiNiO_2$. *Journal of The Electrochemical Society* **149**, A1114 (2002). https://doi.org:10.1149/1.1495495

26 Kanno, R., Kubo, H., Kawamoto, Y., Kamiyama, T., Izumi, F., Takeda, Y. & Takano, M. Phase Relationship and Lithium Deintercalation in Lithium Nickel Oxides. *Journal of Solid State Chemistry* **110**, 216-225 (1994). https://doi.org:10.1006/jssc.1994.1162

27 Koyama, Y., Arai, H., Tanaka, I., Uchimoto, Y. & Ogumi, Z. Defect Chemistry in Layered $LiMO_2$ (M = Co, Ni, Mn, and $Li_{1/3}Mn_{2/3}$) by First-Principles Calculations. *Chemistry of Materials* **24**, 3886-3894 (2012). https://doi.org:10.1021/cm3018314

28 Li, M. & Lu, J. Cobalt in lithium-ion batteries. *Science* **367**, 979-980 (2020). https://doi.org:10.1126/science.aba9168

29 Zheng, J., Teng, G., Xin, C., Zhuo, Z., Liu, J., Li, Q., Hu, Z., Xu, M., Yan, S., Yang, W. & Pan, F. Role of Superexchange Interaction on Tuning of Ni/Li Disordering in Layered $Li(Ni_xMn_yCo_z)O_2$. *The Journal of Physical Chemistry Letters* **8**, 5537-5542 (2017). https://doi.org:10.1021/acs.jpclett.7b02498

30 Kang, K., Meng, Y. S., Bréger, J., Grey, C. P. & Ceder, G. Electrodes with High Power and High Capacity for Rechargeable Lithium Batteries. *Science* **311**, 977-980 (2006). https://doi.org:10.1126/science.1122152

31 Yu, H., Qian, Y., Otani, M., Tang, D., Guo, S., Zhu, Y. & Zhou, H. Study of the lithium/nickel ions exchange in the layered $LiNi_{0.42}Mn_{0.42}Co_{0.16}O_2$ cathode material for lithium ion batteries: experimental and first-principles calculations. *Energy & Environmental Science* **7**, 1068-1078 (2014). https://doi.org:10.1039/C3EE42398K

32 Bianchini, M., Roca-Ayats, M., Hartmann, P., Brezesinski, T. & Janek, J. There and Back Again—The Journey of $LiNiO_2$ as a Cathode Active Material. *Angewandte Chemie*

*International Edition* **58**, 10434-10458 (2019). https://doi.org:https://doi.org/10.1002/anie.201812472

33 Qiao, R., Liu, J., Kourtakis, K., Roelofs, M. G., Peterson, D. L., Duff, J. P., Deibler, D. T., Wray, L. A. & Yang, W. Transition-metal redox evolution in $LiNi_{0.5}Mn_{0.3}Co_{0.2}O_2$ electrodes at high potentials. *Journal of Power Sources* **360**, 294-300 (2017). https://doi.org:10.1016/j.jpowsour.2017.06.009

34 Noh, H.-J., Youn, S., Yoon, C. S. & Sun, Y.-K. Comparison of the structural and electrochemical properties of layered $Li[Ni_xCo_yMn_z]O_2$ ($x$ = 1/3, 0.5, 0.6, 0.7, 0.8 and 0.85) cathode material for lithium-ion batteries. *Journal of Power Sources* **233**, 121-130 (2013). https://doi.org:10.1016/j.jpowsour.2013.01.063

35 Li, W., Asl, H. Y., Xie, Q. & Manthiram, A. Collapse of $LiNi_{1-x-y}Co_xMn_yO_2$ Lattice at Deep Charge Irrespective of Nickel Content in Lithium-Ion Batteries. *Journal of the American Chemical Society* **141**, 5097-5101 (2019). https://doi.org:10.1021/jacs.8b13798

36 Sovacool, B. K. The precarious political economy of cobalt: Balancing prosperity, poverty, and brutality in artisanal and industrial mining in the Democratic Republic of the Congo. *The Extractive Industries and Society* **6**, 915-939 (2019). https://doi.org:10.1016/j.exis.2019.05.018

37 Li, W., Erickson, E. M. & Manthiram, A. High-Nickel Layered Oxide Cathodes for Lithium-Based Automotive Batteries. *Nature Energy* **5**, 26-34 (2020). https://doi.org:10.1038/s41560-019-0513-0

38 Koyama, Y., Makimura, Y., Tanaka, I., Adachi, H. & Ohzuku, T. Systematic Research on Insertion Materials Based on Superlattice Models in a Phase Triangle of $LiCoO_2$-$LiNiO_2$-$LiMnO_2$: I. First-Principles Calculation on Electronic and Crystal Structures, Phase Stability and New $LiNi_{1/2}Mn_{1/2}O_2$ Material. *Journal of The Electrochemical Society* **151**, A1499 (2004). https://doi.org:10.1149/1.1783908

39 Rossen, E., Jones, C. D. W. & Dahn, J. R. Structure and electrochemistry of $Li_xMn_yNi_{1-y}O_2$. *Solid State Ionics* **57**, 311-318 (1992). https://doi.org:10.1016/0167-2738(92)90164-K

40 Zheng, J., Kan, W. H. & Manthiram, A. Role of Mn Content on the Electrochemical Properties of Nickel-Rich Layered $LiNi_{0.8-x}Co_{0.1}Mn_{0.1+x}O_2$ ($0.0 \leq x \leq 0.08$) Cathodes for Lithium-Ion Batteries. *ACS Applied Materials & Interfaces* **7**, 6926-6934 (2015). https://doi.org:10.1021/acsami.5b00788

41 Hwang, B. J., Tsai, Y. W., Chen, C. H. & Santhanam, R. Influence of Mn content on the morphology and electrochemical performance of $LiNi_{1-x-y}Co_xMn_yO_2$ cathode materials. *Journal of Materials Chemistry* **13**, 1962-1968 (2003). https://doi.org:10.1039/B301468C

42 Ahmed, S., Nelson, P. A., Gallagher, K. G., Susarla, N. & Dees, D. W. Cost and energy demand of producing nickel manganese cobalt cathode material for lithium ion batteries. *Journal of Power Sources* **342**, 733-740 (2017). https://doi.org:10.1016/j.jpowsour.2016.12.069

43 Chen, C. H., Liu, J., Stoll, M. E., Henriksen, G., Vissers, D. R. & Amine, K. Aluminum-doped lithium nickel cobalt oxide electrodes for high-power lithium-ion batteries. *Journal of Power Sources* **128**, 278-285 (2004). https://doi.org:10.1016/j.jpowsour.2003.10.009

44 Manthiram, A., Song, B. & Li, W. A perspective on nickel-rich layered oxide cathodes for lithium-ion batteries. *Energy Storage Materials* **6**, 125-139 (2017). https://doi.org:10.1016/j.ensm.2016.10.007

45 Li, J., Li, W., Wang, S., Jarvis, K., Yang, J. & Manthiram, A. Facilitating the Operation of Lithium-Ion Cells with High-Nickel Layered Oxide Cathodes with a Small Dose of Aluminum. *Chemistry of Materials* **30**, 3101-3109 (2018). https://doi.org:10.1021/acs.chemmater.8b01077

46 Zhou, K., Xie, Q., Li, B. & Manthiram, A. An in-depth understanding of the effect of aluminum doping in high-nickel cathodes for lithium-ion batteries. *Energy Storage Materials* **34**, 229-240 (2021). https://doi.org:10.1016/j.ensm.2020.09.015

47 Jo, E., Park, J.-H., Park, J., Hwang, J., Chung, K. Y., Nam, K.-W., Kim, S. M. & Chang, W. Different thermal degradation mechanisms: Role of aluminum in Ni-rich layered cathode materials. *Nano Energy* **78**, 105367 (2020). https://doi.org:10.1016/j.nanoen.2020.105367

48 Ohzuku, T., Ueda, A. & Kouguchi, M. Synthesis and Characterization of $LiAl_{1/4}Ni_{3/4}O_2$ ($R\bar{3}m$) for Lithium-Ion (Shuttlecock) Batteries. *Journal of The Electrochemical Society* **142**, 4033 (1995). https://doi.org:10.1149/1.2048458

49 Sun, H. & Zhao, K. Electronic Structure and Comparative Properties of $LiNi_xMn_yCo_zO_2$ Cathode Materials. *The Journal of Physical Chemistry C* **121**, 6002-6010 (2017). https://doi.org:10.1021/acs.jpcc.7b00810

50 Jung, S.-K., Gwon, H., Hong, J., Park, K.-Y., Seo, D.-H., Kim, H., Hyun, J., Yang, W. & Kang, K. Understanding the Degradation Mechanisms of $LiNi_{0.5}Co_{0.2}Mn_{0.3}O_2$ Cathode

Material in Lithium Ion Batteries. *Advanced Energy Materials* **4**, 1300787 (2014). https://doi.org:10.1002/aenm.201300787

51 Cabana, J., Kwon, B. J. & Hu, L. Mechanisms of Degradation and Strategies for the Stabilization of Cathode–Electrolyte Interfaces in Li-Ion Batteries. *Accounts of Chemical Research* **51**, 299-308 (2018). https://doi.org:10.1021/acs.accounts.7b00482

52 Wandt, J., Freiberg, A. T. S., Ogrodnik, A. & Gasteiger, H. A. Singlet Oxygen Evolution from Layered Transition Metal Oxide Cathode Materials and Its Implications for Lithium-Ion Batteries. *Materials Today* **21**, 825-833 (2018). https://doi.org:10.1016/j.mattod.2018.03.037

53 Jung, R., Linsenmann, F., Thomas, R., Wandt, J., Solchenbach, S., Maglia, F., Stinner, C., Tromp, M. & Gasteiger, H. A. Nickel, Manganese, and Cobalt Dissolution from Ni-Rich NMC and Their Effects on NMC622-Graphite Cells. *Journal of The Electrochemical Society* **166**, A378-A389 (2019). https://doi.org:10.1149/2.1151902jes

54 Yan, P., Zheng, J., Chen, T., Luo, L., Jiang, Y., Wang, K., Sui, M., Zhang, J.-G., Zhang, S. & Wang, C. Coupling of Electrochemically Triggered Thermal and Mechanical Effects to Aggravate Failure in a Layered Cathode. *Nature Communications* **9**, 2437 (2018). https://doi.org:10.1038/s41467-018-04862-w

55 Radin, M. D., Alvarado, J., Meng, Y. S. & Van der Ven, A. Role of Crystal Symmetry in the Reversibility of Stacking-Sequence Changes in Layered Intercalation Electrodes. *Nano Letters* **17**, 7789-7795 (2017). https://doi.org:10.1021/acs.nanolett.7b03989

56 Park, K.-Y., Zhu, Y., Torres-Castanedo, C. G., Jung, H. J., Luu, N. S., Kahvecioglu, O., Yoo, Y., Seo, J.-W. T., Downing, J. R., Lim, H.-D., Bedzyk, M. J., Wolverton, C. & Hersam, M. C. Elucidating and Mitigating High-Voltage Degradation Cascades in Cobalt-Free $LiNiO_2$ Lithium-Ion Battery Cathodes. *Advanced Materials* **34**, 2106402 (2022). https://doi.org:10.1002/adma.202106402

57 Liu, H., Wolfman, M., Karki, K., Yu, Y.-S., Stach, E. A., Cabana, J., Chapman, K. W. & Chupas, P. J. Intergranular Cracking as a Major Cause of Long-Term Capacity Fading of Layered Cathodes. *Nano Letters* **17**, 3452-3457 (2017). https://doi.org:10.1021/acs.nanolett.7b00379

58 Jiang, Z., Li, J., Yang, Y., Mu, L., Wei, C., Yu, X., Pianetta, P., Zhao, K., Cloetens, P., Lin, F. & Liu, Y. Machine-Learning-Revealed Statistics of the Particle-Carbon/Binder Detachment in Lithium-Ion Battery Cathodes. *Nature Communications* **11**, 2310 (2020). https://doi.org:10.1038/s41467-020-16233-5

59 Park, K.-Y., Park, J.-W., Seong, W. M., Yoon, K., Hwang, T.-H., Ko, K.-H., Han, J.-H., Jaedong, Y. & Kang, K. Understanding Capacity Fading Mechanism of Thick Electrodes for Lithium-Ion Rechargeable Batteries. *Journal of Power Sources* **468**, 228369 (2020). https://doi.org:10.1016/j.jpowsour.2020.228369

60 Ma, J., Li, Y., Grundish, N. S., Goodenough, J. B., Chen, Y., Guo, L., Peng, Z., Qi, X., Yang, F., Qie, L., Wang, C.-A., Huang, B., Huang, Z., Chen, L., Su, D., Wang, G., Peng, X., Chen, Z., Yang, J., He, S., Zhang, X., Yu, H., Fu, C., Jiang, M., Deng, W., Sun, C.-F., Pan, Q., Tang, Y., Li, X., Ji, X., Wan, F., Niu, Z., Lian, F., Wang, C., Wallace, G. G., Fan, M., Meng, Q., Xin, S., Guo, Y.-G. & Wan, L.-J. The 2021 battery technology roadmap. *Journal of Physics D: Applied Physics* **54**, 183001 (2021). https://doi.org:10.1088/1361-6463/abd353

61 Gauthier, M., Carney, T. J., Grimaud, A., Giordano, L., Pour, N., Chang, H.-H., Fenning, D. P., Lux, S. F., Paschos, O., Bauer, C., Maglia, F., Lupart, S., Lamp, P. & Shao-Horn, Y. Electrode–Electrolyte Interface in Li-Ion Batteries: Current Understanding and New Insights. *The Journal of Physical Chemistry Letters* **6**, 4653-4672 (2015). https://doi.org:10.1021/acs.jpclett.5b01727

62 Zhang, S. S., Jow, T. R., Amine, K. & Henriksen, G. L. $LiPF_6$–EC–EMC electrolyte for Li-ion battery. *Journal of Power Sources* **107**, 18-23 (2002). https://doi.org:10.1016/S0378-7753(01)00968-5

63 Giordano, L., Karayaylali, P., Yu, Y., Katayama, Y., Maglia, F., Lux, S. & Shao-Horn, Y. Chemical Reactivity Descriptor for the Oxide-Electrolyte Interface in Li-Ion Batteries. *The Journal of Physical Chemistry Letters* **8**, 3881-3887 (2017). https://doi.org:10.1021/acs.jpclett.7b01655

64 Zheng, L., Zhang, H., Cheng, P., Ma, Q., Liu, J., Nie, J., Feng, W. & Zhou, Z. $Li[(FSO_2)(n\text{-}C_4F_9SO_2)N]$ versus $LiPF_6$ for graphite/$LiCoO_2$ lithium-ion cells at both room and elevated temperatures: A comprehensive understanding with chemical, electrochemical and XPS analysis. *Electrochimica Acta* **196**, 169-188 (2016). https://doi.org:10.1016/j.electacta.2016.02.152

65 Østergaard, T. M., Giordano, L., Castelli, I. E., Maglia, F., Antonopoulos, B. K., Shao-Horn, Y. & Rossmeisl, J. Oxidation of Ethylene Carbonate on Li Metal Oxide Surfaces. *The Journal of Physical Chemistry C* **122**, 10442-10449 (2018). https://doi.org:10.1021/acs.jpcc.8b01713

66 Aurbach, D., Gamolsky, K., Markovsky, B., Salitra, G., Gofer, Y., Heider, U., Oesten, R. & Schmidt, M. The Study of Surface Phenomena Related to Electrochemical Lithium Intercalation into $Li_xMO_y$ Host Materials (M = Ni, Mn). *Journal of The Electrochemical Society* **147**, 1322 (2000). https://doi.org:10.1149/1.1393357

67 Yu, Y., Karayaylali, P., Katayama, Y., Giordano, L., Gauthier, M., Maglia, F., Jung, R., Lund, I. & Shao-Horn, Y. Coupled $LiPF_6$ Decomposition and Carbonate Dehydrogenation Enhanced by Highly Covalent Metal Oxides in High-Energy Li-Ion Batteries. *The Journal of Physical Chemistry C* **122**, 27368-27382 (2018). https://doi.org:10.1021/acs.jpcc.8b07848

68 Cherkashinin, G., Motzko, M., Schulz, N., Späth, T. & Jaegermann, W. Electron Spectroscopy Study of $Li[Ni,Co,Mn]O_2$/Electrolyte Interface: Electronic Structure, Interface Composition, and Device Implications. *Chemistry of Materials* **27**, 2875-2887 (2015). https://doi.org:10.1021/cm5047534

69 Dedryvère, R., Martinez, H., Leroy, S., Lemordant, D., Bonhomme, F., Biensan, P. & Gonbeau, D. Surface film formation on electrodes in a $LiCoO_2$/graphite cell: A step by step XPS study. *Journal of Power Sources* **174**, 462-468 (2007). https://doi.org:10.1016/j.jpowsour.2007.06.033

70 Li, W., Dolocan, A., Oh, P., Celio, H., Park, S., Cho, J. & Manthiram, A. Dynamic behaviour of interphases and its implication on high-energy-density cathode materials in lithium-ion batteries. *Nature Communications* **8**, 14589 (2017). https://doi.org:10.1038/ncomms14589

71 Takahashi, I., Kiuchi, H., Ohma, A., Fukunaga, T. & Matsubara, E. Cathode Electrolyte Interphase Formation and Electrolyte Oxidation Mechanism for Ni-Rich Cathode Materials. *The Journal of Physical Chemistry C* **124**, 9243-9248 (2020). https://doi.org:10.1021/acs.jpcc.0c02198

72 Liu, W., Li, J., Li, W., Xu, H., Zhang, C. & Qiu, X. Inhibition of transition metals dissolution in cobalt-free cathode with ultrathin robust interphase in concentrated electrolyte. *Nature Communications* **11**, 3629 (2020). https://doi.org:10.1038/s41467-020-17396-x

73 Kang, S.-H., Abraham, D. P., Yoon, W.-S., Nam, K.-W. & Yang, X.-Q. First-cycle irreversibility of layered Li–Ni–Co–Mn oxide cathode in Li-ion batteries. *Electrochimica Acta* **54**, 684-689 (2008). https://doi.org:10.1016/j.electacta.2008.07.007

74 Zeng, X., Xu, G.-L., Li, Y., Luo, X., Maglia, F., Bauer, C., Lux, S. F., Paschos, O., Kim, S.-J., Lamp, P., Lu, J., Amine, K. & Chen, Z. Kinetic Study of Parasitic Reactions in Lithium-Ion Batteries: A Case Study on $LiNi_{0.6}Mn_{0.2}Co_{0.2}O_2$. *ACS Applied Materials & Interfaces* **8**, 3446-3451 (2016). https://doi.org:10.1021/acsami.5b11800

75 Shafiei Sabet, P. & Sauer, D. U. Separation of predominant processes in electrochemical impedance spectra of lithium-ion batteries with nickel-manganese-cobalt cathodes.

*Journal of Power Sources* **425**, 121-129 (2019). https://doi.org:10.1016/j.jpowsour.2019.03.068

76 Zhan, C., Lu, J., Jeremy Kropf, A., Wu, T., Jansen, A. N., Sun, Y.-K., Qiu, X. & Amine, K. Mn(II) deposition on anodes and its effects on capacity fade in spinel lithium manganate–carbon systems. *Nature Communications* **4**, 2437 (2013). https://doi.org:10.1038/ncomms3437

77 Yang, H., Zhuang, G. V. & Ross, P. N. Thermal stability of $LiPF_6$ salt and Li-ion battery electrolytes containing $LiPF_6$. *Journal of Power Sources* **161**, 573-579 (2006). https://doi.org:10.1016/j.jpowsour.2006.03.058

78 Choi, W. & Manthiram, A. Comparison of Metal Ion Dissolutions from Lithium Ion Battery Cathodes. *Journal of The Electrochemical Society* **153**, A1760 (2006). https://doi.org:10.1149/1.2219710

79 Lopes, P. P., Zorko, M., Hawthorne, K. L., Connell, J. G., Ingram, B. J., Strmcnik, D., Stamenkovic, V. R. & Markovic, N. M. Real-Time Monitoring of Cation Dissolution/Deintercalation Kinetics from Transition-Metal Oxides in Organic Environments. *The Journal of Physical Chemistry Letters* **9**, 4935-4940 (2018). https://doi.org:10.1021/acs.jpclett.8b01936

80 Yang, X., Chen, J., Zheng, Q., Tu, W., Xing, L., Liao, Y., Xu, M., Huang, Q., Cao, G. & Li, W. Mechanism of cycling degradation and strategy to stabilize a nickel-rich cathode. *Journal of Materials Chemistry A* **6**, 16149-16163 (2018). https://doi.org:10.1039/C8TA03041C

81 Zheng, H., Sun, Q., Liu, G., Song, X. & Battaglia, V. S. Correlation between dissolution behavior and electrochemical cycling performance for $LiNi_{1/3}Co_{1/3}Mn_{1/3}O_2$-based cells. *Journal of Power Sources* **207**, 134-140 (2012). https://doi.org:10.1016/j.jpowsour.2012.01.122

82 Knight, J. C. & Manthiram, A. Effect of nickel oxidation state on the structural and electrochemical characteristics of lithium-rich layered oxide cathodes. *Journal of Materials Chemistry A* **3**, 22199-22207 (2015). https://doi.org:10.1039/C5TA05703E

83 Han, J.-G., Lee, S. J., Lee, J., Kim, J.-S., Lee, K. T. & Choi, N.-S. Tunable and Robust Phosphite-Derived Surface Film to Protect Lithium-Rich Cathodes in Lithium-Ion Batteries. *ACS Applied Materials & Interfaces* **7**, 8319-8329 (2015). https://doi.org:10.1021/acsami.5b01770

84 Liu, T., Dai, A., Lu, J., Yuan, Y., Xiao, Y., Yu, L., Li, M., Gim, J., Ma, L., Liu, J., Zhan, C., Li, L., Zheng, J., Ren, Y., Wu, T., Shahbazian-Yassar, R., Wen, J., Pan, F. & Amine,

K. Correlation between manganese dissolution and dynamic phase stability in spinel-based lithium-ion battery. *Nature Communications* **10**, 4721 (2019). https://doi.org:10.1038/s41467-019-12626-3

85 Lin, F., Markus, I. M., Nordlund, D., Weng, T.-C., Asta, M. D., Xin, H. L. & Doeff, M. M. Surface reconstruction and chemical evolution of stoichiometric layered cathode materials for lithium-ion batteries. *Nature Communications* **5**, 3529 (2014). https://doi.org:10.1038/ncomms4529

86 Zhan, C., Wu, T., Lu, J. & Amine, K. Dissolution, migration, and deposition of transition metal ions in Li-ion batteries exemplified by Mn-based cathodes – a critical review. *Energy & Environmental Science* **11**, 243-257 (2018). https://doi.org:10.1039/C7EE03122J

87 Gilbert, J. A., Shkrob, I. A. & Abraham, D. P. Transition Metal Dissolution, Ion Migration, Electrocatalytic Reduction and Capacity Loss in Lithium-Ion Full Cells. *Journal of The Electrochemical Society* **164**, A389-A399 (2017). https://doi.org:10.1149/2.1111702jes

88 Li, W. Review—An Unpredictable Hazard in Lithium-ion Batteries from Transition Metal Ions: Dissolution from Cathodes, Deposition on Anodes and Elimination Strategies. *Journal of The Electrochemical Society* **167**, 090514 (2020). https://doi.org:10.1149/1945-7111/ab847f

89 Hu, E., Yu, X., Lin, R., Bi, X., Lu, J., Bak, S., Nam, K.-W., Xin, H. L., Jaye, C., Fischer, D. A., Amine, K. & Yang, X.-Q. Evolution of Redox Couples in Li- and Mn-Rich Cathode Materials and Mitigation of Voltage Fade by Reducing Oxygen Release. *Nature Energy* **3**, 690-698 (2018). https://doi.org:10.1038/s41560-018-0207-z

90 Kong, F., Liang, C., Wang, L., Zheng, Y., Perananthan, S., Longo, R. C., Ferraris, J. P., Kim, M. & Cho, K. Kinetic Stability of Bulk $LiNiO_2$ and Surface Degradation by Oxygen Evolution in $LiNiO_2$-Based Cathode Materials. *Advanced Energy Materials* **9**, 1802586 (2019). https://doi.org:10.1002/aenm.201802586

91 Bak, S.-M., Hu, E., Zhou, Y., Yu, X., Senanayake, S. D., Cho, S.-J., Kim, K.-B., Chung, K. Y., Yang, X.-Q. & Nam, K.-W. Structural Changes and Thermal Stability of Charged $LiNi_xMn_yCo_zO_2$ Cathode Materials Studied by Combined In Situ Time-Resolved XRD and Mass Spectroscopy. *ACS Applied Materials & Interfaces* **6**, 22594-22601 (2014). https://doi.org:10.1021/am506712c

92 Papp, J. K., Li, N., Kaufman, L. A., Naylor, A. J., Younesi, R., Tong, W. & McCloskey, B. D. A Comparison of High Voltage Outgassing of $LiCoO_2$, $LiNiO_2$, and $Li_2MnO_3$

Layered Li-Ion Cathode Materials. *Electrochimica Acta* **368**, 137505 (2021). https://doi.org:10.1016/j.electacta.2020.137505

93 Armstrong, A. R., Holzapfel, M., Novák, P., Johnson, C. S., Kang, S.-H., Thackeray, M. M. & Bruce, P. G. Demonstrating Oxygen Loss and Associated Structural Reorganization in the Lithium Battery Cathode $Li[Ni_{0.2}Li_{0.2}Mn_{0.6}]O_2$. *Journal of the American Chemical Society* **128**, 8694-8698 (2006). https://doi.org:10.1021/ja062027+

94 Crafton, M. J., Yue, Y., Huang, T.-Y., Tong, W. & McCloskey, B. D. Anion Reactivity in Cation-Disordered Rocksalt Cathode Materials: The Influence of Fluorine Substitution. *Advanced Energy Materials* **10**, 2001500 (2020). https://doi.org:10.1002/aenm.202001500

95 Kong, W., Li, H., Huang, X. & Chen, L. Gas evolution behaviors for several cathode materials in lithium-ion batteries. *Journal of Power Sources* **142**, 285-291 (2005). https://doi.org:10.1016/j.jpowsour.2004.10.008

96 Holzapfel, M., Würsig, A., Scheifele, W., Vetter, J. & Novák, P. Oxygen, hydrogen, ethylene and $CO_2$ development in lithium-ion batteries. *Journal of Power Sources* **174**, 1156-1160 (2007). https://doi.org:10.1016/j.jpowsour.2007.06.182

97 Wuersig, A., Scheifele, W. & Novák, P. $CO_2$ Gas Evolution on Cathode Materials for Lithium-Ion Batteries. *Journal of The Electrochemical Society* **154**, A449 (2007). https://doi.org:10.1149/1.2712138

98 Zheng, J., Liu, T., Hu, Z., Wei, Y., Song, X., Ren, Y., Wang, W., Rao, M., Lin, Y., Chen, Z., Lu, J., Wang, C., Amine, K. & Pan, F. Tuning of Thermal Stability in Layered $Li(Ni_xMn_yCo_z)O_2$. *Journal of the American Chemical Society* **138**, 13326-13334 (2016). https://doi.org:10.1021/jacs.6b07771

99 Seo, D.-H., Lee, J., Urban, A., Malik, R., Kang, S. & Ceder, G. The Structural and Chemical Origin of the Oxygen Redox Activity in Layered and Cation-Disordered Li-Excess Cathode Materials. *Nature Chemistry* **8**, 692-697 (2016). https://doi.org:10.1038/nchem.2524

100 McCalla, E., Abakumov, A. M., Saubanère, M., Foix, D., Berg, E. J., Rousse, G., Doublet, M.-L., Gonbeau, D., Novák, P., Van Tendeloo, G., Dominko, R. & Tarascon, J.-M. Visualization of O-O Peroxo-Like Dimers in High-Capacity Layered Oxides for Li-Ion Batteries. *Science* **350**, 1516-1521 (2015). https://doi.org:10.1126/science.aac8260 %J Science

101 Jung, R., Metzger, M., Maglia, F., Stinner, C. & Gasteiger, H. A. Oxygen Release and Its Effect on the Cycling Stability of $LiNi_xMn_yCo_zO_2$ (NMC) Cathode Materials for Li-Ion

Batteries. *Journal of The Electrochemical Society* **164**, A1361 (2017). https://doi.org:10.1149/2.0021707jes

102 Zou, L., Zhao, W., Jia, H., Zheng, J., Li, L., Abraham, D. P., Chen, G., Croy, J. R., Zhang, J.-G. & Wang, C. The Role of Secondary Particle Structures in Surface Phase Transitions of Ni-Rich Cathodes. *Chemistry of Materials* **32**, 2884-2892 (2020). https://doi.org:10.1021/acs.chemmater.9b04938

103 Sharifi-Asl, S., Soto, F. A., Foroozan, T., Asadi, M., Yuan, Y., Deivanayagam, R., Rojaee, R., Song, B., Bi, X., Amine, K., Lu, J., Salehi-khojin, A., Balbuena, P. B. & Shahbazian-Yassar, R. Anti-Oxygen Leaking $LiCoO_2$. *Advanced Functional Materials* **29**, 1901110 (2019). https://doi.org:10.1002/adfm.201901110

104 Seong, W. M., Cho, K.-H., Park, J.-W., Park, H., Eum, D., Lee, M. H., Kim, I.-s. S., Lim, J. & Kang, K. Controlling Residual Lithium in High-Nickel (>90 %) Lithium Layered Oxides for Cathodes in Lithium-Ion Batteries. *Angewandte Chemie International Edition* **59**, 18662-18669 (2020). https://doi.org:10.1002/anie.202007436

105 Doo, S. W., Lee, S., Kim, H., Choi, J. H. & Lee, K. T. Hydrophobic Ni-Rich Layered Oxides as Cathode Materials for Lithium-Ion Batteries. *ACS Applied Energy Materials* **2**, 6246-6253 (2019). https://doi.org:10.1021/acsaem.9b00786

106 Jung, R., Morasch, R., Karayaylali, P., Phillips, K., Maglia, F., Stinner, C., Shao-Horn, Y. & Gasteiger, H. A. Effect of Ambient Storage on the Degradation of Ni-Rich Positive Electrode Materials (NMC811) for Li-Ion Batteries. *Journal of The Electrochemical Society* **165**, A132-A141 (2018). https://doi.org:10.1149/2.0401802jes

107 Renfrew, S. E., Kaufman, L. A. & McCloskey, B. D. Altering Surface Contaminants and Defects Influences the First-Cycle Outgassing and Irreversible Transformations of $LiNi_{0.6}Mn_{0.2}Co_{0.2}O_2$. *ACS Applied Materials & Interfaces* **11**, 34913-34921 (2019). https://doi.org:10.1021/acsami.9b09992

108 Renfrew, S. E. & McCloskey, B. D. Residual Lithium Carbonate Predominantly Accounts for First Cycle $CO_2$ and CO Outgassing of Li-Stoichiometric and Li-Rich Layered Transition-Metal Oxides. *Journal of the American Chemical Society* **139**, 17853-17860 (2017). https://doi.org:10.1021/jacs.7b08461

109 McCalla, E., Carey, G. H. & Dahn, J. R. Lithium loss mechanisms during synthesis of layered $Li_xNi_{2-x}O_2$ for lithium ion batteries. *Solid State Ionics* **219**, 11-19 (2012). https://doi.org:10.1016/j.ssi.2012.05.007

110 Berbenni, V. & Marini, A. Thermogravimetry and X-ray diffraction study of the thermal decomposition processes in $Li_2CO_3$–$MnCO_3$ mixtures. *Journal of Analytical and Applied Pyrolysis* **62**, 45-62 (2002). https://doi.org:10.1016/S0165-2370(00)00211-4

111 Arai, H., Okada, S., Ohtsuka, H., Ichimura, M. & Yamaki, J. Characterization and cathode performance of $Li_{1-x}Ni_{1+x}O_2$ prepared with the excess lithium method. *Solid State Ionics* **80**, 261-269 (1995). https://doi.org:10.1016/0167-2738(95)00144-U

112 Liu, H., Yang, Y. & Zhang, J. Reaction mechanism and kinetics of lithium ion battery cathode material $LiNiO_2$ with $CO_2$. *Journal of Power Sources* **173**, 556-561 (2007). https://doi.org:10.1016/j.jpowsour.2007.04.083

113 Faenza, N. V., Bruce, L., Lebens-Higgins, Z. W., Plitz, I., Pereira, N., Piper, L. F. J. & Amatucci, G. G. Growth of Ambient Induced Surface Impurity Species on Layered Positive Electrode Materials and Impact on Electrochemical Performance. *Journal of The Electrochemical Society* **164**, A3727-A3741 (2017). https://doi.org:10.1149/2.0921714jes

114 Seong, W. M., Kim, Y. & Manthiram, A. Impact of Residual Lithium on the Adoption of High-Nickel Layered Oxide Cathodes for Lithium-Ion Batteries. *Chemistry of Materials* **32**, 9479-9489 (2020). https://doi.org:10.1021/acs.chemmater.0c02808

115 Cho, D.-H., Jo, C.-H., Cho, W., Kim, Y.-J., Yashiro, H., Sun, Y.-K. & Myung, S.-T. Effect of Residual Lithium Compounds on Layer Ni-Rich $Li[Ni_{0.7}Mn_{0.3}]O_2$. *Journal of The Electrochemical Society* **161**, A920 (2014). https://doi.org:10.1149/2.042406jes

116 Xu, C., Märker, K., Lee, J., Mahadevegowda, A., Reeves, P. J., Day, S. J., Groh, M. F., Emge, S. P., Ducati, C., Layla Mehdi, B., Tang, C. C. & Grey, C. P. Bulk Fatigue Induced by Surface Reconstruction in Layered Ni-Rich Cathodes for Li-Ion Batteries. *Nature Materials* **20**, 84-92 (2021). https://doi.org:10.1038/s41563-020-0767-8

117 Xu, B., Fell, C. R., Chi, M. & Meng, Y. S. Identifying surface structural changes in layered Li-excess nickel manganese oxides in high voltage lithium ion batteries: A joint experimental and theoretical study. *Energy & Environmental Science* **4**, 2223-2233 (2011). https://doi.org:10.1039/C1EE01131F

118 Nam, K.-W., Bak, S.-M., Hu, E., Yu, X., Zhou, Y., Wang, X., Wu, L., Zhu, Y., Chung, K.-Y. & Yang, X.-Q. Combining In Situ Synchrotron X-Ray Diffraction and Absorption Techniques with Transmission Electron Microscopy to Study the Origin of Thermal Instability in Overcharged Cathode Materials for Lithium-Ion Batteries. *Advanced Functional Materials* **23**, 1047-1063 (2013). https://doi.org:10.1002/adfm.201200693

119 Abraham, D. P., Twesten, R. D., Balasubramanian, M., Petrov, I., McBreen, J. & Amine, K. Surface changes on $LiNi_{0.8}Co_{0.2}O_2$ particles during testing of high-power lithium-ion

cells. *Electrochemistry Communications* **4**, 620-625 (2002). https://doi.org:10.1016/S1388-2481(02)00388-0

120 Zheng, J., Xu, P., Gu, M., Xiao, J., Browning, N. D., Yan, P., Wang, C. & Zhang, J.-G. Structural and Chemical Evolution of Li- and Mn-Rich Layered Cathode Material. *Chemistry of Materials* **27**, 1381-1390 (2015). https://doi.org:10.1021/cm5045978

121 Seong, W. M., Yoon, K., Lee, M. H., Jung, S.-K. & Kang, K. Unveiling the Intrinsic Cycle Reversibility of a $LiCoO_2$ Electrode at 4.8-V Cutoff Voltage through Subtractive Surface Modification for Lithium-Ion Batteries. *Nano Letters* **19**, 29-37 (2019). https://doi.org:10.1021/acs.nanolett.8b02902

122 Myeong, S., Cho, W., Jin, W., Hwang, J., Yoon, M., Yoo, Y., Nam, G., Jang, H., Han, J.-G., Choi, N.-S., Kim, M. G. & Cho, J. Understanding Voltage Decay in Lithium-Excess Layered Cathode Materials Through Oxygen-Centred Structural Arrangement. *Nature Communications* **9**, 3285 (2018). https://doi.org:10.1038/s41467-018-05802-4

123 Hayashi, T., Okada, J., Toda, E., Kuzuo, R., Oshimura, N., Kuwata, N. & Kawamura, J. Degradation Mechanism of $LiNi_{0.82}Co_{0.15}Al_{0.03}O_2$ Positive Electrodes of a Lithium-Ion Battery by a Long-Term Cycling Test. *Journal of The Electrochemical Society* **161**, A1007 (2014). https://doi.org:10.1149/2.056406jes

124 Mohanty, D., Dahlberg, K., King, D. M., David, L. A., Sefat, A. S., Wood, D. L., Daniel, C., Dhar, S., Mahajan, V., Lee, M. & Albano, F. Modification of Ni-Rich FCG NMC and NCA Cathodes by Atomic Layer Deposition: Preventing Surface Phase Transitions for High-Voltage Lithium-Ion Batteries. *Scientific Reports* **6**, 26532 (2016). https://doi.org:10.1038/srep26532

125 Lin, F., Nordlund, D., Li, Y., Quan, M. K., Cheng, L., Weng, T.-C., Liu, Y., Xin, H. L. & Doeff, M. M. Metal segregation in hierarchically structured cathode materials for high-energy lithium batteries. *Nature Energy* **1**, 15004 (2016). https://doi.org:10.1038/nenergy.2015.4

126 Wang, C., Han, L., Zhang, R., Cheng, H., Mu, L., Kisslinger, K., Zou, P., Ren, Y., Cao, P., Lin, F. & Xin, H. L. Resolving Atomic-Scale Phase Transformation and Oxygen Loss Mechanism in Ultrahigh-Nickel Layered Cathodes for Cobalt-Free Lithium-Ion Batteries. *Matter* **4**, 2013-2026 (2021). https://doi.org:10.1016/j.matt.2021.03.012

127 Kang, K. & Ceder, G. Factors that affect Li mobility in layered lithium transition metal oxides. *Physical Review B* **74**, 094105 (2006). https://doi.org:10.1103/PhysRevB.74.094105

128 Liu, W., Oh, P., Liu, X., Lee, M.-J., Cho, W., Chae, S., Kim, Y. & Cho, J. Nickel-Rich Layered Lithium Transition-Metal Oxide for High-Energy Lithium-Ion Batteries. *Angewandte Chemie International Edition* **54**, 4440-4457 (2015). https://doi.org:10.1002/anie.201409262

129 Kwon, D.-H., Lee, J., Artrith, N., Kim, H., Wu, L., Lun, Z., Tian, Y., Zhu, Y. & Ceder, G. The Impact of Surface Structure Transformations on the Performance of Li-Excess Cation-Disordered Rocksalt Cathodes. *Cell Reports Physical Science* **1**, 100187 (2020). https://doi.org:10.1016/j.xcrp.2020.100187

130 Chen, D., Kan, W. H. & Chen, G. Understanding Performance Degradation in Cation-Disordered Rock-Salt Oxide Cathodes. *Advanced Energy Materials* **9**, 1901255 (2019). https://doi.org:10.1002/aenm.201901255

131 Zhang, H., Omenya, F., Yan, P., Luo, L., Whittingham, M. S., Wang, C. & Zhou, G. Rock-Salt Growth-Induced (003) Cracking in a Layered Positive Electrode for Li-Ion Batteries. *ACS Energy Letters* **2**, 2607-2615 (2017). https://doi.org:10.1021/acsenergylett.7b00907

132 Xu, G.-L., Liu, Q., Lau, K. K. S., Liu, Y., Liu, X., Gao, H., Zhou, X., Zhuang, M., Ren, Y., Li, J., Shao, M., Ouyang, M., Pan, F., Chen, Z., Amine, K. & Chen, G. Building Ultraconformal Protective Layers on Both Secondary and Primary Particles of Layered Lithium Transition Metal Oxide Cathodes. *Nature Energy* **4**, 484-494 (2019). https://doi.org:10.1038/s41560-019-0387-1

133 Ryu, H.-H., Park, K.-J., Yoon, C. S. & Sun, Y.-K. Capacity Fading of Ni-Rich $Li[Ni_xCo_yMn_{1-x-y}]O_2$ ($0.6 \leq x \leq 0.95$) Cathodes for High-Energy-Density Lithium-Ion Batteries: Bulk or Surface Degradation? *Chemistry of Materials* **30**, 1155-1163 (2018). https://doi.org:10.1021/acs.chemmater.7b05269

134 Liu, T., Yu, L., Liu, J., Lu, J., Bi, X., Dai, A., Li, M., Li, M., Hu, Z., Ma, L., Luo, D., Zheng, J., Wu, T., Ren, Y., Wen, J., Pan, F. & Amine, K. Understanding Co Roles Towards Developing Co-Free Ni-Rich Cathodes for Rechargeable Batteries. *Nature Energy* **6**, 277-286 (2021). https://doi.org:10.1038/s41560-021-00776-y

135 Bi, Y., Tao, J., Wu, Y., Li, L., Xu, Y., Hu, E., Wu, B., Hu, J., Wang, C., Zhang, J.-G., Qi, Y. & Xiao, J. Reversible planar gliding and microcracking in a single-crystalline Ni-rich cathode. *Science* **370**, 1313-1317 (2020). https://doi.org:10.1126/science.abc3167 %J Science

136 Singer, A., Zhang, M., Hy, S., Cela, D., Fang, C., Wynn, T. A., Qiu, B., Xia, Y., Liu, Z., Ulvestad, A., Hua, N., Wingert, J., Liu, H., Sprung, M., Zozulya, A. V., Maxey, E., Harder, R., Meng, Y. S. & Shpyrko, O. G. Nucleation of Dislocations and Their

Dynamics in Layered Oxide Cathode Materials During Battery Charging. *Nature Energy* **3**, 641-647 (2018). https://doi.org:10.1038/s41560-018-0184-2

137 Yano, A., Shikano, M., Ueda, A., Sakaebe, H. & Ogumi, Z. $LiCoO_2$ Degradation Behavior in the High-Voltage Phase Transition Region and Improved Reversibility with Surface Coating. *Journal of The Electrochemical Society* **164**, A6116 (2017). https://doi.org:10.1149/2.0181701jes

138 Tian, C., Xu, Y., Nordlund, D., Lin, F., Liu, J., Sun, Z., Liu, Y. & Doeff, M. Charge Heterogeneity and Surface Chemistry in Polycrystalline Cathode Materials. *Joule* **2**, 464-477 (2018). https://doi.org:10.1016/j.joule.2017.12.008

139 Li, S., Jiang, Z., Han, J., Xu, Z., Wang, C., Huang, H., Yu, C., Lee, S.-J., Pianetta, P., Ohldag, H., Qiu, J., Lee, J.-S., Lin, F., Zhao, K. & Liu, Y. Mutual Modulation Between Surface Chemistry and Bulk Microstructure Within Secondary Particles of Nickel-Rich Layered Oxides. *Nature Communications* **11**, 4433 (2020). https://doi.org:10.1038/s41467-020-18278-y

140 Luu, N. S., Lim, J.-M., Torres-Castanedo, C. G., Park, K.-Y., Moazzen, E., He, K., Meza, P. E., Li, W., Downing, J. R., Hu, X., Dravid, V. P., Barnett, S. A., Bedzyk, M. J. & Hersam, M. C. Elucidating and Mitigating High-Voltage Interfacial Chemomechanical Degradation of Nickel-Rich Lithium-Ion Battery Cathodes via Conformal Graphene Coating. *ACS Applied Energy Materials* **4**, 11069-11079 (2021). https://doi.org:10.1021/acsaem.1c01995

141 Tsai, P.-C., Wen, B., Wolfman, M., Choe, M.-J., Pan, M. S., Su, L., Thornton, K., Cabana, J. & Chiang, Y.-M. Single-Particle Measurements of Electrochemical Kinetics in NMC And NCA Cathodes for Li-Ion Batteries. *Energy & Environmental Science* **11**, 860-871 (2018). https://doi.org:10.1039/C8EE00001H

142 Gent, W. E., Li, Y., Ahn, S., Lim, J., Liu, Y., Wise, A. M., Gopal, C. B., Mueller, D. N., Davis, R., Weker, J. N., Park, J.-H., Doo, S.-K. & Chueh, W. C. Persistent State-of-Charge Heterogeneity in Relaxed, Partially Charged $Li_{1-x}Ni_{1/3}Co_{1/3}Mn_{1/3}O_2$ Secondary Particles. *Advanced Materials* **28**, 6631-6638 (2016). https://doi.org:10.1002/adma.201601273

143 Qian, G., Zhang, J., Chu, S.-Q., Li, J., Zhang, K., Yuan, Q., Ma, Z.-F., Pianetta, P., Li, L., Jung, K. & Liu, Y. Understanding the Mesoscale Degradation in Nickel-Rich Cathode Materials through Machine-Learning-Revealed Strain–Redox Decoupling. *ACS Energy Letters* **6**, 687-693 (2021). https://doi.org:10.1021/acsenergylett.0c02699

144 Yang, Y., Xu, R., Zhang, K., Lee, S.-J., Mu, L., Liu, P., Waters, C. K., Spence, S., Xu, Z., Wei, C., Kautz, D. J., Yuan, Q., Dong, Y., Yu, Y.-S., Xiao, X., Lee, H.-K., Pianetta,

P., Cloetens, P., Lee, J.-S., Zhao, K., Lin, F. & Liu, Y. Quantification of Heterogeneous Degradation in Li-Ion Batteries. *Advanced Energy Materials* **9**, 1900674 (2019). https://doi.org:10.1002/aenm.201900674

145 Park, J., Zhao, H., Kang, S. D., Lim, K., Chen, C.-C., Yu, Y.-S., Braatz, R. D., Shapiro, D. A., Hong, J., Toney, M. F., Bazant, M. Z. & Chueh, W. C. Fictitious Phase Separation in Li Layered Oxides Driven by Electro-Autocatalysis. *Nature Materials* **20**, 991-999 (2021). https://doi.org:10.1038/s41563-021-00936-1

146 Murayama, H., Kitada, K., Fukuda, K., Mitsui, A., Ohara, K., Arai, H., Uchimoto, Y., Ogumi, Z. & Matsubara, E. Spectroscopic X-ray Diffraction for Microfocus Inspection of Li-Ion Batteries. *The Journal of Physical Chemistry C* **118**, 20750-20755 (2014). https://doi.org:10.1021/jp5029273

147 Li, Z., Yin, L., Mattei, G. S., Cosby, M. R., Lee, B.-S., Wu, Z., Bak, S.-M., Chapman, K. W., Yang, X.-Q., Liu, P. & Khalifah, P. G. Synchrotron Operando Depth Profiling Studies of State-of-Charge Gradients in Thick $Li(Ni_{0.8}Mn_{0.1}Co_{0.1})O_2$ Cathode Films. *Chemistry of Materials* **32**, 6358-6364 (2020). https://doi.org:10.1021/acs.chemmater.0c00983

148 Liu, H., Kazemiabnavi, S., Grenier, A., Vaughan, G., Di Michiel, M., Polzin, B. J., Thornton, K., Chapman, K. W. & Chupas, P. J. Quantifying Reaction and Rate Heterogeneity in Battery Electrodes in 3D through Operando X-ray Diffraction Computed Tomography. *ACS Applied Materials & Interfaces* **11**, 18386-18394 (2019). https://doi.org:10.1021/acsami.9b02173

149 Liu, H., Foster, J. M., Gully, A., Krachkovskiy, S., Jiang, M., Wu, Y., Yang, X., Protas, B., Goward, G. R. & Botton, G. A. Three-Dimensional Investigation of Cycling-Induced Microstructural Changes in Lithium-Ion Battery Cathodes Using Focused Ion Beam/Scanning Electron Microscopy. *Journal of Power Sources* **306**, 300-308 (2016). https://doi.org:10.1016/j.jpowsour.2015.11.108

150 Weigel, T., Schipper, F., Erickson, E. M., Susai, F. A., Markovsky, B. & Aurbach, D. Structural and Electrochemical Aspects of $LiNi_{0.8}Co_{0.1}Mn_{0.1}O_2$ Cathode Materials Doped by Various Cations. *ACS Energy Letters* **4**, 508-516 (2019). https://doi.org:10.1021/acsenergylett.8b02302

151 Shin, Y., Kan, W. H., Aykol, M., Papp, J. K., McCloskey, B. D., Chen, G. & Persson, K. A. Alleviating Oxygen Evolution from Li-Excess Oxide Materials through Theory-Guided Surface Protection. *Nature Communications* **9**, 4597 (2018). https://doi.org:10.1038/s41467-018-07080-6

152 Kim, U.-H., Park, G.-T., Son, B.-K., Nam, G. W., Liu, J., Kuo, L.-Y., Kaghazchi, P., Yoon, C. S. & Sun, Y.-K. Heuristic Solution for Achieving Long-Term Cycle Stability for Ni-Rich Layered Cathodes at Full Depth of Discharge. *Nature Energy* **5**, 860-869 (2020). https://doi.org:10.1038/s41560-020-00693-6

153 Yoon, C. S., Kim, U.-H., Park, G.-T., Kim, S. J., Kim, K.-H., Kim, J. & Sun, Y.-K. Self-Passivation of a $LiNiO_2$ Cathode for a Lithium-Ion Battery through Zr Doping. *ACS Energy Letters* **3**, 1634-1639 (2018). https://doi.org:10.1021/acsenergylett.8b00805

154 Lee, J., Papp, J. K., Clément, R. J., Sallis, S., Kwon, D.-H., Shi, T., Yang, W., McCloskey, B. D. & Ceder, G. Mitigating Oxygen Loss to Improve the Cycling Performance of High Capacity Cation-Disordered Cathode Materials. *Nature Communications* **8**, 981 (2017). https://doi.org:10.1038/s41467-017-01115-0

155 Kim, U.-H., Ryu, H.-H., Kim, J.-H., Mücke, R., Kaghazchi, P., Yoon, C. S. & Sun, Y.-K. Microstructure-Controlled Ni-Rich Cathode Material by Microscale Compositional Partition for Next-Generation Electric Vehicles. *Advanced Energy Materials* **9**, 1803902 (2019). https://doi.org:10.1002/aenm.201803902

156 Wang, L., Wang, R., Wang, J., Xu, R., Wang, X. & Zhan, C. Nanowelding to Improve the Chemomechanical Stability of the Ni-Rich Layered Cathode Materials. *ACS Applied Materials & Interfaces* **13**, 8324-8336 (2021). https://doi.org:10.1021/acsami.0c20100

157 Yan, P., Zheng, J., Liu, J., Wang, B., Cheng, X., Zhang, Y., Sun, X., Wang, C. & Zhang, J.-G. Tailoring Grain Boundary Structures and Chemistry of Ni-Rich Layered Cathodes for Enhanced Cycle Stability of Lithium-Ion Batteries. *Nature Energy* **3**, 600-605 (2018). https://doi.org:10.1038/s41560-018-0191-3

158 Yoon, M., Dong, Y., Hwang, J., Sung, J., Cha, H., Ahn, K., Huang, Y., Kang, S. J., Li, J. & Cho, J. Reactive Boride Infusion Stabilizes Ni-Rich Cathodes for Lithium-Ion Batteries. *Nature Energy* (2021). https://doi.org:10.1038/s41560-021-00782-0

159 Sun, H. H., Dolocan, A., Weeks, J. A., Heller, A. & Mullins, C. B. Stabilization of a Highly Ni-Rich Layered Oxide Cathode through Flower-Petal Grain Arrays. *ACS Nano* **14**, 17142-17150 (2020). https://doi.org:10.1021/acsnano.0c06910

160 Ryu, H.-H., Park, N.-Y., Noh, T.-C., Kang, G.-C., Maglia, F., Kim, S.-J., Yoon, C. S. & Sun, Y.-K. Microstrain Alleviation in High-Energy Ni-Rich NCMA Cathode for Long Battery Life. *ACS Energy Letters* **6**, 216-223 (2021). https://doi.org:10.1021/acsenergylett.0c02281

161 Castellanos-Gomez, A. Why all the fuss about 2D semiconductors? *Nature Photonics* **10**, 202-204 (2016). https://doi.org:10.1038/nphoton.2016.53

162 Splendiani, A., Sun, L., Zhang, Y., Li, T., Kim, J., Chim, C.-Y., Galli, G. & Wang, F. Emerging Photoluminescence in Monolayer $MoS_2$. *Nano Letters* **10**, 1271-1275 (2010). https://doi.org:10.1021/nl903868w

163 Reina, A., Jia, X., Ho, J., Nezich, D., Son, H., Bulovic, V., Dresselhaus, M. S. & Kong, J. Large Area, Few-Layer Graphene Films on Arbitrary Substrates by Chemical Vapor Deposition. *Nano Letters* **9**, 30-35 (2009). https://doi.org:10.1021/nl801827v

164 Li, X., Cai, W., An, J., Kim, S., Nah, J., Yang, D., Piner, R., Velamakanni, A., Jung, I., Tutuc, E., Banerjee, S. K., Colombo, L. & Ruoff, R. S. Large-Area Synthesis of High-Quality and Uniform Graphene Films on Copper Foils. *Science* **324**, 1312-1314 (2009). https://doi.org:10.1126/science.1171245

165 Park, J., Mitchel, W. C., Grazulis, L., Smith, H. E., Eyink, K. G., Boeckl, J. J., Tomich, D. H., Pacley, S. D. & Hoelscher, J. E. Epitaxial Graphene Growth by Carbon Molecular Beam Epitaxy (CMBE). *Advanced Materials* **22**, 4140-4145 (2010). https://doi.org:10.1002/adma.201000756

166 Moreau, E., Ferrer, F. J., Vignaud, D., Godey, S. & Wallart, X. Graphene growth by molecular beam epitaxy using a solid carbon source. *physica status solidi (a)* **207**, 300-303 (2010). https://doi.org:10.1002/pssa.200982412

167 Ciesielski, A. & Samorì, P. Graphene via sonication assisted liquid-phase exfoliation. *Chemical Society Reviews* **43**, 381-398 (2014). https://doi.org:10.1039/C3CS60217F

168 Hernandez, Y., Nicolosi, V., Lotya, M., Blighe, F. M., Sun, Z., De, S., McGovern, I. T., Holland, B., Byrne, M., Gun'Ko, Y. K., Boland, J. J., Niraj, P., Duesberg, G., Krishnamurthy, S., Goodhue, R., Hutchison, J., Scardaci, V., Ferrari, A. C. & Coleman, J. N. High-yield production of graphene by liquid-phase exfoliation of graphite. *Nature Nanotechnology* **3**, 563-568 (2008). https://doi.org:10.1038/nnano.2008.215

169 Liang, Y. T. & Hersam, M. C. Highly Concentrated Graphene Solutions via Polymer Enhanced Solvent Exfoliation and Iterative Solvent Exchange. *Journal of the American Chemical Society* **132**, 17661-17663 (2010). https://doi.org:10.1021/ja107661g

170 Kang, J., Sangwan, V. K., Wood, J. D. & Hersam, M. C. Solution-Based Processing of Monodisperse Two-Dimensional Nanomaterials. *Accounts of Chemical Research* **50**, 943-951 (2017). https://doi.org:10.1021/acs.accounts.6b00643

171 Secor, E. B., Prabhumirashi, P. L., Puntambekar, K., Geier, M. L. & Hersam, M. C. Inkjet Printing of High Conductivity, Flexible Graphene Patterns. *The Journal of Physical Chemistry Letters* **4**, 1347-1351 (2013). https://doi.org:10.1021/jz400644c

172 Secor, E. B., Ahn, B. Y., Gao, T. Z., Lewis, J. A. & Hersam, M. C. Rapid and Versatile Photonic Annealing of Graphene Inks for Flexible Printed Electronics. *Advanced Materials* **27**, 6683-6688 (2015). https://doi.org:10.1002/adma.201502866

173 Li, L., Secor, E. B., Chen, K.-S., Zhu, J., Liu, X., Gao, T. Z., Seo, J.-W. T., Zhao, Y. & Hersam, M. C. High-Performance Solid-State Supercapacitors and Microsupercapacitors Derived from Printable Graphene Inks. *Advanced Energy Materials* **6**, 1600909 (2016). https://doi.org:10.1002/aenm.201600909

174 Green, A. A. & Hersam, M. C. Solution Phase Production of Graphene with Controlled Thickness via Density Differentiation. *Nano Letters* **9**, 4031-4036 (2009). https://doi.org:10.1021/nl902200b

175 Backes, C., Szydłowska, B. M., Harvey, A., Yuan, S., Vega-Mayoral, V., Davies, B. R., Zhao, P.-l., Hanlon, D., Santos, E. J. G., Katsnelson, M. I., Blau, W. J., Gadermaier, C. & Coleman, J. N. Production of Highly Monolayer Enriched Dispersions of Liquid-Exfoliated Nanosheets by Liquid Cascade Centrifugation. *ACS Nano* **10**, 1589-1601 (2016). https://doi.org:10.1021/acsnano.5b07228

176 Baumann, A. E., Downing, J. R., Burns, D. A., Hersam, M. C. & Thoi, V. S. Graphene–Metal–Organic Framework Composite Sulfur Electrodes for Li–S Batteries with High Volumetric Capacity. *ACS Applied Materials & Interfaces* **12**, 37173-37181 (2020). https://doi.org:10.1021/acsami.0c09622

177 Chen, K.-S., Balla, I., Luu, N. S. & Hersam, M. C. Emerging Opportunities for Two-Dimensional Materials in Lithium-Ion Batteries. *ACS Energy Letters* **2**, 2026-2034 (2017). https://doi.org:10.1021/acsenergylett.7b00476

178 Bolotin, K. I., Sikes, K. J., Jiang, Z., Klima, M., Fudenberg, G., Hone, J., Kim, P. & Stormer, H. L. Ultrahigh electron mobility in suspended graphene. *Solid State Communications* **146**, 351-355 (2008). https://doi.org:10.1016/j.ssc.2008.02.024

179 Chen, K.-S., Xu, R., Luu, N. S., Secor, E. B., Hamamoto, K., Li, Q., Kim, S., Sangwan, V. K., Balla, I., Guiney, L. M., Seo, J.-W. T., Yu, X., Liu, W., Wu, J., Wolverton, C., Dravid, V. P., Barnett, S. A., Lu, J., Amine, K. & Hersam, M. C. Comprehensive Enhancement of Nanostructured Lithium-Ion Battery Cathode Materials via Conformal Graphene Dispersion. *Nano Letters* **17**, 2539-2546 (2017). https://doi.org:10.1021/acs.nanolett.7b00274

180 Lim, J.-M., Kim, S., Luu, N. S., Downing, J. R., Tan, M. T. Z., Park, K.-Y., Hechter, J. C., Dravid, V. P., He, K. & Hersam, M. C. High Volumetric Energy and Power Density

$Li_2TiSiO_5$ Battery Anodes via Graphene Functionalization. *Matter* **3**, 522-533 (2020). https://doi.org:10.1016/j.matt.2020.07.017

181 Chatterjee, S., Carter, R., Oakes, L., Erwin, W. R., Bardhan, R. & Pint, C. L. Electrochemical and Corrosion Stability of Nanostructured Silicon by Graphene Coatings: Toward High Power Porous Silicon Supercapacitors. *The Journal of Physical Chemistry C* **118**, 10893-10902 (2014). https://doi.org:10.1021/jp502079f

182 Li, Y., Yan, K., Lee, H.-W., Lu, Z., Liu, N. & Cui, Y. Growth of conformal graphene cages on micrometre-sized silicon particles as stable battery anodes. *Nature Energy* **1**, 15029 (2016). https://doi.org:10.1038/nenergy.2015.29

183 Liu, N., Lu, Z., Zhao, J., McDowell, M. T., Lee, H.-W., Zhao, W. & Cui, Y. A pomegranate-inspired nanoscale design for large-volume-change lithium battery anodes. *Nature Nanotechnology* **9**, 187-192 (2014). https://doi.org:10.1038/nnano.2014.6

184 Jaber-Ansari, L., Puntambekar, K. P., Kim, S., Aykol, M., Luo, L., Wu, J., Myers, B. D., Iddir, H., Russell, J. T., Saldaña, S. J., Kumar, R., Thackeray, M. M., Curtiss, L. A., Dravid, V. P., Wolverton, C. & Hersam, M. C. Suppressing Manganese Dissolution from Lithium Manganese Oxide Spinel Cathodes with Single-Layer Graphene. *Advanced Energy Materials* **5**, 1500646 (2015). https://doi.org:10.1002/aenm.201500646

185 Kim, I. T., Knight, J. C., Celio, H. & Manthiram, A. Enhanced electrochemical performances of Li-rich layered oxides by surface modification with reduced graphene oxide/$AlPO_4$ hybrid coating. *Journal of Materials Chemistry A* **2**, 8696-8704 (2014). https://doi.org:10.1039/C4TA00898G

186 Ye, H., Xin, S., Yin, Y.-X. & Guo, Y.-G. Advanced Porous Carbon Materials for High-Efficient Lithium Metal Anodes. *Advanced Energy Materials* **7**, 1700530 (2017). https://doi.org:10.1002/aenm.201700530

187 Shim, J.-H., Kim, Y.-M., Park, M., Kim, J. & Lee, S. Reduced Graphene Oxide-Wrapped Nickel-Rich Cathode Materials for Lithium Ion Batteries. *ACS Applied Materials & Interfaces* **9**, 18720-18729 (2017). https://doi.org:10.1021/acsami.7b02654

188 Park, K.-Y., Lim, J.-M., Luu, N. S., Downing, J. R., Wallace, S. G., Chaney, L. E., Yoo, H., Hyun, W. J., Kim, H.-U. & Hersam, M. C. Concurrently Approaching Volumetric and Specific Capacity Limits of Lithium Battery Cathodes via Conformal Pickering Emulsion Graphene Coatings. *Advanced Energy Materials* **10**, 2001216 (2020). https://doi.org:10.1002/aenm.202001216

189 Zhou, G., Wang, D.-W., Li, F., Zhang, L., Li, N., Wu, Z.-S., Wen, L., Lu, G. Q. & Cheng, H.-M. Graphene-Wrapped $Fe_3O_4$ Anode Material with Improved Reversible

Capacity and Cyclic Stability for Lithium Ion Batteries. *Chemistry of Materials* **22**, 5306-5313 (2010). https://doi.org:10.1021/cm101532x

190 Lim, J.-M., Luu, N. S., Park, K.-Y., Tan, M. T. Z., Kim, S., Downing, J. R., He, K., Dravid, V. P. & Hersam, M. C. Enhancing Nanostructured Nickel-Rich Lithium-Ion Battery Cathodes via Surface Stabilization. *Journal of Vacuum Science & Technology A* **38**, 063210 (2020). https://doi.org:10.1116/6.0000580

191 Lee, J. K., Smith, K. B., Hayner, C. M. & Kung, H. H. Silicon nanoparticles–graphene paper composites for Li ion battery anodes. *Chemical Communications* **46**, 2025-2027 (2010). https://doi.org:10.1039/B919738A

192 Ma, D., Li, Y., Wu, M., Deng, L., Ren, X. & Zhang, P. Enhanced cycling stability of Li-rich nanotube cathodes by 3D graphene hierarchical architectures for Li-ion batteries. *Acta Materialia* **112**, 11-19 (2016). https://doi.org:10.1016/j.actamat.2016.04.010

193 Liang, Z., Lin, D., Zhao, J., Lu, Z., Liu, Y., Liu, C., Lu, Y., Wang, H., Yan, K., Tao, X. & Cui, Y. Composite lithium metal anode by melt infusion of lithium into a 3D conducting scaffold with lithiophilic coating. *Proceedings of the National Academy of Sciences* **113**, 2862-2867 (2016). https://doi.org:10.1073/pnas.1518188113

194 Zhao, J., Zhou, G., Yan, K., Xie, J., Li, Y., Liao, L., Jin, Y., Liu, K., Hsu, P.-C., Wang, J., Cheng, H.-M. & Cui, Y. Air-stable and freestanding lithium alloy/graphene foil as an alternative to lithium metal anodes. *Nature Nanotechnology* **12**, 993-999 (2017). https://doi.org:10.1038/nnano.2017.129

195 Wu, Z.-S., Ren, W., Wen, L., Gao, L., Zhao, J., Chen, Z., Zhou, G., Li, F. & Cheng, H.-M. Graphene Anchored with $Co_3O_4$ Nanoparticles as Anode of Lithium Ion Batteries with Enhanced Reversible Capacity and Cyclic Performance. *ACS Nano* **4**, 3187-3194 (2010). https://doi.org:10.1021/nn100740x

196 Lang, J., Jin, Y., Luo, X., Liu, Z., Song, J., Long, Y., Qi, L., Fang, M., Li, Z. & Wu, H. Surface graphited carbon scaffold enables simple and scalable fabrication of 3D composite lithium metal anode. *Journal of Materials Chemistry A* **5**, 19168-19174 (2017). https://doi.org:10.1039/C7TA05997C

197 Hummers, W. S., Jr. & Offeman, R. E. Preparation of Graphitic Oxide. *Journal of the American Chemical Society* **80**, 1339-1339 (1958). https://doi.org:10.1021/ja01539a017

198 Compton, O. C. & Nguyen, S. T. Graphene Oxide, Highly Reduced Graphene Oxide, and Graphene: Versatile Building Blocks for Carbon-Based Materials. *Small* **6**, 711-723 (2010). https://doi.org:10.1002/smll.200901934

199 Bai, H., Li, C. & Shi, G. Functional Composite Materials Based on Chemically Converted Graphene. *Advanced Materials* **23**, 1089-1115 (2011). https://doi.org:10.1002/adma.201003753

200 Secor, E. B., Gao, T. Z., Islam, A. E., Rao, R., Wallace, S. G., Zhu, J., Putz, K. W., Maruyama, B. & Hersam, M. C. Enhanced Conductivity, Adhesion, and Environmental Stability of Printed Graphene Inks with Nitrocellulose. *Chemistry of Materials* **29**, 2332-2340 (2017). https://doi.org:10.1021/acs.chemmater.7b00029

201 Secor, E. B., Lim, S., Zhang, H., Frisbie, C. D., Francis, L. F. & Hersam, M. C. Gravure Printing of Graphene for Large-area Flexible Electronics. *Advanced Materials* **26**, 4533-4538 (2014). https://doi.org:10.1002/adma.201401052

202 Myung, S.-T., Maglia, F., Park, K.-J., Yoon, C. S., Lamp, P., Kim, S.-J. & Sun, Y.-K. Nickel-Rich Layered Cathode Materials for Automotive Lithium-Ion Batteries: Achievements and Perspectives. *ACS Energy Letters* **2**, 196-223 (2017). https://doi.org:10.1021/acsenergylett.6b00594

203 Xia, Y., Zheng, J., Wang, C. & Gu, M. Designing principle for Ni-rich cathode materials with high energy density for practical applications. *Nano Energy* **49**, 434-452 (2018). https://doi.org:10.1016/j.nanoen.2018.04.062

204 Talyosef, Y., Markovsky, B., Lavi, R., Salitra, G., Aurbach, D., Kovacheva, D., Gorova, M., Zhecheva, E. & Stoyanova, R. Comparing the Behavior of Nano- and Microsized Particles of $LiMn_{1.5}Ni_{0.5}O_4$ Spinel as Cathode Materials for Li-Ion Batteries. *Journal of The Electrochemical Society* **154**, A682 (2007). https://doi.org:10.1149/1.2736657

205 Collins, J., de Souza, J. P., Hopstaken, M., Ott, J. A., Bedell, S. W. & Sadana, D. K. Diffusion-Controlled Porous Crystalline Silicon Lithium Metal Batteries. *iScience* **23**, 101586 (2020). https://doi.org:10.1016/j.isci.2020.101586

206 Collins, J., Gourdin, G., Foster, M. & Qu, D. Carbon surface functionalities and SEI formation during Li intercalation. *Carbon* **92**, 193-244 (2015). https://doi.org:10.1016/j.carbon.2015.04.007

207 Wang, C., Shao, L., Guo, X., Xi, X., Yang, L., Huang, C., Zhou, C., Zhao, H., Yin, D. & Wang, Z. Air-Induced Degradation and Electrochemical Regeneration for the Performance of Layered Ni-Rich Cathodes. *ACS Applied Materials & Interfaces* **11**, 44036-44045 (2019). https://doi.org:10.1021/acsami.9b11452

208 Zhuang, G. V., Chen, G., Shim, J., Song, X., Ross, P. N. & Richardson, T. J. $Li_2CO_3$ in $LiNi_{0.8}Co_{0.15}Al_{0.05}O_2$ cathodes and its effects on capacity and power. *Journal of Power Sources* **134**, 293-297 (2004). https://doi.org:10.1016/j.jpowsour.2004.02.030

209 Grenier, A., Liu, H., Wiaderek, K. M., Lebens-Higgins, Z. W., Borkiewicz, O. J., Piper, L. F. J., Chupas, P. J. & Chapman, K. W. Reaction Heterogeneity in $LiNi_{0.8}Co_{0.15}Al_{0.05}O_2$ Induced by Surface Layer. *Chemistry of Materials* **29**, 7345-7352 (2017). https://doi.org:10.1021/acs.chemmater.7b02236

210 Ramakrishnan, S., Park, B., Wu, J., Yang, W. & McCloskey, B. D. Extended Interfacial Stability through Simple Acid Rinsing in a Li-Rich Oxide Cathode Material. *Journal of the American Chemical Society* **142**, 8522-8531 (2020). https://doi.org:10.1021/jacs.0c02859

211 Jones, J. C., Rajendran, S., Pilli, A., Lee, V., Chugh, N., Arava, L. M. R. & Kelber, J. A. In situ x-ray photoelectron spectroscopy study of lithium carbonate removal from garnet-type solid-state electrolyte using ultra high vacuum techniques. *Journal of Vacuum Science & Technology A* **38**, 023201 (2020). https://doi.org:10.1116/1.5128102

212 Dai, G., Du, H., Wang, S., Cao, J., Yu, M., Chen, Y., Tang, Y., Li, A. & Chen, Y. Improved electrochemical performance of $LiNi_{0.8}Co_{0.15}Al_{0.05}O_2$ with ultrathin and thickness-controlled $TiO_2$ shell via atomic layer deposition technology. *RSC Advances* **6**, 100841-100848 (2016). https://doi.org:10.1039/C6RA21903A

213 Cho, Y. & Cho, J. Significant Improvement of $LiNi_{0.8}Co_{0.15}Al_{0.05}O_2$ Cathodes at 60°C by $SiO_2$ Dry Coating for Li-Ion Batteries. *Journal of The Electrochemical Society* **157**, A625 (2010). https://doi.org:10.1149/1.3363852

214 Huang, Y., Huang, Y. & Hu, X. Enhanced electrochemical performance of $LiNi_{0.8}Co_{0.15}Al_{0.05}O_2$ by nanoscale surface modification with $Co_3O_4$. *Electrochimica Acta* **231**, 294-299 (2017). https://doi.org:10.1016/j.electacta.2017.02.067

215 Qiu, Z., Zhang, Y., Dong, P., Xia, S. & Yao, Y. A facile method for synthesis of $LiNi_{0.8}Co_{0.15}Al_{0.05}O_2$ cathode material. *Solid State Ionics* **307**, 73-78 (2017). https://doi.org:10.1016/j.ssi.2017.04.011

216 Haasch, R. T. & Abraham, D. P. Lithium-based transition-metal oxides for battery electrodes analyzed by x-ray photoelectron spectroscopy. I. $LiNi_{0.8}Co_{0.15}Al_{0.05}O_2$. *Surface Science Spectra* **26**, 014003 (2019). https://doi.org:10.1116/1.5080233

217 Secor, E. B., Gao, T. Z., Dos Santos, M. H., Wallace, S. G., Putz, K. W. & Hersam, M. C. Combustion-Assisted Photonic Annealing of Printable Graphene Inks via Exothermic Binders. *ACS Applied Materials & Interfaces* **9**, 29418-29423 (2017). https://doi.org:10.1021/acsami.7b07189

218 Lee, M.-J., Noh, M., Park, M.-H., Jo, M., Kim, H., Nam, H. & Cho, J. The role of nanoscale-range vanadium treatment in $LiNi_{0.8}Co_{0.15}Al_{0.05}O_2$ cathode materials for Li-ion batteries at elevated temperatures. *Journal of Materials Chemistry A* **3**, 13453-13460 (2015). https://doi.org:10.1039/C5TA01571E

219 Li, Y., Yu, H., Hu, Y., Jiang, H. & Li, C. Surface-engineering of layered $LiNi_{0.815}Co_{0.15}Al_{0.035}O_2$ cathode material for high-energy and stable Li-ion batteries. *Journal of Energy Chemistry* **27**, 559-564 (2018). https://doi.org:10.1016/j.jechem.2017.11.004

220 He, X., Xu, X., Wang, L., Du, C., Cheng, X., Zuo, P., Ma, Y. & Yin, G. Enhanced Electrochemical Performance of $LiNi_{0.8}Co_{0.15}Al_{0.05}O_2$ Cathode Material via $Li_2TiO_3$ Nanoparticles Coating. *Journal of The Electrochemical Society* **166**, A143 (2019). https://doi.org:10.1149/2.0451902jes

221 Lai, C.-H., Ashby, D. S., Lin, T. C., Lau, J., Dawson, A., Tolbert, S. H. & Dunn, B. S. Application of Poly(3-hexylthiophene-2,5-diyl) as a Protective Coating for High Rate Cathode Materials. *Chemistry of Materials* **30**, 2589-2599 (2018). https://doi.org:10.1021/acs.chemmater.7b05116

222 Wu, N., Wu, H., Yuan, W., Liu, S., Liao, J. & Zhang, Y. Facile synthesis of one-dimensional $LiNi_{0.8}Co_{0.15}Al_{0.05}O_2$ microrods as advanced cathode materials for lithium ion batteries. *Journal of Materials Chemistry A* **3**, 13648-13652 (2015). https://doi.org:10.1039/C5TA02767E

223 Ryu, K. S., Lee, S. H., Koo, B. K., Lee, J. W., Kim, K. M. & Park, Y. J. Effects of $Co_3(PO_4)_2$ coatings on $LiNi_{i0.8}Co_{0.16}Al_{0.04}O_2$ cathodes during application of high current. *Journal of Applied Electrochemistry* **38**, 1385-1390 (2008). https://doi.org:10.1007/s10800-008-9576-5

224 Kondrakov, A. O., Schmidt, A., Xu, J., Geßwein, H., Mönig, R., Hartmann, P., Sommer, H., Brezesinski, T. & Janek, J. Anisotropic Lattice Strain and Mechanical Degradation of High- and Low-Nickel NCM Cathode Materials for Li-Ion Batteries. *The Journal of Physical Chemistry C* **121**, 3286-3294 (2017). https://doi.org:10.1021/acs.jpcc.6b12885

225 Zhang, F., Lou, S., Li, S., Yu, Z., Liu, Q., Dai, A., Cao, C., Toney, M. F., Ge, M., Xiao, X., Lee, W.-K., Yao, Y., Deng, J., Liu, T., Tang, Y., Yin, G., Lu, J., Su, D. & Wang, J. Surface regulation enables high stability of single-crystal lithium-ion cathodes at high voltage. *Nature Communications* **11**, 3050 (2020). https://doi.org:10.1038/s41467-020-16824-2

226 Zhang, Y., Yang, Z. & Tian, C. Probing and quantifying cathode charge heterogeneity in Li ion batteries. *Journal of Materials Chemistry A* **7**, 23628-23661 (2019). https://doi.org:10.1039/C9TA06977A

227 Miller, D. J., Proff, C., Wen, J. G., Abraham, D. P. & Bareño, J. Observation of Microstructural Evolution in Li Battery Cathode Oxide Particles by In Situ Electron Microscopy. *Advanced Energy Materials* **3**, 1098-1103 (2013). https://doi.org:10.1002/aenm.201300015

228 Mao, Y., Wang, X., Xia, S., Zhang, K., Wei, C., Bak, S., Shadike, Z., Liu, X., Yang, Y., Xu, R., Pianetta, P., Ermon, S., Stavitski, E., Zhao, K., Xu, Z., Lin, F., Yang, X.-Q., Hu, E. & Liu, Y. High-Voltage Charging-Induced Strain, Heterogeneity, and Micro-Cracks in Secondary Particles of a Nickel-Rich Layered Cathode Material. *Advanced Functional Materials* **29**, 1900247 (2019). https://doi.org:10.1002/adfm.201900247

229 Su, Y., Cui, S., Zhuo, Z., Yang, W., Wang, X. & Pan, F. Enhancing the High-Voltage Cycling Performance of $LiNi_{0.5}Mn_{0.3}Co_{0.2}O_2$ by Retarding Its Interfacial Reaction with an Electrolyte by Atomic-Layer-Deposited $Al_2O_3$. *ACS Applied Materials & Interfaces* **7**, 25105-25112 (2015). https://doi.org:10.1021/acsami.5b05500

230 Shi, Y., Zhang, M., Qian, D. & Meng, Y. S. Ultrathin $Al_2O_3$ Coatings for Improved Cycling Performance and Thermal Stability of $LiNi_{0.5}Co_{0.2}Mn_{0.3}O_2$ Cathode Material. *Electrochimica Acta* **203**, 154-161 (2016). https://doi.org:10.1016/j.electacta.2016.03.185

231 Laskar, M. R., Jackson, D. H. K., Xu, S., Hamers, R. J., Morgan, D. & Kuech, T. F. Atomic Layer Deposited MgO: A Lower Overpotential Coating for $Li[Ni_{0.5}Mn_{0.3}Co_{0.2}]O_2$ Cathode. *ACS Applied Materials & Interfaces* **9**, 11231-11239 (2017). https://doi.org:10.1021/acsami.6b16562

232 Ahn, J., Jang, E. K., Yoon, S., Lee, S.-J., Sung, S.-J., Kim, D.-H. & Cho, K. Y. Ultrathin $ZrO_2$ on $LiNi_{0.5}Mn_{0.3}Co_{0.2}O_2$ electrode surface via atomic layer deposition for high-voltage operation in lithium-ion batteries. *Applied Surface Science* **484**, 701-709 (2019). https://doi.org:10.1016/j.apsusc.2019.04.123

233 Gao, H., Cai, J., Xu, G.-L., Li, L., Ren, Y., Meng, X., Amine, K. & Chen, Z. Surface Modification for Suppressing Interfacial Parasitic Reactions of a Nickel-Rich Lithium-Ion Cathode. *Chemistry of Materials* **31**, 2723-2730 (2019). https://doi.org:10.1021/acs.chemmater.8b04200

234 Hu, W., Zhang, C., Jiang, H., Zheng, M., Wu, Q.-H. & Dong, Q. Improving the electrochemistry performance of layer $LiNi_{0.5}Mn_{0.3}Co_{0.2}O_2$ material at 4.5V cutoff potential using lithium metaborate. *Electrochimica Acta* **243**, 105-111 (2017). https://doi.org:10.1016/j.electacta.2017.05.075

235 Wang, J., Yu, Y., Li, B., Fu, T., Xie, D., Cai, J. & Zhao, J. Improving the electrochemical properties of $LiNi_{0.5}Co_{0.2}Mn_{0.3}O_2$ at 4.6 V cutoff potential by surface coating with $Li_2TiO_3$ for lithium-ion batteries. *Physical Chemistry Chemical Physics* **17**, 32033-32043 (2015). https://doi.org:10.1039/C5CP05319F

236 Chen, Z., Qin, Y., Amine, K. & Sun, Y. K. Role of surface coating on cathode materials for lithium-ion batteries. *Journal of Materials Chemistry* **20**, 7606-7612 (2010). https://doi.org:10.1039/C0JM00154F

237 Duan, J., Tang, X., Dai, H., Yang, Y., Wu, W., Wei, X. & Huang, Y. Building Safe Lithium-Ion Batteries for Electric Vehicles: A Review. *Electrochemical Energy Reviews* **3**, 1-42 (2020). https://doi.org:10.1007/s41918-019-00060-4

238 de Moraes, A. C. M., Obrzut, J., Sangwan, V. K., Downing, J. R., Chaney, L. E., Patel, D. K., Elmquist, R. E. & Hersam, M. C. Elucidating charge transport mechanisms in cellulose-stabilized graphene inks. *Journal of Materials Chemistry C* **8**, 15086-15091 (2020). https://doi.org:10.1039/D0TC03309J

239 Li, G., You, L., Wen, Y., Zhang, C., Huang, B., Chu, B., Wu, J.-H., Huang, T. & Yu, A. Ultrathin Li–Si–O Coating Layer to Stabilize the Surface Structure and Prolong the Cycling Life of Single-Crystal $LiNi_{0.6}Co_{0.2}Mn_{0.2}O_2$ Cathode Materials at 4.5 V. *ACS Applied Materials & Interfaces* **13**, 10952-10963 (2021). https://doi.org:10.1021/acsami.0c22356

240 Mo, Y., Hou, B., Li, D., Jia, X., Cao, B., Yin, L. & Chen, Y. Enhanced high-rate capability and high voltage cycleability of $Li_2TiO_3$-coated $LiNi_{0.5}Co_{0.2}Mn_{0.3}O_2$ cathode materials. *RSC Advances* **6**, 88713-88718 (2016). https://doi.org:10.1039/C6RA20035D

241 Huang, Y., Jin, F.-M., Chen, F.-J. & Chen, L. Improved cycle stability and high-rate capability of $Li_3VO_4$-coated $Li[Ni_{0.5}Co_{0.2}Mn_{0.3}]O_2$ cathode material under different voltages. *Journal of Power Sources* **256**, 1-7 (2014). https://doi.org:10.1016/j.jpowsour.2014.01.003

242 Li, L., Chen, Z., Zhang, Q., Xu, M., Zhou, X., Zhu, H. & Zhang, K. A hydrolysis-hydrothermal route for the synthesis of ultrathin $LiAlO_2$-inlaid $LiNi_{0.5}Co_{0.2}Mn_{0.3}O_2$ as a high-performance cathode material for lithium ion batteries. *Journal of Materials Chemistry A* **3**, 894-904 (2015). https://doi.org:10.1039/C4TA05902F

243 Liang, L., Sun, X., Wu, C., Hou, L., Sun, J., Zhang, X. & Yuan, C. Nasicon-Type Surface Functional Modification in Core–Shell $LiNi_{0.5}Mn_{0.3}Co_{0.2}O_2$@$NaTi_2(PO_4)_3$ Cathode Enhances Its High-Voltage Cycling Stability and Rate Capacity toward Li-Ion Batteries.

*ACS Applied Materials & Interfaces* **10**, 5498-5510 (2018). https://doi.org:10.1021/acsami.7b15808

244 Wang, D., Li, X., Wang, Z., Guo, H., Xu, Y. & Fan, Y. Co-modification of $LiNi_{0.5}Co_{0.2}Mn_{0.3}O_2$ cathode materials with zirconium substitution and surface polypyrrole coating: towards superior high voltage electrochemical performances for lithium ion batteries. *Electrochimica Acta* **196**, 101-109 (2016). https://doi.org:10.1016/j.electacta.2016.02.156

245 Wu, Z., Ji, S., Liu, T., Duan, Y., Xiao, S., Lin, Y., Xu, K. & Pan, F. Aligned $Li^+$ Tunnels in Core–Shell $Li(Ni_xMn_yCo_z)O_2$@$LiFePO_4$ Enhances Its High Voltage Cycling Stability as Li-ion Battery Cathode. *Nano Letters* **16**, 6357-6363 (2016). https://doi.org:10.1021/acs.nanolett.6b02742

246 Jia, X., Yan, M., Zhou, Z., Chen, X., Yao, C., Li, D., Chen, D. & Chen, Y. Nd-doped $LiNi_{0.5}Co_{0.2}Mn_{0.3}O_2$ as a cathode material for better rate capability in high voltage cycling of Li-ion batteries. *Electrochimica Acta* **254**, 50-58 (2017). https://doi.org:10.1016/j.electacta.2017.09.118

247 Doi, T., Matsumoto, R., Cao, Z., Haruta, M., Hashinokuchi, M. & Inaba, M. Fluoroalkyl ether-diluted dimethyl carbonate-based electrolyte solutions for high-voltage operation of $LiNi_{0.5}Co_{0.2}Mn_{0.3}O_2$ electrodes in lithium ion batteries. *Sustainable Energy & Fuels* **2**, 1197-1205 (2018). https://doi.org:10.1039/C8SE00036K

248 Wu, Z., Han, X., Zheng, J., Wei, Y., Qiao, R., Shen, F., Dai, J., Hu, L., Xu, K., Lin, Y., Yang, W. & Pan, F. Depolarized and Fully Active Cathode Based on $Li(Ni_{0.5}Co_{0.2}Mn_{0.3})O_2$ Embedded in Carbon Nanotube Network for Advanced Batteries. *Nano Letters* **14**, 4700-4706 (2014). https://doi.org:10.1021/nl5018139

249 Wang, R., Dai, X., Qian, Z., Sun, Y., Fan, S., Xiong, K., Zhang, H. & Wu, F. In Situ Surface Protection for Enhancing Stability and Performance of $LiNi_{0.5}Mn_{0.3}Co_{0.2}O_2$ at 4.8 V: The Working Mechanisms. *ACS Materials Letters* **2**, 280-290 (2020). https://doi.org:10.1021/acsmaterialslett.9b00476

250 Sánchez-González, J., Macías-García, A., Alexandre-Franco, M. F. & Gómez-Serrano, V. Electrical conductivity of carbon blacks under compression. *Carbon* **43**, 741-747 (2005). https://doi.org:10.1016/j.carbon.2004.10.045

251 Yin, S. C., Rho, Y. H., Swainson, I. & Nazar, L. F. X-ray/Neutron Diffraction and Electrochemical Studies of Lithium De/Re-Intercalation in $Li_{1-x}Co_{1/3}Ni_{1/3}Mn_{1/3}O_2$ (x = 0 → 1). *Chemistry of Materials* **18**, 1901-1910 (2006). https://doi.org:10.1021/cm0511769

252 Lim, J.-M., Hwang, T., Kim, D., Park, M.-S., Cho, K. & Cho, M. Intrinsic Origins of Crack Generation in Ni-rich $LiNi_{0.8}Co_{0.1}Mn_{0.1}O_2$ Layered Oxide Cathode Material. *Scientific Reports* **7**, 39669 (2017). https://doi.org:10.1038/srep39669

253 Strzemiecka, B., Voelkel, A., Donate-Robles, J. & Martín-Martínez, J. M. Assessment of the surface chemistry of carbon blacks by TGA-MS, XPS and inverse gas chromatography using statistical chemometric analysis. *Applied Surface Science* **316**, 315-323 (2014). https://doi.org:10.1016/j.apsusc.2014.07.174

254 Lin, F., Nordlund, D., Pan, T., Markus, I. M., Weng, T.-C., Xin, H. L. & Doeff, M. M. Influence of synthesis conditions on the surface passivation and electrochemical behavior of layered cathode materials. *Journal of Materials Chemistry A* **2**, 19833-19840 (2014). https://doi.org:10.1039/C4TA04497E

255 Chen, Z. & Dahn, J. R. Methods to obtain excellent capacity retention in $LiCoO_2$ cycled to 4.5 V. *Electrochimica Acta* **49**, 1079-1090 (2004). https://doi.org:10.1016/j.electacta.2003.10.019

256 Li, W., Reimers, J. N. & Dahn, J. R. In situ x-ray diffraction and electrochemical studies of $Li_{1-x}NiO_2$. *Solid State Ionics* **67**, 123-130 (1993). https://doi.org:10.1016/0167-2738(93)90317-V

257 Croguennec, L., Pouillerie, C., Mansour, A. N. & Delmas, C. Structural characterisation of the highly deintercalated $Li_xNi_{1.02}O_2$ phases (with $x \leq 0.30$). *Journal of Materials Chemistry* **11**, 131-141 (2001). https://doi.org:10.1039/B003377O

258 Choi, J. & Manthiram, A. Role of Chemical and Structural Stabilities on the Electrochemical Properties of Layered $LiNi_{1/3}Mn_{1/3}Co_{1/3}O_2$ Cathodes. *Journal of The Electrochemical Society* **152**, A1714 (2005). https://doi.org:10.1149/1.1954927

259 Mukhopadhyay, A. & Sheldon, B. W. Deformation and stress in electrode materials for Li-ion batteries. *Progress in Materials Science* **63**, 58-116 (2014). https://doi.org:10.1016/j.pmatsci.2014.02.001

260 Min, K. & Cho, E. Intrinsic origin of intra-granular cracking in Ni-rich layered oxide cathode materials. *Physical Chemistry Chemical Physics* **20**, 9045-9052 (2018). https://doi.org:10.1039/C7CP06615E

261 Molenda, J., Wilk, P. & Marzec, J. Structural, electrical and electrochemical properties of $LiNiO_2$. *Solid State Ionics* **146**, 73-79 (2002). https://doi.org:10.1016/S0167-2738(01)00992-4

262 Amin, R. & Chiang, Y.-M. Characterization of Electronic and Ionic Transport in $Li_{1-x}Ni_{0.33}Mn_{0.33}Co_{0.33}O_2$ (NMC333) and $Li_{1-x}Ni_{0.50}Mn_{0.20}Co_{0.30}O_2$ (NMC523) as a Function of Li Content. *Journal of The Electrochemical Society* **163**, A1512 (2016). https://doi.org:10.1149/2.0131608jes

263 Wan, T. H., Saccoccio, M., Chen, C. & Ciucci, F. Influence of the Discretization Methods on the Distribution of Relaxation Times Deconvolution: Implementing Radial Basis Functions with DRTtools. *Electrochimica Acta* **184**, 483-499 (2015). https://doi.org:10.1016/j.electacta.2015.09.097

264 Toby, B. H. & Von Dreele, R. B. GSAS-II: the genesis of a modern open-source all purpose crystallography software package. *Journal of Applied Crystallography* **46**, 544-549 (2013). https://doi.org:10.1107/S0021889813003531

265 Li, W., Liu, X., Xie, Q., You, Y., Chi, M. & Manthiram, A. Long-Term Cyclability of NCM-811 at High Voltages in Lithium-Ion Batteries: an In-Depth Diagnostic Study. *Chemistry of Materials* **32**, 7796-7804 (2020). https://doi.org:10.1021/acs.chemmater.0c02398

266 Liu, H. S., Zhang, Z. R., Gong, Z. L. & Yang, Y. Origin of Deterioration for $LiNiO_2$ Cathode Material during Storage in Air. *Electrochemical and Solid-State Letters* **7**, A190 (2004). https://doi.org:10.1149/1.1738471

267 Shizuka, K., Kiyohara, C., Shima, K. & Takeda, Y. Effect of $CO_2$ on Layered $Li_{1+z}Ni_{1-x-y}Co_xM_yO_2$ (M=Al, Mn) Cathode Materials for Lithium Ion Batteries. *Journal of Power Sources* **166**, 233-238 (2007). https://doi.org:10.1016/j.jpowsour.2007.01.013

268 Liu, H., Yang, Y. & Zhang, J. Investigation and Improvement on the Storage Property of $LiNi_{0.8}Co_{0.2}O_2$ as a Cathode Material for Lithium-Ion Batteries. *Journal of Power Sources* **162**, 644-650 (2006). https://doi.org:10.1016/j.jpowsour.2006.07.028

269 Toma, T., Maezono, R. & Hongo, K. Electrochemical Properties and Crystal Structure of $Li^+/H^+$ Cation-Exchanged $LiNiO_2$. *ACS Applied Energy Materials* **3**, 4078-4087 (2020). https://doi.org:10.1021/acsaem.0c00602

270 Hartmann, L., Pritzl, D., Beyer, H. & Gasteiger, H. A. Evidence for $Li^+/H^+$ Exchange during Ambient Storage of Ni-Rich Cathode Active Materials. *Journal of The Electrochemical Society* **168**, 070507 (2021). https://doi.org:10.1149/1945-7111/ac0d3a

271 Pritzl, D., Teufl, T., Freiberg, A. T. S., Strehle, B., Sicklinger, J., Sommer, H., Hartmann, P. & Gasteiger, H. A. Washing of Nickel-Rich Cathode Materials for Lithium-Ion Batteries: Towards a Mechanistic Understanding. *Journal of The Electrochemical Society* **166**, A4056-A4066 (2019). https://doi.org:10.1149/2.1351915jes

272 You, Y., Celio, H., Li, J., Dolocan, A. & Manthiram, A. Modified High-Nickel Cathodes with Stable Surface Chemistry Against Ambient Air for Lithium-Ion Batteries. *Angewandte Chemie International Edition* **57**, 6480-6485 (2018). https://doi.org:10.1002/anie.201801533

273 Visbal, H., Fujiki, S., Aihara, Y., Watanabe, T., Park, Y. & Doo, S. The Influence of the Carbonate Species on $LiNi_{0.8}Co_{0.15}Al_{0.05}O_2$ Surfaces for All-Solid-State Lithium Ion Battery Performance. *Journal of Power Sources* **269**, 396-402 (2014). https://doi.org:10.1016/j.jpowsour.2014.07.021

274 Chen, Z., Wang, J., Huang, J., Fu, T., Sun, G., Lai, S., Zhou, R., Li, K. & Zhao, J. The High-Temperature and High-Humidity Storage Behaviors and Electrochemical Degradation Mechanism of $LiNi_{0.6}Co_{0.2}Mn_{0.2}O_2$ Cathode Material for Lithium Ion Batteries. *Journal of Power Sources* **363**, 168-176 (2017). https://doi.org:10.1016/j.jpowsour.2017.07.087

275 Renfrew, S. E. & McCloskey, B. D. Quantification of Surface Oxygen Depletion and Solid Carbonate Evolution on the First Cycle of $LiNi_{0.6}Mn_{0.2}Co_{0.2}O_2$ Electrodes. *ACS Applied Energy Materials* **2**, 3762-3772 (2019). https://doi.org:10.1021/acsaem.9b00459

276 Sicklinger, J., Metzger, M., Beyer, H., Pritzl, D. & Gasteiger, H. A. Ambient Storage Derived Surface Contamination of NCM811 and NCM111: Performance Implications and Mitigation Strategies. *Journal of The Electrochemical Society* **166**, A2322-A2335 (2019). https://doi.org:10.1149/2.0011912jes

277 Zhai, Y., Yang, W., Ning, D., Yang, J., Sun, L., Schuck, G., Schumacher, G. & Liu, X. Improving the Cycling and Air-Storage Stability of $LiNi_{0.8}Co_{0.1}Mn_{0.1}O_2$ through Integrated Surface/Interface/Doping Engineering. *Journal of Materials Chemistry A* **8**, 5234-5245 (2020). https://doi.org:10.1039/C9TA13014D

278 Bi, Y., Li, Q., Yi, R. & Xiao, J. To Pave the Way for Large-Scale Electrode Processing of Moisture-Sensitive Ni-Rich Cathodes. *Journal of The Electrochemical Society* **169**, 020521 (2022). https://doi.org:10.1149/1945-7111/ac4e5d

279 Kim, H., Lee, K., Kim, S. & Kim, Y. Fluorination of Free Lithium Residues on the Surface of Lithium Nickel Cobalt Aluminum Oxide Cathode Materials for Lithium Ion Batteries. *Materials & Design* **100**, 175-179 (2016). https://doi.org:10.1016/j.matdes.2016.03.121

280 Liu, M., Jiang, Y., Qin, Y., Feng, Z., Wang, D. & Guo, B. Enhanced Electrochemical Performance of Ni-Rich Cathodes by Neutralizing Residual Lithium with Acid

Compounds. *ACS Applied Materials & Interfaces* **13**, 55072-55079 (2021). https://doi.org:10.1021/acsami.1c16482

281 Zheng, X., Li, X., Wang, Z., Guo, H., Huang, Z., Yan, G. & Wang, D. Investigation and Improvement on the Electrochemical Performance and Storage of $LiNiO_2$-Based Materials for Lithium Ion Battery. *Electrochimica Acta* **191**, 832-840 (2016). https://doi.org:10.1016/j.electacta.2016.01.142

282 Lv, C., Li, Z., Ren, X., Li, K., Ma, J. & Duan, X. Revealing the Degradation Mechanism of Ni-Rich Cathode Materials After Ambient Storage and Related Regeneration Method. *Journal of Materials Chemistry A* **9**, 3995-4006 (2021). https://doi.org:10.1039/D0TA10378K

283 Xie, Q. & Manthiram, A. Long-Life, Ultrahigh-Nickel Cathodes with Excellent Air Storage Stability for High-Energy Density Lithium-Based Batteries. *Chemistry of Materials* **32**, 7413-7424 (2020). https://doi.org:10.1021/acs.chemmater.0c02374

284 Kim, Y., Park, H., Dolocan, A., Warner, J. H. & Manthiram, A. Wet-$CO_2$ Pretreatment Process for Reducing Residual Lithium in High-Nickel Layered Oxides for Lithium-Ion Batteries. *ACS Applied Materials & Interfaces* **13**, 27096-27105 (2021). https://doi.org:10.1021/acsami.1c06277

285 Yuan, C., Deng, Y., Li, T. & Yang, F. Manufacturing Energy Analysis of Lithium Ion Battery Pack for Electric Vehicles. *CIRP Annals* **66** (2017). https://doi.org:10.1016/j.cirp.2017.04.109

286 Gu, W., Dong, Q., Zheng, L., Liu, Y., Mao, Y., Zhao, Y., Duan, W., Lin, H., Shen, Y. & Chen, L. Ambient Air Stable Ni-Rich Layered Oxides Enabled by Hydrophobic Self-Assembled Monolayer. *ACS Applied Materials & Interfaces* **12**, 1937-1943 (2020). https://doi.org:10.1021/acsami.9b20030

287 Mayer, J. K., Huttner, F., Heck, C. A., Steckermeier, D., von Horstig, M.-W. & Kwade, A. Investigation of Moisture Content, Structural and Electrochemical Properties of Nickel-Rich NCM Based Cathodes Processed at Ambient Atmosphere. *Journal of The Electrochemical Society* **169**, 060512 (2022). https://doi.org:10.1149/1945-7111/ac7358

288 Choi, J., Dong, L., Yu, C.-Y., O'Meara, C., Lee, E. & Kim, J.-H. Relationship of Chemical Composition and Moisture Sensitivity in $LiNi_xMn_yCo_{1-x-y}O_2$ for Lithium-Ion Batteries. *Journal of Electrochemical Energy Conversion and Storage* **18** (2021). https://doi.org:10.1115/1.4051208

289 Lu, Y. & Yuan, W. Superhydrophobic/Superoleophilic and Reinforced Ethyl Cellulose Sponges for Oil/Water Separation: Synergistic Strategies of Cross-linking, Carbon

Nanotube Composite, and Nanosilica Modification. *ACS Applied Materials & Interfaces* **9**, 29167-29176 (2017). https://doi.org:10.1021/acsami.7b09160

290 Liu, Y., Deng, L., Zhang, C., Chen, K., Feng, F. & Zhang, H. Comparison of Ethyl Cellulose–Gelatin Composite Films Fabricated by Electrospinning Versus Solvent Casting. *Journal of Applied Polymer Science* **135**, 46824 (2018). https://doi.org:10.1002/app.46824

291 Liu, Y., Li, Y., Deng, L., Zou, L., Feng, F. & Zhang, H. Hydrophobic Ethylcellulose/Gelatin Nanofibers Containing Zinc Oxide Nanoparticles for Antimicrobial Packaging. *Journal of Agricultural and Food Chemistry* **66**, 9498-9506 (2018). https://doi.org:10.1021/acs.jafc.8b03267

292 Secor, E. B., Dos Santos, M. H., Wallace, S. G., Bradshaw, N. P. & Hersam, M. C. Tailoring the Porosity and Microstructure of Printed Graphene Electrodes via Polymer Phase Inversion. *The Journal of Physical Chemistry C* **122**, 13745-13750 (2018). https://doi.org:10.1021/acs.jpcc.8b00580

293 Li, J., Wang, X., Kong, X., Yang, H., Zeng, J. & Zhao, J. Insight into the Kinetic Degradation of Stored Nickel-Rich Layered Cathode Materials for Lithium-Ion Batteries. *ACS Sustainable Chemistry & Engineering* **9**, 10547-10556 (2021). https://doi.org:10.1021/acssuschemeng.1c02486

294 Aryal, S., Durham, J. L., Lipson, A. L., Pupek, K. Z. & Kahvecioglu, O. Roles of Mn and Co in Ni-Rich Layered Oxide Cathodes Synthesized Utilizing a Taylor Vortex Reactor. *Electrochimica Acta* **391**, 138929 (2021). https://doi.org:10.1016/j.electacta.2021.138929

295 Rodrigues, M.-T. F., Gim, J., Tornheim, A., Kahvecioglu, O., Luo, M., Prado, A. Y. R., Trask, S. E., Croy, J. & Abraham, D. P. Concealed Cathode Degradation in Lithium-Ion Cells with a Ni-Rich Oxide. *Journal of The Electrochemical Society* **169**, 040539 (2022). https://doi.org:10.1149/1945-7111/ac65b7

296 Yabuuchi, N., Nakayama, M., Takeuchi, M., Komaba, S., Hashimoto, Y., Mukai, T., Shiiba, H., Sato, K., Kobayashi, Y., Nakao, A., Yonemura, M., Yamanaka, K., Mitsuhara, K. & Ohta, T. Origin of stabilization and destabilization in solid-state redox reaction of oxide ions for lithium-ion batteries. *Nature Communications* **7**, 13814 (2016). https://doi.org:10.1038/ncomms13814

297 Li, Q., Wang, Y., Wang, X., Sun, X., Zhang, J.-N., Yu, X. & Li, H. Investigations on the Fundamental Process of Cathode Electrolyte Interphase Formation and Evolution of High-Voltage Cathodes. *ACS Applied Materials & Interfaces* **12**, 2319-2326 (2020). https://doi.org:10.1021/acsami.9b16727

298 Ge, A., Zhou, D., Inoue, K.-i., Chen, Y. & Ye, S. Role of Oxygen in Surface Structures of the Solid-Electrolyte Interphase Investigated by Sum Frequency Generation Vibrational Spectroscopy. *The Journal of Physical Chemistry C* **124**, 17538-17547 (2020). https://doi.org:10.1021/acs.jpcc.0c06390

299 Dupré, N., Cuisinier, M., Legall, E., War, D. & Guyomard, D. Contribution of the oxygen extracted from overlithiated layered oxides at high potential to the formation of the interphase. *Journal of Power Sources* **299**, 231-240 (2015). https://doi.org:10.1016/j.jpowsour.2015.08.006

300 Wu, F., Li, W., Chen, L., Su, Y., Bao, L., Bao, W., Yang, Z., Wang, J., Lu, Y. & Chen, S. Renovating the electrode-electrolyte interphase for layered lithium- & manganese-rich oxides. *Energy Storage Materials* **28**, 383-392 (2020). https://doi.org:10.1016/j.ensm.2019.12.017

301 Wang, T., Chen, Z., Zhao, R. & Chen, H. Design and Tailoring of a Three-Dimensional Lithium Rich Layered Oxide-Graphene/Carbon Nanotubes Composite for Lithium-Ion Batteries. *Electrochimica Acta* **211**, 461-468 (2016). https://doi.org:10.1016/j.electacta.2016.06.056

302 Puheng, Y., Wenxu, W., Xiaoliang, Z., Honglei, L., Shichao, Z. & Yalan, X. Self-standing $Li_{1.2}Mn_{0.6}Ni_{0.2}O_2$/graphene membrane as a binder-free cathode for Li-ion batteries. *RSC Advances* **8**, 39769-39776 (2018). https://doi.org:10.1039/C8RA06086J

303 Chen, D., Tu, W., Chen, M., Hong, P., Zhong, X., Zhu, Y., Yu, Q. & Li, W. Synthesis and performances of Li-Rich@$AlF_3$@Graphene as cathode of lithium ion battery. *Electrochimica Acta* **193**, 45-53 (2016). https://doi.org:10.1016/j.electacta.2016.02.043

304 Chen, M., Chen, D., Liao, Y., Zhong, X., Li, W. & Zhang, Y. Layered Lithium-Rich Oxide Nanoparticles Doped with Spinel Phase: Acidic Sucrose-Assistant Synthesis and Excellent Performance as Cathode of Lithium Ion Battery. *ACS Applied Materials & Interfaces* **8**, 4575-4584 (2016). https://doi.org:10.1021/acsami.5b10219

305 Huang, Y., Duan, J., Zheng, X., Wen, J., Dai, Y., Wang, Z., Luo, W. & Huang, Y. Lithium Metal-Based Composite: An Emerging Material for Next-Generation Batteries. *Matter* **3**, 1009-1030 (2020). https://doi.org:10.1016/j.matt.2020.07.005

306 Shi, P., Zhang, X.-Q., Shen, X., Zhang, R., Liu, H. & Zhang, Q. A Review of Composite Lithium Metal Anode for Practical Applications. *Advanced Materials Technologies* **5**, 1900806 (2020). https://doi.org:10.1002/admt.201900806

307 Li, Q., Zhu, S. & Lu, Y. 3D Porous Cu Current Collector/Li-Metal Composite Anode for Stable Lithium-Metal Batteries. *Advanced Functional Materials* **27**, 1606422 (2017). https://doi.org:10.1002/adfm.201606422

308 Yang, C.-P., Yin, Y.-X., Zhang, S.-F., Li, N.-W. & Guo, Y.-G. Accommodating lithium into 3D current collectors with a submicron skeleton towards long-life lithium metal anodes. *Nature Communications* **6**, 8058 (2015). https://doi.org:10.1038/ncomms9058

309 Wang, H., Lin, D., Xie, J., Liu, Y., Chen, H., Li, Y., Xu, J., Zhou, G., Zhang, Z., Pei, A., Zhu, Y., Liu, K., Wang, K. & Cui, Y. An Interconnected Channel-Like Framework as Host for Lithium Metal Composite Anodes. *Advanced Energy Materials* **9**, 1802720 (2019). https://doi.org:10.1002/aenm.201802720

310 Kautz, D. J., Tao, L., Mu, L., Nordlund, D., Feng, X., Zheng, Z. & Lin, F. Understanding the critical chemistry to inhibit lithium consumption in lean lithium metal composite anodes. *Journal of Materials Chemistry A* **6**, 16003-16011 (2018). https://doi.org:10.1039/C8TA01715H

311 Yu, B., Tao, T., Mateti, S., Lu, S. & Chen, Y. Nanoflake Arrays of Lithiophilic Metal Oxides for the Ultra-Stable Anodes of Lithium-Metal Batteries. *Advanced Functional Materials* **28**, 1803023 (2018). https://doi.org:10.1002/adfm.201803023

312 Lin, D., Liu, Y., Liang, Z., Lee, H.-W., Sun, J., Wang, H., Yan, K., Xie, J. & Cui, Y. Layered reduced graphene oxide with nanoscale interlayer gaps as a stable host for lithium metal anodes. *Nature Nanotechnology* **11**, 626-632 (2016). https://doi.org:10.1038/nnano.2016.32

313 Chen, H., Pei, A., Wan, J., Lin, D., Vilá, R., Wang, H., Mackanic, D., Steinrück, H.-G., Huang, W., Li, Y., Yang, A., Xie, J., Wu, Y., Wang, H. & Cui, Y. Tortuosity Effects in Lithium-Metal Host Anodes. *Joule* **4**, 938-952 (2020). https://doi.org:10.1016/j.joule.2020.03.008

314 Hołda, A. K. & Vankelecom, I. F. J. Understanding and guiding the phase inversion process for synthesis of solvent resistant nanofiltration membranes. *Journal of Applied Polymer Science* **132** (2015). https://doi.org:10.1002/app.42130

315 Chen, X., Chen, X.-R., Hou, T.-Z., Li, B.-Q., Cheng, X.-B., Zhang, R. & Zhang, Q. Lithiophilicity chemistry of heteroatom-doped carbon to guide uniform lithium nucleation in lithium metal anodes. *Science Advances* **5**, eaau7728 https://doi.org:10.1126/sciadv.aau7728

316 Park, S.-H., King, P. J., Tian, R., Boland, C. S., Coelho, J., Zhang, C., McBean, P., McEvoy, N., Kremer, M. P., Daly, D., Coleman, J. N. & Nicolosi, V. High Areal

Capacity Battery Electrodes Enabled by Segregated Nanotube Networks. *Nature Energy* **4**, 560-567 (2019). https://doi.org:10.1038/s41560-019-0398-y

317 Vaalma, C., Buchholz, D., Weil, M. & Passerini, S. A cost and resource analysis of sodium-ion batteries. *Nature Reviews Materials* **3**, 18013 (2018). https://doi.org:10.1038/natrevmats.2018.13

318 Stevens, D. A. & Dahn, J. R. High Capacity Anode Materials for Rechargeable Sodium-Ion Batteries. *Journal of The Electrochemical Society* **147**, 1271 (2000). https://doi.org:10.1149/1.1393348

319 Irisarri, E., Ponrouch, A. & Palacin, M. R. Review—Hard Carbon Negative Electrode Materials for Sodium-Ion Batteries. *Journal of The Electrochemical Society* **162**, A2476 (2015). https://doi.org:10.1149/2.0091514jes

320 Xu, J., Lee, D. H., Clément, R. J., Yu, X., Leskes, M., Pell, A. J., Pintacuda, G., Yang, X.-Q., Grey, C. P. & Meng, Y. S. Identifying the Critical Role of Li Substitution in P2–$Na_x[Li_yNi_zMn_{1-y-z}]O_2$ ($0 < x, y, z < 1$) Intercalation Cathode Materials for High-Energy Na-Ion Batteries. *Chemistry of Materials* **26**, 1260-1269 (2014). https://doi.org:10.1021/cm403855t

321 Rozier, P., Sathiya, M., Paulraj, A.-R., Foix, D., Desaunay, T., Taberna, P.-L., Simon, P. & Tarascon, J.-M. Anionic redox chemistry in Na-rich $Na_2Ru_{1-y}Sn_yO_3$ positive electrode material for Na-ion batteries. *Electrochemistry Communications* **53**, 29-32 (2015). https://doi.org:10.1016/j.elecom.2015.02.001

322 Liu, Q., Hu, Z., Li, W., Zou, C., Jin, H., Wang, S., Chou, S. & Dou, S.-X. Sodium transition metal oxides: the preferred cathode choice for future sodium-ion batteries? *Energy & Environmental Science* **14**, 158-179 (2021). https://doi.org:10.1039/D0EE02997A

323 Xie, X., Makaryan, T., Zhao, M., Van Aken, K. L., Gogotsi, Y. & Wang, G. $MoS_2$ Nanosheets Vertically Aligned on Carbon Paper: A Freestanding Electrode for Highly Reversible Sodium-Ion Batteries. *Advanced Energy Materials* **6**, 1502161 (2016). https://doi.org:10.1002/aenm.201502161

324 Xiao, Y., Lee, S. H. & Sun, Y.-K. The Application of Metal Sulfides in Sodium Ion Batteries. *Advanced Energy Materials* **7**, 1601329 (2017). https://doi.org:10.1002/aenm.201601329

325 Wang, Y.-X., Chou, S.-L., Wexler, D., Liu, H.-K. & Dou, S.-X. High-Performance Sodium-Ion Batteries and Sodium-Ion Pseudocapacitors Based on $MoS_2$/Graphene

Composites. *Chemistry – A European Journal* **20**, 9607-9612 (2014). https://doi.org:10.1002/chem.201402563

326 Huang, Z., Hou, H., Zhang, Y., Wang, C., Qiu, X. & Ji, X. Layer-Tunable Phosphorene Modulated by the Cation Insertion Rate as a Sodium-Storage Anode. *Advanced Materials* **29**, 1702372 (2017). https://doi.org:10.1002/adma.201702372

327 Pang, J., Bachmatiuk, A., Yin, Y., Trzebicka, B., Zhao, L., Fu, L., Mendes, R. G., Gemming, T., Liu, Z. & Rummeli, M. H. Applications of Phosphorene and Black Phosphorus in Energy Conversion and Storage Devices. *Advanced Energy Materials* **8**, 1702093 (2018). https://doi.org:10.1002/aenm.201702093

328 Sun, J., Lee, H.-W., Pasta, M., Yuan, H., Zheng, G., Sun, Y., Li, Y. & Cui, Y. A phosphorene–graphene hybrid material as a high-capacity anode for sodium-ion batteries. *Nature Nanotechnology* **10**, 980-985 (2015). https://doi.org:10.1038/nnano.2015.194

329 Sahu, T. S. & Mitra, S. Exfoliated $MoS_2$ Sheets and Reduced Graphene Oxide-An Excellent and Fast Anode for Sodium-ion Battery. *Scientific Reports* **5**, 12571 (2015). https://doi.org:10.1038/srep12571

330 Wang, Y., Kong, D., Shi, W., Liu, B., Sim, G. J., Ge, Q. & Yang, H. Y. Ice Templated Free-Standing Hierarchically $WS_2$/CNT-rGO Aerogel for High-Performance Rechargeable Lithium and Sodium Ion Batteries. *Advanced Energy Materials* **6**, 1601057 (2016). https://doi.org:10.1002/aenm.201601057

331 Bhandavat, R., David, L. & Singh, G. Synthesis of Surface-Functionalized $WS_2$ Nanosheets and Performance as Li-Ion Battery Anodes. *The Journal of Physical Chemistry Letters* **3**, 1523-1530 (2012). https://doi.org:10.1021/jz300480w

332 Kajiyama, S., Szabova, L., Sodeyama, K., Iinuma, H., Morita, R., Gotoh, K., Tateyama, Y., Okubo, M. & Yamada, A. Sodium-Ion Intercalation Mechanism in MXene Nanosheets. *ACS Nano* **10**, 3334-3341 (2016). https://doi.org:10.1021/acsnano.5b06958

333 Wang, X., Kajiyama, S., Iinuma, H., Hosono, E., Oro, S., Moriguchi, I., Okubo, M. & Yamada, A. Pseudocapacitance of MXene nanosheets for high-power sodium-ion hybrid capacitors. *Nature Communications* **6**, 6544 (2015). https://doi.org:10.1038/ncomms7544

334 Wang, J., Zhang, L., Sun, K., He, J., Zheng, Y., Xu, C., Zhang, Y., Chen, Y. & Li, M. Improving ionic/electronic conductivity of $MoS_2$ Li-ion anode via manganese doping and structural optimization. *Chemical Engineering Journal* **372**, 665-672 (2019). https://doi.org:10.1016/j.cej.2019.04.203

335 Deng, Z., Jiang, H. & Li, C. 2D Metal Chalcogenides Incorporated into Carbon and their Assembly for Energy Storage Applications. *Small* **14**, 1800148 (2018). https://doi.org:10.1002/smll.201800148

336 de Moraes, A. C. M., Hyun, W. J., Seo, J.-W. T., Downing, J. R., Lim, J.-M. & Hersam, M. C. Ion-Conductive, Viscosity-Tunable Hexagonal Boron Nitride Nanosheet Inks. *Advanced Functional Materials* **29**, 1902245 (2019). https://doi.org:10.1002/adfm.201902245

337 Secor, E. B. & Hersam, M. C. Emerging Carbon and Post-Carbon Nanomaterial Inks for Printed Electronics. *The Journal of Physical Chemistry Letters* **6**, 620-626 (2015). https://doi.org:10.1021/jz502431r

338 Kuo, L., Sangwan, V. K., Rangnekar, S. V., Chu, T.-C., Lam, D., Zhu, Z., Richter, L. J., Li, R., Szydłowska, B. M., Downing, J. R., Luijten, B. J., Lauhon, L. J. & Hersam, M. C. All-Printed Ultrahigh-Responsivity $MoS_2$ Nanosheet Photodetectors Enabled by Megasonic Exfoliation. *Advanced Materials* **34**, 2203772 (2022). https://doi.org:10.1002/adma.202203772

339 Seo, J.-W. T., Zhu, J., Sangwan, V. K., Secor, E. B., Wallace, S. G. & Hersam, M. C. Fully Inkjet-Printed, Mechanically Flexible $MoS_2$ Nanosheet Photodetectors. *ACS Applied Materials & Interfaces* **11**, 5675-5681 (2019). https://doi.org:10.1021/acsami.8b19817

340 Hyun, W. J., Secor, E. B., Hersam, M. C., Frisbie, C. D. & Francis, L. F. High-Resolution Patterning of Graphene by Screen Printing with a Silicon Stencil for Highly Flexible Printed Electronics. *Advanced Materials* **27**, 109-115 (2015). https://doi.org:10.1002/adma.201404133

341 Hyun, W. J., Thomas, C. M., Chaney, L. E., Mazarin de Moraes, A. C. & Hersam, M. C. Screen-Printable Hexagonal Boron Nitride Ionogel Electrolytes for Mechanically Deformable Solid-State Lithium-Ion Batteries. *Nano Letters* **22**, 5372-5378 (2022). https://doi.org:10.1021/acs.nanolett.2c01364

342 Parate, K., Rangnekar, S. V., Jing, D., Mendivelso-Perez, D. L., Ding, S., Secor, E. B., Smith, E. A., Hostetter, J. M., Hersam, M. C. & Claussen, J. C. Aerosol-Jet-Printed Graphene Immunosensor for Label-Free Cytokine Monitoring in Serum. *ACS Applied Materials & Interfaces* **12**, 8592-8603 (2020). https://doi.org:10.1021/acsami.9b22183

343 Jakus, A. E., Secor, E. B., Rutz, A. L., Jordan, S. W., Hersam, M. C. & Shah, R. N. Three-Dimensional Printing of High-Content Graphene Scaffolds for Electronic and Biomedical Applications. *ACS Nano* **9**, 4636-4648 (2015). https://doi.org:10.1021/acsnano.5b01179

344 Zhang, M., Mei, H., Chang, P. & Cheng, L. 3D printing of structured electrodes for rechargeable batteries. *Journal of Materials Chemistry A* **8**, 10670-10694 (2020). https://doi.org:10.1039/D0TA02099K

# VITA


## Norman Luu

norman.luu@u.northwestern.edu | 480-862-9612 | linkedin.com/in/normanluu/


## EDUCATION

**Northwestern University, McCormick School of Engineering** (Evanston, IL)

***Ph.D in Materials Science and Engineering*** *Sept 2017 – Dec 2022 (anticipated)*

- Thesis: Graphene-Mediated Cathode Interfaces for Lithium-Ion Batteries
- Advisor: Mark Hersam

***Bachelor of Science in Materials Science and Engineering*** *Dec 2016*

## RESEARCH EXPERIENCE

**Northwestern University, Hersam Research Group** (Evanston, IL)

*Ph.D Candidate* *Sept 2017 – present*

- Directed and executed 3 materials development projects to uniformly coat Li-ion battery cathode active materials with graphene, resulting in optimized electrochemical performance and record cycling efficiencies at high operating voltages.
- Conducted chemical and structural evaluation of Li-ion battery cathode, anode, separator, and electrolyte materials, publishing 10+ co-authored articles.
- Created a data analysis program for battery data using the Pandas library in Python to generate cycle life, voltage-capacity, and dQdV plots, accelerating data processing by 10x.
- Mentored 10+ researchers on battery materials processing, testing methods, and data analysis.
- Established and chaired a weekly battery science forum attended by 15+ researchers, resulting in 3 ongoing scientific collaborations and manuscripts in preparation.

**Tesla, Inc.** (Fremont, CA)

*Materials Engineering Intern* *July 2022 – Sept 2022*

- Performed failure analysis to root cause critical mechanical and thermal failure modes in metallic cans and cathode manufacturing equipment used for global production of 4680 cylindrical Li-ion batteries at Tesla.
- Designed a reliability testing platform and procedure to improve accelerated test models for thermal fatigue.
- De-risked mechanical fatigue issues in electrical conductors for battery packs, enabling reuse of 150+ modules.
- Aggregated and fit temperature-dependent properties of metals using SciPy and published results to an internal material properties database for use in thermal and mechanical simulations.

**NanoGraf Corporation** (Chicago, IL)
*Engineering Intern* *Jan 2017 – Aug 2017*

- Studied the interfacial degradation of silicon anodes for lithium-ion batteries using a three-electrode electrochemical cell setup.
- Optimized slurry formulations to maximize stability of cast silicon anode films.
- Developed a geometric model to calculate rated capacity of prismatic cells.

**National Institute of Standards and Technology** (Gaithersburg, MD)
*Summer Undergraduate Research Fellow* *June 2016 – Aug 2016*

- Wrote Python code to interface with an open-source molecular dynamics simulation software to calculate phase transformation energies for elemental compounds.
- Created reference tools for public distribution in the NIST Interatomic Potentials Repository library.

---

## TEACHING AND OUTREACH

**Northwestern University Materials Science and Engineering Department** (Evanston, IL)
*Teaching Assistant for MSE 361: Crystallography and Diffraction* *Jan 2021 – March 2021*

- Led X-ray crystallography and diffraction lab sessions for 25+ students.
- Published 5 Jupyter notebooks containing instructional materials for lab and implemented coding questions within instructional materials to teach Python to students.

*Teaching Assistant for MSE 381: Materials for Energy-Efficient Technology* *Sept 2020 – Dec 2020*

- Developed lab curriculum and led lab sessions for energy materials processing and characterization for 25+ students.
- Lectured about lithium-ion battery materials science and the incumbent commercial landscape.
- Wrote problem sets and graded written assignments, lab writeups, and exams.

**Northwestern University Splash!** (Evanston, IL)
*President* *Sept 2018 – June 2022*

- Directed a team of 8 and oversaw the planning and operations of an annual educational enrichment day attended by 80+ volunteer teachers and 200+ high school students.
- Strengthened partnerships with Northwestern's Materials Research Center and authored annual reports, increasing secured yearly funding by 150%.
- Established a team dedicated to pedagogical training and recruitment, increasing unique classes by 165%.
- Collaborated with the nonprofit Learning Unlimited to organize an annual virtual *Splash* event featuring 250+ classes attended by 900+ students and 200+ teachers nationwide.
- Oversaw an expanded online presence across 3 social media platforms, leading to new collaborations with educational outreach groups at Northwestern.

## PUBLICATIONS

** equal contribution*

- **Luu, N. S.,** Meza, P. E., Tayamen, A. M., Kahvecioglu, O., Rangnekar, S. V., Hui, J., Downing, J. R., Hersam, M. C. *Enabling Ambient Stability of $LiNiO_2$ Lithium-Ion Battery Cathode Materials via Graphene-Cellulose Composite Coatings*. Submitted.
- **Luu, N. S.,*** Park, K. Y.,* Hersam, M. C. *Chemomechanical Degradation in High-Energy Lithium-ion Battery Cathode Materials*. Acc. Mater. Res. (2022), 3, 5, 511–524.
- **Luu, N. S.**, Lim, J.-M., Torres, C. G., Park, K. Y., Moazzen, E., He, K. Meza, P. E., Li, W., Downing, J. R., Dravid, V. P., Barnett, S., Bedzyk, M. J., Hersam, M. C. *Elucidating and Mitigating High-Voltage Chemomechanical Degradation of Nickel-Rich Lithium-Ion Battery Cathodes via Conformal Graphene Coating*. ACS Appl. Energy Mater. (2021), 4, 10, 11069–11079
- Lim, J.-M.,* **Luu, N. S.,*** Park, K. Y., Tan, M. T. Z., Kim, S., Downing, J.R., He, K. Dravid, V. P., Hersam, M.C. *Enhancing Nanostructured Nickel-Rich Lithium-Ion Battery Cathodes via Surface Stabilization*. J. Vac. Sci. Technol. A. (2020) A 38, 063210.
- Hyun, W. J., Thomas, C. M., **Luu, N. S.**, Hersam, M.C. *Heterostructured Ionogel Electrolytes for High-Performance Solid-State Lithium-Ion Batteries*. Adv. Mater. (2021) 33, 2007684.
- Park, K. Y., Zhu, Y., Torres, C. G., Jung, H. J., **Luu, N. S.,** Kahvecioglu, O., Yoo, Y., Seo, J.-W. T., Downing, J. R., Lim, H.-D., Bedzyk, M. J., Wolverton, C., Hersam, M.C. *Elucidating and Mitigating High-Voltage Degradation Cascades in Cobalt-Free LiNiO2 Lithium-Ion Battery Cathodes*. Adv. Mater (2021) 34, 3, 2106402.
- Park, K. Y., Lim, J.-M., **Luu, N. S.**, Downing, J.R., Wallace, S. G., Chaney, L. E., Yoo, H., Hyun, W. J. Kim, H.-U, Hersam, M.C. *Concurrently Approaching Volumetric and Specific Capacity Limits of Lithium Battery Cathodes via Conformal Pickering Emulsion Graphene Coatings*. Adv. Energy Mater. (2020), 10, 25, 2001216.
- Moraes, A. C. M., Hyun, W. J., **Luu, N. S.**, Lim, J.-M., Park, K. Y., Hersam, M. C. *Phase-Inversion Polymer Composite Separators Based on Hexagonal Boron Nitride Nanosheets for High-Temperature Lithium-Ion Batteries*. ACS Appl. Mater. Interfaces. (2020). 12, 7, 8107–8114.
- Lim, J.-M., Kim, S., **Luu, N. S.**, Downing, J.R., Tan, M. T. Z., Park, K. Y., Hechter, J. C., He, K., Dravid, V. P., Hersam, M. C. *High Volumetric Energy and Power Density $Li_2TiSiO_5$ Battery Anodes via Graphene Functionalization*. Matter. (2020). 3, 5, 522–533.
- Chen, K.-S., Balla, I., **Luu, N. S.,** Hersam, M.C. Emerging Opportunities for Two-Dimensional Materials in Lithium-Ion Batteries. ACS Energy Letters. (2017). 2, 9, 2026–2034.
- Chen, K.-S., Xu, R., **Luu, N. S.**, Secor, E.B., Li, Q., Kim, S., Balla, I., Guiney, L., Seo, J.W., Liu, W., Wu, J., Dravid, V.P., Wolverton, C., Lu, J., Amine, K., Hersam, M.C. Comprehensive enhancement of nanostructured lithium-ion battery cathode materials via conformal graphene dispersion. Nano Letters. (2017). 17, 4, 2539–2546.
- Wu, Y.-L., Horwitz, N. Chen, K.S., Gomez-Gualdron, D., **Luu, N. S.**, Ma, L., Wang, T., Hersam, M., Hupp. J.T., Farha, O., Snurr, R., Wasielewski, M. G-Quadruplex Organic Frameworks. Nature Chemistry. (2016). 9, 466–472.

## PRESENTATIONS

- **Luu, N. S.**, Lim, J.-M., Torres, C. G., Park, K. Y., Moazzen, E., He, K. Meza, P. L., Li, W., Downing, J. R., Dravid, V. P., Barnett, S., Bedzyk, M. J., Hersam, M. C. Elucidating and Mitigating High-Voltage Chemomechanical Degradation of Nickel-Rich Lithium-Ion Battery Cathodes via Conformal Graphene Coating. (05/30/2022). 241st Meeting of the Electrochemical Society, Vancouver, B.C.
- **Luu, N. S.**, Hyun, W. J., Villa, C., Torres, C. G., Lim, J.-M., Hu, X., Bedzyk, M. J., Dravid, V. P., Hersam, M. C., Electrochemistry of the Hexagonal Boron Nitride-Ionic Liquid Gel Electrolyte Interface. (07/31/2019). Poster Presentation. Energy Frontier Research Center Meeting, Department of Energy.
- Lim, J.-M., **Luu, N. S.**, Chen, K.S., Li, L., Seo, J.W., Xu, R., Hamamoto, K., Li, Q., Kim S., Yao, Z., Yu, X., Wu, J., Wolverton. C., Dravid, V.P., Barnett, S.A., Lu, J., Amine, K., and Hersam, M.C. Tailoring the Electrochemistry of Metal Oxide Li-ion Battery Materials via Graphene Functionalization. (11/20/2017). Center for Electrochemical Energy Science All-Hands Meeting, Argonne National Laboratory.
- Li, L., **Luu, N. S.**, Yao, Z., Chen, K.-S., Secor, E.B., Zhu, J., Wolverton, C., Hersam, M.C., Characterizing and Enhancing the Electrochemistry of Graphene-Functionalized $LiNi_xMn_yCo_zO_2$ Li-Ion Battery Electrodes. (06/23/2017). Poster presentation at the Center for Electrochemical Energy Science All-Hands Meeting, Argonne National Laboratory.
- **Luu, N. S.,** Hale, L.M., Trautt, Z. Property Calculations Within the Interatomic Potentials Repository Framework. (08/03/2016). Presentation at the NIST Summer Undergraduate Research Fellowship Colloquium.

## PATENTS AND INTELLECTUAL PROPERTY

- U.S. Provisional Patent Application 63/087,385 - Composites with Surface Refining and Conformal Graphene Coating, Electrodes, and Fabricating Methods of Same
- U.S. Provisional Patent Application 63/180,301 - Composite Material with Conformal Graphene Coating, Fabricating Methods and Applications of Same

---

## TECHNICAL SKILLS

- *Data Analysis and Graphics*: Python; Pandas; MATLAB; Adobe Photoshop, Illustrator, Lightroom.
- *Electrochemistry*: galvanostatic cycling; cyclic voltammetry (CV); electrochemical impedance spectroscopy (EIS); performance testing; lithium-ion full cells; cathode synthesis.
- *Materials Characterization*: scanning electron microscopy (SEM); Fourier Transform infrared spectroscopy (FTIR); Raman spectroscopy; thermogravimetric analysis (TGA); X-ray photoelectron spectroscopy (XPS); x-ray diffraction (XRD); energy-dispersive X-ray spectroscopy (EDS); particle size distribution analysis (PSD); inductively coupled plasma spectrometry (ICP); differential scanning calorimetry (DSC); mechanical testing.

## AWARDS AND HONORS

- McCormick School of Engineering Terminal Year Fellowship
- Mentorship Certificate from The Graduate School at Northwestern University
- National Defense Science and Engineering Graduate Fellowship Program Top 200
- National Science Foundation Graduate Research Fellowship Program Honorable Mention
- ASM International Chicago Regional Chapter Award
- Hilliard Award for Leadership, Scholarship and Service
- Northwestern University Materials Science and Engineering Departmental Honors